

Mechanical Properties of Diagonal Laminated Timber (DLT) with Respect to Point-Supported Mass Timber Slabs

Matthias Friedrich Arnold

Vollständiger Abdruck der von der TUM School of Engineering and Design der Technischen Universität München zur Erlangung eines
Doktors der Ingenieurwissenschaften (Dr.-Ing.)
genehmigten Dissertation.

Vorsitz: Prof. Dr.-Ing. Jan-Willem van de Kuilen

Prüfende der Dissertation:

1. Prof. Dr.-Ing. Stefan Winter
2. Prof. Dr.-Ing. Philipp Dietsch
3. Prof. Dr.-Ing. Erik Serrano

Die Dissertation wurde am 02.10.2023 bei der Technischen Universität München eingereicht
und durch die TUM School of Engineering and Design am 01.02.2024 angenommen.

Acknowledgment

This doctoral thesis is a result of my work as a research associate at the Chair of Timber Structures and Building Construction at the Technical University of Munich. It was a privilege and a great honor to be working at Professor Stefan Winter's institute. I thank him for the inspiring and in-depth insights into the research on mass timber structures and for his benevolent support and supervision of this thesis.

My gratitude also goes to Professor Philipp Dietsch for his support and encouragement of this work. I wish to express my appreciation and great respect for his tireless dedication to the education of his students. Many thanks to Professor Erik Serrano for his additional academic review of this dissertation and thank you, Professor Jan-Willem van de Kuilen for chairing the examination committee. Thank you, Dr. Roland Maderebner for the close cooperation during the research on diagonal laminated timber.

I also want to express my gratitude to my former colleagues Dr. Markus Lechner, Dr. Thomas Engel, and Lucas Bienert for the enriching debates on laminated timber elements. And I would like to express my gratitude to the entire team of the Meyer-Jens-Hall, MPA Bau, TU Munich, especially to Klaus Zentner and Armin Lachmann. I was privileged to supervise a number of students during their bachelor's and master's theses. Let me name Thilo Donhauser and Florian Vogel OLY for all the students whom I thank for their great contributions.

I want to thank Dr. Guenther Westner and Carl York Geitner for the many pleasant evenings which we spent delving upon scientific and political discussions. Thank you, Sr. Ruth Ganstaller, for the additional linguistic assistance. I also would like to thank the team of the Oskar von Miller Forum for opening new doors to science and research through a residential grant during my master's studies. And thank you, Dr. Stephan Worack and Dr. Alexander McCluskey[†] for the encouragement to work as a research associate.

Last but not least, I want to thank my family for their continuous and unconditional encouragement and support of my personal development and professional career.

To Mia Arnold 

The research was carried out within the research project InnoCrossLam and has received support by the FNR of the Federal Ministry of Food and Agriculture, Germany, within ERA-NET Cofund ForestValue. The research project received funding from the European Union's Horizon 2020 research and innovation programme under grant agreement N° 773324. The test specimens were produced by Pfeifer Timber GmbH and Holzbau Unterrainer GmbH. Thank you, Mr. Bernd Gusinde, Mr. Matthias Eckert, and Mr. Leonhard Unterrainer.

Abstract

This thesis makes a contribution to the development of diagonal laminated timber (DLT), a composite timber product consisting of individual layers which are rotated to each other at a certain angle to optimize its stiffness properties for specific design situations and applications, such as biaxial bending due to point-supports. Therefore, DLT represents an application-optimized further development of cross laminated timber (CLT).

Within this thesis explanations of mechanical relationships for laminates and their respective behavior are given. The mechanical properties of various different layups of DLT and CLT are investigated by means of analytical, experimental, and numerical investigations. The investigations are carried out with specific DLT series, characterized by layers arranged at angles of $\pm 45^\circ$ respectively $\pm 30^\circ$ ($\pm 60^\circ$). The investigations show that the torsional stiffness of DLT elements is significantly higher compared to CLT elements. This characteristic provides beneficial properties for structures undergoing biaxial bending. At the same time the diagonal arrangement of single layers promises an increase in in-plane stiffness properties, which are of interest for bracing wall and floor systems. The out-of-plane shear stiffness properties of DLT in y direction are higher than those of CLT, while the values in x direction remain in a comparable range. The unidirectional bending properties highly dependent on the chosen layup. Furthermore, DLT provides homogenization effects on the distribution of bending and shear stresses over the cross-section. The outcomes of this research support DLT in becoming an interesting option for mass timber slabs, which are characterized by serviceability limit states (SLS) such as deformations and ultimate limit states (ULS), e.g., concentrated stresses around point-supports.

keywords: diagonal laminated timber (DLT), cross laminated timber (CLT), mass timber composites, laminate theory, out-of-plane shear stiffness, bending stiffness, torsional stiffness, in-plane shear stiffness, deformations, stresses, point-support, serviceability limit state (SLS), ultimate limit state (ULS).

Table of Contents

1	Introduction.....	2	6	Investigations on the out-of-plane shear strength and stiffness.....	59
	1.1 Objective statement.....	2	6.1	Analytical determination of the out-of-plane shear stiffness.....	59
	1.2 Context.....	3	6.1.1	General information.....	59
	1.3 Motivation.....	4	6.1.2	Shear Analogy Method proposed by Kreuzinger.....	59
	1.4 Previous investigations.....	7	6.1.3	Comparison of the analytical results and discussion.....	61
	1.4.1 In-plane load-bearing capacity.....	7	6.2	Experimental determination of the out-of-plane shear strength and stiffness.....	67
	1.4.2 Out-of-plane load-bearing capacity.....	9	6.2.1	Test setup.....	67
	1.4.3 Concentrated loading on laminated mass timber elements.....	11	6.2.2	Description of test evaluation and validation using numerical models.....	69
	1.5 Research gap.....	13	6.2.3	Results of the mechanical testing without external compression.....	75
2	Scope of investigations.....	15	6.2.4	Pre-tests introducing external compression.....	80
	2.1 Structure of the thesis.....	15	6.2.5	Results of the mechanical testing with external compression.....	82
	2.2 Chosen analytical, experimental, and numerical investigations.....	16	6.3	Further investigations using numerical models.....	88
3	Mass timber laminates—general and definitions.....	19	6.3.1	General information and modelling approach.....	88
	3.1 Notation of laminates.....	19	6.3.2	Determination of the shear modulus and comparison of the results.....	88
	3.2 Naming and abbreviations.....	21	7	Investigations on the bending stiffness.....	91
	3.3 Standardization progress of laminated timber elements.....	22	7.1	Theoretical approach and analytical solution.....	91
	3.4 Economic potential.....	24	7.2	Experimental determination of the bending stiffness.....	94
4	Material behavior and configurations.....	25	7.2.1	Test setup.....	94
	4.1 Elastic rheology.....	25	7.2.2	Results of the mechanical testing.....	96
	4.1.1 Linear elastic material law.....	25	8	Investigations on the torsional stiffness.....	99
	4.1.2 Linear elastic material properties of timber.....	27	8.1	Theoretical approach and analytical solution.....	99
	4.2 Viscoelastic rheology.....	29	8.1.1	Theoretical approach.....	99
	4.2.1 Definitions and Boltzmann’s superposition principle.....	29	8.1.2	Analytical solution.....	101
	4.2.2 Time-dependent material law.....	31	8.2	Experimental determination of the torsional stiffness.....	104
	4.2.3 Viscoelastic material properties of timber.....	32	8.2.1	Test setup.....	104
	4.3 Series investigated.....	35	8.2.2	Results of the mechanical testing.....	105
	4.3.1 Configurations, layups, and stacking sequences.....	35	8.3	Investigations on the effective torsional stiffness using numerical models.....	111
	4.3.2 Material parameters of the test series.....	38	8.3.1	General information and modelling approach.....	111
5	Theoretical principles and approaches.....	41	8.3.2	Determination of the torsional stiffness and comparison of the results.....	111
	5.1 Fundamentals of the plate theory.....	41	8.4	Long-term deformation under biaxial bending.....	115
	5.1.1 Drilling of isotropic plates.....	41	8.4.1	General information.....	115
	5.1.2 Kinematics of the 3D continuum.....	42	8.4.2	Proposal for a test setup.....	117
	5.2 Plate stiffness properties.....	44	9	Investigations on the in-plane shear stiffness.....	119
	5.2.1 Stiffness matrix of the unidirectional layer.....	44	9.1	General information and analytical solution.....	119
	5.2.2 Implementation of long-term deformation coefficients.....	44	9.2	Preliminary experimental investigations.....	121
	5.2.3 Transformation of the stiffness matrix.....	45	9.2.1	Test setup and analytical approach—shear frame test.....	121
	5.2.4 Engineering constants in non-principal directions.....	47	9.2.2	Results of the experimental investigations—shear frame test.....	124
	5.2.5 Mechanical coupling and laminate stiffness properties.....	50	9.2.3	Test setup and analytical approach—shear compression test.....	125
	5.2.6 Exemplary ABD - E stiffness matrices for CLT and DLT.....	53	9.2.4	Results of the experimental investigations—shear compression test.....	126
	5.2.7 Derivation of shear correction coefficients.....	54	9.3	Comparison of the experimental and analytical results.....	127

10	Evaluation and quantification using real-scale numerical models.....	129
10.1	Deformation analysis using 2D FE models (SLS).....	129
10.1.1	General information and modelling approach.....	129
10.1.2	Deformation analysis of 5-layered CLT and DLT elements.....	130
10.1.3	Deformation analysis of 7-layered CLT and DLT elements.....	134
10.2	Stress distribution analysis using 3D FE models (ULS).....	140
10.2.1	General information and modelling approach.....	140
10.2.2	Stress distribution analysis of a centric point-supported plate	142
10.2.3	Stress distribution analysis of a plate, point-supported at three corners.....	147
10.3	Discussion based on the results derived from 2D and 3D FE models.....	154
11	Outlook on design processes and production stages of DLT	159
10.4	Design processes of point-supported DLT slabs.....	159
11.1	Considerations on the production stages of DLT.....	162
11.2	Further research tasks regarding the practical implementation of DLT.....	165
12	Summary.....	169
	Bibliography.....	175
	Index of figures and tables.....	189
	Appendix.....	199

Nomenclature

α	angle of load distribution	S_x, S_y	static moment
β_i	angle of tangency	S_{xz}, S_{yz}	out-of-plane shear stiffness
γ_{xy}	in-plane shear strain	$[T]$	transformation matrix
γ_{xz}, γ_{yz}	out-of-plane shear strain	$[T^T]$	inverse transposed transformation matrix
ε_{ij}	strain in the 3D continuum	V_i	shear force
κ_i	single curvature	a_i	shear area
κ_{ij}	double curvature	a, b	side length
ν_{ij}	Poisson's ratio	dx, dy	infinitesimal side length
ϱ	density	e_i	eccentricity
$\sigma_x, \sigma_y, \sigma_z$	stress in the 3D continuum	h	height
τ_{ij}	shear stress	k_z	shear correction coefficient
ξ	ratio of homogenization	$k_{\text{def},i}, k_{\text{T}}, k_{\text{L}}, k_{\text{shear}}$	long-term deformation coefficient
		l_i	length
θ_i	angle of layer orientation	m	slope
$[\Phi]$	creep matrix	m_x, m_y	bending moment on a plate element
Φ_{ij}	creep stiffness terms	m_{xy}	torsional moment on a plate element
$[\Psi]$	relaxation matrix	n_x, n_y	normal force on a plate element
Ψ_{ij}	relaxation stiffness terms	p_i	surface load
		q_{xz}, q_{yz}	shear force on a plate element
A_{ij}	extensional stiffness terms	t	shear flow
B_x, B_y	bending stiffness	t	thickness / depth
B_{xy}	torsional stiffness	t_i	individual layer thickness
B_{ij}	bending-extension coupling stiffness terms	$t_0, t_{\text{fin}}, t_{\infty}$	time points
C_{ij}	stiffness terms in the 3D continuum	u	moisture content
C_i	correction coefficient for accumulated stresses	u_{ij}	shear deformation
D_{ij}	bending-twist coupling stiffness terms	$[u], [v], [w]$	vector notation of displacements
D_x, D_y	extensional stiffness	w_i	deformation, deformation
D_{xy}	in-plane shear stiffness	w	width, board width
E_{ij}	shear stress-strain coupling stiffness terms	x, y, z	global coordinate system
E_i	modulus of elasticity; Young's moduli	x_0, y_0, z_0	initial coordinate system
F	force, load	x', y', z'	local coordinate system of single layers
G_{ij}	shear modulus		
K	plate bending stiffness	<i>mean</i>	mean value
P	point load	<i>max</i>	maximum value
$[Q]$	stiffness matrix	<i>min</i>	minimum value
$[Q]_L$	local stiffness matrix	COV	coefficient of variation
$\overline{[Q]}$	transposed stiffness matrix	FEM	finite element method
Q_{ij}	stiffness terms	FE model	finite element model
$[R]$	Reuter's matrix	MOE	modulus of elasticity
R^2	coefficient of determination	SLS	serviceability limit state
$[S]$	compliance matrix	ULS	ultimate limit state
		UD layer	unidirectional layer

1 Introduction

1.1 Objective statement

The objective of this thesis is to contribute to the development of a construction product made of crosswise and diagonally arranged timber layers towards maturity for application. In particular, diagonal laminated timber (DLT) will be characterized with respect to its mechanical properties as a laminate. Different layouts of conventional cross laminated timber (CLT) are compared to their DLT counterparts regarding the effects of diagonal layer arrangements on the stiffness properties. Theoretical, analytical and numerical approaches for the characterization of DLT are to be derived and applied. For this purpose, the aim must be to transfer approaches already available for CLT to DLT.

By the comparison of DLT to CLT using numerical models on different real-scale static systems of point-supported slabs it will be shown in which design situations diagonal layer arrangements are reasonable and provide benefits regarding deformations and stress distributions around point-supports. In this context, the future goal is to consider DLT as a standard counterpart to CLT for laminated mass timber slabs, which are characterized by serviceability limit states (SLS) like deformations and vibrations, and ultimate limit states (ULS) due to concentrated stresses around point-supports. Consequently, the use of DLT instead of CLT aims at achieving a higher material efficiency within specific applications and thus promotes a more efficient and sustainable use of the resource wood.

Regarding the design process of point-supported mass timber slabs made of DLT, the thesis aims to provide guidance regarding layer orientations and supplementary strength verifications. Based on the findings by the production of the DLT test specimens, suggestions for additional production stages will be given. Another goal is to show which requirements still need to be met in order to reach maturity for the application of DLT and thus which future research needs should be addressed.

In summary, the thesis aims to cover the following issues:

- The derivation of sufficient analytical and experimental approaches for the determination of the stiffness properties of CLT and DLT;
- effects of diagonal layer arrangements on the stiffness properties and resulting advantages within different static systems of laminated mass timber slabs;
- effects of diagonal layer arrangements on the distribution of bending and shear stresses over the cross-section around concentrated load-application;
- and suggestions for the design and production processes and future research on DLT elements.

1.2 Context

In terms of material science, DLT elements belong to the composite materials—more specifically to laminated composites consisting of homogeneous and anisotropic layers. Therefore DLT is a laminated mass timber element, consisting of 3 to 9 layers made from softwood laminations (boards) that are glued together under specific angles θ . For each $-\theta$ layer there is one $+\theta$ layer within the laminate. CLT, on the other hand, consists of individual layers which are glued together in crosswise arrangements only; this occurs at angles of 90° (Figure 1.1). In this context, DLT may be seen as a standard counterpart to CLT.

The individual layers of laminates can either be rigidly connected (glued) or semi-rigidly connected by mechanical fasteners, like nails or screws. With respect to the objective of the thesis, the determination of the stiffness properties is limited to rigidly connected laminates (CLT and DLT). Investigations on nailed laminated timber (NLT) are given within (Krauss 1969), (SCHICKHOFER 1994), and (ARNOLD ET AL. 2023a). It is also important to highlight the divergence of CLT and DLT from laminated veneer lumber (LVL). CLT and DLT consist of layers made of laminations with a thickness of $t_i > 18$ mm in accordance with EN 16351 and thus clearly distinguishes from LVL made of diagonally or star-shaped arranged veneers (see BITTNER 1951 and WINTER 1955).

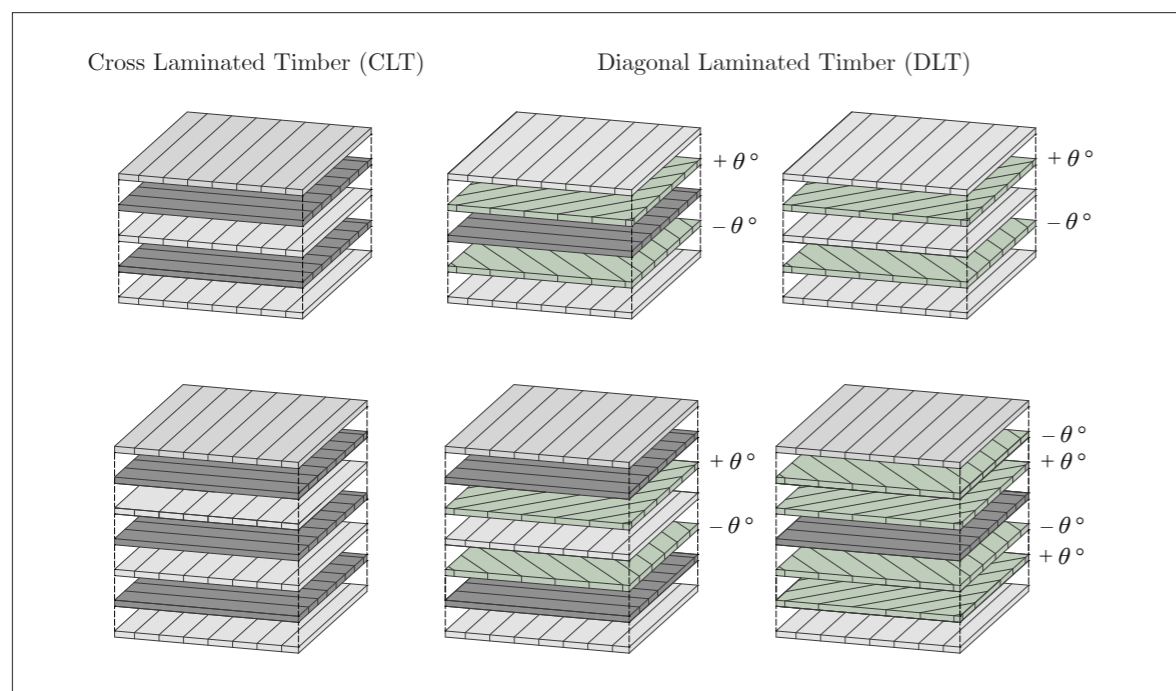


Fig. 1.1: Exemplary layouts of CLT elements compared to DLT elements

1.3 Motivation

The diagonal arrangement of individual layers within laminated mass timber elements promises increased in-plane and out-of-plane stiffness properties. Thus, lower deformations are to be expected for DLT in specific applications, such as point-supported slabs, than for CLT elements using the same thickness and lamination properties. In addition, the diagonal layer arrangement may cause homogenization effects of the orthotropic stiffness and strength properties due to the additional layers oriented in x' and y' directions (Figure 1.2). This could have a positive impact on the stress distributions around concentrated load introduction. Since the SLS (deformations and vibrations, which are directly dependent on the stiffness properties) are usually decisive in the dimensioning of mass timber slabs, as well as concentrated stresses due to concentrated load-application in the ULS, the properties of DLT might lead to a higher efficiency and thus to a more conscious use of the resource wood.

Most applications within mass timber construction are realized with conventional CLT plates for wall, deep beam, and plate elements. Hereby, the construction is designed primarily for uniaxial load transfer, following the major direction of the laminations of the CLT. In recent years the application of mass timber for the construction of multi-story buildings and specific architectural and structural demands have increased the requirements of CLT. Skeleton constructions with point-supported slabs are especially popular for office and multi-story public buildings. The main benefits of this construction are increased clear heights, more flexibility for floor layouts, resource-conscious building due to higher efficiency of the structure by biaxial load transfer, and additional architectural value.

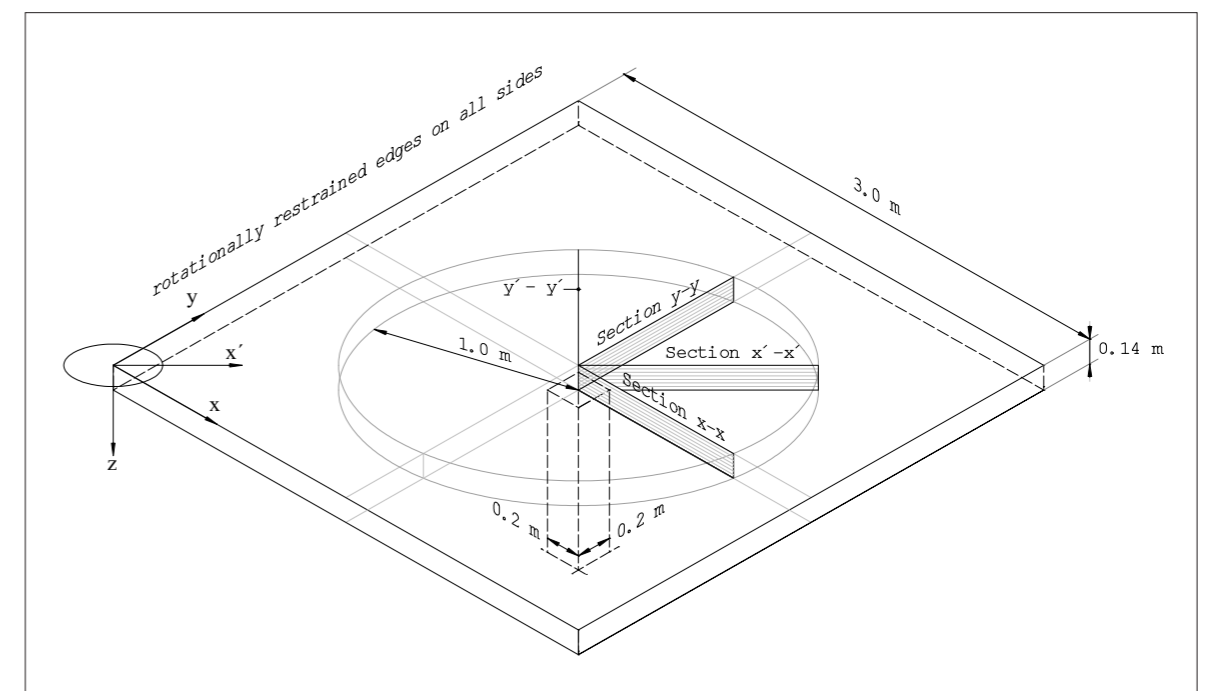


Fig. 1.2: Fictive circular and longitudinal design sections within the centric point-supported mass timber slab

One challenge of point-supported slabs is to handle the concentrated load-introduction. This leads to a concentration of shear stresses, which causes a rolling shear failure in the cross-layers at the ultimate limit state (ULS) (MESTEK 2011, MUSTER 2020, MAURER AND MADEREBNER 2021). Consequently, out-of-plane loaded CLT elements used as slabs tend to be supported linearly on walls or beams (Figure 1.3). The uniaxial load transfer leads to uniaxial bending and thus to a single curvature κ_x , respectively κ_y . The orthotropic design of conventional CLT with one main load-bearing direction is well suited for this purpose.

For a biaxial load transfer, linear supports must be assured on all sides of the plate, i.e., beams or walls must be added in x and y direction or all beams must be removed to achieve point-support. This leads to biaxial bending, i.e., torsion, and thus to a double curvature κ_{xy} (Figure 1.4). Consequently, a mass timber slab designed for point-supports should have, besides a high shear capacity, the highest possible torsional stiffness B_{xy} . This may be achieved by optimizing the arrangement of layers towards this objective. Hence, the focus of this thesis is the evaluation of the increase in torsional stiffness of DLT compared to conventional CLT.

Mass timber elements are often used as bracing and deep beam element within a structure

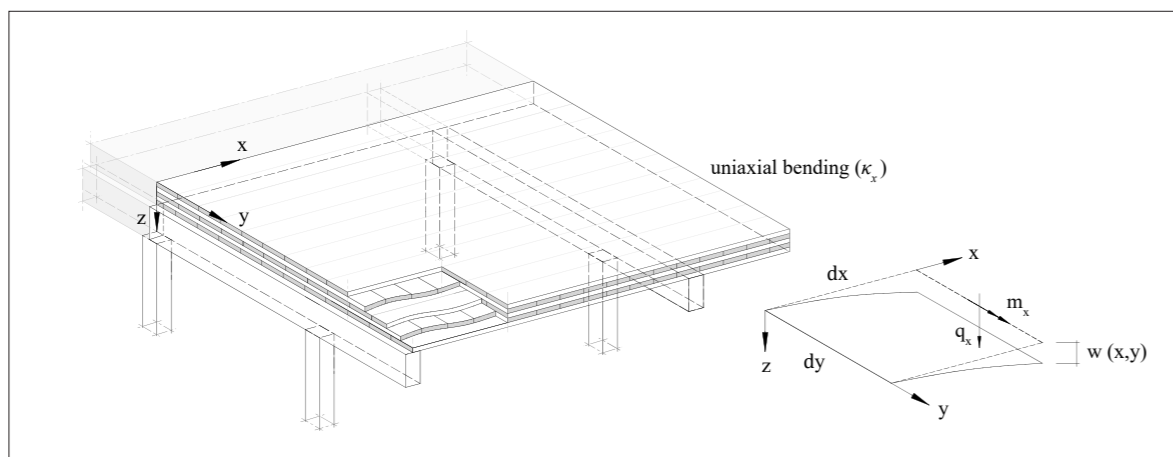


Fig. 1.3: Uniaxial load transfer of conventional CLT elements with linear support

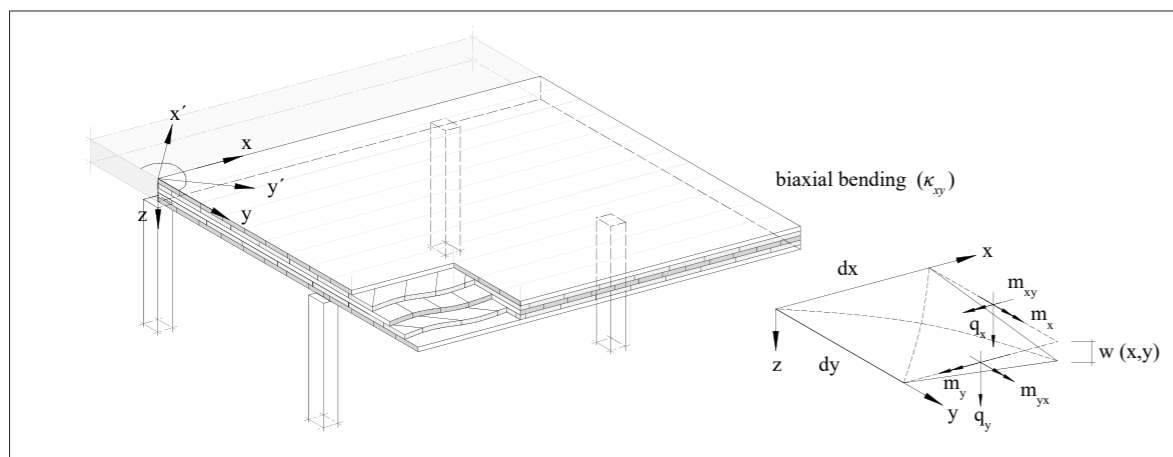


Fig. 1.4: Biaxial load transfer of DLT elements with point-supports

due to its high in-plane shear stiffness (Figure 1.5). It is expected that the rotation of single layers results in the formation of compression and tension struts within the DLT elements. If the longitudinal direction of the laminations follow these compression and tensions struts, an increase in the in-plane shear stiffness of DLT can be expected compared to CLT. This is particularly relevant for the use of DLT for stiffening wall and plate elements as well as for deep beams with large openings and notches.

An application-optimized DLT product that provides the most suitable layup for the respective area of application may be achieved if the layup is adapted to the geometric and static boundary conditions of the overall structure. The maximum deformation of a point-supported slab under a constantly distributed load occurs in the center of the plate, following the respective diagonals between the columns. Transferred to a standard construction grid, the layer arrangements could be adapted to the diagonals (bend lines) between the columns (Figure 1.6). In terms of DLT for in-plane loading, the diagonal layers can be adapted, for example, to the main direction of the respective stress trajectories or to the compression and tension diagonals of a fictive truss.

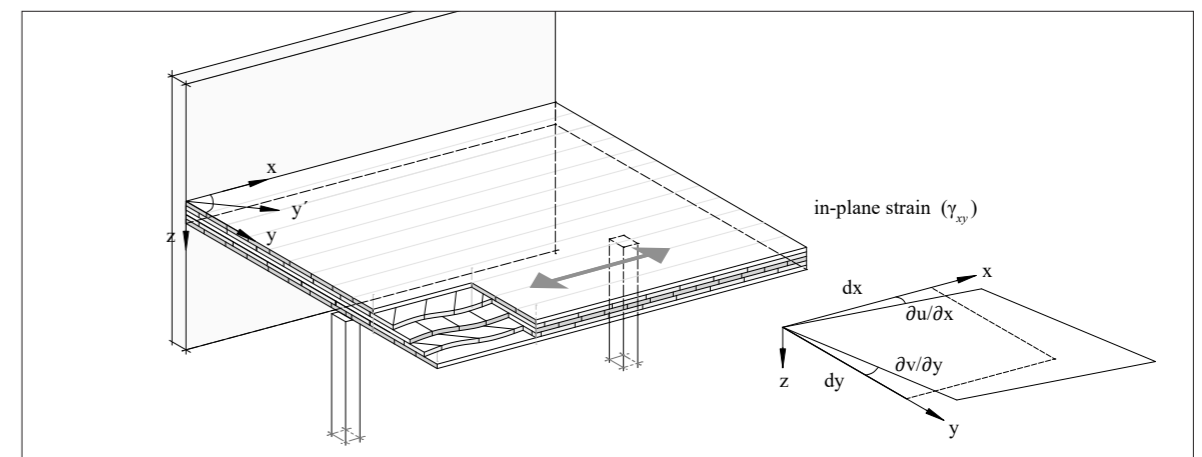


Fig. 1.6: Uniaxial load transfer of conventional CLT elements with linear support

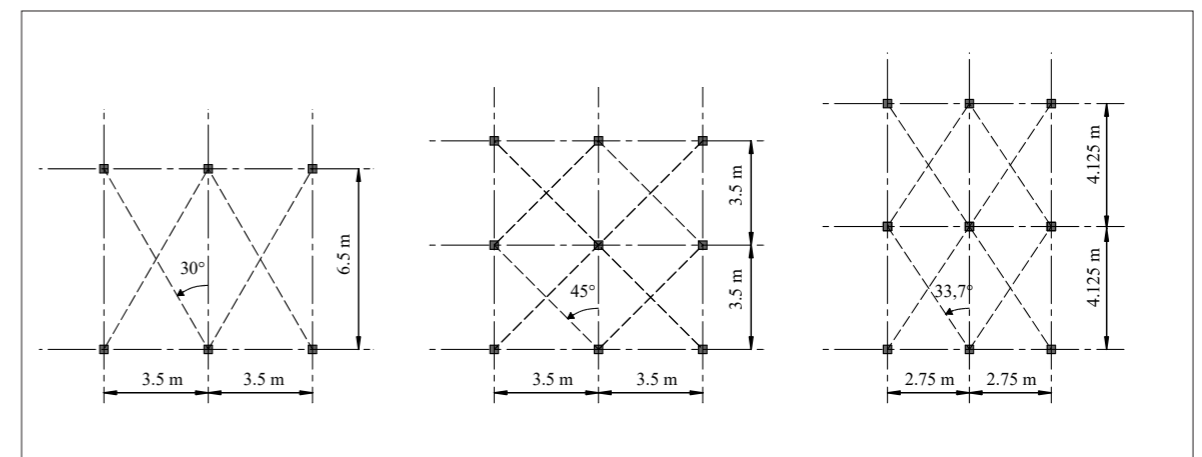


Fig. 1.5: Exemplary construction grid of point-supported slabs with the recommended arrangement of diagonal layers (dashed lines)

1.4 Previous investigations

1.4.1 In-plane load-bearing capacity

This section provides state of the art information on the science of timber laminates—with and without diagonal layer arrangement—and studies on laminated mass timber elements related to experiments carried out within this work. The list is structured chronologically. The in-plane load-bearing capacity of DLT wall elements was investigated first by *Bosl* in 2002 (BOSL 2002). He conducted experiments with modified laminated timber elements where one out of five layers was rotated by 45° , respectively 30° . *Bosl* investigated, among other things, the improved in-plane load-bearing capacity and the effect of the alternative layer arrangement on the in-plane shear stiffness by diagonal compression tests (BOSL 2002) (Figure 1.7). The results show a considerable increase of the in-plane shear capacity by way of the diagonal arrangement of single laminations.

Although there were already construction products such as the Kämpf-web-girder in 1946, that made use of the diagonal arrangements of individual boards (SWISS PATENT NO. 254319, VOORMANN AND PFEIFER 2007), however, these girders are difficult to compare with the mass timber laminate DLT due to their limited number of layers (two) and their interaction as girder with flanges.

In 2010 *Tavoussi*, *Winter* and *Pixner* investigated the in-plane load-bearing capacity of various laminated timber elements with different layer arrangements (diagonal and orthogonal) (TAVOUSSI ET AL. 2010). The investigations were carried out in order to determine high-performance mass timber elements for earthquake-proof bracing structures.

The term DLT was introduced first in 2011, in a publication by the Karlsruhe Institute of Technology (BEJTKA 2011). *Bejtka* used the positive effects of DLT on the in-plane load-bearing capacity and investigated the load-bearing behavior of beam elements made of DLT (BEJTKA 2011).

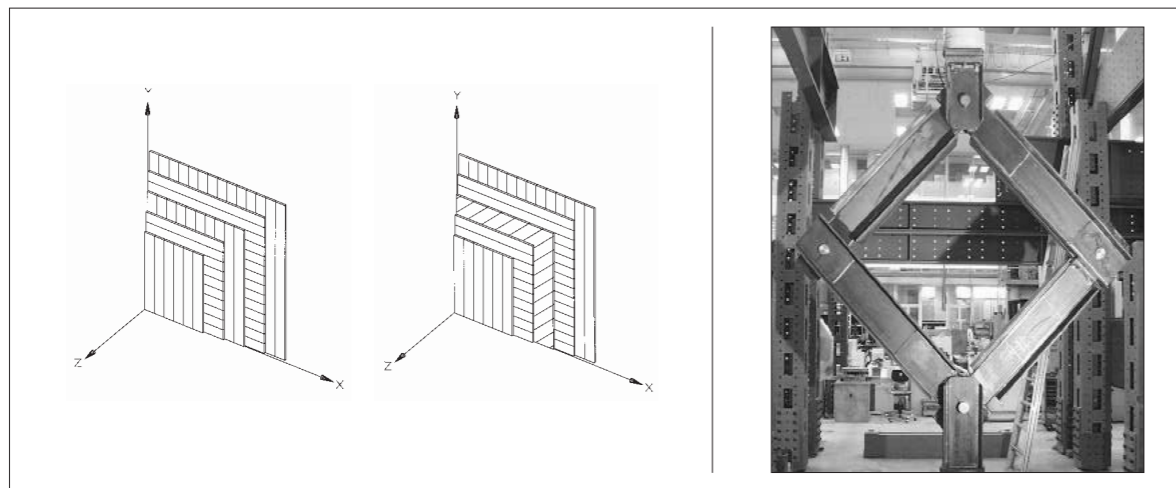


Fig. 1.7: Layup (left) and test setup (right) for investigations on the in-plane load-bearing capacity of mass timber elements with orthogonal and diagonal layer arrangement (Bosl 2002)

Similar to *Bejtka*, *Lechner* also took advantage of the positive influence of diagonal arrangement of individual layers on the in-plane shear stiffness of beam elements. During his Doctoral studies he developed veneer-reinforced timber (VRT)—a composite wood product including veneers inserted under different angles into a glulam cross-section, to act as reinforcement for shear and tensile stresses perpendicular to grain (LECHNER 2021, LECHNER ET AL. 2021). At this point however it is necessary to mind the difference between DLT and LVL again.

With respect to the testing of laminated timber elements in in-plane shear, *Brandner*, *Bogensperger*, and *Schickhofer* developed a test method for the determination of the in-plane shear strength of CLT considering three different failure modes—"net-shear failure" (shear failures perpendicular to grain), "torsion" (failure in the adhesive joint of the single laminations), and "gross-shear failure" (shear failures parallel to the grain in all layers) (BRANDNER ET AL. 2013). These failure modes are based on the investigations of *Blass* and *Görlacher* in 2002 and can be achieved if a corresponding test configuration is applied (BLASS AND GÖRLACHER 2002, BRANDNER ET AL. 2017).

In 2013, *Kreuzinger* and *Sieder* developed a method for the determination of the in-plane shear stiffness and in-plane shear strength of CLT using a simplified method on a representative diaphragm (KREUZINGER AND SIEDER 2013). Based on the method proposed by *Kreuzinger* and *Sieder* and in order to determine shear properties on full-scale CLT diaphragms, *Brandner* and *Dietsch* carried out extensive series of mechanical tests on rectangular CLT elements ($w/l = 0.5/1.5$ m) which took into account various parameters, like the board thickness, gap width and the annual ring patterns (BRANDNER ET AL. 2017).

In order to determine in-plane shear properties on full-scale DLT diaphragms, the so called "picture frame" test configurations can be used, which shows similarities with the chosen test setup of (BOSL 2002). *Andreolli* in 2014 as well as *Turesson* in 2019 investigated the in-plane shear stiffness of CLT using these real-scale "diagonal compression" tests—which are comparable to the previously describes test setup by *Brandner* and *Dietsch*—and "picture frame" tests for the determination of the in-plane stiffness properties of mass timber elements (ANDREOLLI ET AL. 2014, TURESSON ET AL. 2019)(Figure 1.8). The follow-up investigations by *Turesson et al.* in 2020 remark a general problem of "shear compression" tests and "diagonal compression" tests: If the specimens contain layers oriented under $\pm 45^\circ$ and the fibre direction of the laminations is in line with the vertical force flow following the load application, the respective layer is only acting in compression. This may lead to compression failures or buckling, instead of in-plane shear failures. Therefore, *Turesson et al.* investigated 3-layered specimens, making sure no lamella is following the vertical force flow of the load introduction. Using experimental and numerical investigations *Turesson et al.* tried to determine a general equation for calculating the shear moduli of CLT panels, which were tested in diagonal compression and to verify a factor by alternating the main laminate direction of the mid layer from the conventional 90° to 45° and 30° (TURESSON ET AL. 2020) (Figure 1.9).

Since a consistent and unified design approach for CLT at pure in-plane shear loading conditions (shear walls) and at in-plane beam loading conditions is still controversial discussed, *Danielsson* and *Jeleč* presented a review of previously proposed models (DANIELSSON AND JELEČ 2022). Based on comparisons between FE-results and model predictions, they presented a design proposal in order to simplify and unify the different approaches based on consistent mechanical backgrounds (DANIELSSON AND JELEČ 2022).

Compared to the amount of previous research on the in-plane load-bearing capacity of DLT, the out-of-plane load-bearing capacity of DLT has not been pronounced, although diagonal layer arrangement promises numerous advantages for plates acting in bending. In the following, previous research on the out-of-plane load-bearing capacity of DLT elements is summarized.

1.4.2 Out-of-plane load-bearing capacity

The basis of the analytical determination of the stiffness properties of DLT in this thesis is based on previous investigations of *Schickhofer* (SCHICKHOFER 1994) and *Roylance* (ROYLANCE 2000). *Schickhofer* dealt with the fundamentals of the stiffness matrix of the unidirectional layer, specifically of the orthotropic material timber, its transformation into arbitrary orientations, and the interaction/coupling to a laminate. *Schickhofer* also derived an approach for considering out-of-plane shear strains (γ_{xz} , γ_{yz}) and semi-rigid connections between the individual layers.

With respect to biaxial bending, one of the current approaches for the determination of the torsional stiffness of CLT was provided by the diploma thesis of *Silly* in 2010 (SILLY 2010). The focus of the numerical study was the determination of the effects of non-edge-glued laminations or cracked laminations, as well as the number and thickness of layers on the torsional stiffness of CLT (SILLY 2010). Nevertheless, this work was limited to CLT.

The effects of diagonal arrangement of individual layers on the out-of-plane load-bearing capacity were investigated and published first by *Buck et al.* in 2016 (BUCK ET AL. 2016). They carried out four point bending tests on DLT elements. However, the investigations were limited to single-axis bending and a layup mainly suitable for uniaxial load transfer in x direction due to lack of cross-layers (Figure 1.10).

The consideration of the out-of-plane load-bearing capacity inevitably leads to the question how to handle concentrated shear stresses and compression perpendicular to grain for example due to point-supports. Therefore, the following investigations and reference projects are presented with regard to the point-support of mass timber slabs.

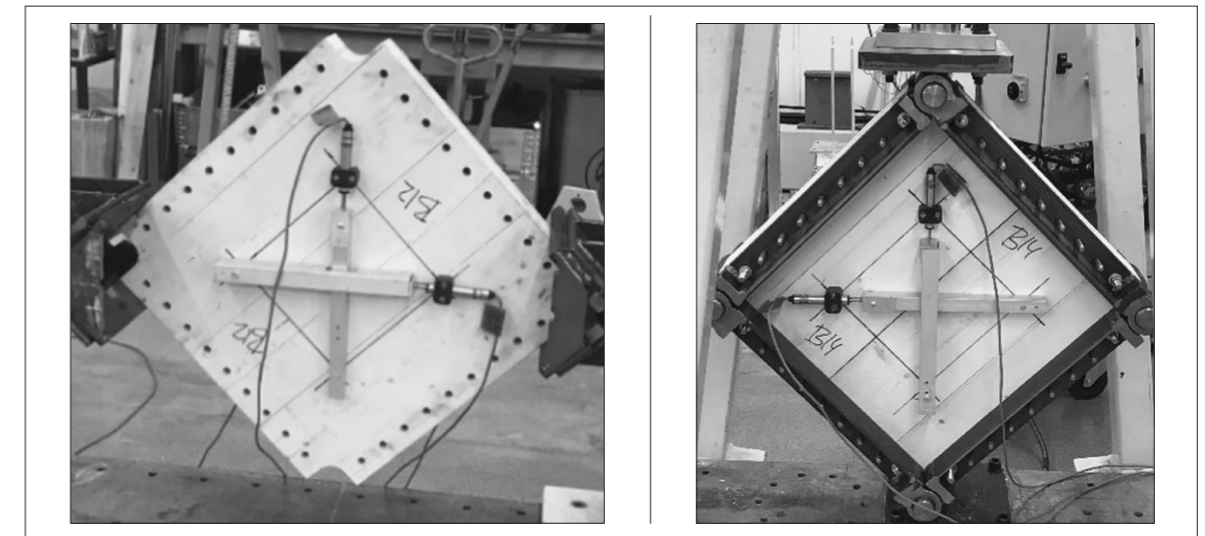


Fig. 1.9: Laminated mass timber elements prepared for the diagonal compression test (left) and picture frame test (right) (TURESSON ET AL. 2019)

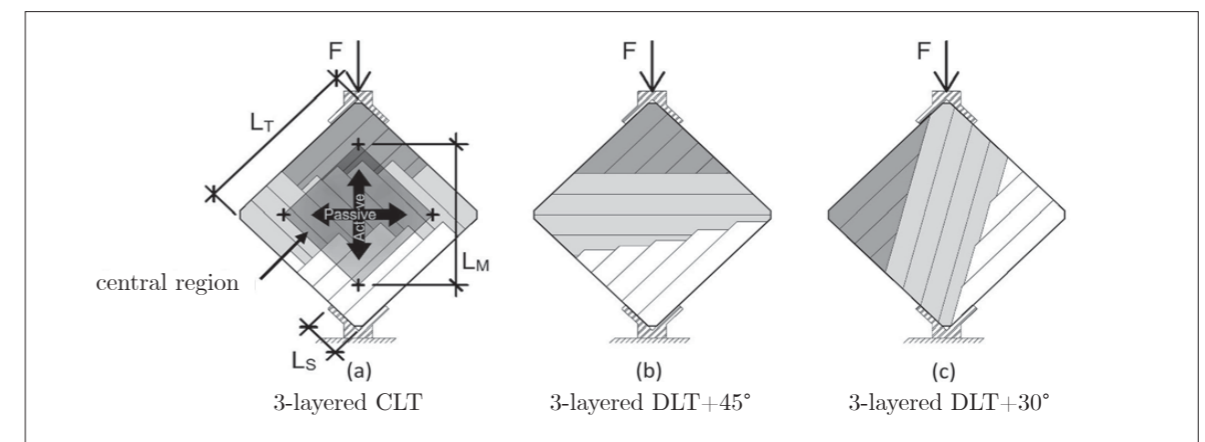


Fig. 1.8: Diagonal compression test on 3-layered CLT and DLT elements (TURESSON ET AL. 2020)



Fig. 1.10: DLT panel with alternating layer configuration in four-point-bending tests (BUCK ET AL 2016)

1.4.3 Concentrated loading on laminated mass timber elements

With respect to point-supported slabs made of laminated mass timber elements, *Mestek* analyzed the interaction of compression perpendicular to grain and rolling shear stresses within CLT elements, with and without reinforcement (MESTEK 2011, MESTEK AND WINTER 2011). His investigations revealed that the distribution of shear stresses in the main and secondary directions under single loads depends on the number of layers and the ratio of the layer thicknesses. The shear strength depends largely on additional compression acting perpendicular to grain, superimposing tensile stresses. The findings provide a simplified method for determining the decisive rolling shear stresses and therefore the load-bearing capacity at points of contracted load introduction into CLT elements. Additionally, *Mestek et al.* used FE volume models to derive a superposition of rolling shear failure and compression perpendicular to grain for CLT.

Maurer and Maderebner at University of Innsbruck investigated the load-bearing behavior of point-supported slabs made of CLT as well as solutions for dealing with stress concentrations in the form of rolling shear and compression perpendicular to grain (MAURER 2020, MAURER AND MADEREBNER 2021). *Maurer* dealt with steel components and system connectors, reinforcing load-introduction points and facilitating load transfer within CLT slabs at the load introduction points (Figure 1.11). Compared to CLT, a potential increase in the out-of-plane capacity of DLT could avoid or reduce the necessity of reinforcement and system connectors (metallic fasteners). This results from the increased shear and torsional stiffness properties.

Muster addresses the problem of column-slab connections in point-supported CLT slabs with central openings at the supports. Since office buildings often have more than one storey, a solution to transfer vertical loads through the slab was developed. To avoid excessive stresses perpendicular to grain in the CLT slab, *Muster* connected the lower column directly to the upper column through an opening in the slab. For the load introduction into the plates he used column-slab connections with additional beech plywood plates, either as column capitals or drop panels (MUSTER 2021) (Figure 1.12).

The publication of *Tapia, Stimpfle, and Aicher* at the University of Stuttgart should also be considered in the context of point-supports of mass timber slabs without additional reinforcements. (TAPIA ET AL. 2021). They investigated a unique column-to-slab bonded connection based on specific orthogonally layered and stepped beech inserts made from laminated veneer lumber (LVL) (Figure 1.13). The upper LVL insert transfers tensile stresses, while the bottom, pyramid-shaped LVL insert is used to support the plate and to handle compressive and out-of-plane shear stresses adequately, both parallel and perpendicular to grain (TAPIA ET AL. 2021).

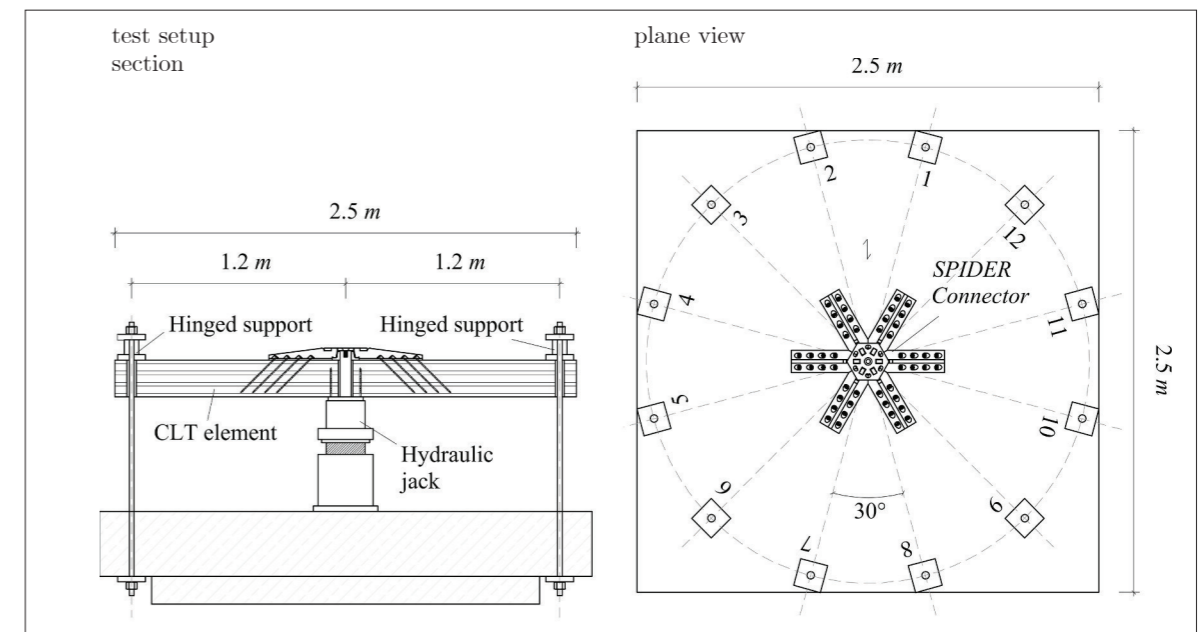


Fig. 1.11: Punching test on CLT element using system connectors (MAURER AND MADEREBNER 2021)

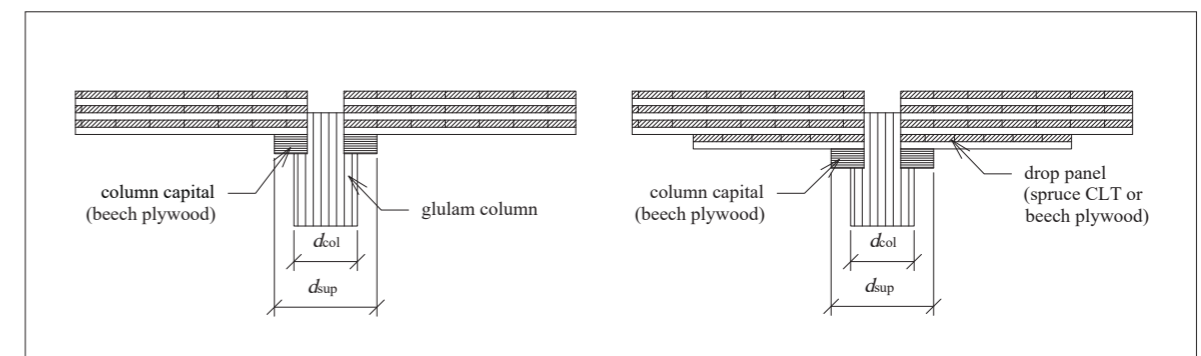


Fig. 1.12: Section through locally reinforced column-slab connections (MUSTER 2021)

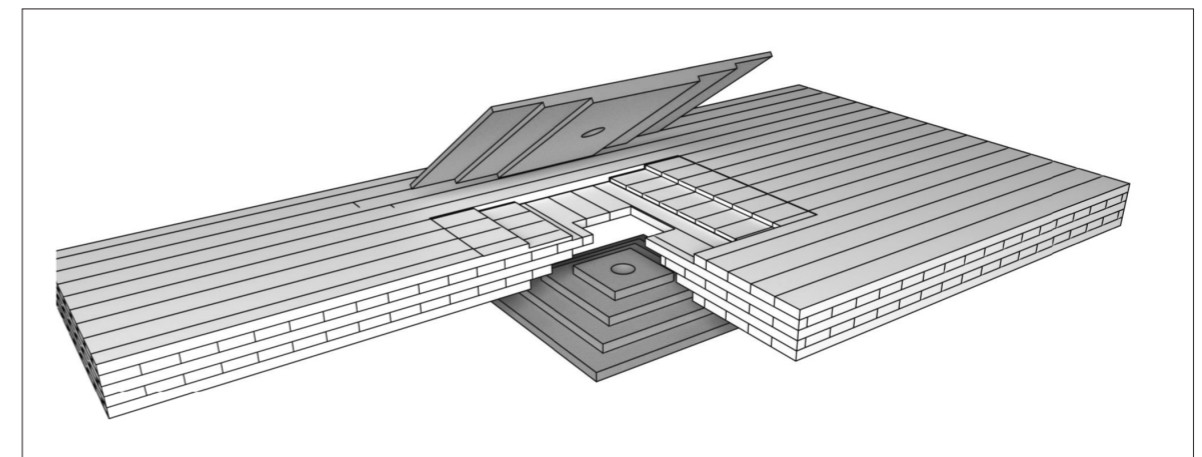


Fig. 1.13: Column-to-slab connection realized by pyramid-shaped LVL inserts (TAPIA ET AL. 2021)

1.5 Research gap

Previous studies mainly dealt with the improved in-plane load-bearing capacity of mass timber laminates by diagonal arrangement of single layers. The state of the art with regard to the out-of-plane load-bearing capacity of DLT is quite different. In the case of uniaxial load transfer, the cross-layers of CLT merely serve as spacers between the layers in the main load-bearing direction. In the interest of resource-conscious building and due to the high value of the material, the cross-layers should be assigned to an increased load-bearing function in addition to their functions such as homogenization towards dimensional stability. Regarding biaxial load transfer of DLT, no results by previous studies were given. This is remarkable, since the load case of torsion or a combination of both, torsion and uniaxial bending, occurs frequently in many structures. For example, this is the case in point-supported plates of any shape, in rectangular plates linearly supported on all sides, in asymmetrically loaded cantilever slabs, and in force-fit hollow sections like stiffening building cores. Although previous numerical investigations on torsional stiffness properties of CLT are abundant, the positive effect due to diagonal layer arrangements has not been investigated up to now.

The same holds true for concentrated load introduction into DLT elements. A more uniform distribution of stresses due to the optimized mechanical properties has not been investigated yet. In concrete slabs as well as in timber slabs, shear force reinforcements are applied in a star-shape on the slab elements around the load application point (see Figure 1.10). In light of this gap, an additional aim is to investigate how far the diagonally arranged layers over point-supports provide homogenization effects on punching shear stresses.

2 Scope of investigations

2.1 Structure of the thesis

Chapter 1 introduces the topic and summarizes previous research on in-plane and out-of-plane load-bearing behavior of CLT and DLT elements. The research gap is identified.

Chapter 2 provides the structure of the thesis and the scope of investigations in full detail.

Chapter 3 introduces fundamentals on laminates and relevant abbreviations. The development of laminated mass timber products is considered in a holistic manner. This includes the current state of standardization as well as the economic relevance.

Chapter 4 summarizes the elastic and viscoelastic rheology of timber. Furthermore, it specifies the material parameters required for the detailed investigations and assigns strength and stiffness classes. The Chapter describes the series chosen for the research.

Chapter 5 summarizes the mathematical principles of laminates and derives the stiffness matrices, forming the basis for analytical solutions.

In Chapter 6, the out-of-plane shear properties of CLT and DLT are determined by using analytical, experimental, and numerical approaches.

Chapter 7 focuses on the determination of the bending stiffness of CLT and DLT and the uniaxial deformation behavior.

In Chapter 8, the torsional stiffness of CLT and DLT is studied by means of analytical, experimental, and numerical investigations. Subsequently statements on the long-term deformation behavior under biaxial bending are derived.

Chapter 9 contains preliminary considerations and different tactile experiments for the determination of the in-plane shear stiffness properties of DLT.

Chapter 10 compares deformations of mass timber slabs made from CLT and DLT within different static systems using real-scale 2D FE models. Stress distributions under concentrated loads and biaxial bending are analyzed using 3D FE models.

Chapter 11 summarizes the design process of DLT slabs based on previous findings. An outlook on the production processes of DLT is presented and future research needs are addressed which are deemed necessary to bring DLT towards maturity for application.

Chapter 12 summarizes the results of the investigations carried out within this thesis.

2.2 Chosen analytical, experimental, and numerical investigations

Within this research, the basics of the plate theories according to *Kirchhoff-Love* and *Reissner-Mindlin* are applied for uniaxial and biaxial bending. These findings lead to an analytical approach for the determination of the stiffness properties of DLT—with and without consideration of the out-of-plane (transverse) shear deformations. The stiffness parameters of timber composites with arbitrary oriented layers can be determined by deriving an extended laminate theory. By implementing girder grid models and applying the working theorem, the out-of-plane stiffness parameters can be extended to effectively existing stiffness values, taking into account out-of-plane shear deformations within the respective static system.

After introducing the theoretical basis for analytical solutions, the experimental investigations start with the determination of the out-of-plane shear stiffnesses of CLT and DLT in global x and y direction. This order was chosen because the shear stiffness is needed when determining the effective bending stiffness values and effective torsional stiffness values. Since the existing and recommended standard shear tests according to EN 16351 and EN 408 refer to single laminations (boards) only, these test setups are in case of DLT not applicable. Within this thesis, a shear test setup based on EN 408 and the findings of (MESTEK 2011) is further developed for the testing of DLT specimens (Figure 2.1). The developed setup enables the shearing of packages of three layers, instead of single layers. In this way, the shear stiffnesses and strength values of entire laminates containing diagonally arranged layers—as is the case for DLT—can be determined. The experiments for determining the out-of-plane shear properties are carried out both, without (Figure 2.1, left) and with (Figure 2.1, right) compression perpendicular to grain.

For the determination of the bending stiffness of DLT an analytical approach is developed and validated by four-point bending tests. The test setup is based on bending tests according to EN 16351 (Figure 2.2). Numerical parameter studies determine the increase in bending stiffness in the major load-bearing direction (x direction) due to diagonal layer arrangements. The investigations of the bending stiffness properties (uniaxial bending) are followed by investigations on the torsional stiffness properties (biaxial bending). Biaxial bending appears to be a complex and challenging load-case. Torsion leads to the coupling of different stresses resulting from combined torsion, unidirectional bending, and out-of-plane shear in both, global x and y direction. After the investigations of the out-of-plane shear stiffness values, the in-plane stiffness properties are determined by way of analytical methods and biaxial bending tests. Therefore, an test setup based on findings of (MESTEK 2011) and (LÖBUS AND WINTER 2017) was further developed, suitable to carry out biaxial bending test on a high number of specimens (see Figure 2.3). The proposed test setup and some of the results including numerical parameter studies were pre-published in (ARNOLD ET AL. 2022a).

Even though this dissertation prioritizes on CLT and DLT loaded out-of-plane, and especially the biaxial load transfer, tactile in-plane shear tests are carried out in order to

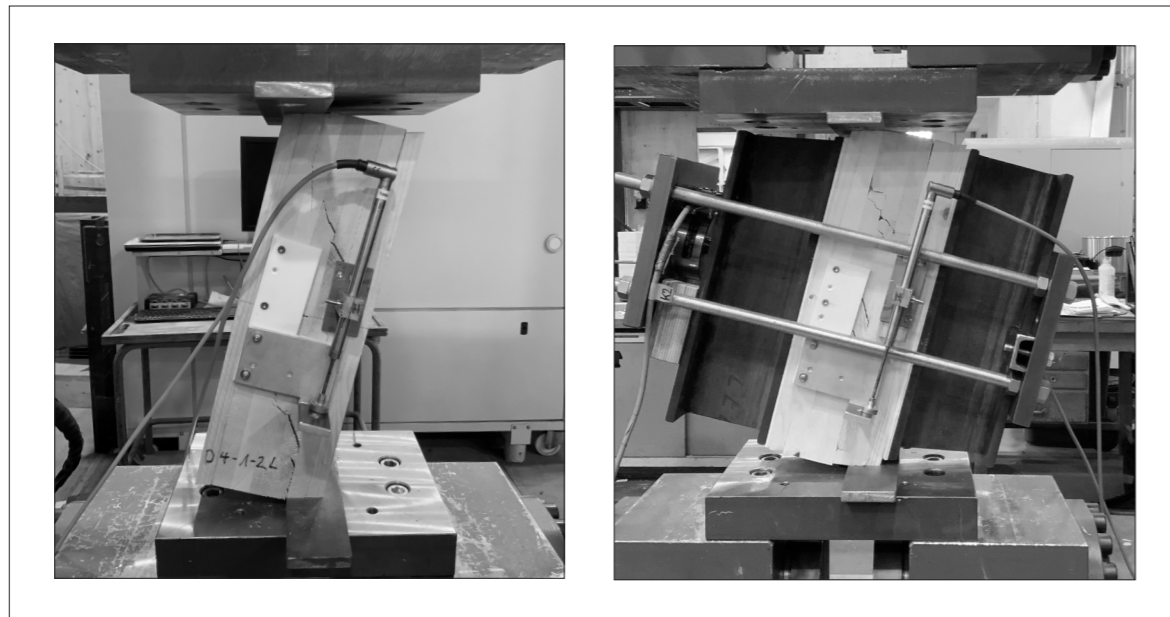


Fig. 2.1: Small-scale shear testing on CLT and DLT specimens, without (left) and with (right) compression perpendicular to grain

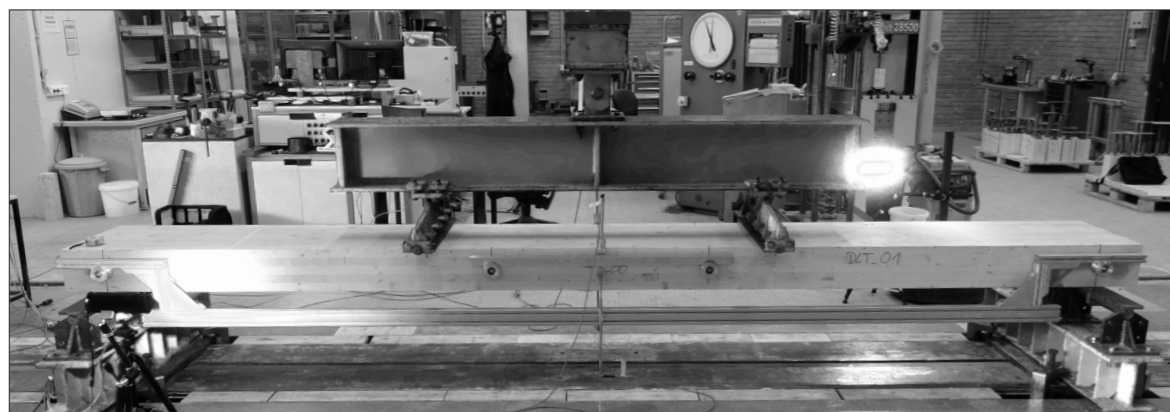


Fig. 2.2: Four-point bending tests on DLT elements at University of Innsbruck



Fig. 2.3: Biaxial bending tests on CLT and DLT elements

give a statement on the in-plane shear capacity of DLT, compared to CLT. The diagonal arrangement of single layers may lead to an increase in in-plane shear stiffness properties. For the experimental investigations on the in-plane shear stiffness, two different test methods are applied. One is the "shear compression" test in accordance with the method proposed by Kreuzinger and Sieder, which is applicable for CLT elements (KREUZINGER AND SIEDER 2013). For the determination of the in-plane shear stiffness of DLT elements, a test setup is chosen in accordance with the "picture frame" ("shear frame") and "diagonal compression" test by Andreolli and Turesson (ANDREOLLI ET AL. 2014, TURESSON ET AL. 2019) (Figure 2.4).



Fig. 2.4: Determination of the in-plane shear stiffness using shear frame tests

In addition to the analytical and experimental investigations using numerical models, the investigated stiffness properties are introduced into numerical 2D and 3D models. These models help to analyze the deformation behavior and stress distributions using the finite element method (FEM). The 2D FE models lead to a quantitative statement on the efficiency of DLT compared to CLT within real-scale application scenarios, regarding deformations of laminated mass timber slabs. The 3D FE models provide information on the distribution of concentrated stresses as a function of different layups around point-supports of mass timber slabs within the ultimate limit state (ULS). Table 2.1 summarizes the analytical, experimental and numerical investigations carried out within this thesis.

Tab. 2.1: Investigations carried out within this thesis

investigations	analytical investigations	experimental investigation	numerical investigations
out-of-plane shear	■	■ ¹	■
uniaxial bending	■	■	
biaxial bending (torsion)	■	■	■
in-plane shear	■	■ ²	
deformation analysis and stress distribution analysis			■ ³

¹out-of-plane shear tests according to EN 408 and (MESTEK 2011) with and without compression perpendicular to grain

²compression tests according to (KREUZINGER AND SIEDER 2013) and shear frame tests according to (TURESSON ET AL. 2019)

³2D and 3D FE models of different static systems of point-supported slabs

3 Mass timber laminates—general and definitions

3.1 Notation of laminates

CLT and DLT elements belong to the mass timber laminates consisting of homogeneous and anisotropic layers. In general, the construction product DLT follows the descriptions and specifications according to the European Assessment Document (EAD) 130005-00-0304 (mass timber slab elements to be used as structural elements in buildings). A deviation from these specifications arises from the orientation of the individual layers to each other under arbitrary angles. The coordinate system used for the laminate determines its stacking sequence. The number of layers can vary between 3 to 9, depending on the specific area of application and the required mechanical properties. The layers oriented in x direction are defined 0° layer according to their wood fiber direction (Figure 3.1). Laminates are denoted by the rotation of the layers, referred to as x axis. With respect to the orientation of the z-axis, the coordinate system is counter-clockwise positive. The laminate at the right side of Figure 3.1 can be exemplarily denoted to the stacking sequence (bottom to top) $[0^\circ, 45^\circ, 90^\circ, -45^\circ, 0^\circ]_s$.

Each layer of the laminate is considered to be an unidirectional layer (UD layer) with ideally straight fibers, providing transversal isotropy. Thus, the following assumptions are made:

- The fiber arrangement over the cross-section of each layer is considered to be continuous.
- Normal stresses perpendicular to grain do not cause displacements
- Each layer is considered to have a reduced stiffnesses matrix $[Q]$ to act in the plane stress state ($\sigma_z = 0$) (SCHÜRMAN 2007).
- The bond between the layers is ideal and considered rigid. The thickness of the adhesive layer is neglected (SCHÜRMAN 2007).
- There is no restraint in the thickness direction, which leads to a reduction of the stiffnesses in the plane (NETTLES 1994).
- Lateral strains are coupled to the normal strains by the *Poisson's* ratio following *Hooke's* law of elasticity.

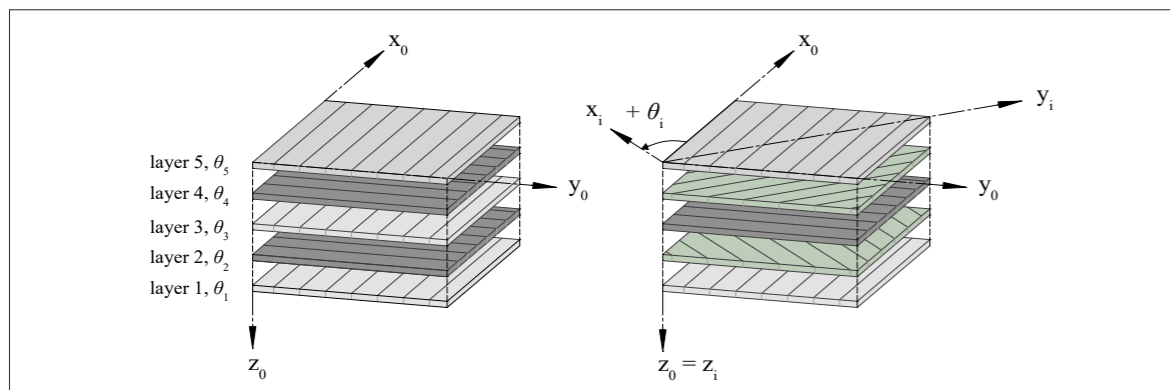


Fig. 3.1: Notation of laminates on a CLT element (left) and DLT element (right)

The detailed derivation of the stiffness properties follows the laminate theory and is provided in Chapter 5. Thereby, the notation of the stiffness matrix of the unidirectional layer is described, followed by the derivation of the stress resultants and their mechanical coupling. Laminates are characterized by their response to mechanical loading, which is associated with a description of their coupling behavior. In addition, the matrix notation of the law of elasticity on the plate element is presented.

A laminate is called balanced and symmetric, if the material properties, the thickness of the layers, and the orientation of the layers are symmetric about the midplane. CLT is a balanced and symmetric laminate resulting in simplifications within the stiffness matrix ($A_{16} = A_{26} = D_{16} = D_{26} = E_{54} = 0$). Furthermore, laminates with described characteristics have no coupling between the bending and extension stiffness terms ($B_{ij} = 0$) (REDDY 2004). The laminate stiffness matrix of a balanced, symmetrical laminate is given by Equation (3.1) (Without taking into account *Poisson's* ratios) (JONES 2014).

$$[Q] = \begin{bmatrix} A_{11} & A_{12} & 0 & 0 & 0 & 0 & 0 & 0 \\ A_{12} & A_{22} & 0 & 0 & 0 & 0 & 0 & 0 \\ 0 & 0 & A_{66} & 0 & 0 & 0 & 0 & 0 \\ 0 & 0 & 0 & D_{11} & D_{12} & 0 & 0 & 0 \\ 0 & 0 & 0 & D_{12} & D_{22} & 0 & 0 & 0 \\ 0 & 0 & 0 & 0 & 0 & D_{66} & 0 & 0 \\ 0 & 0 & 0 & 0 & 0 & 0 & E_{55} & 0 \\ 0 & 0 & 0 & 0 & 0 & 0 & 0 & E_{44} \end{bmatrix} \quad (3.1)$$

DLT is a balanced and antisymmetric laminate. The layers of the laminate are a mirror image with respect to the geometrical midplane. Consequently, for each $+\theta$ layer in the laminate there is an equally thick $-\theta$ layer (NETTLES 1994). In addition, these layers have the same thicknesses. For antisymmetric, balanced laminates, simplifications according to (REDDY 2004) can be made ($A_{16} = A_{26} = D_{16} = D_{26} = B_{11} = B_{12} = B_{22} = B_{66} = E_{54} = 0$) which leads to the stiffness matrix in Equation (3.2) (JONES 2014).

$$[Q] = \begin{bmatrix} A_{11} & A_{12} & 0 & 0 & 0 & B_{16} & 0 & 0 \\ A_{12} & A_{22} & 0 & 0 & 0 & B_{26} & 0 & 0 \\ 0 & 0 & A_{66} & B_{16} & B_{26} & 0 & 0 & 0 \\ 0 & 0 & B_{16} & D_{11} & D_{12} & 0 & 0 & 0 \\ 0 & 0 & B_{26} & D_{12} & D_{22} & 0 & 0 & 0 \\ B_{16} & B_{26} & 0 & 0 & 0 & D_{66} & 0 & 0 \\ 0 & 0 & 0 & 0 & 0 & 0 & E_{55} & 0 \\ 0 & 0 & 0 & 0 & 0 & 0 & 0 & E_{44} \end{bmatrix} \quad (3.2)$$

3.2 Naming and abbreviations

Nowadays, the abbreviation DLT is also used for dowel laminated timber (SOTAYO ET AL. 2020), a mass timber panel created by stacking laminations together on its edge, fit together with dowels made of softwood or hardwood. A more general designation of dowel laminated timber is dowelled wood (DW) (EPP 2018).

On the other hand, the abbreviation DLT was already introduced in 2011 by *Bejtka* for diagonal laminated timber (BEJTKA 2011) (see Chapter 1.4). As for CLT, the use of the abbreviation DLT for diagonal laminated timber describes the geometric property of the mass timber product, and not a method of fitting. In 2021 and 2022 *Maderebner*, *Dietsch*, and *Arnold* established the abbreviation DLT for diagonal laminated timber, among, others within a publication on the torsional stiffness (MADEREBNER 2021; ARNOLD ET AL. 2022a). However, a possible alternative term for the description of DLT could be inclined laminated timber, which would be abbreviated as ILT.

The compendium in Table 3.1 represents a list of abbreviations used for widely known mass timber products. These abbreviations can be found in various sources and literature and are generally used in the timber production and forest-based industries. For diagonal laminated timber the abbreviation DLT is suggested—for dowel laminated timber the abbreviation DW is suggested, following (EPP 2018).

Tab. 3.1: Abbreviations used for mass timber products

abbreviation	alternative	naming	naming in German language
CLT	X-Lam	cross laminated timber	Brettsperrholz
CLT-D		cross laminated timber made from hardwood	Brettsperrholz aus/mit Hartholz-Lamellen
DLT ¹	ILT	diagonal laminated timber/ inclined laminated timber	Diagonallagenholz ² / Diagonal verklebtes Brettsperrholz
NLT		nailed laminated timber/ nail-laminated timber	Vernageltes Brettsperrholz/ Genageltes Brettsperrholz
DLT	DW ³	dowel laminated timber/ dowelled wood	Gedübelte Brettstapeldecke/ Dübelholz
GLT	Glulam	glued laminated timber	Brettschichtholz
VRT	VRW ⁴	veneer reinforced timber/ veneer reinforced wood	Holzbewehrtes Holz
MPP		mass plywood panel	Sperrholzplatten
LVL		laminated veneer lumber	Funierschichtholz

¹Suggested abbreviation by BEJTKA 2011, MADEREBNER 2021 and ARNOLD ET AL. 2022a
²Suggested naming by DIETSCH 2022 and ARNOLD ET AL. 2023b
³Abbreviation recommended for future use
⁴Recently introduced by LECHNER 2021

3.3 Standardization progress of laminated timber elements

In the context of the European Cooperation in Science and Technology Program (COST Action FP1402/WG2, "Basis of Structural Timber Design – from Research to Standards") a state of the art report (STAR) on the properties, testing, and design of CLT was carried out by several European research institutions (BRANDNER ET AL. 2018). Within this STAR, all prior research and developments on CLT were summarized and unified, and put into chronological order. The aim of these outputs was to develop a draft for the implementation of CLT in a revised version of the European Design Standard, Eurocode 5 (EC 5) (BRANDNER ET AL. 2018).

Mass timber slab or wall elements are primarily made of softwood boards, which may be finger jointed to endless laminations, bonded together in order to form CLT (EAD 130005-00-0304). Currently, DLT is not covered by EAD 130005-00-0304, due to the orientation of individual layers deviating from 0° and 90° to each other. A future goal could be to extend EAD 130005-00-0304, in order to cover mass timber slabs containing diagonal layer arrangement as well as laminations made of hardwood, like beech or oak. Alternatively, the introduction of a new EAD for DLT could be announced.

CLT shall be produced according to EN 16351 (product provisions) or a European Technical Assessment (ETA) on the basis of European Assessment Document EAD 130005-00-0304. By now, EN 16351:2021 has not yet been published in the Official Journal of the European Union. Therefore, product provisions for CLT are not covered by a harmonized

European standard. This leads to relatively heterogeneous manufacturer-specific products without harmonized dimensions and layups. Mass timber elements, like CLT, thus cannot be replaced easily by another without redesigning the respective structure or assembly situation. Furthermore, the design of CLT is not covered in the current EC 5. The latter is an aim for the future.

Following standardization mandate M/515 (EUROPEAN COMMISSION 2012) the Eurocodes are amended and updated towards a second generation in order to ensure applicability and focus further on users' needs (SCHENK AND WINTER 2021). EC 5 is part of the Structural Euro-codes under the European Committee for Standardization (CEN) Technical Committee CEN/TC 250 (Figure 3.2).

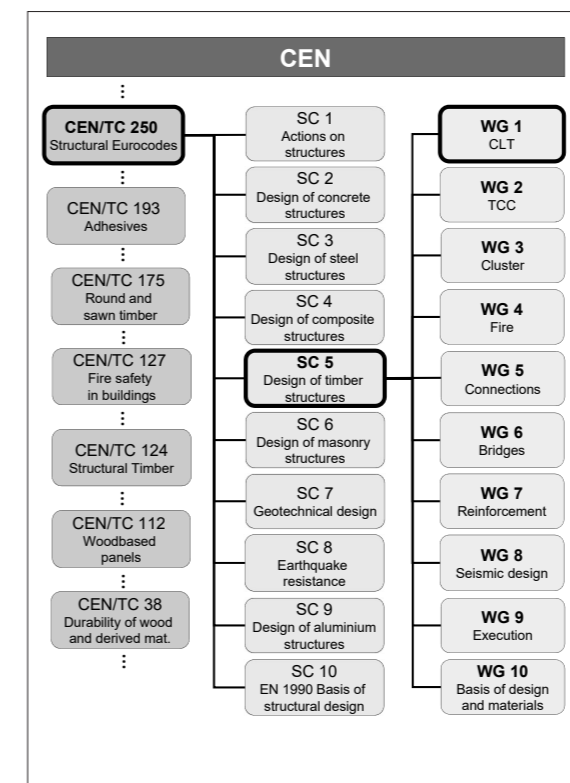


Fig. 3.2: CEN/TC 250 and CEN/TC 250/SC 5 work structure (SCHENK AND WINTER 2021)

Within the second generation, new clauses within EC 5-1-1 are added with a narrow and specific scope to CLT and its design rules. The draft of the design rules for CLT—submitted within the scope of working group CEN/TC 250/SC 5/WG 1—is currently available (prEN 1995-1-1:2023). The future goal is to continue implementing a strength class system for CLT within EN 16351, analogous to those of GLT (see BRANDNER ET AL. 2023).

The publication of the second generation of EC 5 in Europe is planned until September 2027. In Germany, the building authorities coordinate the availability and publication of the revised EC 5 for 2026. The date for the withdrawal of the old generation of EC 5 is March 2028 (SCHENK AND WINTER 2021). A more detailed schedule on the process of the second generation of Structural Eurocodes and further information on the revision of the first generation of Structural Eurocodes can be found in (KLEINHENZ ET AL. 2016) and (SCHENK AND WINTER 2021).

3.4 Economic potential

The manifold advantages of mass timber construction—and specifically laminated mass timber plates—had a huge impact on growing production capacities over the past decades. Surveys of the Portal *Holzkurier* show that, prior to 2010, the estimated CLT production volume in the European countries Austria, Switzerland, Germany, Italy, and the Czech Republic was approximately 250,000 m³ per year, while the production volume in 2022 has already reached 1,28 million m³ (JAUK 2020, JAUK 2023). Forecasts for the production volume in 2023 for Europe as a whole are up to 2.3 million m³ CLT (JAUK 2023) and—as a reference value—up to 4.6 million m³ GLT (EBNER 2022)).

The majority of the laminated mass timber plates currently available on the European market are manufactured by gluing (bonding) and have symmetrical, cross laminated layups. Currently, EAD 130005-00-0304 covers 51 ETAs for CLT (EOTA 2023). A glued mass timber product using diagonal arrangement of single layers (like DLT), is not available on the market up to now. As previously mentioned, EAD 130005-00-0304 could be extended towards diagonal layer arrangements as a first step.

Despite many advantages, the application of mass timber products—such as CLT or DLT—still lags behind mineral-based building materials such as (reinforced) concrete structures and masonry. One of the reasons are deficiencies in standardization (see Chapter 3.3). A lack of information on the fire resistance and local and inconsistent policies and legislation may still hinder the erection of timber buildings (also see SCHENK ET AL. 2022). The future economic potential of laminated mass timber products is also linked to further development and advancement of new and existing mass timber products, such as DLT or VRT. In addition, BIM based general design models and 3D-planning should be established (WINTER ET AL. 2018). While timber is a predestined material for prefabrication, further development is a chance for timber construction to take the lead in a future industrialization process of the building industry (WINTER ET AL. 2018).

The optimization of mass timber products for application by adding additional functionality may also encourage this process. Mass timber products for optimized applications or with additional functionality add value and have a future market potential. For example a CLT element, being multifunctional in terms of its thermal activation, had been further developed toward maturity for application at Technical University of Munich (MINDRUP 2019; ARNOLD ET AL. 2022b). In previous research, CLT has also been improved by adding channels for prestressing-cables (GRÄFE ET AL. 2018).

4 Material behavior and configurations

4.1 Elastic rheology

4.1.1 Linear elastic material law

Hooke's Law of elasticity describes the fundamentals of the linear elastic deformation behavior of solid materials. The constitutive Equations describe the relationship between stresses σ_{ij} and strains ε_{ij} . In case of an uniaxial stress state, *Hooke's Law* considers a linear relationship between stresses and strains. These constitutive Equations (material Equations) are presented by Equations (4.1) to (4.3).

$$\sigma = E \cdot \varepsilon_{\parallel} \quad (4.1)$$

$$\tau = G \cdot \gamma \quad (4.2)$$

$$\nu = -\frac{\varepsilon_{\perp}}{\varepsilon_{\parallel}} \quad (4.3)$$

Considering a 3D continuum, elasticity stiffness tensors C_{ij} are used to describe the elasticity of an element—instead of the moduli of elasticity E_i (Equation (4.1)) or the shear moduli G_{ij} (Equation (4.2)). Considering infinitesimally small elements, the stresses and strains acting in the three principal directions are shown in Figure 4.1. The law of elasticity of a 3D continuum can be described according to Equation (4.4) using matrix notation of the stiffness matrix $[C]$. The compliance matrix $[S]$ is given by Equation (4.5) ($[S] = [C]^{-1}$).

$$\begin{bmatrix} \sigma_1 \\ \sigma_2 \\ \sigma_3 \\ \tau_{23} \\ \tau_{13} \\ \tau_{12} \end{bmatrix} = \begin{bmatrix} C_{11} & C_{12} & C_{13} & C_{14} & C_{15} & C_{16} \\ C_{21} & C_{22} & C_{23} & C_{24} & C_{25} & C_{26} \\ C_{31} & C_{32} & C_{33} & C_{34} & C_{35} & C_{36} \\ C_{41} & C_{42} & C_{43} & C_{44} & C_{45} & C_{46} \\ C_{51} & C_{52} & C_{53} & C_{54} & C_{55} & C_{56} \\ C_{61} & C_{62} & C_{63} & C_{64} & C_{65} & C_{66} \end{bmatrix} \cdot \begin{bmatrix} \varepsilon_1 \\ \varepsilon_2 \\ \varepsilon_3 \\ \gamma_{23} \\ \gamma_{13} \\ \gamma_{12} \end{bmatrix} \quad (4.4)$$

$$\begin{bmatrix} \varepsilon_1 \\ \varepsilon_2 \\ \varepsilon_3 \\ \gamma_{23} \\ \gamma_{13} \\ \gamma_{12} \end{bmatrix} = \begin{bmatrix} S_{11} & S_{12} & S_{13} & S_{14} & S_{15} & S_{16} \\ S_{21} & S_{22} & S_{23} & S_{24} & S_{25} & S_{26} \\ S_{31} & S_{32} & S_{33} & S_{34} & S_{35} & S_{36} \\ S_{41} & S_{42} & S_{43} & S_{44} & S_{45} & S_{46} \\ S_{51} & S_{52} & S_{53} & S_{54} & S_{55} & S_{56} \\ S_{61} & S_{62} & S_{63} & S_{64} & S_{65} & S_{66} \end{bmatrix} \cdot \begin{bmatrix} \sigma_1 \\ \sigma_2 \\ \sigma_3 \\ \tau_{23} \\ \tau_{13} \\ \tau_{12} \end{bmatrix} \quad (4.5)$$

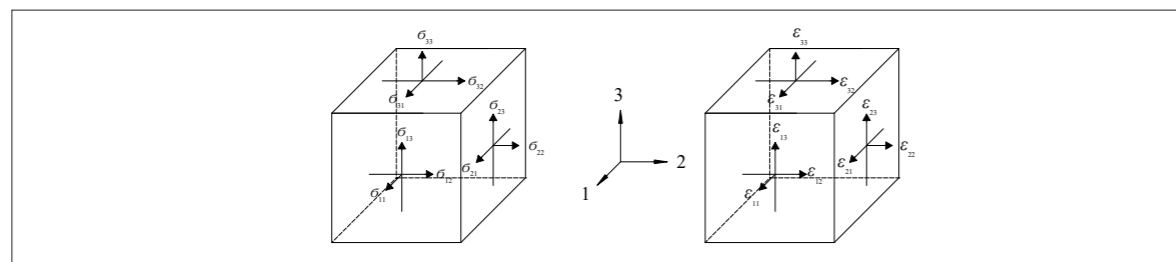


Fig. 4.1: Stresses and Strains acting on the 3D continuum, according to (NIEMZ AND SONDEREGGER 2017)

Symmetries to the midplane or rotational symmetries can reduce the number of necessary independent stiffness tensors. With respect to the description of the material properties of wood, three symmetric planes, aligned perpendicular to each other, are describing its orthotropic material behavior (Figure 4.2). The three principal directions of wood describe its material properties with respect to the fibre direction (longitudinal to the grain (x axis), tangential to the grain (y axis), and radial to the grain (z axis)). Adapting the principal directions to a Cartesian coordinate system and taking into account the orthotropic material behavior, the matrix notation is described by Equation (4.6):

$$\begin{bmatrix} \sigma_x \\ \sigma_y \\ \sigma_z \\ \tau_{yz} \\ \tau_{xz} \\ \tau_{xy} \end{bmatrix} = \begin{bmatrix} C_{11} & C_{12} & C_{13} & 0 & 0 & 0 \\ C_{21} & C_{22} & C_{23} & 0 & 0 & 0 \\ C_{31} & C_{23} & C_{33} & 0 & 0 & 0 \\ 0 & 0 & 0 & C_{44} & 0 & 0 \\ 0 & 0 & 0 & 0 & C_{55} & 0 \\ 0 & 0 & 0 & 0 & 0 & C_{66} \end{bmatrix} \cdot \begin{bmatrix} \varepsilon_x \\ \varepsilon_y \\ \varepsilon_z \\ \gamma_{yz} \\ \gamma_{xz} \\ \gamma_{xy} \end{bmatrix} \quad (4.6)$$

By replacing the stiffness tensors C_{mn} with the respective moduli of elasticity E_i and shear moduli G_{ij} taking into account the *Poisson's* ratios, the law of elasticity of wood is described using the compliance matrix $[S]$ within Equation (4.7):

$$\begin{bmatrix} \varepsilon_x \\ \varepsilon_y \\ \varepsilon_z \\ \gamma_{xy} \\ \gamma_{xz} \\ \gamma_{yz} \end{bmatrix} = \begin{bmatrix} \frac{1}{E_x} & -\frac{\nu_{xy}}{E_y} & -\frac{\nu_{xz}}{E_z} & 0 & 0 & 0 \\ -\frac{\nu_{yx}}{E_x} & \frac{1}{E_y} & -\frac{\nu_{yz}}{E_z} & 0 & 0 & 0 \\ -\frac{\nu_{zx}}{E_x} & -\frac{\nu_{zy}}{E_y} & \frac{1}{E_z} & 0 & 0 & 0 \\ 0 & 0 & 0 & \frac{1}{G_{xy}} & 0 & 0 \\ 0 & 0 & 0 & 0 & \frac{1}{G_{xz}} & 0 \\ 0 & 0 & 0 & 0 & 0 & \frac{1}{G_{yz}} \end{bmatrix} \cdot \begin{bmatrix} \sigma_x \\ \sigma_y \\ \sigma_z \\ \tau_{xy} \\ \tau_{xz} \\ \tau_{yz} \end{bmatrix} \quad (4.7)$$

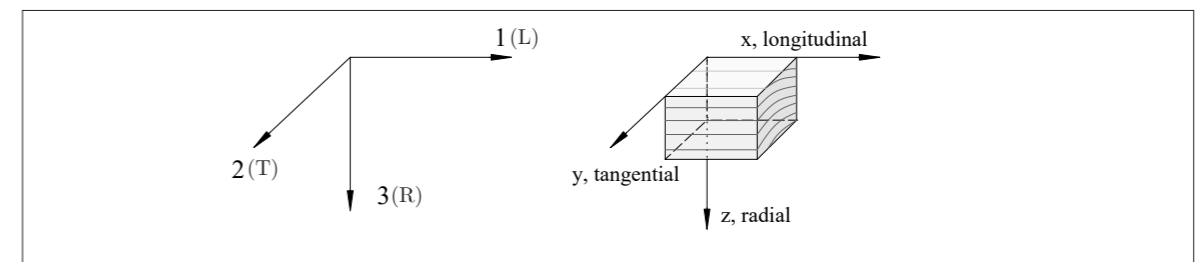
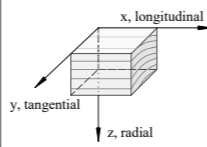


Fig. 4.2: Principal material directions of unprocessed wood

4.1.2 Linear elastic material properties of timber

The entries of the stiffness matrix are filled by mean values derived from mechanical investigations within various previous studies (see exemplary (GOODMAN AND BODIG 1970), (SCHICKHOFER 1994), (KATZ ET AL 2007), or (NIEMZ AND SONDEREGGER 2017)). This is explained by the fact that the moduli of elasticity and shear moduli of the natural product wood are subject to a certain degree of variation. The calculation of the mean values of mechanical properties and density is carried out according to European Standard EN 384. Table 4.1 lists the mean values of the orthotropic linear elastic material properties of different softwood and hardwood species under a moisture content of $u = 12\%$.

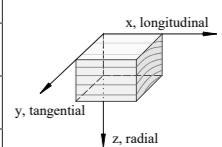
Tab. 4.1: Exemplary orthotropic material properties of different wood species (mean values) (GOODMAN AND BODIG 1970), (SCHICKHOFER 1994), (KATZ ET AL 2007), (NIEMZ AND SONDEREGGER 2017), (DIN 68364)

	E_x [MPa]	E_y [MPa]	E_z [MPa]	G_{yz} [MPa]	G_{xy} [MPa]	G_{xz} [MPa]	orientation
Spruce <i>Picea abies</i>	11000	370	370	40	650	600	
Pine <i>Pinus sylvestris</i>	11000	370	370	70	680	/	
Douglas Fir <i>Pseudotsuga menziesii</i>	13000	370	370	80	900	800	
Maple <i>Acer pseudoplatanus</i>	10500	890	1550	/	1120	1240	
Oak <i>Quercus petraea</i>	13000	920	1580	400	800	1150	
Beech <i>Fagus sylvatica</i>	14000	1160	2280	470	1080	1640	
Bongossi <i>Lophira alata</i>	17000	2060	3230	/	/	/	

European Standard EN 338 establishes a system of strength classes for general use in design codes and therefore lists the strength classes, material properties and density values which are applicable to timber for structural use (EN 338:2016). This allows engineers to specify particular strength classes—softwood (C and T classes) and hardwood (D classes)—and use its characteristic strength values as the basis for structural analysis.

The classification and sorting of individual species of softwood and hardwood to the appropriate strength class is carried out by machines in accordance with EN 14081-2. This standard specifies requirements for visually and mechanically machine graded structural timber for load-bearing purposes with a rectangular cross-section formed by sawing, planing or other processes. The timber specimens are sorted into the strength classes in accordance to EN 338 (Table 4.2).

Tab. 4.2: Elastic material properties of different strength classes according to EN 338 (mean values)

	E_x [MPa]	E_y [MPa]	E_z [MPa]	G_{yz} [MPa]	G_{xy} [MPa]	G_{xz} [MPa]	orientation
C24	11000	370	370	/	690	690	
T14	11000	370	370	/	690	690	
D40	13000	870	870	/	810	810	
D50	14000	930	930	/	880	880	

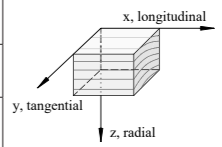
In addition Table 4.3 lists the characteristic strength values as well as the density values for softwood graded into strength class C24 and T14 according to EN 338. The characteristic strength values were, like the elastic material properties, determined according to EN 384.

Tab. 4.3: Strength parameters and density values for spruce or equivalent softwood (strength class C24 / T14) according to EN 338 (characteristic values)

	$f_{m,k}$ [MPa]	$f_{t,0,k}$ [MPa]	$f_{t,90,k}$ [MPa]	$f_{c,0,k}$ [MPa]	$f_{c,90,k}$ [MPa]	$f_{v,k}$ [MPa]	ρ_k [kg/m ³]	ρ_{mean} [kg/m ³]
C24	24.0	14.5	0.4	21.0	2.5	4.0	350	420
T14	20.5	14.0	0.4	21.0	2.5	4.0	350	420

Poisson's ratios ν describe the coupling of longitudinal strains in the respective direction of load application to its transverse strains in transversal direction. The *Poisson's* ratios are considered to be constants, even though they depend on physical influences such as wood moisture content (NEUHAUS 1981, WINTER 2021). Different values of the *Poisson's* ratio at a wood moisture content of 12% are provided by Table 4.4.

Tab. 4.4: *Poisson's* ratios for spruce or equivalent softwood (strength class C24 / T14) according to selected authors

	ν_{xz}	ν_{xy}	ν_{yz}	ν_{zx}	ν_{yx}	ν_{zy}	orientation
HALÁSZ AND SCHEER 1996	0.220	0.380	0.203	0.018	0.017	0.360	
NEUHAUS 1981	0.410	0.550	0.310	0.056	0.035	0.600	
KEYLWERTH 1951	0.463	0.532	0.240	0.019	0.013	0.420	

Experimental investigations and different experimental approaches, like those of Neuhaus (NEUHAUS 1981), vary considerably due to the inhomogeneity of wood. The *Poisson's* ratios according to Halász and Scheer (HALÁSZ AND SCHEER 1996) have been chosen for the calculation of the stiffness matrix of the unidirectional layer (UD layer) in this thesis. However, when calculating the stiffness properties of laminates like CLT and DLT, the chosen values for the *Poisson's* ratio have no decisive influence (Winter 2021, ARNOLD ET AL. 2022a).

4.2 Viscoelastic rheology

4.2.1 Definitions and Boltzmann's superposition principle

For linear elastic material behavior the relation between stresses and strains is given by constant elastic properties. As for any other materials in nature, this criteria is also not fulfilled for wood. If solid materials behave elastic, the deformation behavior is valid for small stresses and strains only (SCHÜRMAN 2007).

A solid material that returns into its original shape after an experienced stress-induced deformation is designated as an elastic material. Thus, the strains are stress dependent only. The elastic work of deformation is stored during loading and totally released after unloading (DIN 13343:1994). *Newtonian* fluids are considered viscous if the strains are exclusively dependent on the stresses and the deformation energy is completely and irreversibly converted into heat during loading (DIN 13343:1994).

Materials combining both, elastic and viscous material properties, are called viscoelastic materials. The combination of the respective material properties can vary. Due to the fact that parts of the deforming energy are irreversibly converted to heat, the deformation energy is not always stored in the same range. Therefore, viscoelastic materials can not be represented by stress and strain values or deformation rates only. They are described by the history of all individual stress events they experienced (DIN 13343).

A material is defined as linear viscoelastic if it exhibits a linear stress-strain curve and long-term deformation behavior is independent on the magnitude of the applied stress. In addition, linear viscoelastic materials follow the rules of *Boltzmann's* superposition principles. The total effect of a sum of causes is equal to the sum of the effects of each individual cause. Accordingly, time-dependent individual effects (creep deformations) can be accumulated relative to individual causes (for example concentrated loads) (SCHÜRMAN 2007). Strains that already exist or will occur in the future do not influence the time history of individual effects. Therefore, a corresponding distortion history can be calculated for a given load history and vice versa (Equation (4.8)).

$$\varepsilon(t) = \Phi(t - \tau_0) \cdot \Delta\sigma(\tau_0) + \Phi(t - \tau_1) \cdot \Delta\sigma(\tau_1) + \dots + \Phi(t - \tau_j) \cdot \Delta\sigma(\tau_j) \quad (4.8)$$

If a constant stress gradient is applied at time t_i , it is followed by a time dependent curve of strain that is based on the time-dependent material law (creep curve), but independent of the applied stress gradient. Already existing or still added stresses do not influence the actual course of the respective strains as a function of time, but are superimposed as a leap within the function when adding additional or removing existing stresses. The strains over time are therefore superimposed as a function of the history of stresses and vice versa (Figure 4.3) (SCHÜRMAN 2007).

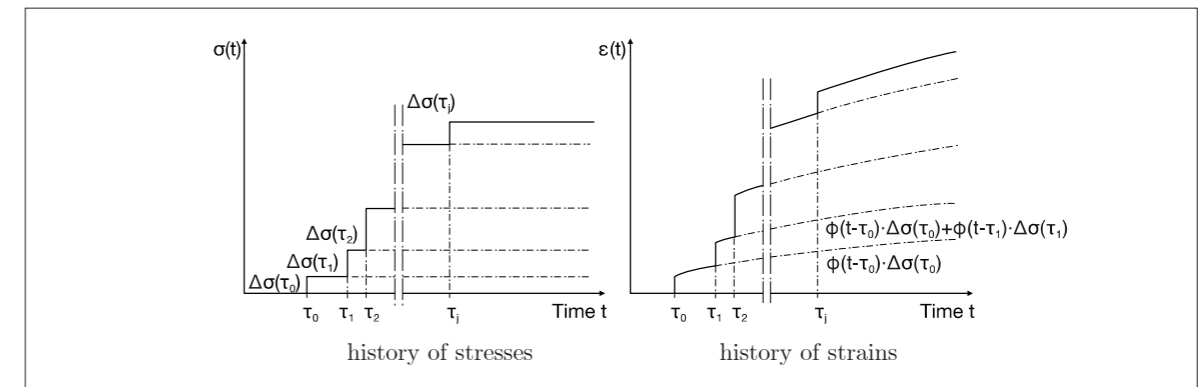


Fig. 4.3: Boltzmann's superposition principle (VOGEL 2021) based on (SCHÜRMAN 2007)

Processes that describe linear viscoelastic material behavior are creeping and relaxation. The creep behavior describes the increase of the deformations (strains) under a constant stress state as a function of the time. This time-dependent relationship is described using the creep function or retard function $\Phi(t)$ (Equation (4.9)).

Relaxation describes the decrease of internal stresses whilst the deformation maintains constant. The related relaxation function $\Psi(t)$ describes a time-dependent stiffness value (Equation (4.10)).

$$\Phi(t) = \frac{\varepsilon(t)}{\sigma(0)} \quad (4.9)$$

$$\Psi(t) = \frac{\sigma(t)}{\varepsilon(0)} \quad (4.10)$$

Both, creep and relaxation processes are subject to a non-linear behavior and approach asymptotically a final value. There is no limited period for the creep and relaxation processes. Nevertheless, there is experimental data that prove that hardly any relevant creep and relaxation process occurs after material specific ranges of time. For wood, the values vary between 10 and 15 years (NIEMZ AND SONDEREGGER 2017). Creeping and relaxation rarely occur by themselves in structures. Usually both time-dependent processes occur simultaneously (SCHÜRMAN 2007).

The correspondence principle is based on *Boltzmann's* superposition principle (SCHÜRMAN 2007). In this case, the constitutive Equations following *Hooke's* law, remain valid (Equations (4.1) and (3.2)). However, the description of viscoelastic materials results in changes in the material law. Based on the correspondence principle, the elasticity matrix $[C]$ as well as the compliance matrix $[S]$ forming the elastic theory are replaced by the time-dependent creep matrix $[\Phi]$ and the relaxation matrix $[\Psi]$ (Equations (4.11) and (4.12)) (SCHÜRMAN 2007).

$$\sigma(t) = \Psi(t) \cdot \varepsilon(0) \quad (4.11)$$

$$\varepsilon(t) = \Phi(t) \cdot \sigma(0) \quad (4.12)$$

4.2.2 Time-dependent material law

DIN 13343 represents the time-dependent material law by using rheological models. Thereby, the elastic properties are represented by a *Hooke's* spring. The viscous properties are described by a *Newtonian* damper (Figure 4.4). Both models can be combined and connected in parallel (superposition of stresses) or in series (superposition of strains).

Depending on the number of coupled springs and dampers, the represented materials are denoted n-parameter materials (models). The 2-parameter *Maxwell* model (spring and damper in series) characterizes viscoelastic fluids, the *Kelvin-Voigt* model (spring and damper parallel) makes possible the description of viscoelastic solids. In addition, models of higher order can be used, depending on the material behavior to be represented. Thus, for example, a distinction can be made between the material behavior of solids with liquid-like initial behavior and solids with solid-like initial behavior. *Schänzlin* compared different rheological models for the description of the time-dependent material law of timber with respect to the variation of the moisture content (SCHÄNZLIN 2010). Most of the models consist of serial chains of *Kelvin-Voigt* elements.

Using matrix notation for orthotropic viscoelasticity, nine independent creep or relaxation functions are required, which are usually determined by experimental investigations (Equation (4.13))

$$\begin{bmatrix} \sigma_x(0) \\ \sigma_y(0) \\ \sigma_z(0) \\ \tau_{xy}(0) \\ \tau_{xz}(0) \\ \tau_{yz}(0) \end{bmatrix} = \begin{bmatrix} \Psi_{11}(t) & \Psi_{12}(t) & \Psi_{13}(t) & 0 & 0 & 0 \\ \Psi_{12}(t) & \Psi_{22}(t) & \Psi_{23}(t) & 0 & 0 & 0 \\ \Psi_{13}(t) & \Psi_{23}(t) & \Psi_{33}(t) & 0 & 0 & 0 \\ 0 & 0 & 0 & \Psi_{44}(t) & 0 & 0 \\ 0 & 0 & 0 & 0 & \Psi_{55}(t) & 0 \\ 0 & 0 & 0 & 0 & 0 & \Psi_{66}(t) \end{bmatrix} \begin{bmatrix} \varepsilon_x(t) \\ \varepsilon_y(t) \\ \varepsilon_z(t) \\ \gamma_{xy}(t) \\ \gamma_{xz}(t) \\ \gamma_{yz}(t) \end{bmatrix} \quad (4.13)$$

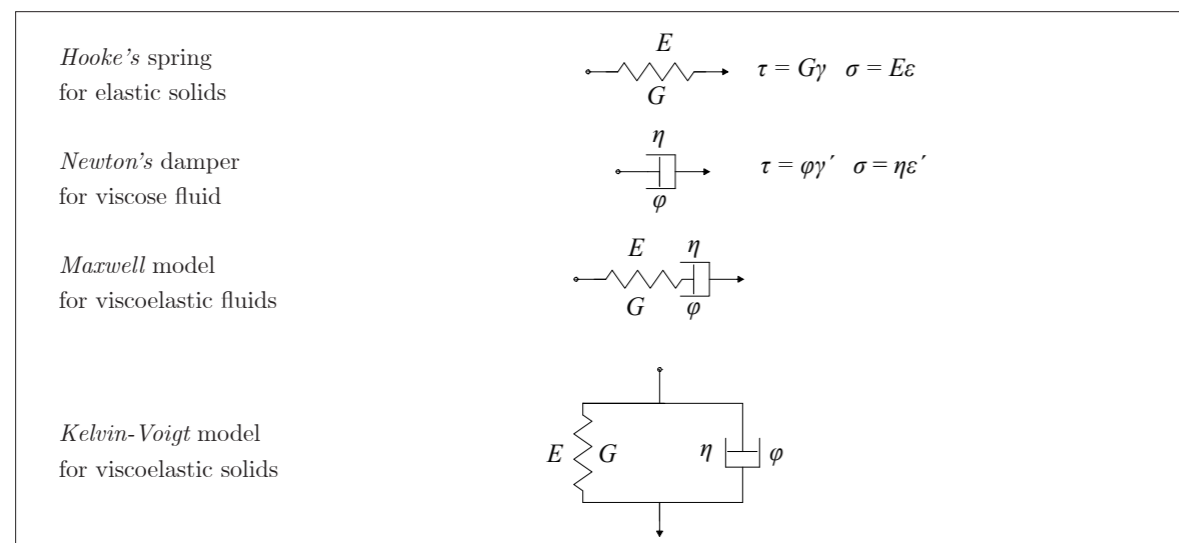


Fig. 4.4: Presentation of the rheological models according to DIN 13343

Considering viscoelastic materials, the quasi-stationary solution provides good approximation for stress and deformation analyses (NAVI AND STANZL-TSCHEGG 2009). Within the creep matrix $[\Phi]$ and relaxation matrix $[\Psi]$ of timber, the moduli of elasticity E_i , shear moduli G_{ij} , and *Poisson's* ratios ν_{ij} are replaced by time-dependent values $E_i(t)$, $G_{ij}(t)$, and $\nu_{ij}(t)$ (Equations (4.14) and (4.15)).

$$[\Phi] = \begin{bmatrix} \frac{1}{E_x}(t) & -\frac{\nu_{xy}}{E_y}(t) & -\frac{\nu_{xz}}{E_z}(t) & 0 & 0 & 0 \\ -\frac{\nu_{yx}}{E_x}(t) & \frac{1}{E_y}(t) & -\frac{\nu_{yz}}{E_z}(t) & 0 & 0 & 0 \\ -\frac{\nu_{zx}}{E_x}(t) & -\frac{\nu_{zy}}{E_y}(t) & \frac{1}{E_z}(t) & 0 & 0 & 0 \\ 0 & 0 & 0 & \frac{1}{G_{xy}}(t) & 0 & 0 \\ 0 & 0 & 0 & 0 & \frac{1}{G_{xz}}(t) & 0 \\ 0 & 0 & 0 & 0 & 0 & \frac{1}{G_{yz}}(t) \end{bmatrix} \quad (4.14)$$

$$[\Psi] = [\Phi]^{-1} \quad (4.15)$$

4.2.3 Viscoelastic material properties of timber

To determine the entries of viscoelastic stiffness matrices, further models are needed. The viscoelastic material properties are basically dependent on five different parameters:

- The elastic material properties and density. The lower the density, the slightly higher the existing creep rates (TONG ET AL. 2020),
- The environmental conditions with respect to the temperature and the range of temperature change. An increase in temperature at constant humidity leads to increased creep rates and reduced elastic properties (JONG AND CLANCY 2004),
- The environmental conditions with respect to the relative humidity and therefore with respect to the wood moisture content,
- The load level with respect to the maximum short-term strength
- and the load duration.

Ozyhar provides a parametric exponential equation for calculating the moduli of elasticity and *Poisson's* ratios as a function of time in the orthotropic directions (OZYHAR ET AL. 2013). Due to the fact that these studies refer to an investigation period of 24 hours, these results can be used to a limited extent only for the evaluation of the long-term stiffness properties. Long-term stiffness properties, taking into account creep and relaxation, are calculated under the consideration of deformation coefficients following Equation (4.16) and Equation (4.17) (EN 1995-1-1).

$$E_{i,mean,fin} = \frac{E_{i,mean}}{1 + k_{def,i,tension}} \quad (4.16)$$

$$G_{ij,mean,fin} = \frac{G_{ij,mean}}{1 + k_{def,shear}} \quad (4.17)$$

The deformation coefficients need to be modified, so as to consider the influence of climatic conditions, load duration, and fibre orientation (NIEMZ AND SONDEREGGER 2017). Based on various experimental and analytical investigations by Gressel in 1984, Niemz and Sonderegger offer a fiber-parallel deformation coefficient of $k_L = 0.1$ to 0.3 for timber loaded in tension in service class 1 (20°C , 65% relative humidity) (GRESSEL 1984; NIEMZ AND SONDEREGGER 2017). Perpendicular to the grain they consider deformation coefficients k_T between 0.8 and 1.6 . In transversal direction, Aondio recommends deformation coefficients within the range $k_{shear} = 2.0$ to 3.0 (AONDIO 2014). This recommendation is consistent with the experiments and calculations made by Jöbstl and Schickhofer at the University of Graz in 2007 ($k_{shear} = 2.3$) (JÖBSTL AND SCHICKHOFER 2007).

Following the objective of a long-term deformation analysis, statements are necessary about the deformation as a function of time. For a consistent evaluation, different points in time (t_0 , t_{fin} , t_∞) are defined, on the basis of which time-dependent deformation curves can be derived. Figure 4.5 demonstrates different phases of long-term deformations according to (GRESSEL 1971). The curve of σ_1 gives the load-level of maximum 40% of the short-term strength in which a failure load is not reached (tertiary phase).

The start of the long-term deformation at t_0 represents a 1 minute delay after loading, taking into account the linear elastic deformations (DIN EN 1156). The second defined time t_{fin} describes the end of the primary phase. Due to the 40% load level, the long-term deformation asymptotically reaches a final value.

The time value t_{fin} can be approximated with a load duration of 11 years (GRESSEL 1984). At this time, the deformations related to creeping are mostly completed. Therefore, the deformation coefficient according to EC 5 can be used for calculating the deformations at the end of primary phase.

The value t_∞ describes a fictitious infinite final state. With respect to laminates, within this phase, stresses migrate from cross-layers to layers featuring fibres oriented longitudinal to the respective loading direction (SCHÜRMAN 2007) (Figure 4.6). This means, that in the infinite final state t_∞ , the stiffness parameters of the transversal layers are set to about 5% of their initial elastic stiffness values at t_0 . This corresponds to a period of more than 50 years (SCHÜRMAN 2007). Using Equations (4.16) and (4.17) the deformation coefficient k_T and k_{shear} result at around 19.0 (using the initial stiffness values—engineering constants—of spruce, strength class T14, according to Tab. 4.2). The longitudinal stiffness values, on the other hand, remain at the same level as at t_{fin} ($k_L = 0.2$) (SCHÜRMAN 2007).

Table 4.5 summarizes deformation coefficient previously described taking into account the different time phases. An exemplary long-term deformation analysis using the deforma-

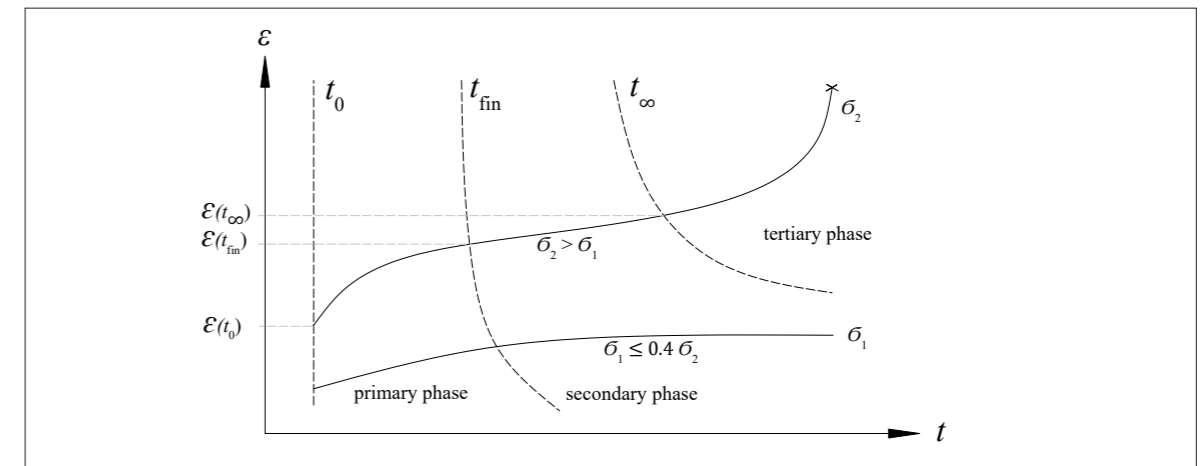


Fig. 4.5: Phases of the long-term deformation behavior of timber, according to (GRESSEL 1971)

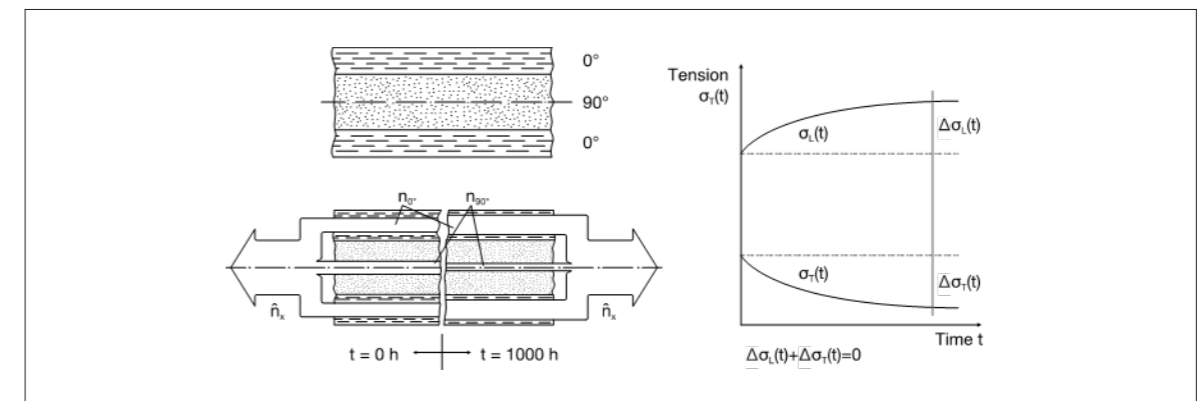


Fig. 4.6: Load redistribution principle within laminates like CLT (Vogel 2021) based on (SCHÜRMAN 2007)

tion coefficients given in Table 4.5 is carried out in Chapter 8.4. Regarding the deformation coefficients at t_{fin} an additional analysis is carried out using extreme values (minimal deformation coefficients).

Tab. 4.5: Deformation coefficients for different phases of the long-term deformation

	k_L	k_T	k_{shear}
t_0	0	0	0
t_{fin}^1	0.2	1.2	2.5
(NIEMZ AND SONDEREGGER 2017) following (GRESSEL 1984)	0.1-0.3	0.8-1.6	/
(JÖBSTL AND SCHICKHOFER 2007)	/	/	2.3
(AONDIO 2014)	/	/	2.0-3.0
t_∞	0.2	19.0	19.0

¹Mean values based on previous investigations

After introducing the elastic and viscoelastic rheology of timber the following Section describes the series chosen for the investigations and its material parameters.

4.3 Series investigated

4.3.1 Configurations, layups, and stacking sequences

For the analytical, experimental, and numerical investigations series of conventional CLT specimens with 3 to 7 layers and total thicknesses of $t = 100$ mm, $t = 140$ mm, $t = 150$ mm and $t = 200$ mm were chosen. The specific DLT series are related to the CLT specimens according the number of layers and the layer thicknesses. This enables comparability of the respective results. Qualitative and quantitative evaluations of the effects of diagonal layer arrangements on stiffness parameters, deformations and stress distributions are possible.

The CLT and DLT series within Table 4.6 represent layups suitable and chosen for experimental investigations on the out-of-plane shear stiffness, the torsional stiffness, and the in-plane shear properties. The orientation of the diagonal layers was chosen to follow the specific angles of 45° and $30^\circ/60^\circ$ (30° related to global x direction; 60° related to global y direction). The middle layer of the DLT specimens follows an orientation of 90° (cross-layer). All series according to Table 4.6 are antisymmetric and balanced laminates. The last line in Table 4.6 offers the graphical representation of the stacking sequence of each series defined in the lines above. The specimens are made of laminations from spruce (*picea abies*) that were classified in strength class T14 according to EN 338 (see Chapter 4.3.2). The laminations (boards) have a width of $w = 180$ mm and are not edge-glued (bonding on the narrow side of the boards). The boards do not feature stress reliefs.

Tab. 4.6: Chosen series for the analytical, experimental and, numerical investigations—mainly on the out-of-plane shear stiffness, the torsional stiffness, and the in-plane shear stiffness

series ¹		t [mm]	layup t_i [mm]	arrangement of the layers Θ	board width w [mm]	edge- glued	stress reliefs
O1	CLT	100	20-20-20-20-20	$0^\circ, 90^\circ, 0^\circ, 90^\circ, 0^\circ$	180	no	no
O3	CLT	60	20-20-20	$0^\circ, 90^\circ, 0^\circ$	180	no	no
O5	CLT	200	40-40-40-40-40	$0^\circ, 90^\circ, 0^\circ, 90^\circ, 0^\circ$	180	no	no
D3	DLT $\pm 45^\circ$	100	20-20-20-20-20	$0^\circ, 45^\circ, 90^\circ, -45^\circ, 0^\circ$	180	no	no
D4	DLT $\pm 30^\circ$	100	20-20-20-20-20	$0^\circ, 30^\circ, 90^\circ, -30^\circ, 0^\circ$	180	no	no
D5	DLT $\pm 45^\circ$	200	40-40-40-40-40	$0^\circ, 45^\circ, 90^\circ, 45^\circ, 0^\circ$	180	no	no
D6	DLT $\pm 30^\circ$	200	40-40-40-40-40	$0^\circ, 30^\circ, 90^\circ, -30^\circ, 0^\circ$	180	no	no

O1, O5

O3

D3, D5

D4, D6

¹naming and order of the series in accordance to (ARNOLD ET AL. 2022a)

For the experimental investigation on the uniaxial load-bearing capacity (bending stiffness properties), an additional laminate was chosen. This series (D1) does not contain a cross-layer (layer oriented under 90° to the global x direction). As mentioned in the introduction of the thesis, the aim regarding "application-optimized" laminated timber elements is to adopt the layups and stacking sequences regarding the respective static system (loading, span, and support conditions).

For the layups given within Table 4.7, all layers have a load-bearing function under uniaxial bending, which means that the given layup might be more suitable for uniaxial load transfer than conventional CLT or DLT featuring cross-layers (compare to Table 4.6). In order to distinguish between DLT elements with cross-layers and DLT elements without cross-layers, the specific DLT elements according Table 4.7 are denoted with the abbreviation uDLT. The adding of the prefix "u" signifies the suitability for uniaxial load transfer mainly. The specimens are made of laminations from spruce (*picea abies*) that were classified in strength class T14 according to EN 338 (see Chapter 4.3.2). The boards have a width of $w = 180$ mm, are not edge-glued, and do not feature stress reliefs.

Due to the fact that the uDLT specimens were produced with both diagonal layers arranged under $+45^\circ$ (see uDLT $+45^\circ$ D1 series, Table 4.2), uDLT $\pm 45^\circ$ series D2 is complementary introduced within Table 4.7 for better understanding. D1 and D2 series hold the same bending stiffness parameters in global x and y directions. From D1 series, ten real-scale specimens were produced.

Tab. 4.7: Chosen series for the analytical, experimental, and numerical investigations on the bending stiffness

series		t [mm]	layup t_i [mm]	arrangement of the layers Θ	board width w [mm]	edge- glued	stress reliefs
D1 ¹	uDLT $+45^\circ$	200	40-40-40-40-40	$0^\circ, 45^\circ, 0^\circ, 45^\circ, 0^\circ$	180	no	no
D2 ²	uDLT $\pm 45^\circ$	200	40-40-40-40-40	$0^\circ, 45^\circ, 0^\circ, -45^\circ, 0^\circ$	180	no	no

D1

D2

¹The uniaxial bending tests on the D1 series were carried out by the Timber Construction Unit of the University of Innsbruck and are evaluated within the scope of this thesis; the chosen layer arrangement is comparable to the layer arrangements of the investigations on the bending stiffness of DLT according to Buck et al. (BUCK ET AL. 2016)

²D2 series: bending stiffnesses B_x and B_y of D1 series equal those of D1 series within linear elastic range)

The series and layups chosen for the experimental investigations (Tables 4.6 and 4.7) only represent a small selection of possible layups. Of course, CLT and DLT elements could also be produced with a larger number of layers and differing layer arrangements within the boundary conditions of the production processes. This is why the produced series (Tables 4.6 and 4.7) are in the following supplemented by virtual series featuring a differing number of layers and layer thicknesses (Table 4.8). These series form the basis for the later deformation and stress distribution analysis for different static systems (application scenarios).

The layups of O7 and D7 series provide common layups as may be used for mass timber slabs following construction grids with spans of $l \leq 3.5$ m. Their overall thickness is $t = 150$ mm and they consist of 5 layers each ($n = 5$). The O8 and D8 series provide a comparable thickness of $t = 140$ mm but consist of seven layers each ($n = 7$). The additional DLT D9 series features four diagonally arranged layers and stays in reference to the O8 and D8 series in number and thickness of its layers.

Tab. 4.8: Chosen virtual series for the additional numerical investigations using real-scale 2D and 3D FE models

series		t [mm]	layup t_i [mm]	arrangement of the layers θ	board width w [mm]	edge- glued	stress reliefs
O7	CLT	150	30-30-30-30-30	$0^\circ, 90^\circ, 0^\circ, 90^\circ, 0^\circ$	180	no	no
O8	CLT	140	20-20-20-20-20-20-20	$0^\circ, 90^\circ, 0^\circ, 90^\circ, 0^\circ, 90^\circ, 0^\circ$	180	no	no
D7	DLT $\pm 45^\circ$	150	30-30-30-30-30	$0^\circ, 45^\circ, 90^\circ, -45^\circ, 0^\circ$	180	no	no
D8	DLT $\pm 45^\circ$	140	20-20-20-20-20-20-20	$0^\circ, 90^\circ, 45^\circ, 0^\circ, -45^\circ, 90^\circ, 0^\circ$	180	no	no
D9	DLT $\pm 45^\circ$	140	20-20-20-20-20-20-20	$0^\circ, -45^\circ, 45^\circ, 90^\circ, -45^\circ, 45^\circ, 0^\circ$	180	no	no

4.3.2 Material parameters of the test series

The CLT specimens of O1 and O3 series were manufactured by *Pfeifer Timber GmbH*, Germany, in December 2019 under the framework of the European Research Project INNOCROSSLAM (2019-2022) (founded by the European Union's Horizon 2020 research and innovation programme under grant agreement N° 773324). The CLT series O1 and O3 therefore also served as reference series to numerous experiments on the strength and stiffness parameters of multifunctional CLT featuring channels in one of its layers (see ARNOLD ET AL. 2021; ARNOLD ET AL. 2022b).

The specific DLT specimens of the D1, D3, D4, D5, and D6 series as well as the CLT specimens of the O5 series were produced by *Holzbau Unterrainer GmbH*, Austria, in March 2021 free of charge (HOLZBAU UNTERRAINER GMBH 2021a).

The CLT O1 and O3 series were produced in accordance to European Technical Assessment document ETA-20/0023. The CLT O5 series and the DLT series were produced in accordance to ETA-16/0055. Even though *Holzbau Unterrainer GmbH* does not yet hold its own ETA for DLT, the DLT test specimens were manufactured in one batch together with the CLT series O5. Table 4.9 lists the engineering constants in principal directions of the laminations according to the two ETAs.

Tab. 4.9: Moduli of elasticity and shear moduli of single laminations used for the production of the specimens according to two different ETAs

	E_x [MPa]	E_y [MPa]	G_{yz} [MPa]	G_{xz} [MPa]	G_{xy} [MPa]	orientation
ETA-20/0023	11000	370	50	690	690	
ETA-16/0055	11550	370	50	690	690	

Geometric parameters, such as the load-fiber angle, the orientation of the growth rings, and the microfibril angle have an influence on the strengths and stiffnesses properties of various wood species; In addition, the density, the moisture content, and the temperature are important influencing factors (ARMSTRONG ET AL. 1984; NIEMZ AND SONDEREGGER 2017).

Different material tests according to EN 408 (modulus of elasticity, compression strength, and density), EN 13183 (moisture content) and EN 16351 (delamination) were carried out on the produced series, in order to verify the material parameters given in the ETAs:

The moisture content and density were determined by kiln drying tests (EN 13183) on the O1 and O3 series after delivery. The mean value of the density was $\rho_{\text{mean}} = 458$ kg/m³ (COV 4.3 %) (also see ARNOLD ET AL. 2021). The modulus of elasticity $E_{c,0}$ and the compression strength $f_{c,0}$ of O1 and O3 series were determined by compression tests according to EN 408. The mean value of $E_{c,0,\text{mean}}$ was 10682 MPa (COV 5.3 %); the mean value $f_{c,0,\text{mean}}$

was 34.3 MPa. The mean value $E_{c,0,\text{mean}} = 10682$ appears to be close to the given value within ETA 20/0023 ($E_x = 11000$ MPa) considering the COV of 5.3 %.

The material parameters of all DLT series and the CLT O5 series were determined before and after the production of the test specimens by *Holzbau Unterrainer GmbH*. After technical drying to a moisture content of $u = 12$ % and visual grading, the density of the respective batch was determined on 20 specimens by kiln drying tests. The mean value of the density was $\rho_{\text{mean}} = 416$ kg/m³ (COV 4.3 %) (HOLZBAU UNTERRAINER GMBH 2021b). This confirms a grading in strength class T14 according to EN 338 ($\rho_{\text{mean,T14}} = 420$ kg/m³). Assuming a linear correlation of density to the modulus of elasticity, results in mean values $E_{0,\text{mean}} = 10600$ MPa, $E_{90,\text{mean}} = 370$ MPa, $G_{0,\text{mean}} = 690$ MPa (see also Tables 1 and 2 of EN 338), and in $G_{90,\text{mean}} = 50$ MPa (FELLMOSER AND BLASS 2004). Additional 20 specimens of the DLT series were subjected to delamination tests according to EN 16351 ($\text{Delam}_{\text{tot,mean}} = 4.1$ %; COV 4.7 %) (HOLZBAU UNTERRAINER GMBH 2021b).

The linear correlation between the density and the engineering constants in principal directions (E_i and G_{ij}) has been investigated and confirmed in several experimental studies (ARMSTRONG ET AL. 1984; GINDL ET AL. 2001; FELLMOSER AND BLASS 2004; RAVENSHORST 2015). *Armstrong et al.* and *Ravenshorst* even derived formulas for the calculation of the bending strength and the modulus of elasticity for different wood species as a function of the density (ARMSTRONG ET AL. 1984; RAVENSHORST 2015).

The laminations of all series are assigned to strength class T14 regarding the investigations on the material parameters, even if the density of the O1 and O3 series appears rather high in reference to the experimentally determined moduli of elasticity. The recommended COV for the modulus of elasticity of European softwood as prior value is 13.0 % for a number of tests equal to 10 (JCSS 2006). Therefore, the achieved COV of 5.3 % and COV 4.3 % provide good correlation to the respective mean values and therefore to strength class T14 (C24).

The achieved COVs and the respective mean values (10682 MPa for the O1 and O3 series and 10600 MPa for the D1, D3, D4, D5, D6, and O5 series) exemplary lead to min/max values of $E_{\text{min}} = 10144$ MPa and $E_{\text{max}} = 11248$ MPa. All in all, the use of the engineering constants according to ETA-20/0023 (E_i and G_{ij}) for the later analytical investigations seems appropriate. This statement is based on the results of the experiments previously described and consents with investigations of *Fellmoser* and *Blass* (FELLMOSER AND BLASS 2004),

For the later experimental investigation, all specimens were stored at 65 % relative humidity and a temperature of 20°C. The moisture content of each specimen was determined by an electrical resistance moisture meter using ram-in electrodes within a depth of 15 mm before each experiment (EN 13183-2). The respective values of the moisture content are provided in the corresponding evaluation of the experimental investigations.

Within the following Chapter 5 the laminate theory and therefore the stiffness matrix of laminates with arbitrary oriented layers is derived. Chapter 5 forms the basis of later theoretical approaches and leads to the analytical determined stiffness values of the investigated series.

When comparing the analytical solutions with experimental results, the scatter of the material parameters must be kept in mind. The scatter is expressed by the COV of about 5.0 % and a deviation of around 3.5 % to the engineering constants given in ETA-20/0023.

5 Theoretical principles and approaches

5.1 Fundamentals of the plate theory

5.1.1 Drilling of isotropic plates

The loading of a plate element under pure torsion can be described by torsional moments acting along the edges of the plate (Figure 5.1, a). Considering infinitesimal plate elements (dx/dy), these moments can be replaced by force couples (Figure 5.1, b). Following the derivation of effective shear forces and according to the *Kirchhoff-Love* plate theory, these moments correspond to equivalent forces $R = 2m_{xy} = 2m_{yx}$ acting at the corners of the plate (Figure 5.1, c). Consequently, the load case of pure torsion leads to the equivalent load case of a square plate loaded at its corners by opposing single forces (ALTENBACH ET AL. 2016).

Equation (5.1) represents the general expression of the plate bending stiffness K of isotropic plates according to the *Kirchhoff-Love* plate theory.

$$K = \frac{Eh^3}{12(1-\nu^2)} \begin{pmatrix} 1 & \nu & 0 \\ \nu & 1 & 0 \\ 0 & 0 & \frac{1-\nu}{2} \end{pmatrix} \quad (5.1)$$

With regard to CLT and DLT, a distinction must be made between the plate theory according to *Kirchhoff-Love* (span/depth: $10/1 > l/t > 50/1$) and according to *Reissner-Mindlin* (span/depth: $5/1 > l/t > 10/1$). Following the plate theory of *Reissner-Mindlin* for moderately thick plates the out-of-plane shear deformation must be taken into account. This is even more pronounced for laminates consisting of orthotropic layers. The out-of-plane shear deformation cannot be neglected due to the low shear moduli G_{yz} . Therefore, the plate stiffness is composed of the bending and an additional shear stiffness component S shown in Equation (5.2):

$$S = \frac{Ehk}{2(1+\nu)} \begin{pmatrix} 1 & 0 \\ 0 & 1 \end{pmatrix} \quad (5.2)$$

The plate theory according to *Reissner-Mindlin* assumes that the shear stresses are constantly distributed over the cross-section. An error arises in this simplification in the calculation of shear deformations. This error is adjusted by the shear correction coefficient k (for rectangular and isotropic cross-sections $k = 5/6$) (ALTENBACH ET AL. 2016).

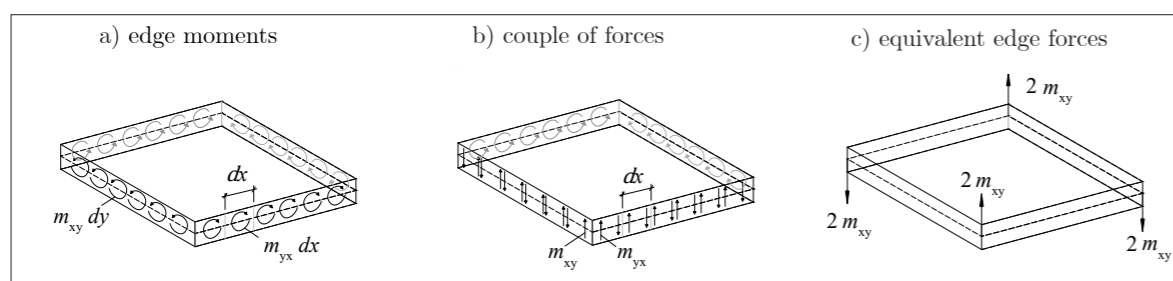


Fig. 5.1: Load case of pure torsion acting on a plate element

5.1.2 Kinematics of the 3D continuum

To describe the interaction of strains and deformations on a twisted plate element and the subsequent formulation of the matrix notation of the law of elasticity it is necessary to derive the kinematics on a 3D continuum. The relationship between strain and deformation on a 3D continuum can be formulated in matrix notation as follows (Equation (5.3)):

$$\{\varepsilon\} = \begin{bmatrix} \varepsilon_x \\ \varepsilon_y \\ \varepsilon_z \\ \gamma_{xz} \\ \gamma_{yz} \\ \gamma_{xy} \end{bmatrix} = \begin{bmatrix} \partial/\partial x & 0 & 0 \\ 0 & \partial/\partial y & 0 \\ 0 & 0 & \partial/\partial z \\ \partial/\partial z & 0 & \partial/\partial x \\ 0 & \partial/\partial z & \partial/\partial y \\ \partial/\partial x & \partial/\partial y & 0 \end{bmatrix} \cdot \begin{bmatrix} u \\ v \\ w \end{bmatrix} = [G] \cdot \{u\} \quad (5.3)$$

Out-of-plane shear stresses τ_{xz} and τ_{yz} and thus also the out-of-plane shear deformations are taken into account in the form of an advanced deformation model according to *Reissner-Mindlin* (previously described). Here, a plane section normal to the midsection no longer stays normal during deformation. Additional angles β_x and β_y are introduced (Figure 5.2). If the section is considered to remain plane (Figure 5.2, a), the approach follows the first-order shear deformation theory. Usually this theory provides sufficient results. The improved or so called second-order shear deformation theory takes into account an additional distortion of the formerly plan section (Figure 5.2, b). The vector notation of the displacements for a linear consideration of the shear strain are highlighted in vector notation by Equation (5.4) (SCHICKHOFER 1994):

$$\{u\}_{R-M} = \begin{bmatrix} u_0 \\ v_0 \\ w_0 \end{bmatrix} + z \cdot \begin{bmatrix} \beta_y \\ \beta_x \\ 0 \end{bmatrix} \quad (5.4)$$

Substituting the displacement vectors according to *Reissner-Mindlin* in Equation (5.3) by Equation (5.4) leads to the respective vector notation of the strains (Equation (5.5)). The single curvatures κ_x and κ_y of the individual layers are understood to be the change in the angle of inclination β ($\delta w_0/\delta x$ or $\delta w_0/\delta y$) along the respective indexed axis. The double curvature κ_{xy} of the central surface of each layer relates to the change of the angles β_x and β_y (SCHICKHOFER 1994).

$$\{\varepsilon\}_{R-M} = \begin{bmatrix} \varepsilon_x \\ \varepsilon_y \\ \varepsilon_z \\ \gamma_{xz} \\ \gamma_{yz} \\ \gamma_{xy} \end{bmatrix}_{R-M} = \begin{bmatrix} \varepsilon_x \\ \varepsilon_y \\ 0 \\ \gamma_{xz} \\ \gamma_{yz} \\ \gamma_{xy} \end{bmatrix} + z \cdot \begin{bmatrix} \kappa_x \\ \kappa_y \\ 0 \\ \beta_x/z \\ \beta_y/z \\ \kappa_{xy} \end{bmatrix} = \{\varepsilon\} + z \cdot \{\kappa\} = [G] \cdot \{u\}_{R-M} \quad (5.5)$$

The relationship between deformations and strains of the 3D continuum is provided in Equation (5.6) (SCHICKHOFER 1994):

$$\{\varepsilon\}_{3D,R-M} = \begin{bmatrix} \varepsilon_x \\ \varepsilon_y \\ \gamma_{xy} \\ \kappa_x \\ \kappa_y \\ \kappa_{xy} \\ \gamma_{xz} \\ \gamma_{yz} \end{bmatrix}_{3D,R-M} = \begin{bmatrix} \partial/\partial x & 0 & 0 & 0 & 0 \\ 0 & \partial/\partial y & 0 & 0 & 0 \\ \partial/\partial y & \partial/\partial x & 0 & 0 & 0 \\ 0 & 0 & 0 & \partial/\partial x & 0 \\ 0 & 0 & 0 & 0 & \partial/\partial y \\ 0 & 0 & 0 & \partial/\partial y & \partial/\partial x \\ 0 & 0 & \partial/\partial x & 1 & 0 \\ 0 & 0 & \partial/\partial y & 0 & 1 \end{bmatrix} \cdot \begin{bmatrix} u_0 \\ v_0 \\ w_0 \\ \beta_y \\ \beta_x \end{bmatrix} = [B] \cdot \{u\}_{R-M} \quad (5.6)$$

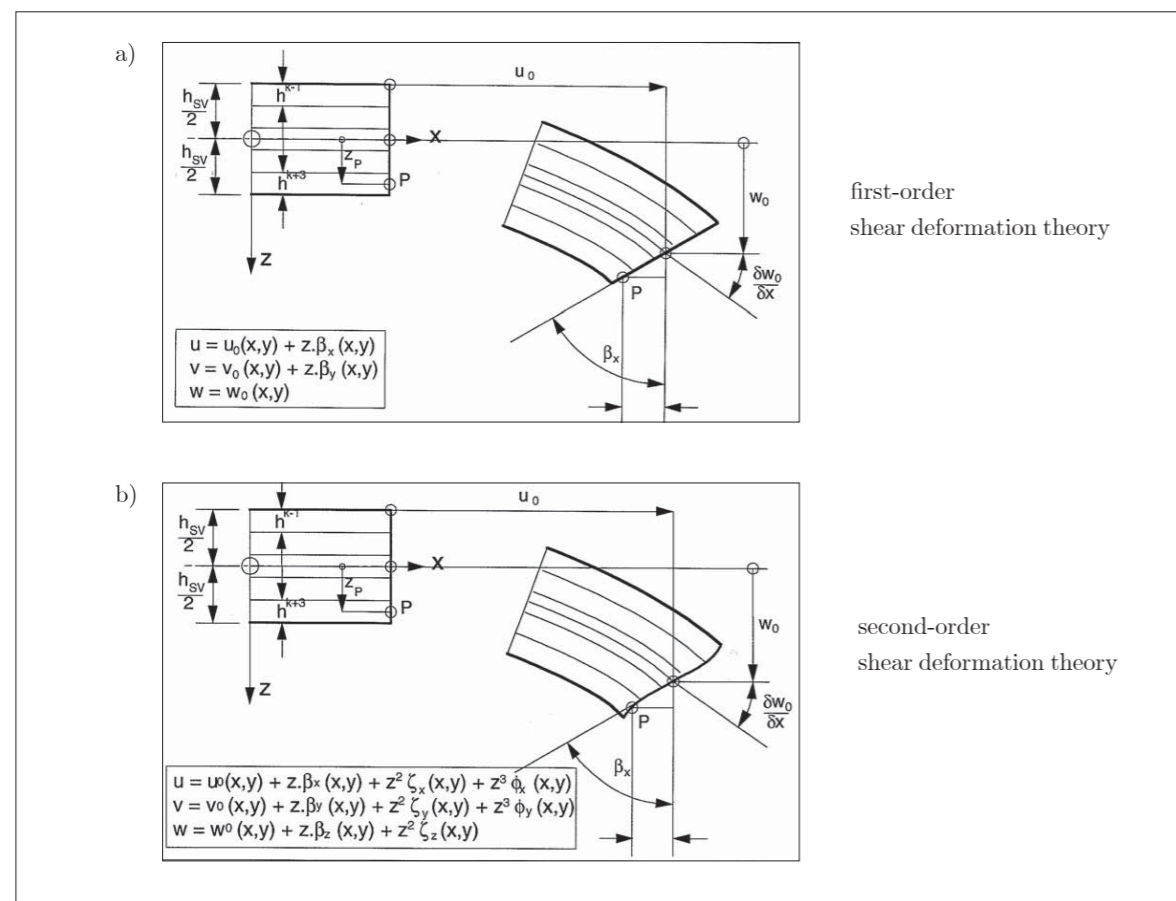


Fig. 5.2: Linear and non-linear approach for considering the out-of-plane shear strain of a formerly plane section, formerly normal to the midplane (SCHICKHOFER 1994)

5.2 Plate stiffness properties

5.2.1 Stiffness matrix of the unidirectional layer

Each layer of the laminate is considered as a unidirectional layer (UD layer) with ideally straight fibers providing transversal isotropy (see Chapter 3.1). Following the classical laminate theory, a UD layer is considered being in the plane stress state ($\sigma_3 = 0$). The out-of-plane shear stiffness values and stresses are not considered ($\tau_{13} = \tau_{23} = 0$). The stress-strain relationship on the reduced stiffness matrix of the UD layer for an orthotropic material ($\bar{Q}_{16} = \bar{Q}_{26} = 0$) are provided in Equation (5.7), where Q_{ij} are the reduced stiffnesses for a plane stress state in the 1-2 plane, and where the 1-2 is the plane of the UD layer.

$$\begin{bmatrix} \sigma_1 \\ \sigma_2 \\ \tau_{12} \end{bmatrix}_L = \begin{bmatrix} Q_{11} & Q_{12} & 0 \\ Q_{12} & Q_{22} & 0 \\ 0 & 0 & Q_{66} \end{bmatrix}_L \cdot \begin{bmatrix} \varepsilon_1 \\ \varepsilon_2 \\ \gamma_{12} \end{bmatrix}_L \quad (5.7)$$

$$\text{with } Q_{11} = \frac{E_x}{1 - \nu_{xy} \cdot \nu_{yx}}; \quad Q_{12} = \frac{\nu_{yx} \cdot E_x}{1 - \nu_{xy} \cdot \nu_{yx}} = \frac{\nu_{yx} \cdot E_y}{1 - \nu_{xy} \cdot \nu_{yx}}; \quad Q_{22} = \frac{E_y}{1 - \nu_{xy} \cdot \nu_{yx}}; \quad Q_{66} = G_{xy}$$

In the so called “modified laminate theory” the out-of-plane shear stiffness parameters are taken into account. Furthermore, the assumption of normality of plane sections is not valid, given that plane section normal to the midplane remains plane but not normal to the surface after deformation (DANIEL AND ISHAI 2006) (also see Figure 5.2). The stress-strain relationship on the reduced stiffness matrix of the three-dimensional UD layer of an orthotropic material are given by Equation (5.8), where \bar{Q}_{55} and \bar{Q}_{44} are the shear stiffnesses in the 1-3 and 2-3 plane, and where these planes are perpendicular to the plane of the UD layer.

$$\begin{bmatrix} \sigma_1 \\ \sigma_2 \\ \tau_{12} \\ \tau_{13} \\ \tau_{23} \end{bmatrix}_L = \begin{bmatrix} Q_{11} & Q_{12} & 0 & 0 & 0 \\ Q_{12} & Q_{22} & 0 & 0 & 0 \\ 0 & 0 & Q_{66} & 0 & 0 \\ 0 & 0 & 0 & Q_{55} & 0 \\ 0 & 0 & 0 & 0 & Q_{44} \end{bmatrix}_L \cdot \begin{bmatrix} \varepsilon_1 \\ \varepsilon_2 \\ \gamma_{12} \\ \gamma_{13} \\ \gamma_{23} \end{bmatrix}_L \quad (5.8)$$

$$\text{with } Q_{55} = G_{xz}; \quad Q_{44} = G_{yz}$$

5.2.2 Implementation of long-term deformation coefficients

In reference to Chapter 4.2, a time-dependent viscoelastic material law for timber is defined by considering the deformation coefficients k_{def} within the stiffness matrix of the UD layer of an orthotropic material. With respect to Equation (5.8), the time-dependent stiffness matrix of the UD layer is provided by Equation (5.9) (stress-strain relationship). Hereby it is assumed that the *Poisson's* ratios are independent regarding the load duration.

$$\begin{bmatrix} \sigma_{1,t} \\ \sigma_{2,t} \\ \tau_{12,t} \\ \tau_{13,t} \\ \tau_{23,t} \end{bmatrix}_L = \begin{bmatrix} \frac{E_{x,t}}{1 - \nu_{xy} \cdot \nu_{yx}} & \frac{\nu_{yx} \cdot E_{x,t}}{1 - \nu_{xy} \cdot \nu_{yx}} & 0 & 0 & 0 \\ \frac{\nu_{yx} \cdot E_{y,t}}{1 - \nu_{xy} \cdot \nu_{yx}} & \frac{E_{y,t}}{1 - \nu_{xy} \cdot \nu_{yx}} & 0 & 0 & 0 \\ 0 & 0 & G_{xy,t} & 0 & 0 \\ 0 & 0 & 0 & G_{xz,t} & 0 \\ 0 & 0 & 0 & 0 & G_{yz,t} \end{bmatrix} \begin{bmatrix} \varepsilon_{1,t} \\ \varepsilon_{2,t} \\ \gamma_{12,t} \\ \gamma_{13,t} \\ \gamma_{23,t} \end{bmatrix}_L \quad (5.9)$$

Inserting the deformation coefficients (see Equations (4.16) and (4.17)) into the time-dependent stiffness matrix of the UD layer, the time-dependent stress-strain relation results in Equation (5.10).

$$\begin{bmatrix} \sigma_{1,t} \\ \sigma_{2,t} \\ \tau_{12,t} \\ \tau_{13,t} \\ \tau_{23,t} \end{bmatrix}_L = \begin{bmatrix} \frac{E_x}{(1 - \nu_{xy} \cdot \nu_{yx}) \cdot (1 + k_L)} & \frac{\nu_{yx} \cdot E_x}{(1 - \nu_{xy} \cdot \nu_{yx}) \cdot (1 + k_T)} & 0 & 0 & 0 \\ \frac{\nu_{yx} \cdot E_y}{(1 - \nu_{xy} \cdot \nu_{yx}) \cdot (1 + k_L)} & \frac{E_y}{(1 - \nu_{xy} \cdot \nu_{yx}) \cdot (1 + k_T)} & 0 & 0 & 0 \\ 0 & 0 & \frac{G_{xy}}{1 + k_{shear}} & 0 & 0 \\ 0 & 0 & 0 & \frac{G_{xz}}{1 + k_{shear}} & 0 \\ 0 & 0 & 0 & 0 & \frac{G_{yz}}{1 + k_{shear}} \end{bmatrix} \begin{bmatrix} \varepsilon_{1,t} \\ \varepsilon_{2,t} \\ \gamma_{12,t} \\ \gamma_{13,t} \\ \gamma_{23,t} \end{bmatrix}_L \quad (5.10)$$

5.2.3 Transformation of the stiffness matrix

The transformation of stresses from the global coordinate system to the local coordinate system of the UD layers is realized by way of multiplication of the stiffness matrix with the transformation matrix $[T]$ (Equation (5.11)). The terms of the transformation matrix follow the plane stress and plane strain conditions (Figure 5.3) and their interaction on the *Mohr's* circle.

$$\begin{bmatrix} \sigma_1 \\ \sigma_2 \\ \tau_{12} \\ \tau_{13} \\ \tau_{23} \end{bmatrix}_L = [T] \cdot \begin{bmatrix} \sigma_x \\ \sigma_y \\ \tau_{xy} \\ \tau_{xz} \\ \tau_{yz} \end{bmatrix} = \begin{bmatrix} \cos^2 \theta & \sin^2 \theta & 2 \cos \theta \sin \theta & 0 & 0 \\ \sin^2 \theta & \cos^2 \theta & -2 \cos \theta \sin \theta & 0 & 0 \\ -\cos \theta \sin \theta & \cos \theta \sin \theta & (\cos^2 \theta - \sin^2 \theta) & 0 & 0 \\ 0 & 0 & 0 & \cos \theta & \sin \theta \\ 0 & 0 & 0 & -\sin \theta & \cos \theta \end{bmatrix} \begin{bmatrix} \sigma_x \\ \sigma_y \\ \tau_{xy} \\ \tau_{xz} \\ \tau_{yz} \end{bmatrix} \quad (5.11)$$

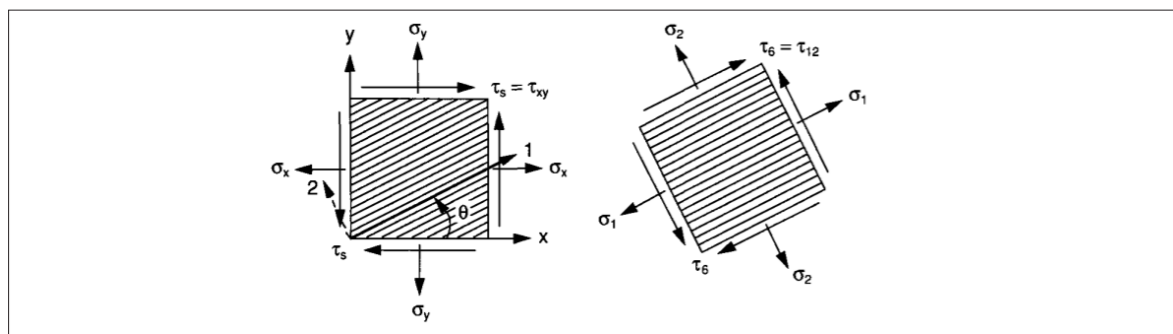


Fig. 5.3: Stress components in unidirectional lamina referred to loading and material axes (DANIEL AND ISHAI 2006)

The *Reuter's* matrix $[R]$ is used to adapt the transformation matrix regarding the transformation of in-plane and out-of-plane shear strains to the assumption of the technical shear strain theory ($2\gamma = \varepsilon$) (Equation (5.12)) (REUTERS 1971; ROYLANCE 2000; (DANIEL AND ISHAI 2006)).

$$\begin{bmatrix} \varepsilon_1 \\ \varepsilon_2 \\ \gamma_{12} \\ \gamma_{13} \\ \gamma_{23} \end{bmatrix}_L = [R] \cdot [T^{-T}] \cdot \begin{bmatrix} \varepsilon_x \\ \varepsilon_y \\ \gamma_{xy} \\ \gamma_{xz} \\ \gamma_{yz} \end{bmatrix} = \begin{bmatrix} 1 & 0 & 0 & 0 & 0 \\ 0 & 1 & 0 & 0 & 0 \\ 0 & 0 & 2 & 0 & 0 \\ 0 & 0 & 0 & 2 & 0 \\ 0 & 0 & 0 & 0 & 2 \end{bmatrix} \cdot [T^{-T}] \cdot \begin{bmatrix} \varepsilon_x \\ \varepsilon_y \\ \gamma_{xy} \\ \gamma_{xz} \\ \gamma_{yz} \end{bmatrix} \quad (5.12)$$

Conversely, the transformation of stresses and strains from the local coordinate system to the global coordinate system is realized by way of multiplication with the inverse transformation matrix $[T^{-1}]$. The global stresses are calculated from the global strains multiplied with the reduced and transformed stiffness matrix $[\bar{Q}]$. The transformed stiffness matrix takes into account the individual arrangements of the layers i under an angle θ_i (Equation (5.13)) (JONES 2014; SCHICKHOFER 1994):

$$\begin{bmatrix} \sigma_x \\ \sigma_y \\ \tau_{xy} \\ \tau_{xz} \\ \tau_{yz} \end{bmatrix} = [T^{-1}] \cdot [Q]_L \cdot [R^{-1}] \cdot \begin{bmatrix} \varepsilon_1 \\ \varepsilon_2 \\ \gamma_{12} \\ \gamma_{13} \\ \gamma_{23} \end{bmatrix}_L = [T^{-1}] \cdot [Q]_L \cdot [R^{-1}] \cdot [R] \cdot [T] \cdot \begin{bmatrix} \varepsilon_x \\ \varepsilon_y \\ \gamma_{xy} \\ \gamma_{xz} \\ \gamma_{yz} \end{bmatrix} = [\bar{Q}] \cdot \begin{bmatrix} \varepsilon_x \\ \varepsilon_y \\ \gamma_{xy} \\ \gamma_{xz} \\ \gamma_{yz} \end{bmatrix} \quad (5.13)$$

with $[T^{-1}] \cdot [Q]_L \cdot [R^{-1}] \cdot [R] \cdot [T] = [T^{-1}][Q]_L \cdot [T^{-T}] = [\bar{Q}]$

The stress-strain relationship by means of the transformed stiffness matrix $[\bar{Q}]$ of the UD layer is highlighted by Equation (5.14). Herby the derivation of the transformed stiffness terms \bar{Q}_{ij} follows Equations (5.11), (5.12), and (5.13). The respective matrix product ($[T^{-1}][Q]_L[T^{-T}]$) consisting of trigonometric functions can exemplarily be taken from various literature as for example (SCHICKHOFER 1994), (DANIEL AND ISHAI 2006), or (JONES 2014) and is also provided in Appendix A1 of this thesis (Derivation of the transformed stiffness terms). Equations (5.15) and (5.16) exemplarily give the (global) reduced stiffness terms \bar{Q}_{11} and \bar{Q}_{55} as a function of the angle θ (tensor transformation).

$$\begin{bmatrix} \sigma_x \\ \sigma_y \\ \tau_{xy} \\ \tau_{xz} \\ \tau_{yz} \end{bmatrix} = \begin{bmatrix} \bar{Q}_{11} & \bar{Q}_{12} & \bar{Q}_{16} & 0 & 0 \\ \bar{Q}_{12} & \bar{Q}_{22} & \bar{Q}_{26} & 0 & 0 \\ \bar{Q}_{16} & \bar{Q}_{26} & \bar{Q}_{66} & 0 & 0 \\ 0 & 0 & 0 & \bar{Q}_{55} & \bar{Q}_{45} \\ 0 & 0 & 0 & \bar{Q}_{45} & \bar{Q}_{44} \end{bmatrix} \begin{bmatrix} \varepsilon_x \\ \varepsilon_y \\ \gamma_{xy} \\ \gamma_{xz} \\ \gamma_{yz} \end{bmatrix} \quad (5.14)$$

$$\bar{Q}_{11} = Q_{11} \cos^4 \theta + 2(Q_{12} + 2Q_{66}) \sin^2 \theta \cos^2 \theta + Q_{22} \sin^4 \theta \quad (5.15)$$

$$\bar{Q}_{55} = Q_{55} \cos^2 \theta + Q_{44} \sin^2 \theta + 2Q_{45} \cos \theta \sin \theta \quad (5.16)$$

Note that the transformed stiffness matrix has terms in all nine positions of the in-plane stress-strain relations, since the UD layer is stressed in non-principal directions ($\bar{Q}_{16} = \bar{Q}_{26} \neq 0$). Also, the asymmetric out-of-plane stiffness terms are no longer zero, as it is for orthotropic materials stressed in non-principal directions ($\bar{Q}_{45} \neq 0$). The asymmetric stiffnesses terms of the UD layer have to be taken into account for the calculation of the overall laminate stiffness (see Chapter 5.2.5).

5.2.4 Engineering constants in non-principal directions

The principal engineering constants for timber according to Equation (4.7) are inserted into the transformed and reduced stiffness matrix of the UD layer (Equation (5.14)) and its reduced stiffness terms in order to achieve the engineering constants E_i and G_{ij} as a function of the layer orientation (see Equations (5.15) and (5.16) as well as Appendix A1).

Equations 5.17 and 5.18 exemplary give the modulus of elasticity $E_1(\theta)$ and the out-of-plane shear modulus $G_{13}(\theta)$ as a function of fibre orientation, derived as previously described. Further Equations for engineering constants ($E_2(\theta)$, $G_{12}(\theta)$, $G_{23}(\theta)$) in non-principal directions are given in Appendix A1. Note, that the indices 1, 2, and 3 no longer represent the principal material axes but the initial orientation of the transformed constant.

$$E_1(\theta) = \left[\frac{1}{E_x} \cos^4 \theta + \left(\frac{1}{G_{xy}} - \frac{2\nu_{xy}}{E_x} \right) \sin^2 \theta \cos^2 \theta + \frac{1}{E_y} \sin^4 \theta \right]^{-1} \quad (5.17)$$

$$G_{13}(\theta) = \left[\frac{1}{G_{xz}} \left(\cos^2 \theta + \sin^2 \theta \cdot \frac{G_{xz}}{G_{yz}} \right) \right]^{-1} \quad (5.18)$$

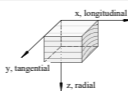
Table 5.1 and Figure 5.4 demonstrate the distribution of the modulus of elasticity and the shear modulus as a function of the fibre orientation to the global x axis following the tensor transformation (Equations (5.11) to (5.18)). The initial values of E_0 (E_x) and E_{90} (E_y) as well as G_0 (G_{xz}) and G_{90} (G_{yz}) are chosen in accordance with the mean values following ETA-20/0023 (Tab. 4.9, Chapter 4.3.2). The *Poisson's* ratios are chosen according to (HALÁSZ AND SCHEER 1996).

In addition, the analytical values are compared to the well-known interpolation by *Hankinson* (Equations (5.19) and (5.20)) (HANKINSON 1921). The *Hankinson's* approach was initially predicted to compression strength of wood at varying angles but may also be used for the determination of the moduli of elasticity and the shear moduli (see RADCLIFFE 1965 and BAHMANZAD ET AL. 2020).

$$E_1(\theta) = \frac{E_x \cdot E_y}{E_x \cdot \sin^2 \theta + E_y \cdot \cos^2 \theta} \quad (5.19)$$

$$G_{13}(\theta) = \frac{G_{xz} \cdot G_{yz}}{G_{xz} \cdot \sin^2 \theta + G_{yz} \cdot \cos^2 \theta} \quad (5.20)$$

Tab. 5.1: Moduli of elasticity and shear moduli of spruce of single laminations as a function of the layer arrangements, following different analytical approaches

 L-T θ [°]	analytical investigations on spruce tensor transformation Equations (5.11) to (5.18)		analytical investigations on spruce <i>Hankinson's</i> approach Equations (5.19) and (5.20)	
	$E_{\text{transf.}}$ [MPa]	$G_{\text{transf.}}$ [MPa]	$E_{\text{Hankinson}}$ [MPa]	$G_{\text{Hankinson}}$ [MPa]
0.0	11000	690	11000	690
15.0	5633	371	3761	371
30.0	2088	164	1344	164
45.0	958	93	716	93
60.0	560	65	488	65
75.0	410	53	396	53
90.0	370	50	370	50

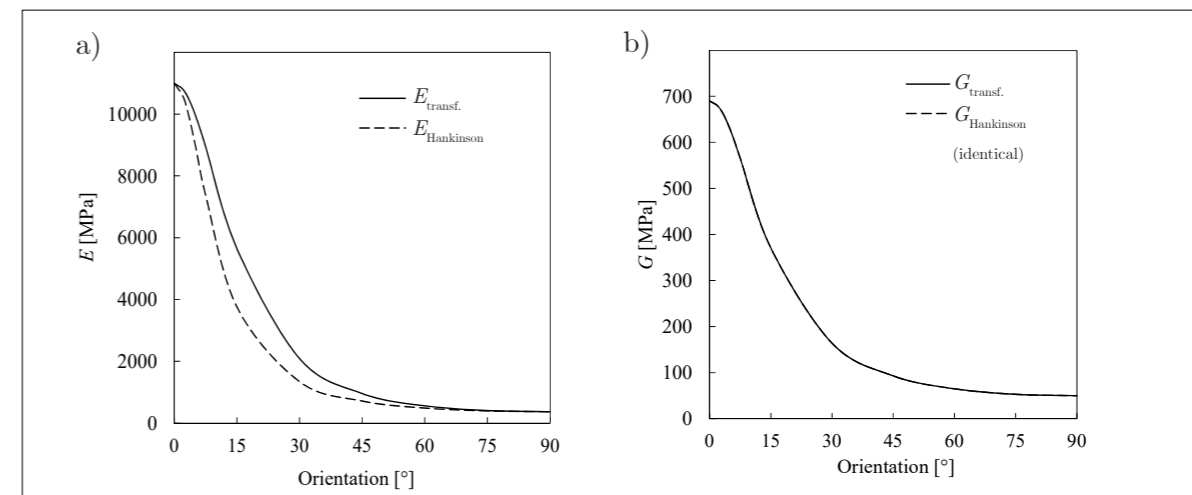


Fig. 5.4: Modulus of elasticity (a) and shear modulus (b) of spruce as a function of the fibre orientation

Equations (5.18) and (5.20) show that the analytical solutions for the derivation of the shear modulus as a function of θ are identical to the *Hankinson's* approach (Figure 5.4 b).

The discrepancy between the analytical solution for the modulus of elasticity as a function of θ (Equations (5.11) to (5.18)) and the analytical solution following the *Hankinson's* approach are large. The decrease of the moduli of elasticity with increasing fibre angle is more pronounced according to the *Hankinson's* approach than according to the transformation of the UD layer. This discrepancy is most pronounced at an angle of $\theta = 15^\circ$ ($\Delta E = 1872$ MPa) (Figure 5.4 a). The reason for this is the influence of the shear modulus G_{xy} as well as the *Poisson's* ratio ν_{xy} within Equation (5.17). Considering $G_{xy} = 690$ MPa and $\nu_{xy} = 0.38$, the analytical solution following the tensor transformation may achieve more realistic values, than *Hankinson's* approach. This statement is validated below by comparing the analytical approaches with experimental investigations.

The moduli of elasticity following the analytical approaches are compared to experimental investigations in order to verify the values of the analytical solutions (compression tests on ash (*Fraxinus Excelsior*) by (CLAUSS ET AL. 2014)). The results of the experimental measurements are summarized for the compression tests in steps of 15° (rotation in the 1-2 plane) within Table 5.2. For the analytical solution, the respective mean values of the compression tests at 0° and 90° are chosen as input parameters ($E_x = 9196$ MPa and $E_y = 696$ MPa; $G_{xy} = 690$ MPa). Additional experimental investigations on the longitudinal-radial plane (1-3 plane) and radial-tangential plane (2-3 plane) of the compression and tension tests are given within (CLAUSS ET AL. 2014).

With respect to the description of the orthotropic material properties of wood (three symmetric planes aligned perpendicular to each other describe its orthotropic material behavior) the analytical approaches are valid for a rotation under the angle θ within the longitudinal-radial plane (1-3 plane) and the longitudinal-tangential plane (1-2 plane) of the UD layer (also see Chapter 4.1).

The analytical approaches on the shear moduli are compared to experimental investigations on the shear moduli for verification reasons (small-scale shear tests on eastern hemlock (*Tsuga Canadensis*) by (BAHMANZAD ET AL. 2020)). The results of the experimental measurements are summarized for angles of 0°, 30°, 45°, 60°, and 90° within Table 5.2 for a rotation from the longitudinal to radial plane. Note that no experimental results for fiber orientation under 15° and 75° are given within (BAHMANZAD ET AL. 2020). For the analytical solution the respective experimental mean values of the shear tests at 0° and 90° are chosen as input parameters ($G_{0^\circ} = 398$ MPa and $G_{90^\circ} = 45$ MPa).

Due to the similarity of Equations (5.18) and (5.20) the analytical solution according to *Hankinson's* approach and the tensor transformation are the same. The experimental investi-

Tab. 5.2: Moduli of elasticity of ash and shear moduli of eastern hemlock of single laminations following different experimental and analytical investigations

orientation θ [°]	experimental investigations compression tests (CLAUSS ET AL. 2014)	analytical investigations following tensor transformation and <i>Hankinson's</i> approach		experimental investigations (BAHMANZAD ET AL. 2020)	analytical investigations
	E_{exp}^1 (1-2 plane) [MPa]	$E_{analytical}$ [MPa]	$E_{Hankinson}$ [MPa]	G_{exp}^2 (1-3 plane) [MPa]	$G_{transf./Hankins.}^3$ [MPa]
0.0	9196	9160	9160	398	398
15.0	7004	5374	5048	/	261
30.0	2403	2469	2267	151	134
45.0	1488	1379	1294	88	81
60.0	984	936	905	61	58
75.0	704	749	742	/	48
90.0	696	696	696	45	45

¹average COV 5.1 % (CLAUSS ET AL. 2014)
²average COV 13.8 % (BAHMANZAD ET AL. 2020)-
³ $G_{transf.} = G_{Hankinson}$

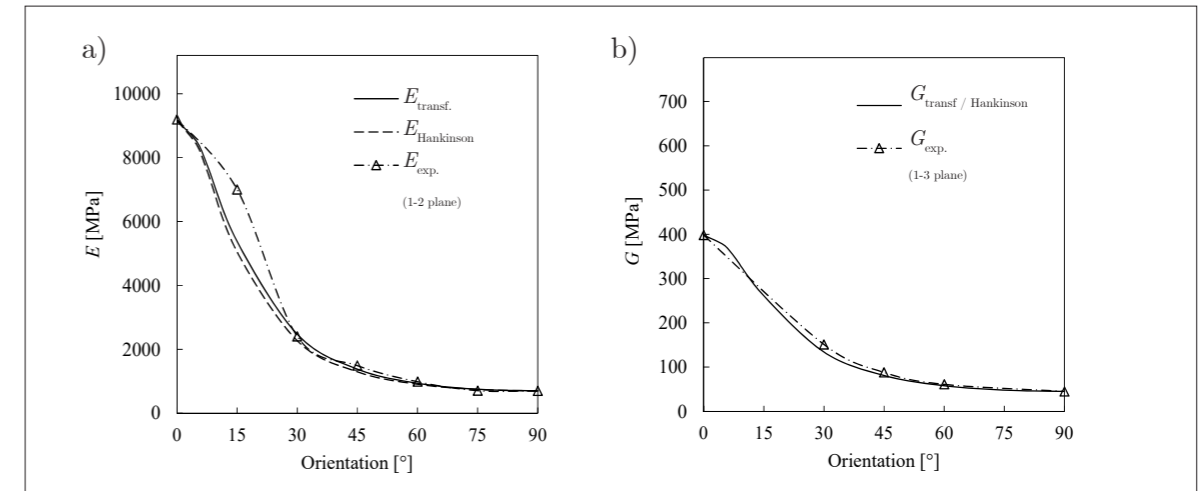


Fig. 5.5: Modulus of elasticity of ash (a) and shear modulus of eastern hemlock (b) as a function of the fibre orientation (experimental values based on (CLAUSS ET AL. 2014 and BAHMANZAD 2020))

gations on the moduli of elasticity differ from the analytical solution under 15° by 1630 MPa. The deviation may be due to material scattering or influences of the microfibril angle (NAVI AND GILANI 2004). For angles $\theta > 30^\circ$ the analytical solution is confirmed by the experiments. With respect to the shear modulus, the analytical solution of the tensor transformation and the *Hankinson's* approach match the experimentally determined values quite well.

5.2.5 Mechanical coupling and laminate stiffness properties

Laminates are characterized by their response to mechanical loading, which is associated with a description of the coupling behavior. The matrix notation of the law of elasticity on the plate element consists of different sub matrices. These are referred to as the extensional stiffness A , the bending-extension coupling stiffness B , and the bending-twist coupling stiffness D (also see Appendix A2 and Equations (A15) to (A18)). The ABD relation is often expressed using compact notation (Equation (5.21)) (NETTLES 1994):

$$\begin{Bmatrix} N \\ M \end{Bmatrix} = \begin{bmatrix} A & B \\ B & D \end{bmatrix} \begin{Bmatrix} \varepsilon \\ \kappa \end{Bmatrix}$$

with

$$A_{ij} = \int_{-t/2}^{t/2} \bar{Q}_{ij} dz = \sum_{k=1}^n [\bar{Q}_{ij}]_k \cdot (z_k - z_{k-1}) \quad (A15)$$

$$B_{ij} = \int_{-t/2}^{t/2} \bar{Q}_{ij} z dz = \frac{1}{2} \sum_{k=1}^n [\bar{Q}_{ij}]_k \cdot (z_k^2 - z_{k-1}^2) \quad (A16)$$

$$D_{ij} = \int_{-t/2}^{t/2} \bar{Q}_{ij} z^2 dz = \frac{1}{3} \sum_{k=1}^n [\bar{Q}_{ij}]_k \cdot (z_k^3 - z_{k-1}^3) \quad (A17)$$

With respect to the out-of-plane shear deformations a fourth sub matrix E is introduced. While the ABD relation refers to the assumptions of the classical laminate theory, E refers to the out-of-plane shear stress-strain relations and is therefore **decoupled** from the ABD relation (Equation (A18)).

$$E_{ij} = k_{i,z} \cdot \int_{-t/2}^{t/2} \bar{Q}_{ij} dz = k_i^S \cdot \sum_{k=1}^n [\bar{Q}_{ij}]_k \cdot (z_k - z_{k-1}) \quad (\text{A18})$$

The out-of-plane shear stiffness values refer to the entries E_{44} and E_{55} of the extended $ABD-E$ matrix and therefore to the sum of the out-of-plane stiffness terms of the UD layer $\sum \bar{Q}_{ij}$ multiplied by the respective layer thickness t_i . Within (A18), the asymmetric stiffness terms \bar{Q}_{45} of diagonally oriented UD layers may be taken into account according to Equation (5.22) and Equation (5.23).

$$E_{55} = k_{xz} \cdot \sum_{k=1}^n \left[\frac{\bar{Q}_{44}}{\bar{Q}_{44} \cdot \bar{Q}_{55} - \bar{Q}_{45}^2} \right]_k \cdot (z_k - z_{k-1}) \quad (5.22)$$

$$E_{44} = k_{yz} \cdot \sum_{k=1}^n \left[\frac{\bar{Q}_{55}}{\bar{Q}_{55} \cdot \bar{Q}_{44} - \bar{Q}_{45}^2} \right]_k \cdot (z_k - z_{k-1}) \quad (5.23)$$

Additionally a shear correction coefficient for laminates is introduced, as is the case for isotropic plates. For laminates with orthotropic layers, the shear correction coefficients k_{xz} and k_{yz} differ significantly to the shear correction coefficient for isotropic plates ($k = 5/6$). The determination of shear correction coefficients—valid for CLT and DLT—is given within Chapter 5.2.7. The matrix notation of the law of elasticity on CLT and DLT elements, taking into account out-of-plane shear stiffness terms, can be noted as Equation (5.24). The ABD relation extended by the fourth sub matrix E is referred to as the $ABD-E$ matrix in this thesis.

$$\begin{bmatrix} N_x \\ N_y \\ N_{xy} \\ M_x \\ M_y \\ M_{xy} \\ V_x \\ V_y \end{bmatrix} = \begin{bmatrix} A_{11} & A_{12} & A_{16} & B_{11} & B_{12} & B_{16} & 0 & 0 \\ A_{21} & A_{22} & A_{26} & B_{12} & B_{22} & B_{26} & 0 & 0 \\ A_{16} & A_{26} & A_{66} & B_{16} & B_{26} & B_{66} & 0 & 0 \\ \bar{B}_{11} & \bar{B}_{12} & \bar{B}_{16} & D_{11} & D_{12} & D_{16} & 0 & 0 \\ \bar{B}_{12} & \bar{B}_{22} & \bar{B}_{26} & D_{12} & D_{22} & D_{26} & 0 & 0 \\ \bar{B}_{16} & \bar{B}_{26} & \bar{B}_{66} & D_{16} & D_{26} & D_{66} & 0 & 0 \\ 0 & 0 & 0 & 0 & 0 & 0 & E_{55} & E_{54} \\ 0 & 0 & 0 & 0 & 0 & 0 & E_{45} & E_{44} \end{bmatrix} \cdot \begin{bmatrix} \varepsilon_x \\ \varepsilon_y \\ \gamma_{xy} \\ \kappa_x \\ \kappa_y \\ \kappa_{xy} \\ \gamma_{xz} \\ \gamma_{yz} \end{bmatrix} \quad (5.24)$$

A possible compact notation of the $ABD-E$ relation is given by Equation (5.25).

$$\begin{Bmatrix} N \\ M \\ V \end{Bmatrix} = \begin{bmatrix} A & B & 0 \\ B & D & 0 \\ 0 & 0 & E \end{bmatrix} \begin{Bmatrix} \varepsilon \\ \kappa \\ \gamma \end{Bmatrix} \quad (5.25)$$

The coupling of the transformed reduced stiffnesses following the $ABD-E$ relations, and in particular the coupling of the out-of-plane shear stiffness values, are obviously complicated to understand. The response of an laminate to out-of-plane shear stresses may be better understood when the transformed shear moduli of the respective layers are examined. Or, "Nothing should, therefore, be taken for granted with a new composite material: its moduli as a function of θ must be examined to truly understand its character." (JONES 2014, p. 81). Based on the findings within Chapter 5.2.4 and with respect to the statement of (JONES 2014), the transformed engineering $G_{13}(\theta)$ and $G_{23}(\theta)$ of the UD-layers may be used for the calculation of the out-of-plane stiffness properties E_{ij} , instead of the transformed stiffness terms of the UD-layer (Equation (5.26)).

$$E_{ij} = k_{i,z} \cdot \int_{-t/2}^{t/2} G_{ij}(\theta) dz = k_i^S \cdot \sum_{k=1}^n G_{ij}(\theta) \cdot (z_k - z_{k-1}) \quad (5.26)$$

The values of $G_{13}(\theta)$ and $G_{23}(\theta)$ within Equation (5.26) are calculated according to Equations (A13) and (A14). Both approaches—Equation (5.26) as well as Equations (5.22) and (5.33)—result in the same out-of-plane shear stiffness values $E_{55} = S_{xz}$ and $E_{44} = S_{yz}$ (see following Chapter 5.2.6).

Figure 5.6 gives the flowcharts for the determination of transformed stiffness properties and transformed engineering constants in non-principal directions, leading to the $ABD-E$ stiffness matrix for laminates. The flowcharts are extended by Equation (5.26) for better understanding of the out-of-plane stiffness properties (also see Appendix A2).

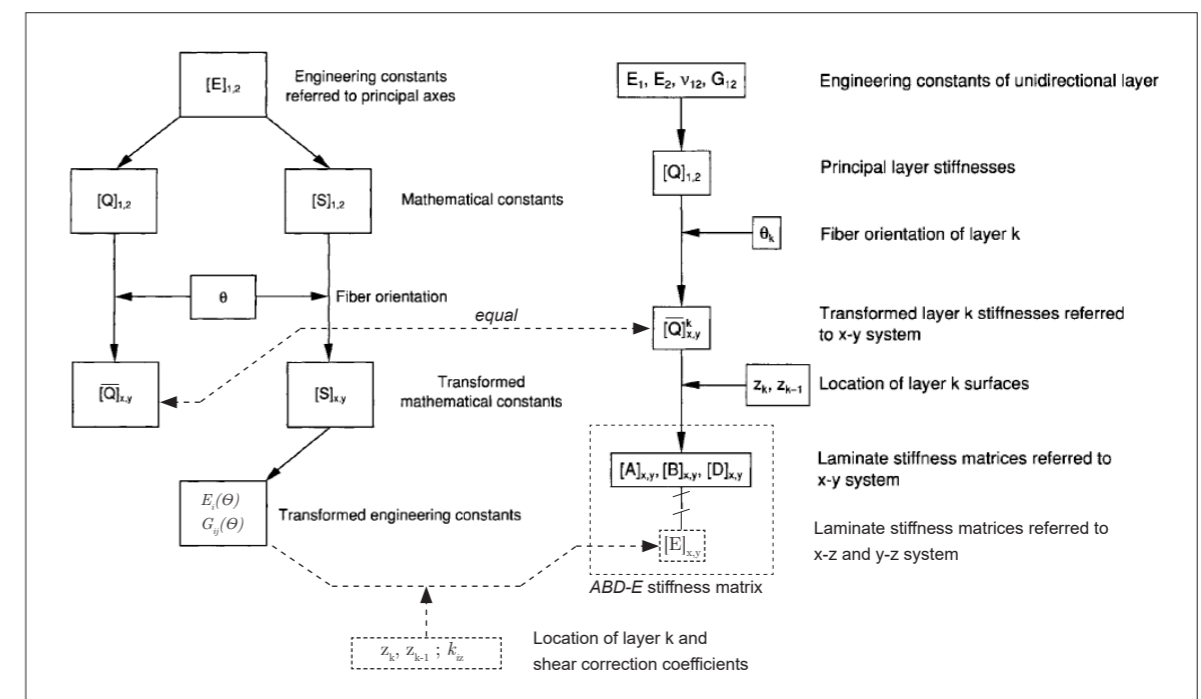


Fig. 5.6: Flowcharts for determination of transformed elastic constants (left) and laminate stiffness matrices (right) based on DANIEL AND ISHAI (2006), extended by own approaches (dashed lines)

5.2.6 Exemplary ABD - E stiffness matrices for CLT and DLT

The laminate stiffness is given by the ABD - E matrix. Equations (5.27) and (5.28) exemplary give the ABD - E matrices for the 5-layered CLT series O1 ($t = 100$ mm; $[0^\circ, 90^\circ, 0^\circ, 90^\circ, 0^\circ]$ and the 5-layered DLT $\pm 45^\circ$ series D3 ($t = 100$ mm; $[0^\circ, 45^\circ, 90^\circ, -45^\circ, 0^\circ]_s$). The initial (input) values of E_{0° and E_{90° as well as G_{0° and G_{90° are chosen in accordance with the mean values following ETA-20/0023 (Tab. 4.9), *Poisson's* ratios according to (HALÁSZ AND SCHEER 1996).

The ABD - E matrix of a 5-layered CLT element according to the O1 series takes the following values in $[\text{MNm}^2/\text{m}]$ and $[\text{MN}/\text{m}]$, without the calculation of shear correction coefficients (Equation (5.27)).

$$[Q] = \begin{bmatrix} 679.00 & 141.00 & 0 & 0 & 0 & 0 & 0 & 0 \\ 141.00 & 465.00 & 0 & 0 & 0 & 0 & 0 & 0 \\ 0 & 0 & 69.00 & 0 & 0 & 0 & 0 & 0 \\ 0 & 0 & 0 & -0.74 & -0.01 & 0 & 0 & 0 \\ 0 & 0 & 0 & -0.01 & -0.22 & 0 & 0 & 0 \\ 0 & 0 & 0 & 0 & 0 & -0.058 & 0 & 0 \\ 0 & 0 & 0 & 0 & 0 & 0 & k_{xz} \cdot 43.40 & 0 \\ 0 & 0 & 0 & 0 & 0 & 0 & 0 & k_{yz} \cdot 30.60 \end{bmatrix} \quad (5.27)$$

The ABD - E matrix of a 5-layered DLT $\pm 45^\circ$ element according to the D3 series takes the following values ($[\text{MNm}^2/\text{m}]$ and $[\text{MN}/\text{m}]$) (Equation (5.28)):

$$[Q] = \begin{bmatrix} 597.00 & 103.00 & 0 & 0 & 0 & 0.002 & 0 & 0 \\ 103.00 & 383.00 & 0 & 0 & 0 & 0.002 & 0 & 0 \\ 0 & 0 & 151.93 & 0.002 & 0.002 & 0 & 0 & 0 \\ 0 & 0 & 0.002 & -0.79 & -0.05 & 0 & 0 & 0 \\ 0 & 0 & 0.002 & -0.05 & -0.10 & 0 & 0 & 0 \\ 0.002 & 0.002 & 0 & 0 & 0 & -0.093 & 0 & 0 \\ 0 & 0 & 0 & 0 & 0 & 0 & k_{xz} \cdot 32.33 & 0 \\ 0 & 0 & 0 & 0 & 0 & 0 & 0 & k_{yz} \cdot 19.53 \end{bmatrix} \quad (5.28)$$

Equation (5.29) exemplary determines the entries $k_{xz} \cdot E_{55}$ of the DLT $\pm 45^\circ$ D3 series using the transformed stiffness terms \bar{Q}_{ij} according to Equation (A18) and compares them to the sum of the transformed out-of-plane shear moduli multiplied by the respective layer thicknesses $\sum G_{13,i}(\theta)$ according to Equation (5.26).

$$\begin{aligned} E_{55} &= k_{xz} \cdot \sum_{k=1}^n \left[\frac{\bar{Q}_{44}}{\bar{Q}_{44} \cdot \bar{Q}_{55} - \bar{Q}_{45}^2} \right]^{-1} \cdot t_i \quad (5.29) \\ &= k_{xz} \cdot \left[2 \cdot \left(\frac{370 \cdot 370 - (320)^2}{370} \right) \cdot 0.02 + 2 \cdot \left(\frac{690 \cdot 50}{50} \right) \cdot 0.02 + \left(\frac{50 \cdot 690}{690} \right) \cdot 0.02 \right] = k_{xz} \cdot 32.33 \\ &= k_{xz} \cdot \sum_{k=1}^n G_{ij}(\theta) \cdot t_i = 2 \cdot 690 \cdot 0.02 + 2 \cdot 93.24 \cdot 0.02 + 50 \cdot 0.02 = k_{xz} \cdot 32.33 = E_{55} \end{aligned}$$

5.2.7 Derivation of shear correction coefficients

According to the *Timoshenko Beam Theory* (TIMOSHENKO 1921), as is the case in the *Reissner-Mindlin Plate Theory*, transversal shear deformations are taken into account (plane sections normal to the mid-plane do not stay normal during deformation). For laminates, the specific transversal deformation behavior of each layer has to be considered. Therefore, the respective entries of the ABD - E stiffness matrix (E_{55} and E_{44}) are multiplied with shear correction coefficients, taking into account the deformation behavior of each layer (see Equation (5.26)). The derivation of shear correction coefficients in x and y direction is based on the principle of virtual displacements and the equilibrium between shear and bending stiffnesses (BOGENSPERGER AND SILLY 2014). Equation (5.30) gives the shear deformation of the single layer as a function on the shear modulus G_{iz} , the shear stresses τ and the shear force dV_i . Equation (5.31) gives the overall shear deformation of the laminate, leading to the shear correction coefficient $k_{i,z}$. Figure 5.7 gives the designations of the chosen indices for z .

$$u_i = \frac{1}{2} \tau \cdot \gamma \cdot dV_i = \frac{1}{2G_{iz}} \tau^2 \cdot dV_i \quad (5.30)$$

$$\text{with: } \gamma = \frac{\tau}{G} \quad ; \quad \tau = \frac{V \cdot ES}{EI \cdot b} \quad ; \quad dV_i = \int dA_i di = b \, dz \, di$$

$$\Delta u = \int_t \frac{1}{2G_{iz,i}} \left(\frac{V_i \cdot E_i S}{E_i I \cdot b} \right)^2 b \, dz \, di \quad (5.31)$$

$$\begin{aligned} &= \frac{1}{2 \sum G_{iz,i} A_i} \cdot \frac{\sum G_{iz,i} A_i}{\left(\int_{-\frac{t}{2}}^{\frac{t}{2}} E_i(z) z^2 dz \right)^2} \cdot \int_{-\frac{t}{2}}^{\frac{t}{2}} \frac{\left(\int_z^{\frac{t}{2}} E_i(z) z dz \right)^2}{G_{iz}(z)} dz \\ &= \frac{1}{2 \sum G_{iz,i} A_i} \cdot \underbrace{\frac{\sum G_{iz,i} A_i}{EI^2 b} \int_t \frac{ES_i^2}{G_{iz}} dz}_{k_{i,z}} \end{aligned}$$

Equation (5.31) now contains the sum of the shear stiffnesses of each single layer, divided by the square of the bending stiffness (including the *Steiner*-terms) multiplied by a double integral involving the modulus of elasticity and the static moment S (ES).

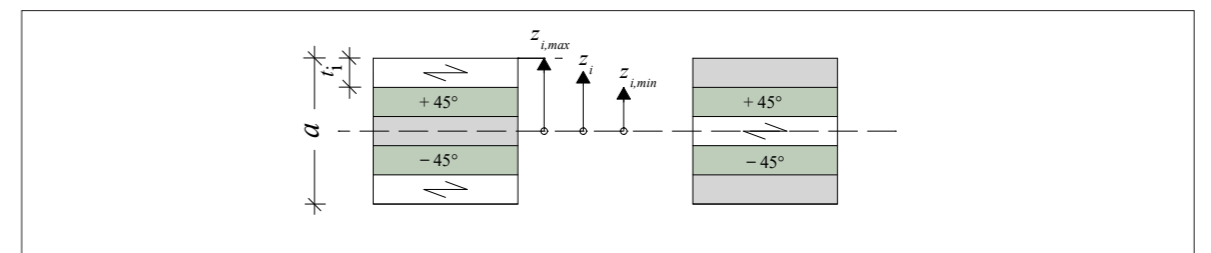


Fig. 5.7: Designation of the parameters and indices of z .

The double integral is determined for each layer using polynomials (Equations (5.32) to (5.34)). A detailed derivation can also be found in (FEICHTER 2013). Due to its complexity, the calculation is usually carried out in tabular manner. The calculation for shear correction coefficients according to the *Timoshenko beam theory* is exemplary given for the O1 and D3 series in Appendix **A3** in tabular manner.

$$\begin{aligned} ES_i &= \int_{t/2}^{z_{i,max}} E z dz = E_i \int_{t/2}^{z_{i,max}} z dz + \sum_{i+1}^n E_i \int_{z_{i,min}}^{z_{i,max}} z dz \\ &= \frac{1}{2} E_i^2 (z_{i,min}^2 - z_i^2) + \sum_{i+1}^n E_i z_i t_i \\ &= \frac{1}{2} E_i^2 (z_{i,min}^2 - z_i^2) + ES_i \end{aligned} \quad (5.32)$$

$$\begin{aligned} [ES_i]^2 &= \frac{1}{4} E_i^2 (z_{i,min}^2 - z_i^2)^2 + E_i^2 (z_{i,min}^2 - z_i^2) ES_i + ES_i^2 \\ &= \frac{1}{4} E_i^2 (z_{i,min}^2 - 2z_{i,min}^2 z_i^2 + z_i^4) + E_i^2 (z_{i,min}^2 - z_i^2) ES_i + ES_i^2 \end{aligned} \quad (5.33)$$

$$\begin{aligned} \int_{z_{i,max}}^{z_{i,min}} [ES_i]^2 dz &= \frac{E_i^2}{60} (8z_{i,min}^5 + 10z_{i,min}^2 z_{i,max}^3 - 15z_{i,max}^4 z_{i,min} - 3z_{i,max}^5) \\ &+ ES_i \frac{E_i^2}{60} (40z_{i,min}^3 - 60z_{i,max}^2 z_{i,min} + 20z_{i,max}^3) \\ &+ ES_i^2 (z_{i,min} - z_{i,max}) \end{aligned} \quad (5.34)$$

Note that again the engineering constants—for $\pm\Theta$ layers in non-principal directions—form the basis of the determination of the shear correction coefficient. For the given example of the CLT O1 series, k_{xz} appears to be 0.181 and k_{yz} to be 0.163. For the given example of the DLT D3 series, k_{xz} appears to be 0.238 and k_{yz} to be 0.659.

Hence, the out-of-plane stiffness values for the CLT O1 series take the values $E_{55} = S_{xz} = 7.96$ MN/m and $E_{44} = S_{yz} = 4.89$ MN/m and $E_{55} = S_{xz} = 7.68$ MN/m and $E_{44} = S_{yz} = 12.86$ MN/m for the DLT D3 series. In x direction the shear stiffness of the DLT is by 58.0 % higher compared to the CLT element. In y direction the shear stiffness value of the DLT appears to be higher by a factor of 2.6 ($S_{yz} = 12.86$ MN/m).

To explain these values, it is necessary to calculate the actual shear deformations of the DLT D3 series under a virtual shear load $V = 100$ kN. The distribution of shear stresses over the cross-section is highly dependent on the respective static moment S and the modulus of elasticity (Equation (5.35)). The shear deformation u_{ij} depends on the shear moduli of the respective layer and the shear stresses (Equation (5.36)). Figure 5.8 compares the quantitative values and distributions of the shear stresses and shear deformations in x direction, to those in y direction. By now, it may become more clear, why the shear stiffness in y direction of the chosen D3 series is much higher, than in x direction. The orientation of the middle

layer under 90° in x direction leads to a high shear strain within this layer. In y direction, the middle layer is oriented under 0° . Therefore, the shear strain of the inner layer is comparably small. The overall shear deformation in y direction is $u_{xz,max} = 1.06$ mm, which is higher by 39.5 % compared to the one in y direction ($u_{yz,max} = 0.76$ mm).

For CLT, the out-of-plane shear properties are influenced mostly by the cross-layers. The approximate distribution of the shear stresses can often be estimated without great effort. In y direction, the maximum shear stresses hit the middle layer with its comparably low shear moduli G_{90} .

For DLT, in addition to the longitudinal and cross-layers, the deformation behavior and stress distribution over arbitrary oriented layers have to be considered. This leads to difficulties in the estimation of the distribution of shear stresses and shear deformations over the cross-section since the interaction between shear stresses and shear moduli has to be considered. Recalling Chapter 5.2.4, the response of an laminate to out-of-plane shear stresses may be better understood when the transformed shear moduli of the respective layers are examined in advance. For the DLT D3 series in y direction, the maximum shear stresses hit the middle layer, which is oriented under 0° and thus provides the maximum shear moduli G_0 . This leads to the much higher shear stiffness in y direction, than in x direction (Figure 5.8).

$$\tau_{ij} = \frac{V \cdot ES}{EI \cdot b} \quad (5.35)$$

$$u_{ij} = \int_0^z \gamma_i dz = \int_0^z \frac{\tau_{ij}}{G_{ij}} dz = \frac{\tau_{ij}}{G_{ij}} \cdot t_i \quad (5.36)$$

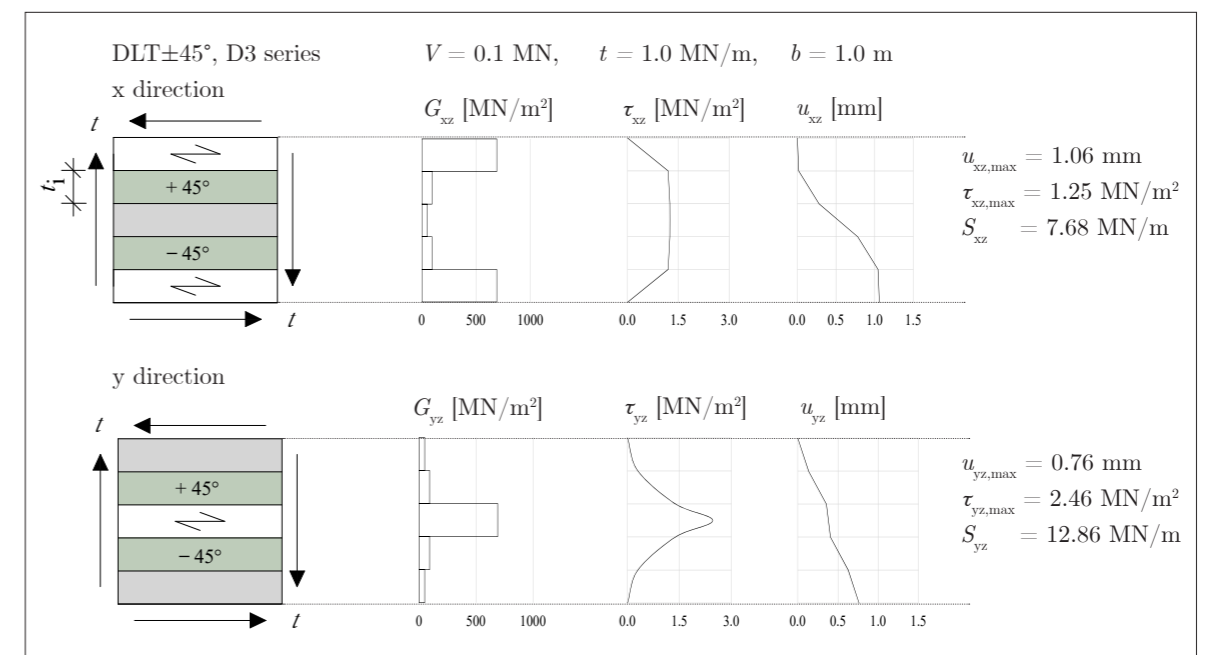


Fig. 5.8: Quantitative shear stresses and shear deformations of an exemplary 5-layered DLT element

When looking at the output of the stiffness matrix of the 2D FE program RF-Laminate (Multilayer Surfaces) (DLUBAL SOFTWARE GMBH 2016), it is noticeable that in the solution stored in the program, the shear stiffness values could be calculated incorrectly on the basis of the transformed stiffness terms \bar{Q}_{55} and \bar{Q}_{44} only, without considerations of the eccentric terms \bar{Q}_{45} (see Equations (5.22) and (5.23)). Furthermore, the output indicates, that the shear correction coefficients are not calculated on the basis of the transformed engineering constants in non-principal directions (Equations (5.17) and (5.18)) (stated as of 2023-09-20).

This is not of importance for CLT, since the layer stiffness values only follow the principal directions ($\bar{Q}_{55} = G_{0^\circ}$; $\bar{Q}_{44} = G_{90^\circ}$; $\bar{Q}_{45} = 0$). For diagonal layer arrangements, on the other hand, this is no longer the case ($\bar{Q}_{55,45^\circ} = 370$ MPa, $\bar{Q}_{45,45^\circ} = 320$ MPa for spruce T14) (see Chapter 5.2.4). Using only the stiffness terms \bar{Q}_{55} and \bar{Q}_{44} within the calculations leads to shear correction coefficients of $k_{xz} = 0.261$ and $k_{yz} = 0.916$ for the exemplary DLT $\pm 45^\circ$ D3 series. The shear stiffness takes the values $S_{xz} = 11.36$ MN/m and $S_{yz} = 28.02$ MN/m for the DLT D3 series. This would mean that the shear stiffness in y direction would be twice as high as if the engineering constants in non-principal directions are used within the calculation of shear correction coefficients and within the ABD-E stiffness matrix ($S_{yz} = 12.86$ MN/m).

Taking into mind the quantitative comparison of the shear deformations on DLT D3 series (Figure 5.8) a shear stiffness of $S_{yz} = 28.02$ MN/m seems to be too high and less realistic, even if the laminate theory is based on the assumptions of a homogeneous layer without gaps. This discrepancy in the solution to shear stiffness values was discussed with Dr. Hochreiner from TU Vienna and Dr. Danielsson from Lund University. Dlubal Software GmbH was also notified in 2022 and 2023 of the risk of overestimating shear stiffness values in laminates with layer orientations deviating from 0° and 90° .

In summary, the use of transformed engineering constants should be considered for the calculation of out-of-plane shear stiffness values of DLT and its future implementation within software tools ($G_{45^\circ} = 93$ MPa for spruce T14). The mechanical background is complex and the output of software tools needs to be further discussed and investigated—also regarding additional aspects like shear-shear coupling (JONES 2014).

With the end of Chapter 5, the first objective of the thesis—the transfer and extension of mechanical basics on the coupling behavior of special anisotropic composites with diagonal layer arrangements towards the stiffness matrix—was covered. The information assembled on the stiffness properties of laminates and the shear correction coefficients serves as a theoretical basis for the determination of analytical reference values to the experimental and numerical determined stiffness parameters within Chapter 6 (investigations on the out-of-plane shear stiffness), Chapter 7 (investigations on the bending stiffness), Chapter 8 (investigations on the torsional stiffness), and Chapter 9 (investigations of the in-plane shear stiffness).

The out-of-plane stiffness properties of the test series according to Tables 4.6 to 4.8 are summarized and compared to each other within Appendix A8 by means of radar charts. In addition, next to the radar charts, the graphical displays of the respective layups are given. The pages of Appendix A8 can be unfolded, to present and link the series and layups investigated to the respective experimental results.

6 Investigations on the out-of-plane shear strength and stiffness

6.1 Analytical determination of the out-of-plane shear stiffness

6.1.1 General information

For the determination of the out-of-plane shear stiffness values of CLT, two methods are commonly used and provide sufficient correlation to previous experimentally determined values. One is the laminate theory taking into account shear correction coefficients within the $ABD-E$ stiffness matrix as previously described. For CLT, the use of shear correction coefficients is incorporated within the Austrian National Annex of EC 5 (ÖNORM B 1995-1-1) as well as proposed by *Schickhofer* and *Wallner-Novak* (SCHICKHOFER ET AL. 2010; WALLNER-NOVAK ET AL. 2013). As described before, the derivation of shear correction coefficients should also be possible for DLT considering the engineering constants in non-principal directions. The other method is the *Shear Analogy Method* proposed by *Kreuzinger* in 1999 (KREUZINGER AND SCHOLZ 1999; KREUZINGER AND SCHOLZ 2001), implemented within the German National Annex to EC 5 (DIN EN 1995-1-1/NA). The *Shear Analogy Method* applied to CLT is independent of the laminate theory. The transfer of the *Shear Analogy Method* from CLT to DLT is investigated in the following section. A third approach is based on energy considerations. The mechanical derivation of the *Energy Method* is sophisticated and not common for the application on CLT and DLT. Various publications introduce the *Energy Method*, such as *Klarmann* and *Schweizerhofer* (KLARMANN AND SCHWEIZERHOF 1993). A further approach is the *Refined Zigzag Theory*—a highly accurate and computational shear-deformation theory for homogeneously laminated composites (TESSLER 2015).

6.1.2 Shear Analogy Method proposed by Kreuzinger

Choosing specific evaluation areas a_x and a_y , within which the distribution of shear stresses can be considered as constant, the shear stiffness values can be calculated without using a shear correction coefficient ($k = 1.0$), in the light of the fact that the evaluation area a_x does not correspond to the total height of the cross-section. The balance of forces between the force resulting from the integration of the shear stresses over the total cross-section and the force resulting from the integration of the shear stresses over the equivalent evaluation area is given. The shear deformation within the respective evaluation area a_x is considered to be roughly linear distributed, forming the angle γ_{xz} (shear strain) (see Figure 6.1). Within *Kreuzinger's* model, for the outer layers in y direction (without edge-gluing), no normal stresses are transferred and therefore negligible shear stresses occur (KREUZINGER AND SCHOLZ 2001). Therefore, outer layers are not considered within a_y .

The shear strain is calculated by the deformations in x or y direction (Equation (6.1)). Considering UD layers acting in the plane stress state, the deformations in z direction are neglected. This assumption corresponds to the technical shear strain theory (see also Equation (5.12)).

$$\gamma_{xz} = \frac{du_x}{dz} + \frac{du_z}{dx} \quad (6.1)$$

Equation (6.2) presents the relationship between shear deformations and the shear strains ($b = 1.0$ m). Bearing in mind the respective shear moduli of each layer, the shear deformations can be summed up over the chosen evaluation area (Equation (6.2)). Due to the assumption of constantly distributed shear stresses, only half of the thickness the first layer ($t_1 = d_1$) and last layer ($t_n = d_n$) is taken into account, resulting in the evaluation area a_x (described previously).

$$\Delta u = \sum_1^n u_i = \left[\frac{d_1}{2 \cdot G_1} + \sum_{i=2}^{n-1} \frac{d_i}{G_i} + \frac{d_n}{2 \cdot G_n} \right] \cdot \tau \quad (6.2)$$

Introducing once more the term $u = \tau/G \cdot a$ (Equation (6.3), also see Equation (5.36)), the out-of-plane shear stiffness S_{ij} as a function of the shear area, of the shear deformation, and of the shear stress is achieved (Equation (6.4), $b = 1.0$ m).

$$u = \frac{\tau}{G} \cdot a = \frac{\tau}{S/a} \cdot a = \tau \cdot \frac{A}{S} \cdot a = \frac{\tau}{S} \cdot a^2 \quad (6.3)$$

$$\frac{1}{S_{ij}} = \frac{1}{a_i^2} \cdot \Delta u \cdot \frac{1}{\tau} \quad (6.4)$$

Inserting the shear deformations for a laminate featuring different shear moduli (Equation (6.2)) into Equation (6.4), the out-of-plane shear stiffness, calculated according to the formula of the *Shear Analogy Method*, is derived (see also KREUZINGER AND SCHOLZ 1999) (Equation (6.5)):

$$\frac{1}{S_{xz}} = \frac{1}{a_x^2} \cdot \left(\frac{d_1}{2 \cdot G_{xz}} + \sum_{i=2}^{n-1} \frac{d_i}{G_{xz}} + \frac{d_n}{2 \cdot G_{xz}} \right) \quad (6.5)$$

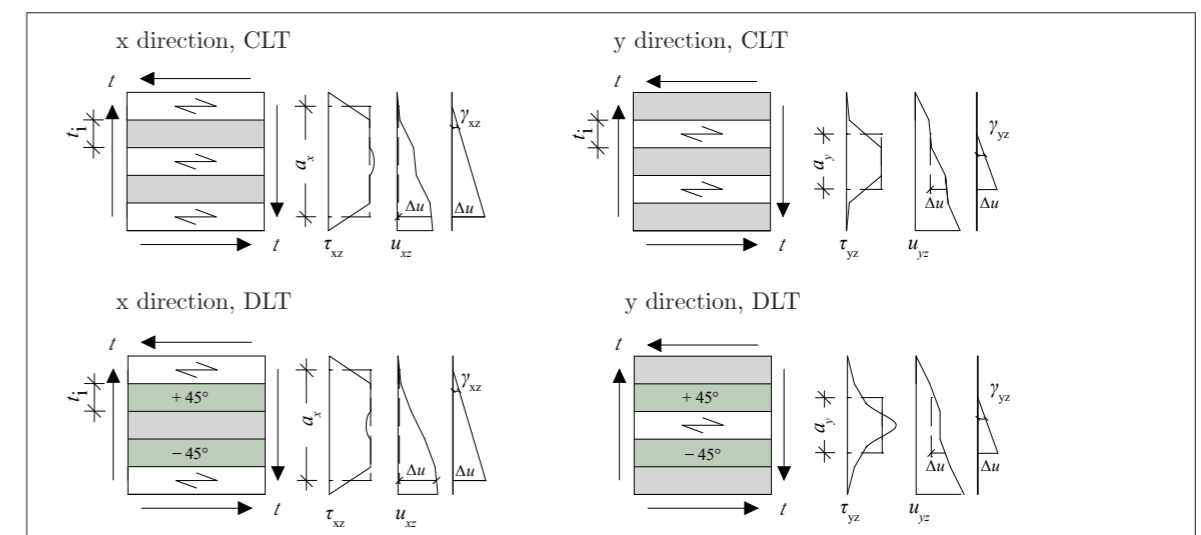


Fig. 6.1: Shear stresses and shear deformations in global x and y direction of an exemplary 5-layered CLT element (upper sketch) and an exemplary 5-layered DLT element (lower sketch)

For the exemplary 5-layered CLT element according to the O1 series ($t_i = 20$ mm), using the material parameters according to Table 4.9 (ETA-20/0023; T14), the out-of-plane shear stiffnesses form the values $S_{xz} = 7.46$ MN/m and $S_{yz} = 3.73$ MN/m. These shear stiffness values of CLT are in comparable range to the values according to the laminate theory using shear correction coefficients ($S_{xz} = 7.96$ MN/m and $S_{yz} = 4.89$ MN/m).

Transferring the approaches and simplifications of the *Shear Analogy Method* from CLT to DLT is rather challenging, which is due to the arrangement of individual laminations deviating from 0° and 90° . Assuming a linear distribution of shear stresses in a chosen evaluation area a_i is only possible to a limited extent. Consequently, the result is a risk of underestimation or overestimation of the out-of-plane shear stiffness values in x direction and y direction. Figure 6.2 (lower sketch) shows the cross-section of a 5-layered DLT $\pm 45^\circ$ element—equivalent to the D3 series. The element is in reference to the CLT element, also displayed by Figure 6.1 (upper sketch) regarding number and thickness of the layers.

As it is for the determination of the shear correction coefficient, the engineering constants for $\pm\theta$ layers in non-principal directions should be considered according to Equation (5.18). This means that in the case of DLT the solution according to the *Shear Analogy Method* is based on intermediate results from the laminate theory. Alternatively, the engineering constants of the diagonal layers can be determined using the *Hankinson's* approach (Equations (5.19) and (5.20)). For the exemplary 5-layered DLT element according to the D3 series, the stiffness values appear to be $S_{xz} = 7.49$ MN/m and $S_{yz} = 6.62$ MN/m following the *Shear Analogy Method*. Compared to the laminate theory using shear correction coefficients ($S_{xz} = 7.68$ MN/m and $S_{yz} = 12.86$ MN/m) the stiffness values S_{yz} following the *Shear Analogy Method* appears to be low. However, Figure 6.1 suggests that the shear stiffnesses in y direction may be underestimated by the *Shear Analogy Method*, since the shear stress distribution is clearly non-linear within a_y (also see quantitative shear stress distribution within Figure 5.8). In conclusion, the stiffness values for DLT according to the *Shear Analogy Method* following the y direction have to be reassessed critically by further analytical, experimental and numerical investigation.

6.1.3 Comparison of the analytical results and discussion

Table 6.1 provides a comparison of the out-of-plane shear stiffness values calculated according to the methods described previously. 5-layered and 7-layered elements of different layer thicknesses are analyzed. The layups of the CLT and DLT elements represent the series according to Tables 4.6, 4.7, and 4.8. Based on the findings within Chapter 4.3.2 (Material parameters of the test series) the engineering constants in principal directions are chosen in accordance to Table 4.9; T14 (ETA-20/0023: $E_x = 11000$ MPa, $E_y = 370$ MPa, $G_{xy} = 690$ MPa, $G_{xz} = G_{yz} = 50$ MPa; *Poison's* ratios according to (HALÁSZ AND SCHEER 1996)). Based on previous findings, the engineering constants for $\pm\theta$ layers in non-principal directions are considered according to Equations (5.17) and (5.18) within the laminate theory, the shear correction coefficients, and the *Shear Analogy Method*.

Tab. 6.1: Comparison of the out-of-plane shear stiffnesses of CLT compared to DLT following different approaches

out-of-plane shear stiffness values [MN/m]		Laminate Theory ¹		<i>Shear Analogy Method</i> ¹
type	series		using shear correction coefficients	$a_x \neq a_y$
CLT $t = 60$ mm $n = 3$	O3	S_{xz}	4.41	3.73
		S_{yz}	11.88	/ ²
CLT $t = 100$ mm $n = 5$	O1	S_{xz}	7.96	7.46
		S_{yz}	4.89	3.73
DLT $\pm 45^\circ$ $t = 100$ mm $n = 5$	D3	S_{xz}	7.68	7.49
		S_{yz}	12.86	6.62
DLT $\pm 30^\circ$ $t = 100$ mm $n = 5$	D4	S_{xz}	9.52	9.51
		S_{yz}	10.33	4.75
CLT $t = 200$ mm $n = 5$	O5	S_{xz}	15.92	14.92
		S_{yz}	9.78	7.46
DLT $\pm 45^\circ$ $t = 200$ mm $n = 5$	D5	S_{xz}	15.36	14.98
		S_{yz}	25.72	13.24
DLT $\pm 30^\circ$ $t = 200$ mm $n = 5$	D6	S_{xz}	19.03	19.02
		S_{yz}	20.66	9.50
uDLT $\pm 45^\circ$ $t = 200$ mm $n = 5$	D1	S_{xz}	28.08	26.47
		S_{yz}	9.94	5.22
CLT $t = 140$ mm $n = 7$	O8	S_{xz}	11.35	11.19
		S_{yz}	8.31	7.46
DLT $\pm 45^\circ$ $t = 140$ mm $n = 7$	D8	S_{xz}	11.65	11.22
		S_{yz}	8.05	7.49
DLT $\pm 45^\circ$ $t = 140$ mm $n = 7$	D9	S_{xz}	11.23	11.25
		S_{yz}	14.22	9.59
CLT $t = 150$ mm $n = 5$	O7	S_{xz}	11.94	11.19
		S_{yz}	7.34	7.33
DLT $\pm 45^\circ$ $t = 150$ mm $n = 5$	D7	S_{xz}	11.52	11.23
		S_{yz}	19.29	9.93

¹Using the transformed engineering constants $G_{30^\circ} = 164$ MPa, $G_{45^\circ} = 94$ MPa, $G_{60^\circ} = 65$ MPa
²No solution for 3-layered elements in y-direction for $a_x \neq a_y$

Table 6.1 reveals, that the stiffness values of all CLT series are in comparable range following the different analytical approaches. The results according to the *Shear Analogy Method* and according the laminate theory for CLT are nearly identical and can therefore be adopted reliably correct. For the DLT elements, the different approaches provide inconsistent results

for the out-of-plane shear stiffnesses in y direction. While the shear stiffness values in x direction are still in a comparable range, the values diverge in y direction.

Both, the *Shear Analogy Method* and the laminate theory using shear correction coefficients provide higher values in y direction, than in x direction for the DLT±45° series (with exception of the uDLT D1 series). Looking exemplary at the DLT±45° D5 series, the laminate theory using shear correction coefficients provides a stiffness value of $S_{yz} = 25.72$ MN/m. Compared to the *Shear Analogy Method* ($S_{yz} = 13.24$ MN/m). The discrepancy appears to be high. As previously described, the high analytical values for S_{yz} (following the laminate theory) result from the distribution of shear stresses over the cross-section, interacting with the distribution of the shear moduli. For the uniaxial uDLT D1 series, this effect is much less pronounced. This is due to the change of the orientation of the middle layer ($n_1 = 3$) from 90° to 0°. The approach of a constant distribution of shear stresses over the cross-section in y direction is for this example more applicable and so is the *Shear Analogy Method* in y direction.

For the DLT±30° series, the discrepancy between the shear stiffness values in y direction following both approaches appears to be even higher, as is for the DLT±45°. Looking at DLT±30° in the y direction, the diagonal layers are oriented under locally 60° to the y axis, meaning the distribution of the shear moduli is even more inconsistent than within DLT±45° ($[90°, 60°, 0°, -60°, 90°]_s$ for DLT±30° compared to $[90°, 45°, 0°, -45°, 90°]_s$ DLT±45° related to the global y direction).

Figures 6.2 and 6.3 compare the out-of-plane shear stiffness values in x and y direction of the 5-layered CLT and DLT series. The displayed series are part of the later experimental investigations. The bright grey bar charts signify the values according to the laminate theory using shear correction coefficients (subscript LT) and the dark grey bar charts represent the values according to the *Shear Analogy Method* (subscript SA). Within this comparison it becomes clear, that according to both analytical solutions, the diagonal orientation of the second and fourth layer leads to an increase in the out-of-plane stiffness properties mainly in y direction.

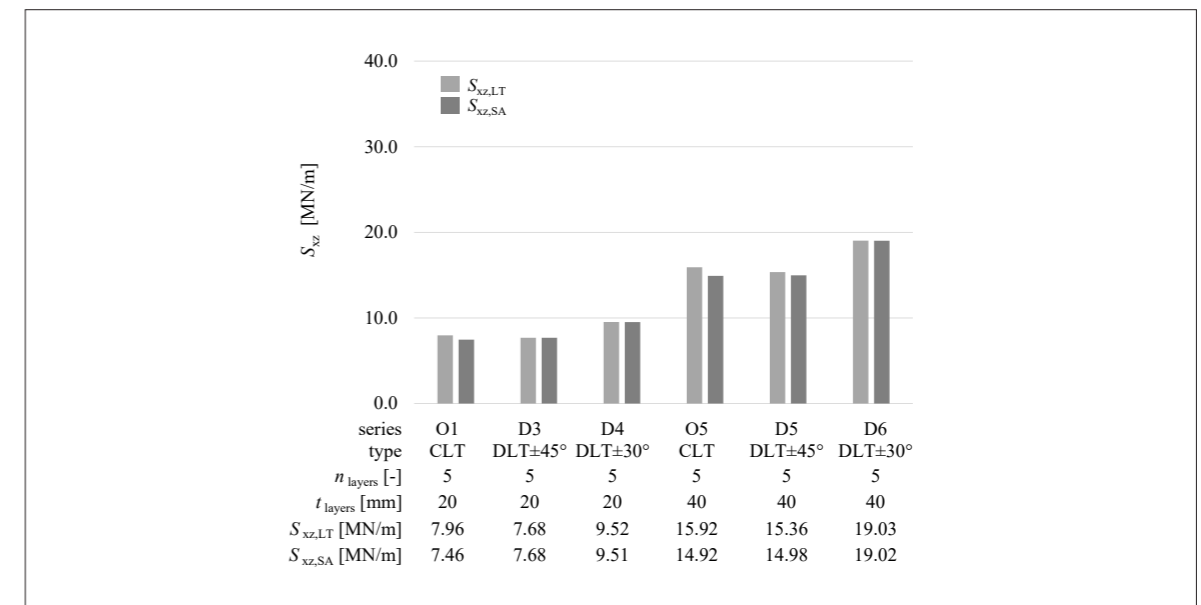


Fig. 6.2: Analytical out-of-plane shear stiffness values of selected 5-layered CLT and DLT series in x direction

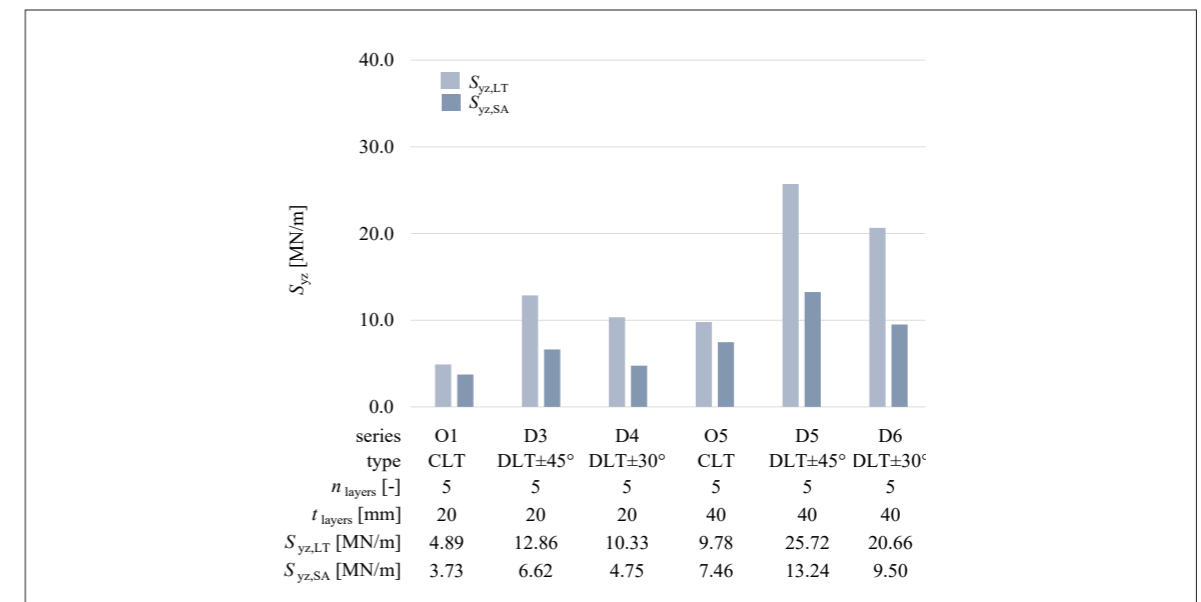


Fig. 6.3: Analytical out-of-plane shear stiffness values of selected 5-layered CLT and DLT series in y direction

The out-of-plane shear stiffness values in x and y direction using shear correction coefficients (laminate theory) provide the more accurate computational stiffness values, since the mechanically based approach arises without assumptions or simplifications. The *Shear Analogy Method* on the other hand, considers a constant distribution of the shear stress over the evaluation range. Furthermore, the influence and the interaction of the moduli of elasticity and the shear moduli is not given within the *Shear Analogy Method*. Whether this conclusion can be confirmed by experimental investigations will be investigated in Chapter 6.2.

In the following—and before the experimental investigations—, intermediate stiffness values for DLT with layer orientations deviating from 45° and 30° (60°) are added to the 5-layered series with a thickness of $t = 100$ mm, presented in Figures 6.2 and 6.3. This leads to the representation of the shear stiffness values as function of the layer orientation following both analytical approaches. The parameter studies on the out-of-plane shear stiffness values in global x and y direction using the laminate theory with shear correction coefficients and the *Shear Analogy Method* are carried out by varying the orientation (arrangement) of the second and fourth layer. The DLT elements range within $[0^\circ, +n^\circ, 90^\circ, -n^\circ, 0^\circ]_s$ according to the parameter set. The layers are rotated in opposite directions in steps of 15°, up to the limits of 0° and 90°, respectively (Figure 6.4). Additionally, the stiffness values of a standard CLT element $[0^\circ, 90^\circ, 0^\circ, 90^\circ, 0^\circ]_s$ are given. The layer thickness t_i is set to 20 mm.

Figure 6.5 displays the out-of-plane shear stiffness values in global x and y directions in steps of 15° against the respective boundary values following the *Shear Analogy Method*. The thickness t_i remains constant at $t_i = 20$ mm. Figure 6.6 shows the out-of-plane shear stiffness values in global x and y direction in steps of 15° following the laminate theory using shear correction coefficients. The parameter study in Figure 6.5 is in direct reference to the parameter study in Figure 6.6.

As was expected in light of the previous investigation, the parameter studies according to the laminate theory and the *Shear Analogy Method* mostly differ regarding the stiffness values in y direction. However, both studies confirm that the maximum out-of-plane shear stiffness S_{xz} is to be achieved with two additional layers oriented at 0°. Consequently, the same layup has the lowest out-of-plane shear stiffness in the y-direction. Since the layups $[0^\circ, 0^\circ, 90^\circ, 0^\circ, 0^\circ]_s$ and $[0^\circ, 90^\circ, 90^\circ, 90^\circ, 0^\circ]_s$ cannot be designated as DLT elements and are also not a reasonable CLT layup—suitable for biaxial load transfer—these values only provide the boundary values (limits).

Within the *Shear Analogy Theory* for DLT S_{xz} is almost similar to S_{yz} at an orientation of the second and fourth layer at $\pm 45^\circ$. This follows a quite logical order, since the solution is based on the sum of the transformed engineering constants G_{ij} . Under 45° G_{xz} equals G_{yz} . For the laminate theory on the other hand, S_{xz} equals S_{yz} at an approximate angle of 30°. It can be clearly seen that for both analytical approaches, the shear stiffness value S_{xz} decreases slightly with increasing angle, whereas S_{yz} increases disproportionately strongly with increasing angle.

In the following Chapter, the experimental investigations (small-scale shear tests according to EN 408) as well as the numerical investigations are used to evaluate and validate the analytical solutions. However, it must be noted that the shear tests according to EN 408 provoke a constant distribution of the shear stresses over the cross-section, unlike the bending shear tests according to EN 16351 (parabolic distribution of shear stresses). Therefore, the experimental results might correspond most closely to values according to the *Shear Analogy Method*. The latter is to be examined in the following, among others.

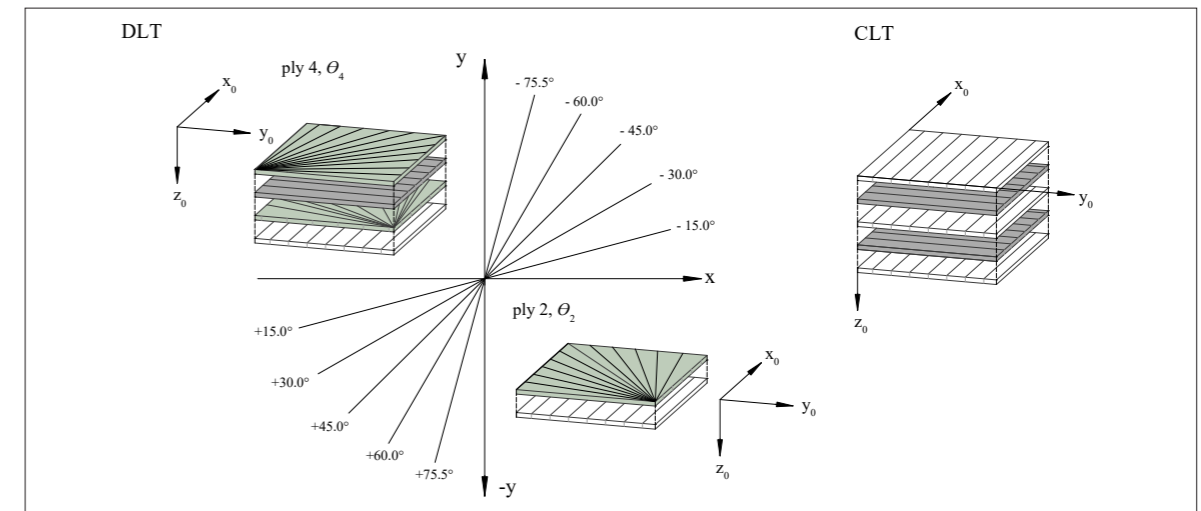


Fig. 6.4: Parameter set for the arrangement of the second and fourth layer of 5-layered DLT elements

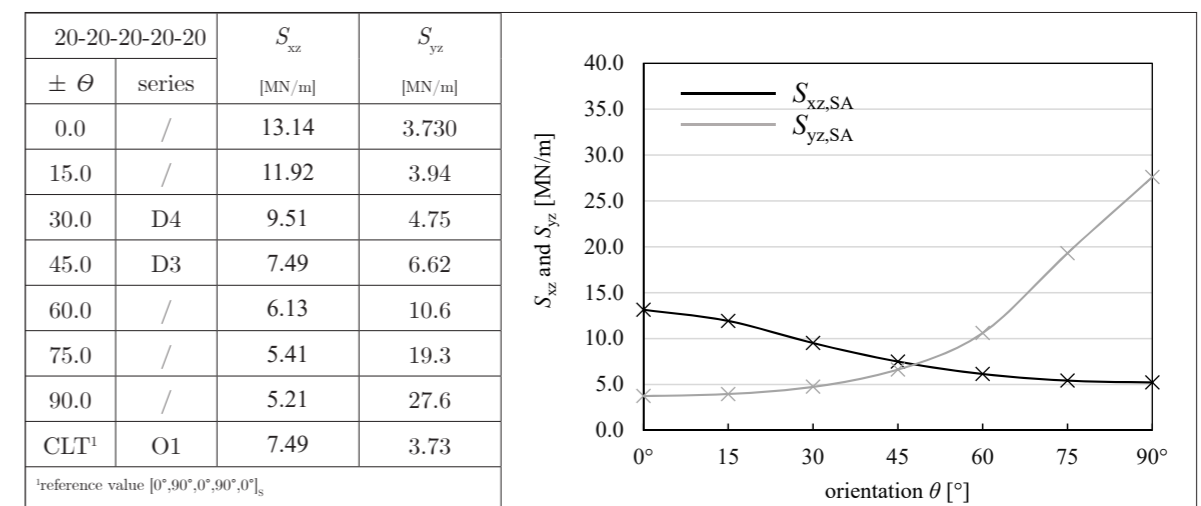


Fig. 6.5: Out-of-plane shear stiffness (*Shear Analogy Method*) as a function of the layer arrangement

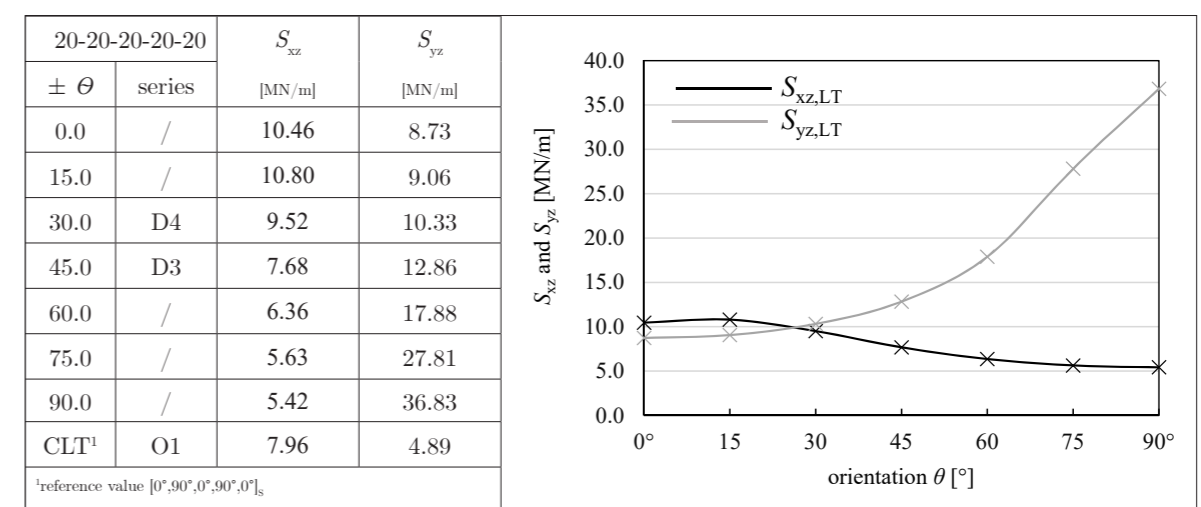


Fig. 6.6: Out-of-plane shear stiffness (*laminate theory*) as a function of the layer arrangement

6.2 Experimental determination of the out-of-plane shear strength and stiffness

6.2.1 Test setup

Various standardized test setups are available for the determination of the out-of-plane shear stiffness properties of timber (Figure 6.7). In general, the out-of-plane shear stiffness and strength of CLT can be determined in four-point-bending test or small-scale shear tests. The focus of this thesis lies on the small-scale shear tests according to EN 408. EN 16351 and EN 789 form the basis for the determination of the shear moduli and the rolling shear strengths of CLT. According to EN 16351, CLT is split into 3-layered elements, ensuring that the lamella tested is oriented under 90° and is acting in shear only. The rolling shear strength and the rolling shear modulus G_r (G_{90}) of single timber laminations can be determined according to the Equation (6.6) and Equation (6.7) (DIN EN 789).

$$f_r = \frac{F_{max}}{l \cdot b} \quad (6.6)$$

$$G_r = \frac{(F_{40\%} - F_{10\%}) \cdot t}{(u_{40\%} - u_{10\%}) \cdot l \cdot b} \quad (6.7)$$

Shear tests according to EN 408 refer to structural timber. The load is applied by means of steel plates bonded on each side of single lamellas. In addition, the specimen are inclined by 14° to guarantee that no horizontal forces are introduced by eccentricities. The dimensions of the test specimens result from the inclined test geometry (see Figure 6.7).

In order to avoid the material and time-consuming bonding of steel lamellas, *Mestek* has further optimized the test setup according to EN 408 toward the testing of 3-layered CLT elements (MESTEK 2011). During his investigations, the load was applied via the layers adjacent to the tested center layer of the specimen. Therefore, it is no longer necessary to bond steel plates on the specimens for load introduction (MESTEK 2011). Unfortunately, the approach according to *Mestek* is not entirely transferable to DLT. The diagonal arrangement

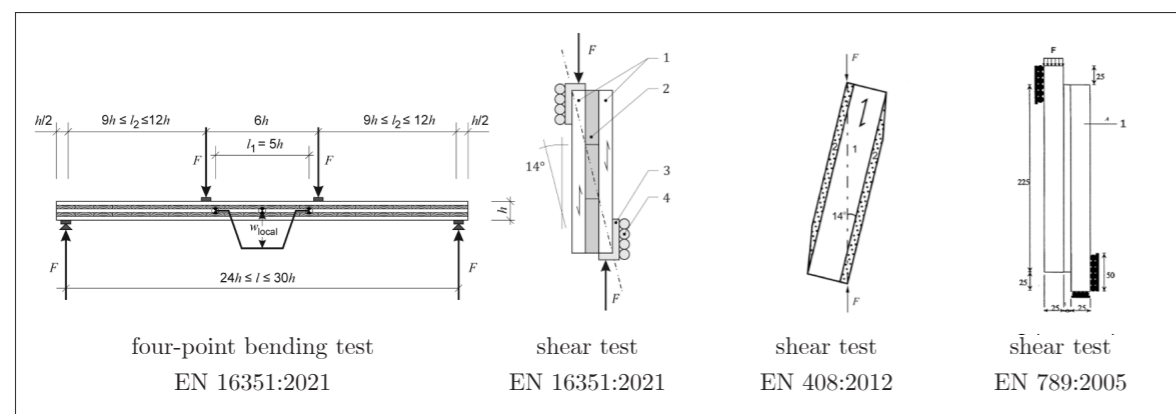


Fig. 6.7: Different tests setups for the determination of out-of-plane shear properties

of individual layers requires the testing of more than one layer, in order to represent the interaction as a composite material. The testing of a single layer/lamination under an orientation differing from 0 and 90° would, in contrast to CLT, not allow any statement regarding the out-of-plane shear stiffness properties of DLT. Thus, at least three layers, which include the diagonally oriented layers and the middle layer, are loaded out-of-plane (named "inner layers" in the following). However, this also means that within the chosen test setup, the test results refer to the three inner layers of the test specimens only. To ensure the load introduction, additional layers have to be bonded to the specimens (see Figure 6.8).

Specimens with the dimensions $400/120/100$ mm were cut from plates of the O1, D3 and D4 series. In order to investigate the out-of-plane shear stiffness in x and y direction, test specimens were cut out oriented under 0° and 90° to the front layers. 18 mm thick boards of grade T14 (C24) were bonded to the outer layers on both sides of the of the specimens. In this way, the load can be applied via two laminations on each side. The additional laminations were attached by means of screw-press gluing in accordance with DIN 1052-10 (screw dimensions: $4.0/30$ mm) (see Figure 6.8). The difficulty of tests with specimens oriented in global y direction, is the load introduction into the outer layers. For specimens cut out in y direction, the fibre orientation of the outer layers is perpendicular to the loading. So as to reinforce the load introduction point, three fully-threaded screws (screw dimensions: $5.0/70$ mm) were additionally inserted into each of the 90° outer layers (see Figure 6.8).

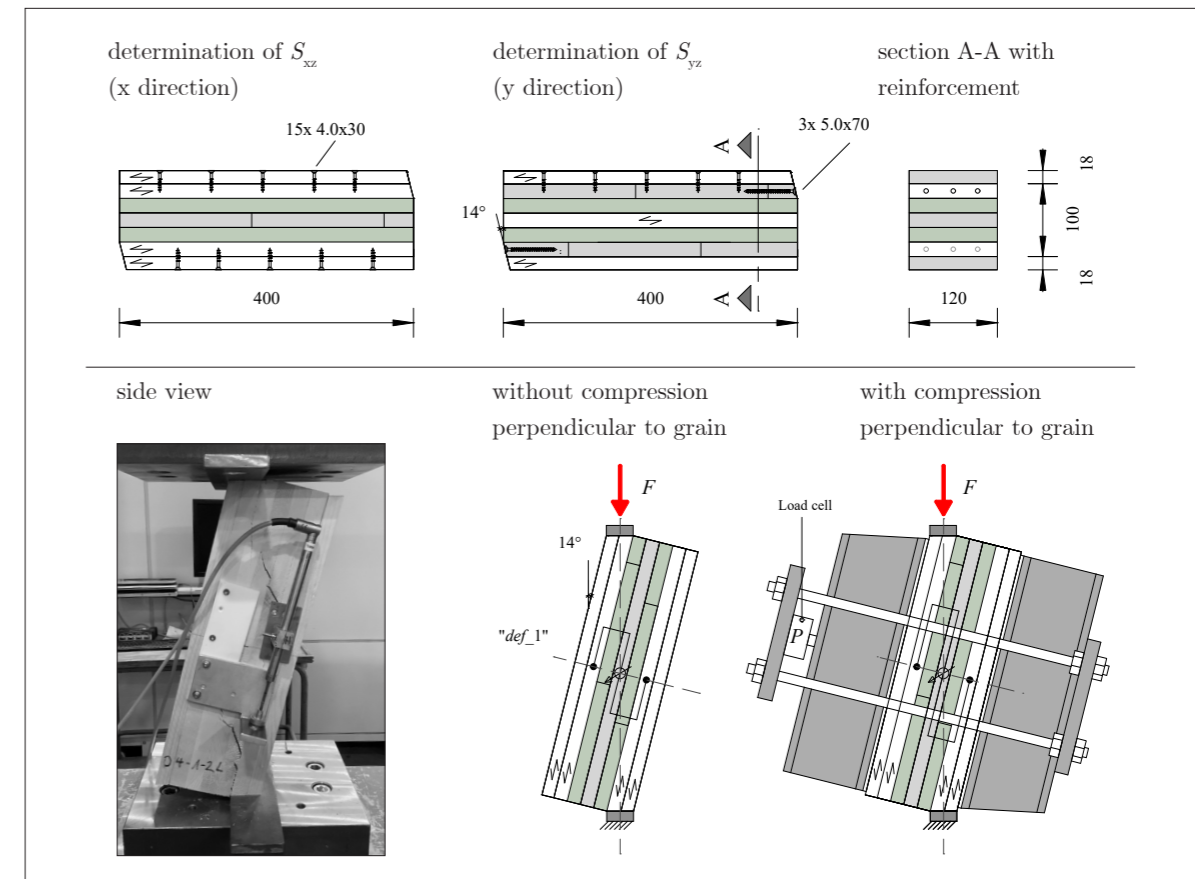


Fig. 6.8: Test setup of the shear testing—with and without compression perpendicular to grain

The chosen test setup enables the determination of out-of-plane shear strength values f_v in addition to the stiffness values. This enables statements on the failure mechanisms of CLT and DLT, for example under biaxial bending (shear failures are achieved). Additional tests are carried out under external compression perpendicular to grain, since out-of-plane shear stresses and compression stresses perpendicular to grain often occur hand in hand. This is the case, e.g., for concentrated loads due to point-supports.

A total of 36 test specimens of O1, D3 and D4 series were placed in the test stand. 18 specimens were used to investigate the shear stiffness in the x direction and 18 in y direction. 9 out of the 18 test specimens were additionally loaded in compression perpendicular to grain. The compression perpendicular to grain was applied by tightening the nuts on the threaded rods (M16 - 8.8) (Figure 6.8). Steel plates transfer the load into steel profiles (HEB 120), which then transfer the compression to the specimen. The load cell installed between the steel plate and the steel profile provides information about the load level perpendicular to grain (see load cell P in Figure 6.8).

Inductive displacement transducers were attached to both sides of the specimens. The relative deformation was measured within a range of 60 mm, ensuring the recording the deformations of the inner layers ("path_1"). The shear testing is carried out deformation-controlled with a constant feed rate of 1.0 mm/min. Following EN 408, the experiments ended either after failure of the specimens or after reaching the maximum testing time of $t = 420$ s. The moisture content of each specimen was measured by means an electrical resistance moisture meter using ram-in electrodes within a depth of 15 mm prior to the tests. The moisture contents were in the range of $u = 12 \pm 2$ %.

6.2.2 Description of test evaluation and validation using numerical models

Following the test setup, the effective shear moduli $G_{iz,eff}$ for the three inner layers of each specimen are calculated, similar to EN 789, within the linear elastic range $0.1F_{max}$ and $0.4F_{max}$ using linear regression and considering the shear deformations u_i measured within the respective evaluation area of $a_x = a_y = 60$ mm (Equations (6.8) and (6.9)). Additionally the angle of inclination α is introduced following the chose test setup (Figure 6.8).

$$u = \int_0^z \gamma_{ers} dz = \int_0^z \frac{\tau}{G} dz = \frac{\tau}{G} \cdot a = \frac{F \cdot a \cdot \cos(\alpha)}{G_{iz,eff} \cdot w \cdot l} \quad (6.8)$$

$$G_{iz,eff} = \frac{F \cdot a \cdot \cos(\alpha)}{u \cdot w \cdot l} = \frac{(0.4F_{max} - 0.1F_{max}) \cdot a \cdot \cos(\alpha)}{(u_{0.4F_{max}} - u_{0.1F_{max}}) \cdot w \cdot l} = m \cdot \frac{a \cdot \cos(\alpha)}{b \cdot l} \quad (6.9)$$

Figure 6.9 illustrates the expected shear deformations at a DLT element according to the chosen test setup and compares them with the expected shear deformations at a DLT

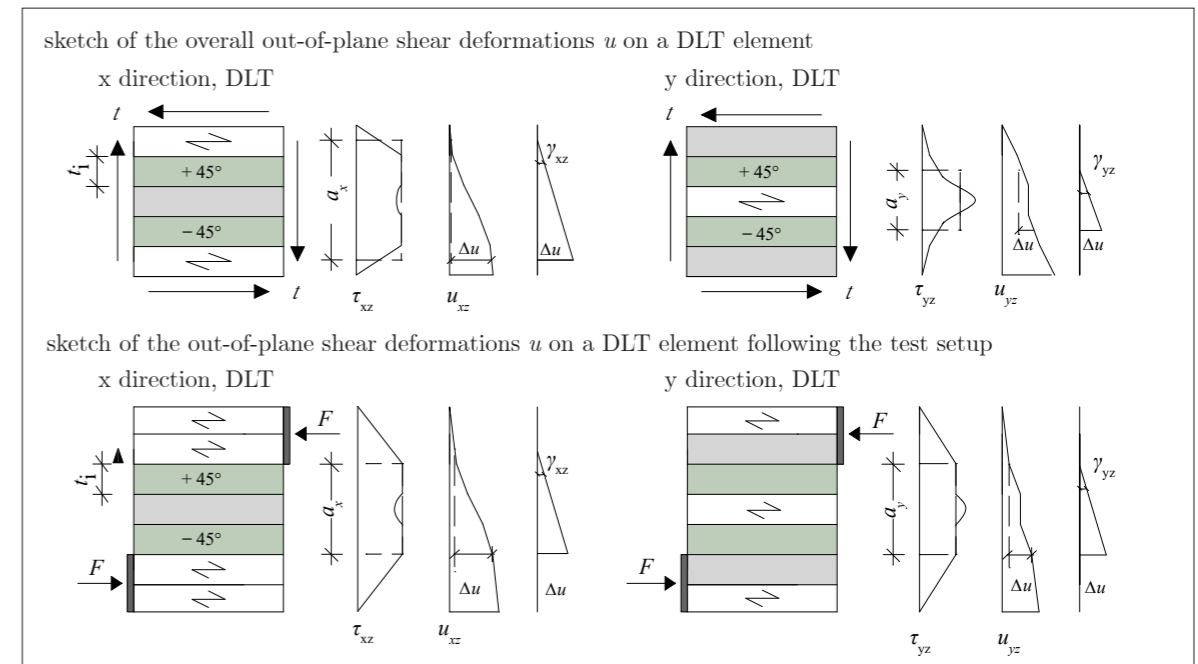


Fig. 6.9: Expected shear stresses, shear deformations, and shear strains in x (left) and y (right) direction of DLT following the Shear Analogy Method (upper sketch) and the test setup (lower sketch)

element under a constant shear flow t , analogous to the graphical representations and assumptions following the *Shear Analogy Method* previously introduced and explained within Chapter 6.1.2 and Figure 6.1.

The test setup provokes a linear distribution of the shear stresses over the cross-section of the inner layers in x and y direction (a_x and a_y , Figure 6.9). Bearing in mind Equation (6.5) for the calculation of the out-of-plane shear stiffness following the *Shear Analogy Method*, the shear deformations are summed up over the chosen evaluation area a_i . This means, to achieve experimental stiffness values with regard to the x direction of the respective series, also including the outer layers, the stiffness values of the overall specimens are calculated according to Equation (6.10). Herby the contribution of the shear deformation at the outer layers is analytically taken into account and added to those of the inner layers.

Since the outer layers in y direction (oriented under 90° to the y direction) are without noteworthy contribution to the out-of-plane shear stiffness—also see the remarks by (KREUZINGER AND SCHOLZ 2001) regarding the *Shear Analogy Method*—the experimentally determined effective shear moduli $G_{yz,eff}$ multiplied with the experimental evaluation area $a_y = 60$ mm of the inner layers, represents the out-of-plane stiffness values in y direction of the overall five layers of the series (Figure 6.9, Equation (6.11)).

$$S_{xz} = \left(\frac{1}{(a_x + t_i)^2} \cdot \left(\frac{t_i}{G_0} + \frac{a_x}{G_{xz,eff}} \right) \right)^{-1} \quad (6.10)$$

$$S_{yz} = G_{yz,eff} \cdot a_y \quad (6.11)$$

In order to cross-check the chosen test setup and evaluation approach, knowledge about the stresses actually occurring within the specimens is decisive. To counter check the test setup, shear stresses and the stresses perpendicular to grain were investigated preliminary using FE volume models (see Figure 6.10). In further investigations, the created FE models also serve to determine numerical shear stiffness values (see Chapter 6.3).

The layups of the O1, D3 and D4 series were remodeled and introduced into the software Ansys (Version 2022.R1). All laminations (boards) were modeled separately and the contacts were defined thereafter. The board width was 180 mm—the boards were non-edge-glued. For volume modelling in three dimensions, solid elements with 8, 10 or 20 nodes can be used. The modelling of the CLT and DLT specimens was carried out with Solid186 elements with 20 nodes each. The size of the mesh was set to 6.67 mm (layer thickness $t_i/3 = 20/3$ mm). The base function for mesh generation was set to a quadratic function, suitable for solid models, providing sufficiently accurate results given the high number of nodes. All parameters chosen for the numerical models are summarized in tabular manner in Appendix A4.

The bearing as well as the application of the loading was carried out using "external displacements" which are related to the respective surfaces of the volume models. Therefore the load is constantly distributed. The compression perpendicular to grain ($\sigma_{c,90}$) was applied as a uniformly distributed surface load (pressure). On the bottom of the elements a support in x , y , and z direction was defined. The opposite surface was only fixed in the global x and y direction and was free in the global z direction, in order to model a support free of constraint (Figure 6.10). The fully threaded screws are applied to the models using cylindrical volume elements (5.0/70 mm) which were rigidly connected to the surrounding volume elements (Figure 6.10, left). The material parameters according to Table 4.9 (T14; ETA20/0023) were applied to the FE models taking into account the orthotropic material behavior of wood. The tangential and radial material parameters of the orthotropic material were combined, due to the similarity of their properties (analogous to the previous analytical investigations). Thus, the number of required material parameters is reduced from 9

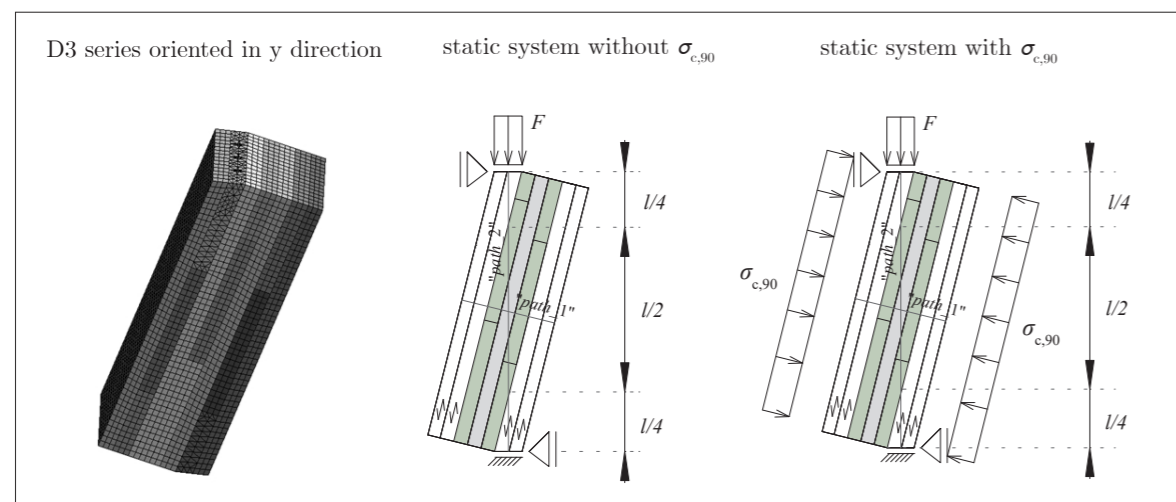


Fig. 6.10: Exemplary FE volume model of D3 series and static systems of the numerical test setup

to 6 within the numerical model. ($E_x = 11000$ MPa, $E_y = E_z = 370$ MPa, $G_{xy} = G_{xz} = 690$ MPa, $G_{yz} = 50$ MPa, Poisson's ratios according to (HALÁSZ AND SCHEER 1996)). A reference load of $F = 60$ kN was chosen for the validation of the test setup by the numerical models ($F = 60$ kN is close to the average expected failure loads). For the compression perpendicular to grain, a value of $\sigma_c = 0.5$ MN/m² was decided upon. This value corresponds to previous small-scale shear test on CLT, like those by (MESTEK 2011).

Table 6.2 provides the distribution of shear stresses τ_{xz} and τ_{yz} over the cross-section of each series following "path_1" (Figure 6.11)—with and without compression perpendicular to grain. In particular, "path_1" follows the measuring range of the inductive displacement transducers, to cross-check the approximate constant stress distribution within the inner layers following the analytical assumptions (Equations (6.9) and (6.10)).

The graphics show that the distribution of the shear stresses within the inner layers of nearly all series appears to be almost constant, following "path_1". The O1 series oriented in y direction, with and without external compression, are an exception. In their case, the shear stresses are not constantly distributed over the inner layers according to Table 6.2. This could be an indication, that the selected test setup is not suitable for the testing of CLT with more than one cross-layer within the shearing area and has to be kept in mind during the evaluation of the test results. For the O1 series in x direction, with and without external compression, the shear stresses over middle layer show a slight decrease instead of a peak value in the middle layer. This effect can be attributed to the missing edge-gluing of the laminations and has also been observed in numerical models used by previous studies (see MESTEK 2011).

Tab. 6.2: Shear stresses in global x and y direction, with and without external compression ($\sigma_{c,90} = 0.50$ MN/m²), following the 3D-FE models for $F = 60$ kN following "path_1" (graphics by DONHAUSER 2022)

	specimens following x direction			specimens following y direction		
	O1-x CLT	D3-x DLT±45°	D4-x DLT±30°	O1-y CLT	D3-y DLT±45°	D4-y DLT±30°
τ_{xz} [MN/m ²] and τ_{yz} [MN/m ²]						
max	1.26	1.32	1.33	1.33	1.11	1.08
	O1-x-p CLT	D3-x-p DLT±45°	D4-x-p DLT±30°	O1-y-p CLT	D3-y-p DLT±45°	D4-y-p DLT±30°
τ_{xz} [MN/m ²] and τ_{yz} [MN/m ²]						
max	1.25	1.31	1.31	1.33	1.10	1.08

Within the mechanical testing, the measured shear deformations, and therefore the shear moduli and stiffness values, are expected to be similar to those without external compression. The models show that, as expected, the additional compression perpendicular to grain has no significant influence on the out-of-plane shear stresses.

However, this is different with regard to the shear strength. The calculation of the shear strengths is carried out following Equation (16) of EN 408, taking into account the maximum load reached or the load at initial failure (Equation (6.12)). The failure load, in turn, and thus the failure mechanism depends on the compressions stresses perpendicular to grain within the specimen.

$$f_v = \frac{F_{max/init} \cdot \cos(\alpha)}{a \cdot l} \quad (6.12)$$

Table 6.3 gives the stresses perpendicular to grain for the reference load $F = 60$ kN with and without external compression perpendicular to grain. The adjustment of "path_2" ensures, that the stresses acting at the load-introduction areas as well as the stresses within all of the three inner layers are represented. The stresses acting perpendicular to grain within the inner layer are therefore represented by exactly half of the length ($l/2$) of "path_2" (see Table 6.3).











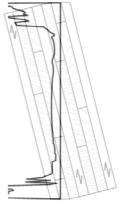

Regarding the stresses occurring perpendicular the grain both, specimens following x direction and y direction, experience maximum values of compression stresses at the load introduction areas (see $l/4$ of "path_2") (Table 6.3). These compression stresses are the consequence of the chosen test setup that uses specimens inclined under an angle of 14° . Hence, the applied load is distributed into a local vertical and local horizontal component ($F \cdot \sin(14^\circ)$). The compression stresses within $l/4$ of "path_2" dissipate and lead to very small tensile stresses within $l/2$. Consequently, the initial failure of the specimens is expected to occur at the edges of $l/2$ regarding "path_2" (zero point of stresses). Further explanations can be found in (MESTEK 2011) and (DONHAUSER 2022).

The same amount of numerical studies is repeated by introducing external compression perpendicular to grain ($\sigma_{c,90} = 0.5$ MN/m²). Using the numerical setup described in Figure 6.10, right, leads to compression stresses acting within $l/2$, superimposing potential tensile stresses.

With respect to the stresses acting perpendicular to grain, the external compression leads to constant compression stresses within $l/2$ (-0.41 MN/m² to -0.46 MN/m²). The tensile stresses introduced by the horizontal force component is superimposed by the compression stresses. Within the mechanical testing, an increase of the shear strength is to be expected, compared to the specimens tested without external compression perpendicular to grain. The reason for this is the expectation of a higher initial failure load.

In the following, the actual results of the mechanical testing are given (load-deformation curves, failure mechanisms, shear strength and stiffness values).

Tab. 6.3: Stresses perpendicular to grain for $F = 60$ kN, without and with external compression perpendicular to grain ($\sigma_{c,90} = 0.50$ MN/m²) following "path_2", (graphics by DONHAUSER 2022)

	specimens following x direction			specimens following y direction		
O1-x CLT	D3-x DLT $\pm 45^\circ$	D4-x DLT $\pm 30^\circ$	O1-y CLT	D3-y DLT $\pm 45^\circ$	D4-y DLT $\pm 30^\circ$	
$\sigma_{c,90}$ [MN/m ²] or $\sigma_{t,90}$ [MN/m ²]						
¹ mean	0.06	0.08	0.05	0.03	0.04	0.03
	O1-x-p CLT	D3-x-p DLT $\pm 45^\circ$	D4-x-p DLT $\pm 30^\circ$	O1-y-p CLT	D3-y-p DLT $\pm 45^\circ$	D4-y-p DLT $\pm 30^\circ$
$\sigma_{c,90}$ [MN/m ²] or $\sigma_{t,90}$ [MN/m ²]						
¹ mean	-0.41	-0.41	-0.44	-0.46	-0.45	-0.43
	¹ within $l/2$ of path_2					

6.2.3 Results of the mechanical testing without external compression

Figure 6.11 provides the load-deformation curves for the 5-layered CLT and DLT series examined in the shear testing in x direction (left) and y direction (right). The curves signify the mean value of the measured deformations w ("def_1") on both sides of the specimens. F_0 represents the crossing-point of the respective deformation and the y axis. Therefore, the definition of the linear elastic range ($0.1w_{F_{\max}}$ and $0.1F_{F_{\max}}$; $0.4w_{F_{\max}}$ and $0.4F_{F_{\max}}$) refers to the evaluation area between F_0 and F_{\max} in accordance to EN 408 (Figure 6.12). The linearity is verified further for each specimen by the coefficient of determination R^2 .

Figure 6.12 shows the load-deformation diagrams measured by the hydraulic cylinder, needed to identify the maximum failure load and therefore to calculate the shear strength.

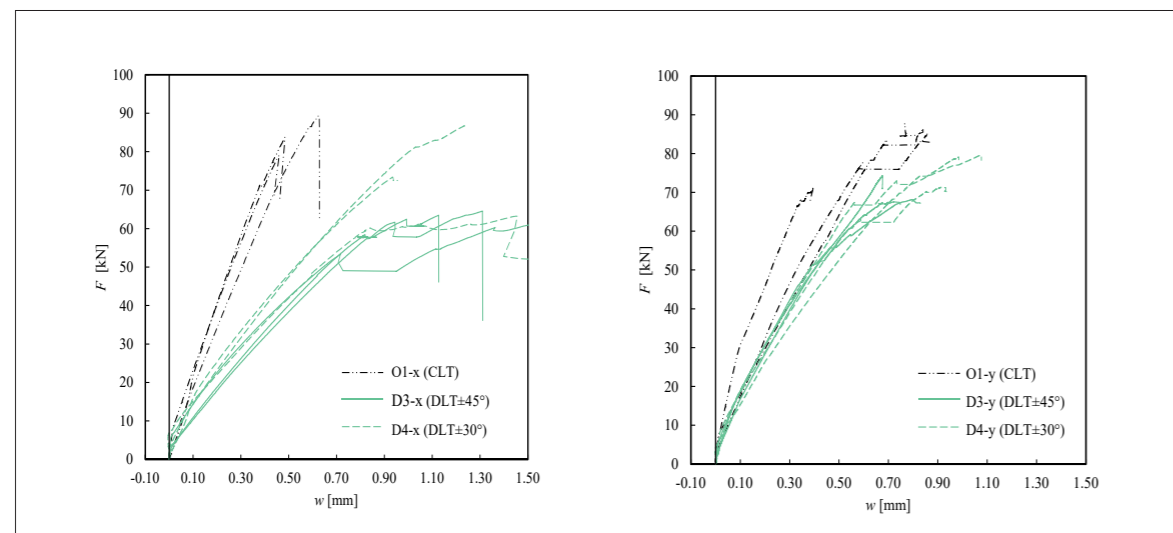


Fig. 6.11: Load-deformation diagrams (def_1) for the specimens oriented in x (left) and y (right) direction, without external compression

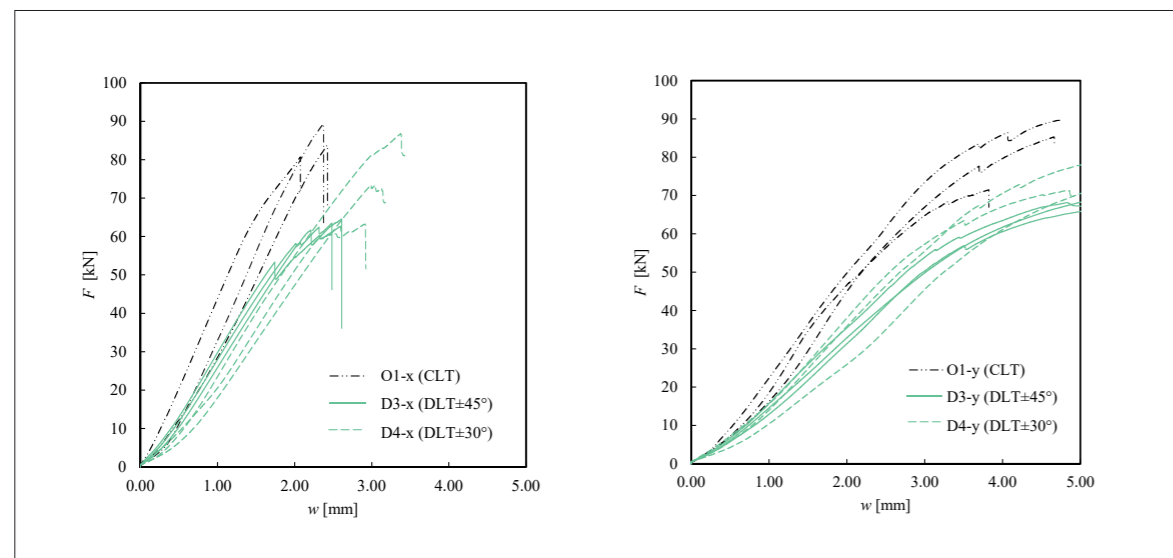
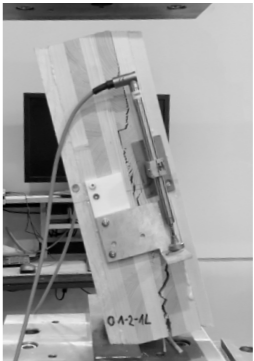

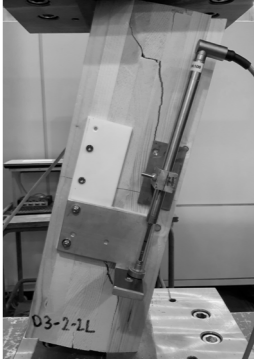
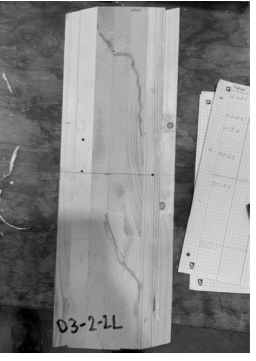
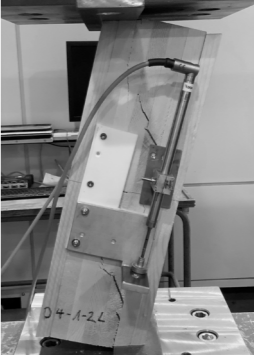
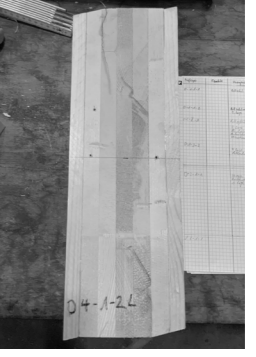


Fig. 6.12: Load-deformation diagrams (hydraulic cylinder) for the specimens oriented x (left) and y (right) direction, without external compression


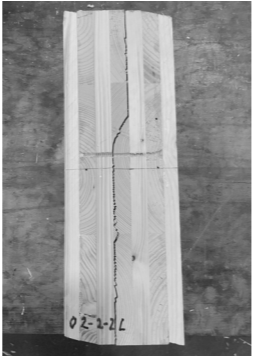
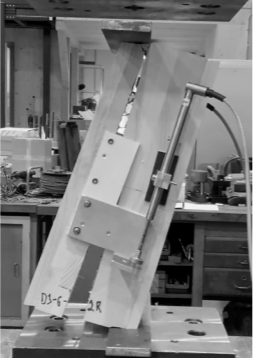
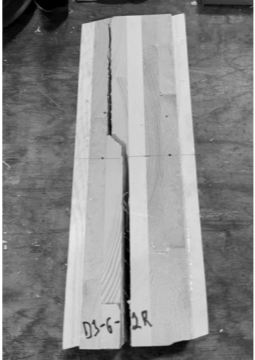

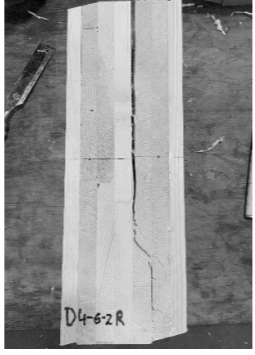
The observed failure mechanisms of the specimens oriented in x direction were, on the one hand rolling shear failures along the annual rings of the 90° oriented layers and on the other hand shear failures in the 45° (D3 series) and 30° (D4 series) following the respective fiber direction. Table 6.4 summarizes the failure mechanisms and observations for each series oriented in x direction (tested without external compression). For the O1 series oriented in x direction rolling shear failure in only one of its cross-layers were observed. The DLT D3 and the D4 series on the other hand achieved shear failures in all three inner layers.

Tab. 6.4: Failure mechanisms of the CLT and DLT series oriented in x direction, without external compression

series	layup [mm] / [°]	observations	side view
O1-x	CLT inner layers (20-20-20) [90;0;90] _s	» rolling shear failure in one of the cross-layers	 
D3-x	DLT±45° inner layers (20-20-20) [45;90;-45] _s	» shear failures in the ±45° layers » rolling shear failure in the cross-layers (middle layer)	 
D4-x	DLT±30° (40-40-40) [30;90;-30] _s	» shear failures in the ±30° layers » rolling shear failure in the cross-layers (middle layer)	 

Following the shear tests of the specimens oriented in y direction, deformations at the load application area occurred. This is due to the orientation of the outer (load-introducing) layers at force grain angles of 90° . The additional lamella glued under a force grain angle of 0° to the outer layers and the fully threaded screws (see Figure 6.8) were able to minimize these deformations. Even though the deformations at the load application area may have no influence on the determination of the shear modulus via "path_1", the deformation due to the additional eccentricity and the resulting compression or tensile stresses influence the maximum failure load and thus the shear strength. The later tests under compression perpendicular to grain are intended to prevent this from happening. Table 6.5 highlights the failure mechanisms of each series oriented in y direction. The O1 specimens oriented in y direction achieved a rolling shear failure in the cross-layers. The brittle failure of

Tab. 6.5: Failure mechanisms of the CLT and DLT series in y direction, without external compression

series	layup [mm] / [n°]	observations	side view	
O1-y	CLT inner layers (20-20-20) [0;90;0] _s	<ul style="list-style-type: none"> » deformations at the load introduction area leading to an eccentricity and thus to additional tension perpendicular to grain » rolling shear failure in the cross-layers 		
D3-y	DLT±45° inner layer (20-20-20) [45;0;-45] _s	<ul style="list-style-type: none"> » deformations at the load introduction area leading to an eccentricity and thus to additional tension perpendicular to grain » shear failure within the ±45° layers combined with tension perpendicular to grain 		
D4-y	DLT±30° innerlayer (20-20-20) [60;0;-60] _s	<ul style="list-style-type: none"> » deformations at the load introduction area leading to an eccentricity and thus to additional tension perpendicular to grain » shear failure within the ±30° layers combined with tension perpendicular to grain 		

the specimens indicates additional tensile stresses perpendicular to grain. Nevertheless, the shear stiffness values of O1 series in y direction str more close to the analytical solution than the ones in x direction and may therefore be in a more realistic range (Figure 6.13). The D3 and D4 series achieved rolling shear failures in the diagonal layers, in combination with tension perpendicular to grain. The failure mechanisms of the DLT specimens appeared to be abrupt and thus even more brittle than those of the CLT specimens.

Table 6.6 gives the evaluation of the experiments on the out-of-plane shear strength and stiffness without additional compression perpendicular to grain. The values of $G_{ij,eff}$ refer to the inner layers, the values of $S_{ij,exp}$ refer to the overall series (see Figure 6.10 and Equations (6.10) and (6.11)). The shear strength values f_v refer to the maximum load F_{max} . For specimens that did not achieve failure, no shear strength is calculated.

Tab. 6.6: Evaluation of the mechanical testing on the out-of-plane shear properties in global x and y direction of the CLT and DLT series ($t = 100$ mm), without compression perpendicular to grain

	F_{max} [kN]	$0.4F_{max}$ [kN]	$0.1F_{max}$ [kN]	$w_{0.4F_{max}}$ [mm]	$w_{0.1F_{max}}$ [mm]	m [l]	R^2 [l]	$G_{xz/yz,eff}$ [MNm ² /m]	$S_{xz/yz}$ [MN/m]	f_v [MN/m ²]
O1-1-x	71.3	53.5	32.1	0.273	0.154	179.6	1.0	217.81	21.02	1.69
O1-2-x	79.1	41.6	17.9	0.208	0.070	170.7	1.0	207.00	20.07	1.60
O1-3-x	86.6	46.6	20.7	0.283	0.113	153.9	1.0	186.70	18.27	1.75
<i>mean, (COV_{Sxz} 4.4)</i>								203.84	19.79	1.68
O1-1-y	67.8	57.1	36.8	0.271	0.141	154.6	1.0	187.46	11.25	1.37
O1-2-y	77.7	41.1	17.8	0.259	0.104	129.8	1.0	157.43	9.45	1.57
O1-3-y	83.5	48.4	23.4	0.360	0.145	116.1	1.0	140.76	8.45	1.69
<i>mean, (COV_{Syz} 11.9)</i>								161.88	9.71	1.54
D3-1-x	58.2	28.3	10.8	0.328	0.098	76.1	1.0	92.27	9.42	1.18
D3-2-x	61.6	28.6	10.2	0.351	0.098	73.4	1.0	89.01	9.10	1.25
D3-3-x	53.4	28.3	12.3	0.279	0.078	79.0	1.0	95.84	9.77	1.08
<i>mean, (COV_{Sxz} 2.9)</i>								92.37	9.43	1.17
D3-1-y	¹ 72.1	38.9	17.2	0.279	0.087	112.9	1.0	136.98	8.22	/
D3-2-y	55.8	37.3	20.6	0.258	0.115	116.1	1.0	140.84	8.45	1.13
D3-3-y	52.3	35.9	20.2	0.267	0.130	114.7	1.0	139.07	8.34	1.06
<i>mean, (COV_{Syz} 1.1)</i>								138.96	8.34	1.10
D4-1-x	81.3	45.5	21.1	0.474	0.176	81.6	1.0	98.98	10.08	1.64
D4-2-x	60.2	39.1	21.0	0.454	0.185	67.7	1.0	82.05	8.42	1.22
D4-3-x	73.3	49.3	27.3	0.517	0.223	74.8	1.0	90.66	9.26	1.48
<i>mean, (COV_{Sxz} 7.4)</i>								90.56	9.25	1.45
D4-1-y	¹ 74.3	39.7	17.4	0.347	0.120	97.3	1.0	118.01	7.08	/
D4-2-y	67.5	45.0	24.8	0.335	0.149	108.5	1.0	131.62	10.53	1.37
D4-3-y	63.5	35.4	16.4	0.265	0.081	102.6	1.0	124.40	9.95	1.28
<i>mean, (COV_{Syz} 4.5)</i>								124.68	9.19	1.33
¹ F_{max} for $w = 5.0$ mm (no failure achieved)										

For improved readability, Figure 6.13 gives the mean values of the out-of-plane shear stiffnesses in x direction (left) and y direction (right) according to the mechanical testing and compares them to the respective analytical solutions. Shear stiffness values following the experimental investigations of the specimens oriented in x direction are specified in gray, and those of the series oriented in y direction are gray-blue. For the CLT elements oriented in both, x and y direction, the experimental results are higher compared to the analytical values. This is particularly clear for the O1 series oriented in x direction, since the discrepancy in x direction is significantly high. Neither the analytical solution according to the laminate theory, nor according to the shear analogy method are compatible with the experimental values for O1. Following the analytical solutions, the CLT O1 series should feature the lowest shear stiffness S_{xz} . The investigations using the FE models may provide an explanation for the high experimental results (Table 6.2) due to the parabolic (non-linear) shear stress distribution over the cross-section within the given test setup. Furthermore the O1 series in x direction is the only series featuring two layers oriented under 90° within the three inner layers. In the y direction, the discrepancy of O1 series is less significant and only one out of the three inner layers is oriented under 90° . Yet, regardless of the number of cross-layers, other causes for these discrepancies must be considered. The O1 series was produced by *Pfeifer Timber*; the D3 and the D4 series by *Holzbau Unterrainer*. Therefore, it is possible that the material parameters of O1 series provides higher shear moduli based on the comparable high density of O1 series (see Chapter 4.3.2). This needs to be further investigated. For D3 series, however, the experimental results in x direction provide good correlation to the analytical solutions. The test results on D4 series slightly deviate from the analytical values in x direction. The test results in y direction are close to the analytical solution following the *Shear Analogy Method* for the D3 series, and close to the laminate theory for D4.

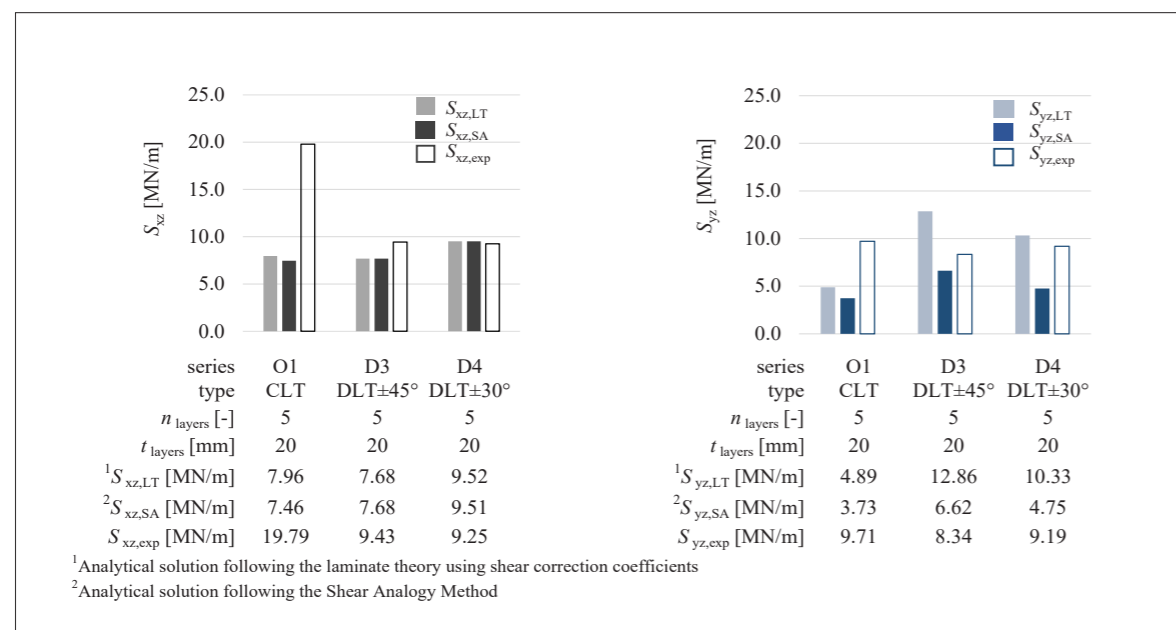


Fig. 6.13: Out-of-plane shear stiffnesses of the CLT and DLT series ($t = 100$ mm) following the experimental investigations and analytical solutions, without compression perpendicular to grain

6.2.4 Pre-tests introducing external compression

After the out-of-plane shear testing without external compression perpendicular to grain, additional tests were carried using steel profiles to apply additional compression stresses perpendicular to grain of $\sigma_{c,90} = 0.5$ MN/m² to the specimens (see Figure 6.8, right). In order to determine a possible influence of the test setup on the evaluation of the shear strength and stiffness, pre-tests were conducted. One of them investigated the influence of the friction between the specimen and the steel profiles (Figure 6.14, left), the other focused on the resistance of the test setup to shearing (Figure 6.14, right). Figure 6.15 shows the load-deformation diagrams of the pre-tests and the respective force values (static values and sliding values).

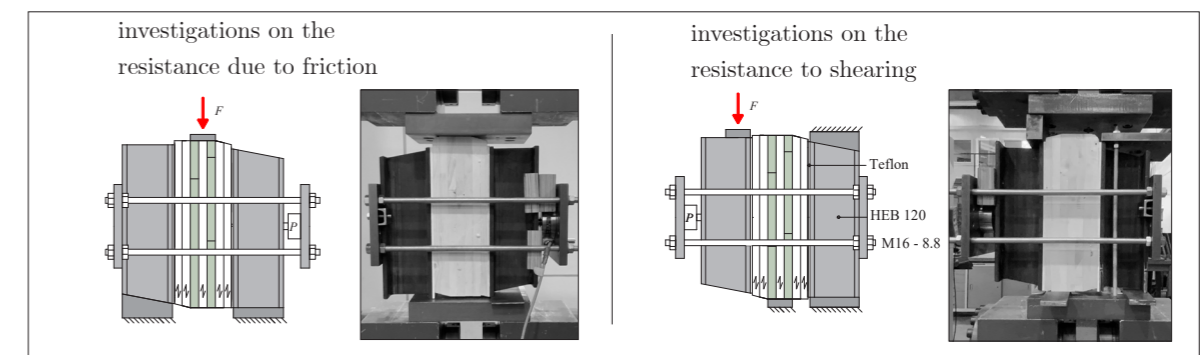


Fig. 6.14: Pre-tests on the test setup to determine the friction (left) and resistance to shearing (right)

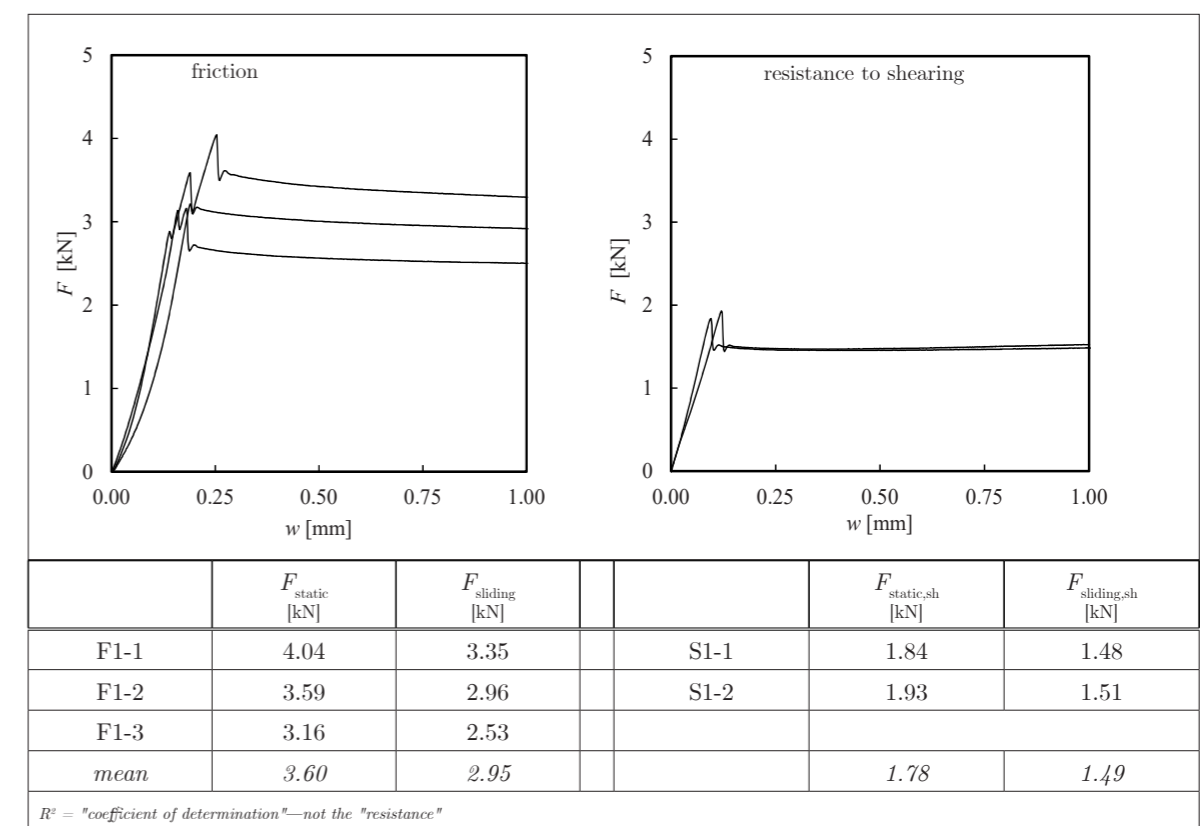


Fig. 6.15: Load-deformation diagrams and evaluation of the pre-tests on the test setup

Within the investigations on the friction, the static frictional force F_{static} and the sliding frictional force F_{slide} were determined under compression stresses of $\sigma_c = 0.5 \text{ MN/m}^2$. The pre-tests were carried out deformation controlled with a constant feed rate of 1 mm/min. The static force corresponds to the peak within the load-deformation diagram on the left side of Figure 6.15. The sliding force corresponds to the values in the range of $w = 0.5 \text{ mm}$ and $w = 1.0 \text{ mm}$ using linear regression. This also holds for the evaluation of the pre-tests on the shear resistance of the test setup.

Regarding the pre-tests on friction, the mean value of the static frictional force ($F_{\text{static,mean}} = 3.6 \text{ kN}$) is significantly lower compared to the total loading F_{max} within the later experimental investigations on the shear strength and stiffness. The overall influence of friction on the test results is small; consequently for these reasons, within the evaluation of O1-p, D3-p, and D4-p series, the influence of the test setup on the results is neglected. The static friction is exceeded at low loads compared to the expected failure load of the specimens and the decrease of the sliding frictional force as a function of the test duration.

Regarding the pre-tests on the resistance of the test setup to shearing, the maximum static shear force ($F_{\text{static,sh,mean}} = 1.78 \text{ kN}$) is only half as large as the static frictional force $F_{\text{static,mean}}$ in the previous pre-test. The sliding (shear) force $F_{\text{sliding,sh}}$ was once again determined between $w = 0.5$ and $w = 1.0 \text{ mm}$ using linear regression. This means that the frame is not subjected to any further shear loading after achieving a deformation of $w = 0.25 \text{ mm}$. Compared to the expected failure load of the specimens, and compared to the deformation of the specimens till failure, the resistance of the setup to shearing can be neglected.

6.2.5 Results of the mechanical testing with external compression

The evaluation of the out-of-plane shear tests with external compression perpendicular to grain follows the procedure described in Chapter 6.2.1. The validation of the test setup was carried out in Chapter 6.2.2. The chosen value of $\sigma_c = 0.5 \text{ MN/m}^2$ superimposes tension stresses perpendicular to grain, caused by the inclination of the specimens and the fibre orientation of the outer lamellas (Table 6.3).

Figure 6.16 gives the load-deformation diagrams of the specimens oriented in x and y direction under external compression. Figure 6.17 shows the load-deformation diagrams measured by the hydraulic cylinder.

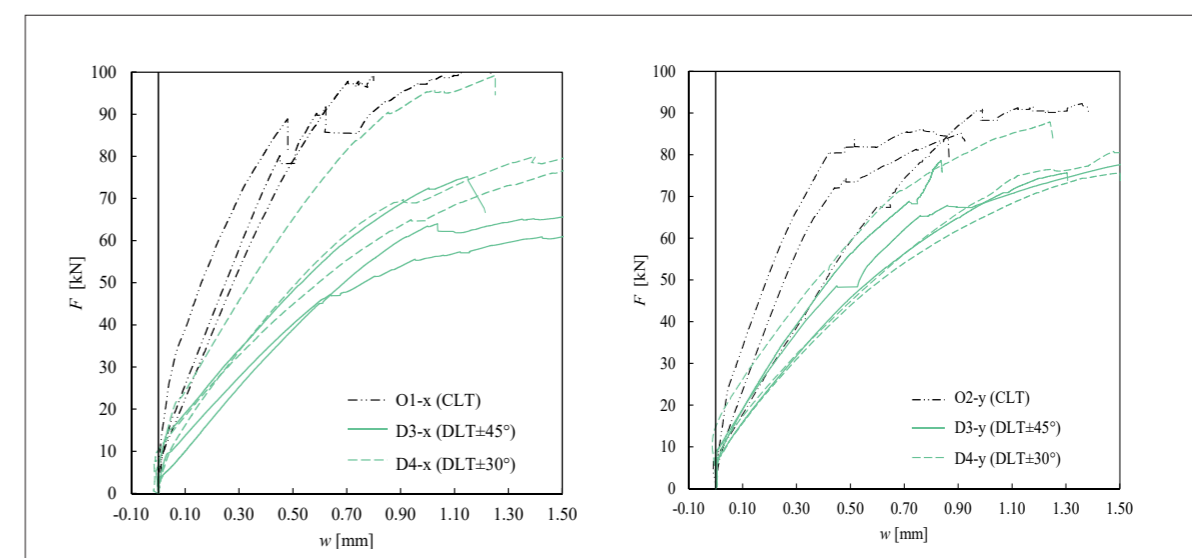


Fig. 6.16: Load-deformation diagrams (*def_1*) in x (left) and y (right) direction, with external compression perpendicular to grain ($\sigma_c = 0.5 \text{ MN/m}^2$)

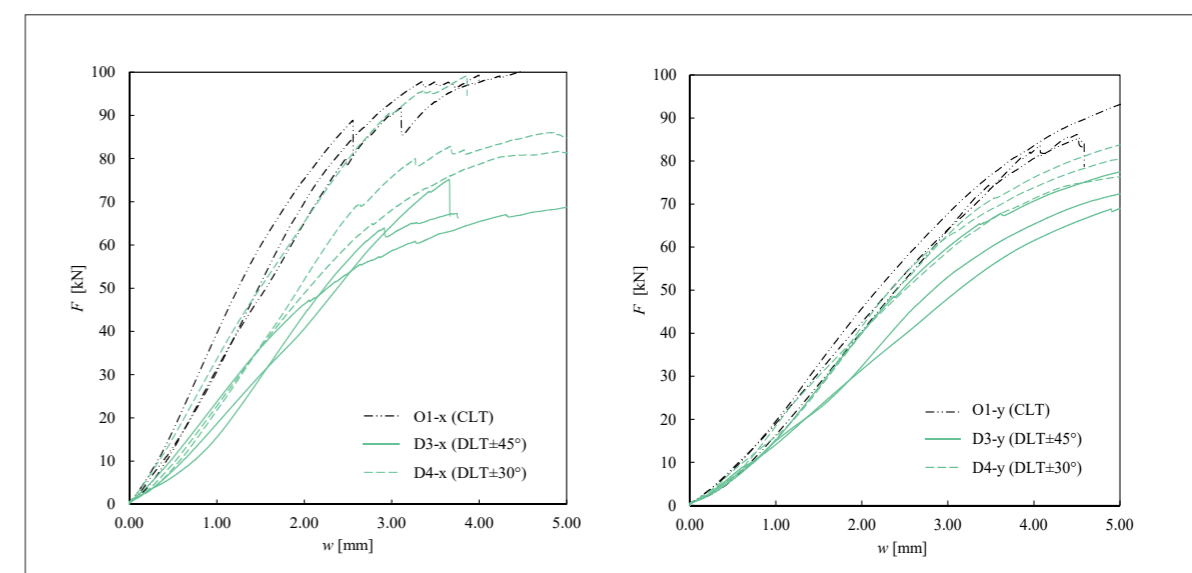


Fig. 6.17: Load-deformation diagrams (hydraulic cylinder) in x (left) and y (right) direction, with external compression perpendicular to grain ($\sigma_c = 0.5 \text{ MN/m}^2$)

The failure mechanisms of the specimens oriented in x direction under additional compression perpendicular to grain follow the observations made with the specimens without external compression (see Table 6.4). Rolling shear failures along the annual rings of the 90° oriented lamellas were achieved. Also, shear failures in the 45° (D3 series) and 30° (D4 series) following the fiber direction occurred. Table 6.7 summarizes the failure mechanisms and observations for the inner layers of each series oriented in x direction. The observed failure mechanisms may confirm, that the selected test setup is applicable only to a limited extent for the shear testing of CLT with more than one layer oriented under 90° within the shearing area. As previously described and carried out by (MESTEK IN 2011), EN 408 initially proposes shearing only one lamella, so as to avoid a chain of springs connected in parallel.

Tab. 6.7: Failure mechanisms of the CLT and DLT series in x direction, with ext. compression ($\sigma_{c,90} = 0.50 \text{ MN/m}^2$)


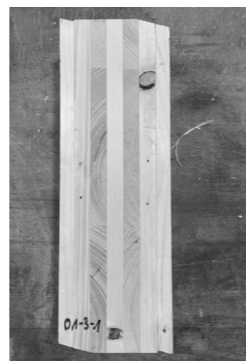
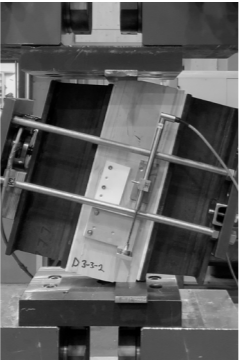
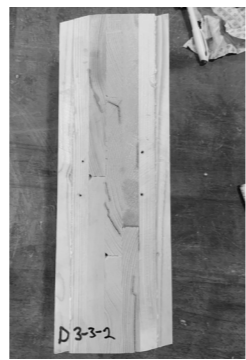
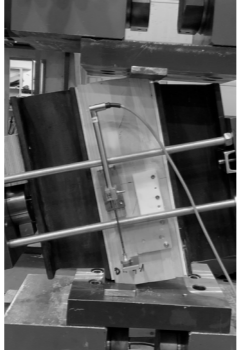
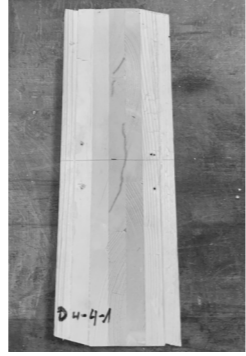
series	layup [mm] / [n°]	observations	side view	
O1-x-p	CLT inner layers (20-20-20) [90;0;90] _s	<ul style="list-style-type: none"> » small deformations at the load application area » rolling shear failure in one of the cross-layers 		
D3-x-p	DLT±45° inner layers (20-20-20) [45;90;-45] _s	<ul style="list-style-type: none"> » small deformations at the load application area » shear failures in the ±45° layers » rolling shear failure in the cross-layers (middle layer) 		
D4-x-p	DLT±30° inner layers (20-20-20) [30;90;-30] _s	<ul style="list-style-type: none"> » small deformations at the load application area » shear failures in the ±30° layers » rolling shear failure in the cross-layers (middle layer) 		

Table 6.8 summarizes the failure mechanisms of the specimens oriented in y direction under additional compression perpendicular to grain. The orientation of outer layers under 90° entailed additional eccentricities. Unlike before, the eccentricity, does not lead to a combined rolling shear failure with tension perpendicular to grain, as the tensile stresses were superimposed by the external compression. Therefore, the deformations at the load-introduction area increased. A shear failure could not be observed. Suggested improvements for future experimental setups are given on page 86.

Tab. 6.8: Failure mechanisms of the CLT and DLT series in y direction, with ext. compression ($\sigma_{c,90} = 0.50 \text{ MN/m}^2$)


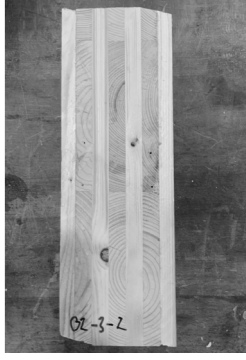

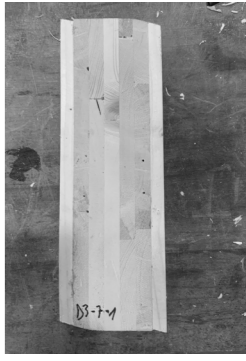

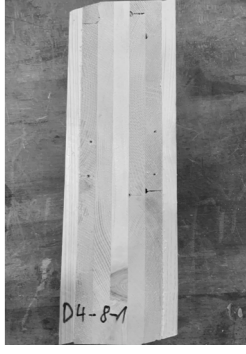
series	layup [mm] / [n°]	observations	side view	
O1-y-p	CLT inner layers (20-20-20) [0;90;0] _s	<ul style="list-style-type: none"> » high deformations at the load application area » failure at the load introduction due to compression perpendicular to grain » no shear failure achieved 		
D3-y-p	DLT±45° inner layers (20-20-20) [45;0;-45] _s	<ul style="list-style-type: none"> » high deformations at the load application area » failure at the load introduction due to compression perpendicular to grain » no shear failure achieved 		
D4-y-p	DLT±30° inner layers (20-20-20) [60;0;-60] _s	<ul style="list-style-type: none"> » high deformations at the load application area » failure at the load introduction due to compression perpendicular to grain » no shear failure achieved 		

Table 6.9 contains the evaluation of the investigations on the shear strength and stiffness with additional compression perpendicular to grain. Due to the additional compression, nearly no specimen oriented in y direction achieved failure (see Table 6.8). Therefore, values of the shear strength $f_{v,p}$ under additional compression perpendicular to grain are only evaluated for series oriented in x direction. Again, The values of $G_{ij,eff}$ refer to the inner layers, the values of $S_{ij,exp}$ refer to the overall series (see Figure 6.9 and Equations (6.10) and (6.11)).

Figure 6.18 extends the presentation of the test results and analytical solutions of Figure 6.13 by shear stiffness values following Table 6.9. The mean values of the out-of-plane shear stiffnesses, resulting from the experiments under additional compression perpendicu-

Tab. 6.9: Evaluation of the mechanical testing on the out-of-plane shear properties in global x and y direction of the CLT and DLT specimens ($t = 100$ mm) with compression perpendicular to grain ($\sigma_{c,90} = 0.50$ MN/m²)

	F_{max} [kN]	$0.4F_{max}$ [kN]	$0.1F_{max}$ [kN]	$w_{0.4F_{max}}$ [mm]	$w_{0.1F_{max}}$ [mm]	m [l]	R^2 [l]	$G_{xz/yz,eff}$ [MNm ² /m]	$S_{xz/yz}$ [MN/m]	$f_{v,p}$ [MN/m ²]
O1-1-x-p	88.9	57.8	42.2	0.209	0.117	167.8	1.0	203.47	19.76	1.80
O1-2-x-p	80.2	42.9	24.2	0.205	0.090	162.9	1.0	197.55	19.24	1.62
O1-3-x-p	97.8	46.3	20.6	0.254	0.088	155.3	1.0	188.36	18.42	1.98
($COV_{S_{xz}}$ 3.2) mean								196.46	19.14	1.80
O1-1-y-p	80.8	49.1	33.3	0.184	0.096	178.8	1.0	216.88	13.01	/
O1-2-y-p	72.1	34.9	16.2	0.164	0.058	177.0	1.0	214.70	12.88	/
O1-3-y-p	62.2	41.7	31.4	0.213	0.125	116.2	1.0	140.96	8.46	/
($COV_{S_{yz}}$ 18.5) mean								190.85	11.45	/
D3-1-x-p	72.5	39.8	23.4	0.381	0.159	72.5	1.0	87.97	9.00	1.47
D3-2-x-p	45.1	24.0	13.5	0.283	0.145	76.3	1.0	92.58	9.45	1.36
D3-3-x-p	47.3	26.1	15.5	0.278	0.125	68.9	1.0	83.55	8.57	1.40
($COV_{S_{xz}}$ 4.2) mean								88.03	9.01	1.41
D3-1-y-p	68.9	33.5	15.9	0.236	0.073	107.6	1.0	130.51	7.83	/
D3-2-y-p	75.6	36.2	16.6	0.359	0.108	78.2	1.0	94.80	5.69	/
D3-3-y-p	48.6	26.7	15.7	0.177	0.067	99.6	1.0	120.77	7.25	/
($COV_{S_{yz}}$ 13.1) mean								115.36	6.92	/
D4-1-x-p	65.0	38.0	24.5	0.382	0.180	82.4	1.0	99.94	10.17	1.65
D4-2-x-p	83.8	48.5	30.9	0.327	0.161	106.3	1.0	128.98	12.95	1.69
D4-3-x-p	69.7	36.3	19.6	0.331	0.134	84.5	1.0	102.51	10.42	1.41
($COV_{S_{xz}}$ 11.9) mean								110.48	11.18	1.58
D4-1-y-p	69.6	33.8	16.0	0.325	0.083	73.9	1.0	89.62	5.38	/
D4-2-y-p	87.9	44.1	22.3	0.301	0.060	90.4	1.0	109.58	6.58	/
D4-3-y-p	66.9	38.8	24.7	0.212	0.088	115.5	1.0	140.08	8.40	/
($COV_{S_{yz}}$ 18.3) mean								113.09	6.79	/

¹ F_{max} for $w = 5.0$ mm (no failure achieved)

lar to grain, are given by the fourth bar chart for each series. The left-hand side of Figure 6.18 refers the stiffness values in x direction. On the right-hand side the stiffness values in y direction are presented.

Overall, the bar charts in Figure 6.18 reveal that the shear stiffnesses of all series do not experience a remarkable change due to the additional external compression perpendicular to grain, compared to those without external compression. This follows the analytical approach, due to which the compression perpendicular has no influence on the stiffness properties; instead, it influences the failure mechanism and therefore the shear strength.

For the O1 series in x direction the out-of-plane shear stiffness $S_{xz,exp,p}$ (19.14 MN/m) is again much higher than the analytical solutions. As previously described, the reasons may be found within different material parameters or the non-linear shear distribution over the inner layers due to the two layers oriented under 90°. For D3 and D4 series, the experimental shear stiffness values in x direction are close to those without external compression perpendicular to grain and hence approximates the analytical solution. The discrepancy between the analytical and experimental shear stiffness values of the D3 and D4 series in y direction is further increased. This might be explained by the additional eccentricity due to the difficult load introduction and deformations in the outer (1st and 5th) layers, leading to additional stresses perpendicular to grain and therefore to higher shear deformations.

All in all, the results in y direction are inconsistent. The high coefficients of variation of the experimental stiffness values in y direction additionally indicate uncertainties among the results. For a more precise statement on the shear stiffness values of CLT and DLT in y direction, additional experiments should be carried—for example by using steel lamellas, glued to the edges of the inner layers.

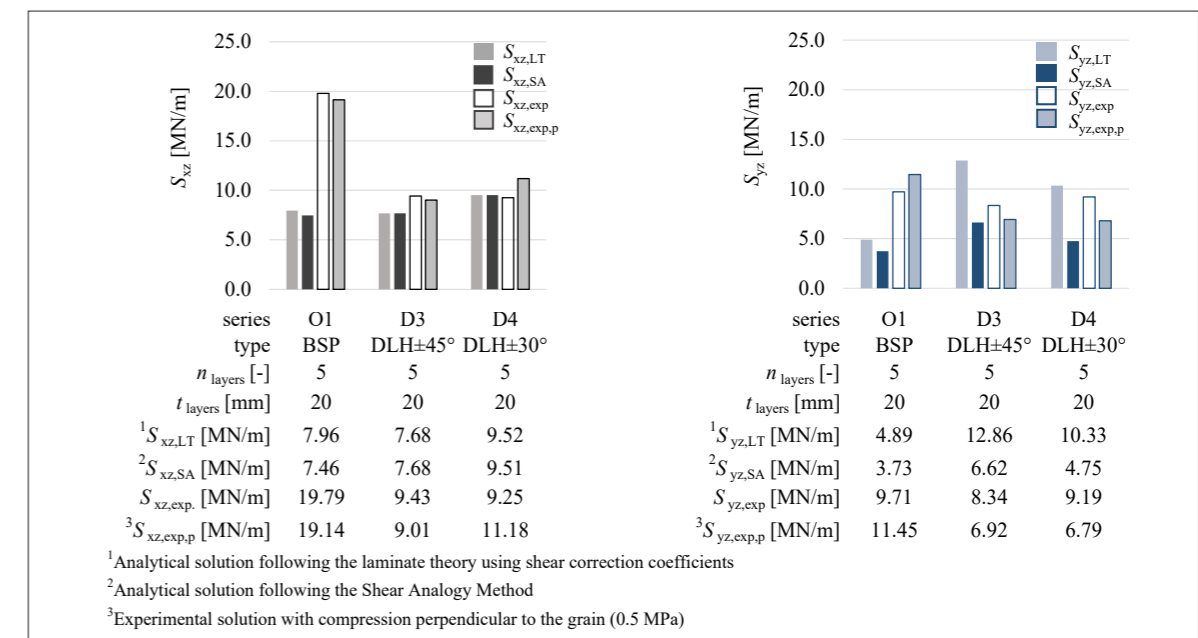


Fig. 6.18: Out-of-plane shear stiffnesses of the CLT and DLT series ($t = 100$ mm) following the experimental investigations and analytical solutions, with and without external compression ($\sigma_c = 0.50$ MN/m²)

The out-of-plane shear strengths, determined by the initial failure loads, are increased by the external compression (Table 6.10). The mean values in x direction with additional compression perpendicular to grain ($\sigma_{c,90} = 0.5 \text{ MN/m}^2$) are increased by 7.1 % for the O1 series, compared to the strength values without external compression. For the D3 series, an increase of even 20.5 % is achieved in x direction. The D4 series experiences an increase of 8.9 % on average. In y direction, as previously described, no strength values with external compression could be determined, given that no failure occurred. Table 6.10 gives the mean values of the shear strengths, with and without compression, for each of the investigated series.

The increase in shear strength by compression perpendicular to grain can be validated by comparing the results of the CLT series to the results provided by (MESTEK 2011). The rolling shear strengths determined by *Mestek* refer to compression stresses perpendicular to grain of $\sigma_{c,90} = 0.33 \text{ MN/m}^2$ and $\sigma_{c,90} = 0.80 \text{ MN/m}^2$. For comparability, the strengths values determined by *Mestek* are linear interpolation for $\sigma_{c,90} = 0.5 \text{ MN/m}^2$. Using a comparable test setup to the one chosen for this investigation, *Mestek* increased the shear strength of a CLT series from $f_v = 1.47 \text{ MN/m}^2$ to $f_{v,p} = 1.63 \text{ MN/m}^2$, which represents an increase of shear strength by 11.1 %. This percentage value is close to the increase achieved for O1 series by the experimental investigation in this thesis (+7.1 %). The test setup by *Mestek* differs from the one chosen here, as *Mestek* sheared only one cross-layer of the CLT specimens (oriented under 90°).

Within the following Chapter 6.3 shear stiffness values determined by the previously introduced FE models are compared to the analytical and numerical values.

Tab. 6.10: Percentage increase of the shear strength f_v due to external compression

series	f_v [MNm ² /m]	$f_{v,p}$ [MNm ² /m]	increase [%]
O1-x	1.68	1.80	+7.1
D3-x	1.17	1.41	+20.5
D4-x	1.45	1.58	+8.9
O1-y	1.54	/	/
D3-y	1.10	/	/
D4-y	1.65	/	/

6.3 Further investigations using numerical models

6.3.1 General information and modelling approach

The numerical models, previously introduced in Chapter 6.2.2, are used for further investigations on the shear stiffness values, in order to validate and confirm the analytical and experimental investigations. The "path_1" within the models follows the deformation measured by the inductive displacement transducer. The "path_2" within the models follows the vertical axis within the specimens and was already used for the validation of the test setup—with and without compression perpendicular to grain. The models are acting linear elastic and without implementation of fracture mechanics and therefore do not provide the possibility to calculate strength values. On the other hand, the calculation of stiffness values from the linear elastic deformations within the FE models is possible

6.3.2 Determination of the shear modulus and comparison of the results

The load levels applied to the models are in reference to the linear elastic range of the experimental investigations, so as to derive deformations in a comparable range (between $0.1 F_{\max}$ and $0.4 F_{\max}$). The shear deformations refer to the chosen evaluation area ($a_x = a_y = 60 \text{ mm}$; "path_1"). Table 6.11 compares the out-of-plane shear stiffness values determined by the numerical models to the stiffness values of the mechanical testing and the analytical approach.

Tab. 6.11: Out-of-plane shear stiffness values of the O1, D3, and D4 series following the numerical investigations, the mechanical testing, and the analytical approach

	numerical model			mechanical testing	analytical ²
	Δu^1 [mm]	$G_{xz/yz,eff}$ [MNm ² /m]	$S_{xz,mm}/S_{yz,mm}$ [MN/m]	$S_{xz,exp}/S_{yz,exp}$ [MN/m]	S_{xz}/S_{yz} [MN/m]
O1-x	0.372	67.57	7.17	19.79	7.96
D3-x	0.376	66.46	7.09	9.43	7.46
D4-x	0.284	88.00	9.38	9.25	11.82
O1-y	0.227	166.91	11.75	9.71	4.89
D3-y	0.268	112.83	9.97	8.34	12.86
D4-y	0.340	81.40	7.85	9.19	13.05
O1-x-p	0.376	61.31	7.10	19.14	7.96
D3-x-p	0.376	60.74	7.10	9.01	7.46
D4-x-p	0.284	78.59	9.38	11.18	11.82
O1-y-p	0.251	124.61	10.63	11.45	4.89
D3-y-p	0.272	89.18	9.79	6.92	12.86
D4-y-p	0.340	69.11	7.85	6.79	13.05

¹Respective values in accordance to the linear-elastic range of the experimental investigations
²Laminate theory using shear correction coefficients

For the CLT O1 series in x direction, the numerical solution confirms the analytical solution, but not the experimental values. The significantly high experimental results of the O1 series in x direction could therefore indicate a measurement error. On the other hand, the O1 series in x direction is the only series featuring two layers oriented under 90° within the three inner layers (shear area), which is contrary to an actual homogeneous distribution of the shear stress over the inner layers. This needs to be further investigated.

Overall, both, the experimental results and the numerical solution, correspond well to the analytical solutions in x direction for the DLT $\pm 45^\circ$ D3 and the DLT $\pm 30^\circ$ D4 series (Figure 6.19). In y direction the numerical solution corresponds well to the analytical solution following the *Shear Analogy Method* for the D3 and D4 series. This is not surprising, since both approaches are based on the same assumption of a linear distribution of shear stresses over the cross-section. The chosen experimental test setup also provokes a linear distribution of shear stresses within the inner layer, which however—at least in the y-direction—is in contrast to the actual distribution of the shear stresses (see Chapter 6.1).

It is therefore questionable, whether the chosen experimental test setup is suitable for the investigation of the actual shear stiffness of DLT in y direction. As explained in Chapter 6.1, the laminate theory, using shear correction coefficients, represents the mechanically more accurate analytical solution for DLT, than the *Shear Analogy Method*. On the other hand, the conjecture, namely that the chosen test setup is not suitable for the investigations of the shear stiffness of CLT and DLT, was confirmed only partly, since the numerical results additionally provide results close to the experimental results for DLT in y direction. This also holds true for the numerical results of CLT in x direction, compared to both analytical solutions.

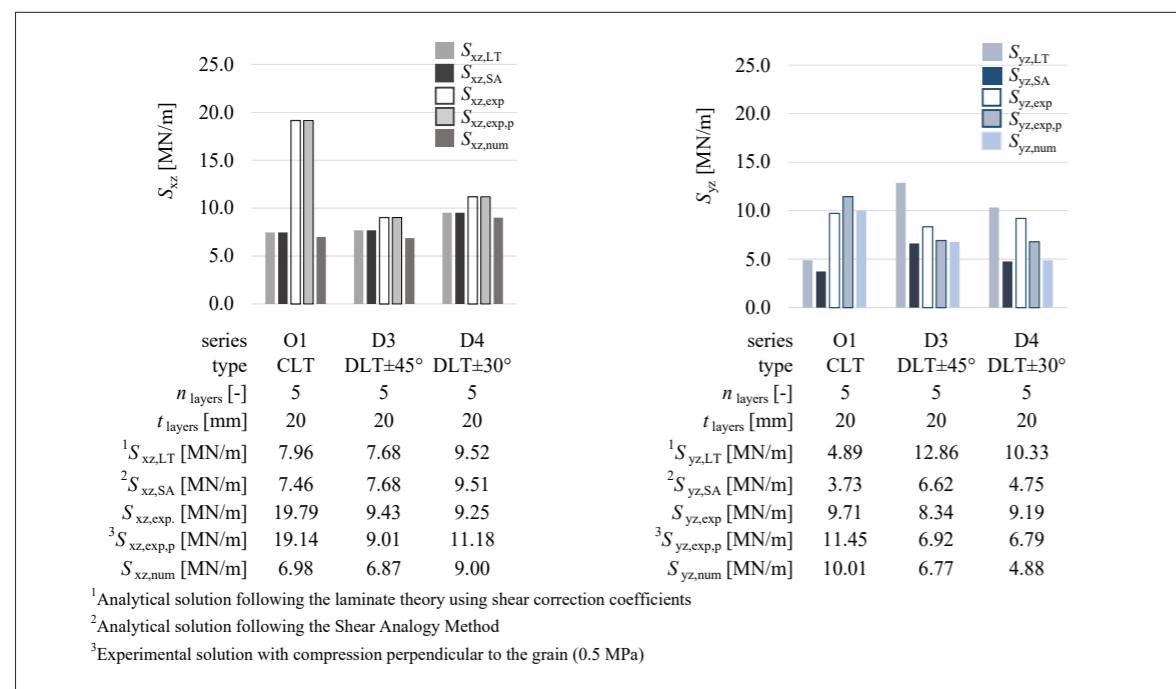


Fig. 6.19: Out-of-plane shear stiffnesses of the CLT and DLT series ($t = 100$ mm) following the experimental investigations and analytical solutions with and without external compression ($\sigma_c = 0.50$ MN/m²)

Nevertheless, investigations on the out-of-plane stiffness properties of CLT and DLT could alternatively be carried out on one layer only, as proposed in EN 408. Afterwards, the determined shear moduli could be summed up, using the laminate theory and shear correction coefficients or the *Shear Analogy Method*. If a package of layers or a whole cross-section is to be tested, shear-bending tests (four-point bending tests) according to EN 16351 may provide an appropriate test setup. When the test setup according to EN 16351 is used for the determination of shear stiffness values for DLT in y direction, analytical values following the laminate theory using shear correction coefficients could be more close to the experimental results, than shear stiffness values according to the *Shear Analogy Method*, due to the non-linear and parabolic distribution of shear stresses under the four-point bending tests.

All in all, the experimentally determined shear stiffness values failed to point-out the increase in shear stiffness due to diagonal layer arrangements according to the analytical approaches (also see comparison within Appendix A8). Following the laminate theory and compared to CLT, the shear stiffness values of DLT are in comparable range in x direction and highly improved in y direction. For further investigations on the out-of-plane stiffness properties of CLT and DLT, test specimens from the same batch and with identical material parameters should be used and an alternative test setup, e.g. according to EN 16351 should be considered.

The investigations on the out-of-plane shear stiffness values are followed by the investigations on the bending stiffness (Chapter 7) and the investigations on the torsional stiffness (Chapter 8).

7 Investigations on the bending stiffness

7.1 Theoretical approach and analytical solution

Besides the impact of diagonal layer arrangements on the out-of-plane shear stiffness according to the analytical solutions, DLT may achieve increased uniaxial bending properties compared to CLT.

The bending stiffness values B_x and B_y of a laminate can be taken from the entries D_{11} and D_{22} of the stiffness matrix (see ABD - E matrix, Chapter 5). The deformation of a beam under a single load in mid-span is given by Equation (7.1). This deformation includes components from bending and out-of-plane shear deformations. If an effective bending stiffness (including bending and shear stiffness terms) is to be calculated, deformations on equivalent static systems under a unit load can be used to recalculate to the corresponding stiffness terms $B_{x,eff,exp}$ and $B_{y,eff,exp}$ (Equation (7.2)). The same holds true for various static systems under different loadings. Analytically, an effective bending stiffnesses $B_{x,eff}$ can exemplary be determined on the system of a beam element under a single load F in mid-span using the force method (method of consistent deformations). Following the force method, the superposition of bending and shear deformations according to Equation (7.1) can be written according to Equation (7.3).

$$w_{EI+GA} = \frac{F \cdot l^3}{48EI} + \frac{F \cdot l}{4GA} \quad (7.1)$$

$$B_{x,eff} = \frac{F \cdot l^3}{48w_{EI+GA}} \quad (7.2)$$

$$w\delta_{ij} = \int_0^1 \frac{\delta m_x \cdot m_x}{|B_x|} dx + \int_0^1 \frac{\delta V_x \cdot V_x}{|S_{xz}|} dx \quad ; \quad \frac{Fl^3}{48B_{x,eff}} = \frac{Fl^3}{48|D_{11}|} + \frac{Fl}{4|E_{44}|} \quad (7.3)$$

The effective bending stiffness is therefore - in contrast to the pure bending stiffness - always dependent on the span of the selected equivalent static system. Unlike actual pure stiffness values, effective stiffness values are always coupled to an equivalent static system. Therefore, a general comparison of effective stiffness values with actual stiffness values requires a corresponding static system and only then allows a conclusion to be drawn on the influence of the shear deformation components.

Table 7.1 compares the percentage increases and decreases in bending stiffness of diagonal layer arrangements (DLT) in relation to the respective series of the same thickness and orthogonal layers arrangements (CLT). The out-of-plane shear stiffness values follow the laminate theory using shear correction coefficients according to Chapter 5 (material parameters according to Table 4.9; T14 (ETA-20/0023); *Poisson's* ratios according to (HALÁSZ AND SCHEER 1996)).

Tab. 7.1: Percentage increase and decrease of the bending stiffness due to diagonal layer arrangements

thickness	$t = 100$ mm			$t = 200$ mm			
	series type	O1 CLT	D3 DLT±45°	D4 DLT±30°	O5 CLT	D5 DLT±45°	D6 DLT±30°
B_x [MNm ² /m] rate [%]	0.74 (= 100 %)	0.79 +6.6 %	0.84 +14.2 %	5.90 (= 100 %)	6.29 +6.7 %	6.74 +14.2 %	6.35 +7.6 %

The bending stiffnesses of the DLT±45° D3 series is by 6.6 % higher compared to the 5-layered CLT series O1 with an overall thickness of $t = 100$ mm, and higher by 14.2 % for DLT±30° (D4 series). Consequentially, the diagonal layer orientation leads to the same increase in bending stiffness for the series with a thickness of 200 mm as well. In y direction, the bending stiffness values of DLT are significantly lower, compared to CLT (D3 series -73.6 %). For the additional uDLT+45° series D1 (equals uDLT±45° series D2) the increase in the bending stiffness in x direction (+7.6 %) is only slightly higher than for DLT±45° (+6.7 %). Therefore, the influence of the rotation of the center layer (3rd layer) by 90° has nearly no influence on the bending stiffness in x direction. This is quite different for the bending stiffness in y direction. By rotating the center layer into 0° direction, the uDLT loses 39.9 % of its bending stiffness in y direction compared to CLT, while DLT±45 series D3 loses only 35.0 %.

A parameter study on the bending stiffness of DLT element ($t = 100$ mm) under varying orientation of the second and fourth layer—similar to the parameter study on the out-of-plane shear stiffness (Chapter 6.1)—highlights the above findings. The layer thickness is chosen as a constant at $t_1 = 20$ mm. The layers are rotated in opposite directions in steps of 15°, up to the limits of 15° and 75°, respectively (see Figure 6.4). Figure 7.1, left, additionally gives the bending stiffness values in global x and y direction.

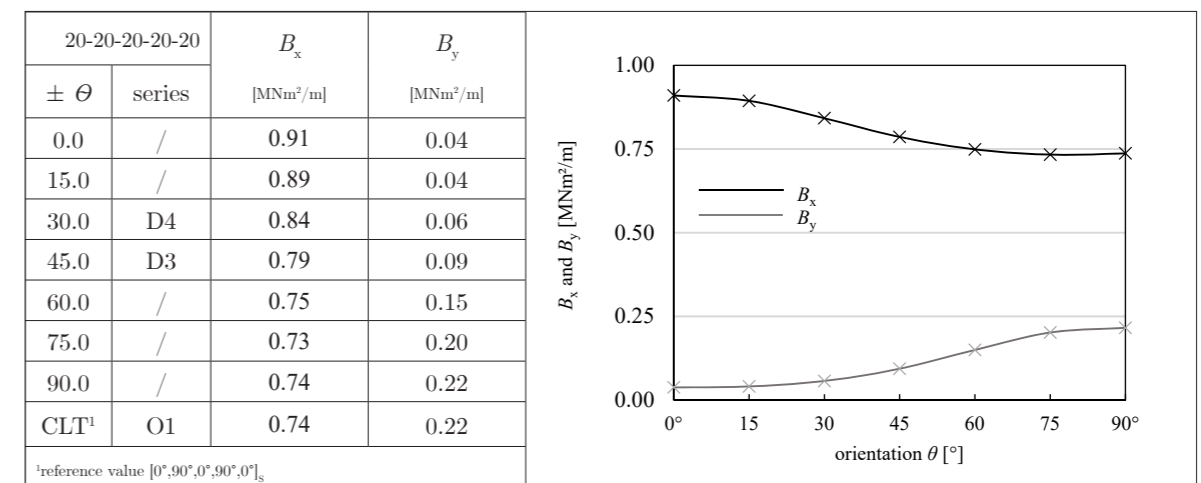


Fig. 7.1: Bending stiffness of 5-layered CLT and DLT elements as a function of the layer arrangement θ

In addition to the representations within Figure 7.1, Figures 7.2 and 7.3 depict the increase of the bending stiffness B_x as a function of the increasing layer thickness of CLT and DLT. The quadratic increase can be explained by the weighting of the *Steiner*-terms with increasing distance of the partial centers of gravity to the total center of gravity.

The increase in x direction is approximately the same for the 5-layered CLT and DLT. The respective bending stiffness values are calculated in steps of $\Delta t_i = 5$ mm. The same parameter is used on the bending stiffness values B_y of 5-layered CLT and DLT elements (Figure 7.3). An increase in the layer thickness of, for example, DLT $\pm 45^\circ$ elements does not result in an increase of the bending stiffness in y direction to the same extent as is the case in x direction (Figure 7.3).

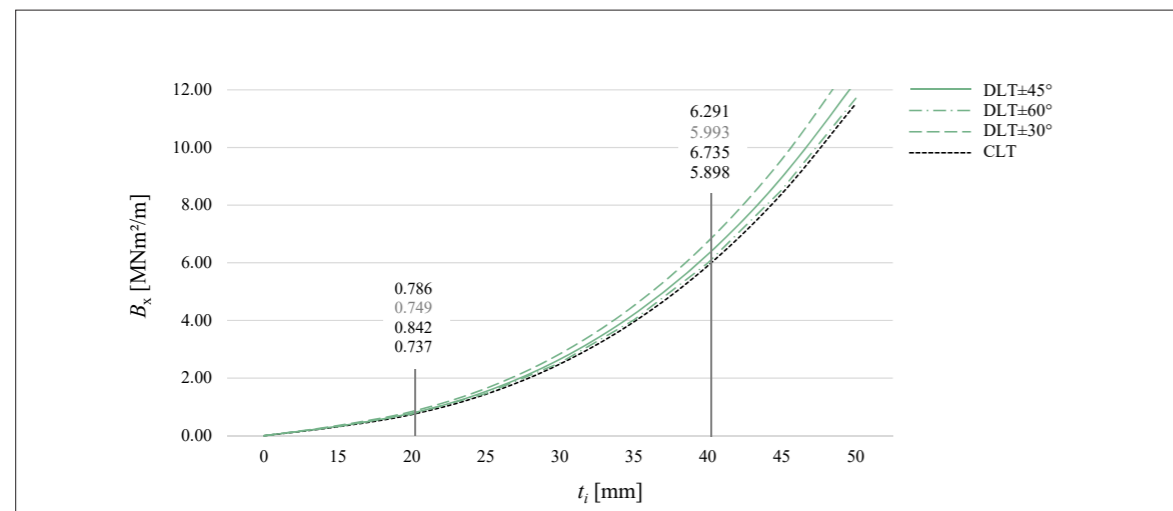


Fig. 7.2: Bending stiffness B_x of 5-layered CLT and DLT elements as a function of the layer thickness t_i

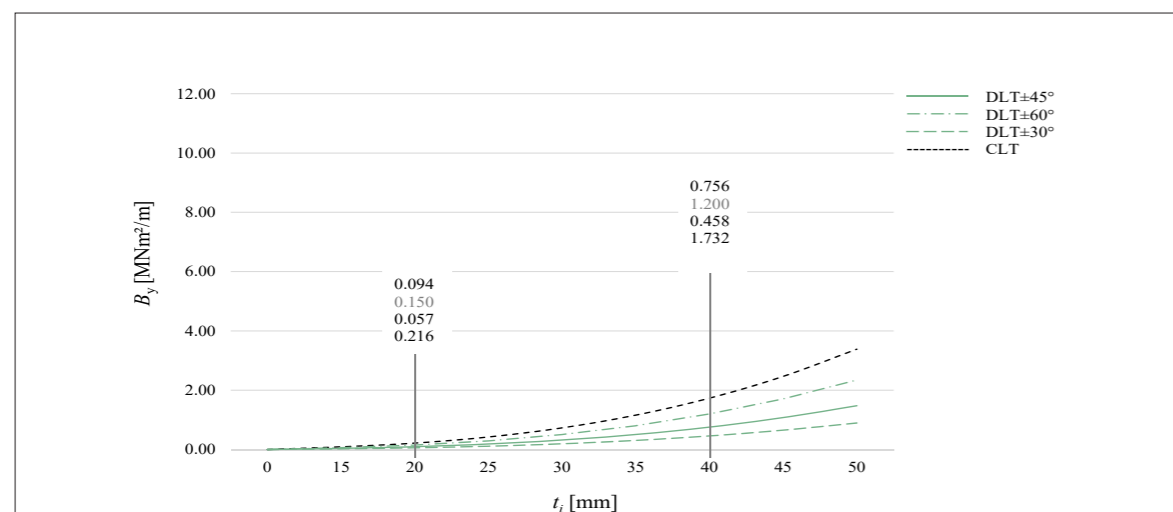


Fig. 7.3: Bending stiffness B_y of 5-layered CLT and DLT elements as a function of the layer thickness t_i

7.2 Experimental determination of the bending stiffness

7.2.1 Test setup

In order to experimentally determine the bending stiffness properties of DLT, four-point bending tests were carried out on the uDLT $\pm 45^\circ$ series D1. The experiments were carried out by our partners of the Timber Construction Unit at the University of Innsbruck. D1 series is suitable mainly for applications requiring uniaxial load transfer. This is due to the missing cross-layer (90°) (see Chapter 4.3). For all other series, the analytical and numerical investigations form the basis for future experimental investigations on the bending stiffness. Hence, the test series D1 can be seen as tactile testing series, that can be placed in context and relation to the experimental investigations of *Buck et al.* in 2016 (BUCK ET AL. 2016).

The test setup of the uniaxial bending test follows the test setup of the four-point bending test according to EN 16351. Smaller adjustments had been carried out within the test setup. The span between the load introduction points was set to $8h$ instead of $6h$. Figure 7.4 exhibits the chosen test setup of the four-point bending test.

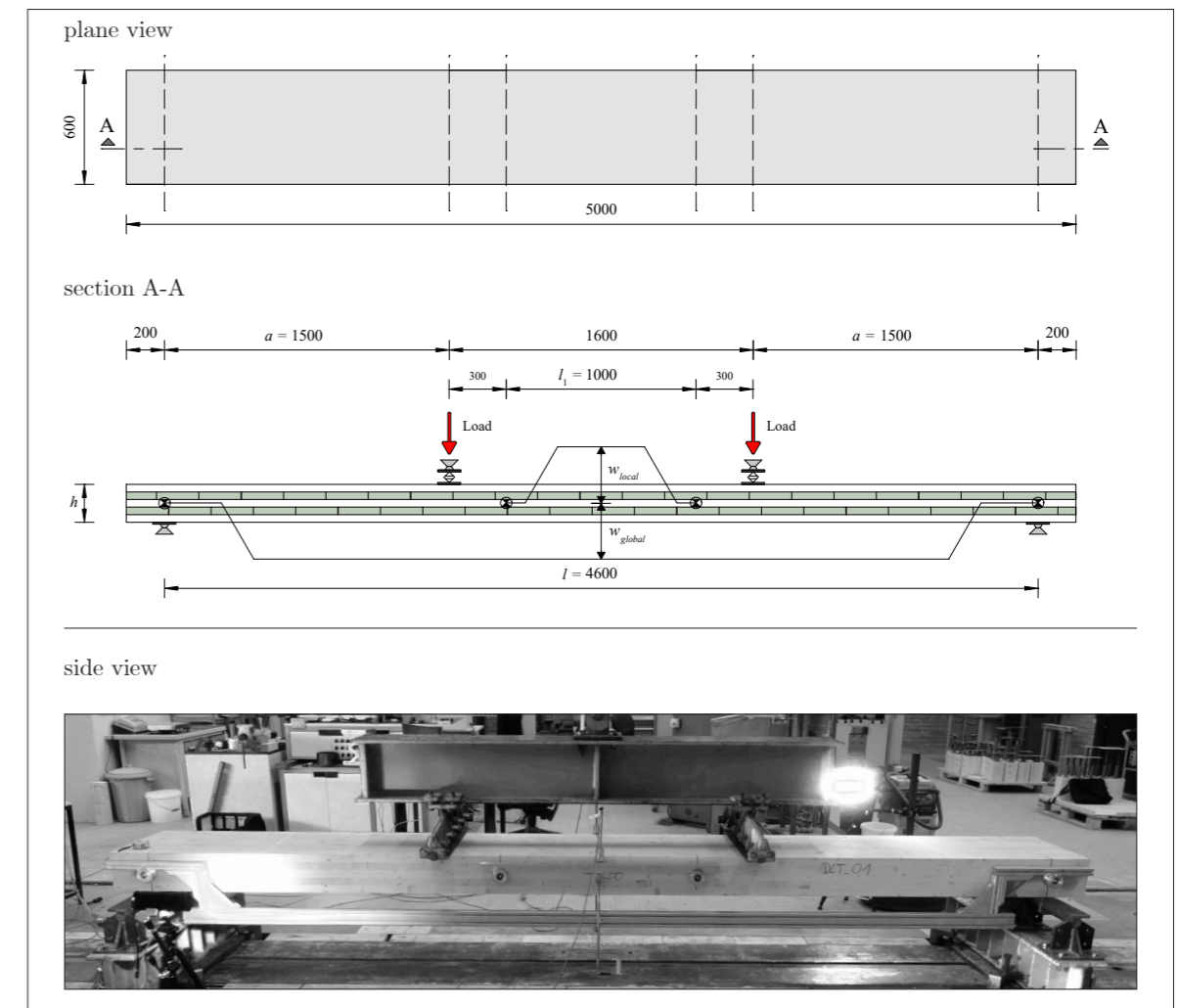


Fig. 7.4: Test setup of the four-point bending tests

The overall span l was set to $23 h = 4600$ mm. This length shall ensure failures due to normal stresses caused by bending, instead of shear failures within the diagonal layers. EN 16351 recommends a span of $24 \leq h \leq 30 h$. The minor deviations from the standard are included in the evaluation. Brandner *et al.* summarize and analyze test setups of four-point bending test configurations provided in different standards (EN 408, EN 16351, EN 789), so as to harmonize the test setups (BRANDNER ET AL. 2018). Following their breakdown, EN 16351 provides the most appropriate basis for determining the bending stiffnesses of mass timber laminates.

Each specimen had the dimension of 4600/600/200 mm (Figure 7.4). The load introduction was realized by steel plates ($w = 100$ mm). The point-loads were directed vertically downward with a distance of $8h$ to each other. Hereby, half of the force from the hydraulic cylinder was applied via a cross-member to the test specimen. The point-loads were introduced by way of the steel plates over the depth (600 mm) of the specimen. Each specimen was set on a roller bearing, resulting in vertical support and a static defined system ($l = 600$ mm). Therefore, the distance between the load-introduction points and the supports is $l_2 = 1500$ mm. Within the span of $l_1 = 5h = 1000$ mm the local deformation w_{local} was measured using inductive displacement transducers that were fixed to an aluminium profile. The profile was fixed pivotably on each side of the specimens (Figure 7.4). In the same way, the global deformation w_{global} within the overall span ($l = 4600$ mm) was measured on both sides of the specimens. The experiments were carried out deformation controlled with a feed rate of 10 mm/min until failure.

The uDLT D1 specimens were produced in conjunction with the other DLT specimens. Thus, the boards are from the same batch as those used in D3, D4, O5, D5, and D6 series (see Table 4.9). The moisture content of each specimen was measured before the mechanical testing and was in the range of $u = \pm 12$ %.

The bending stiffness for each specimen is calculated according to EN 16351 within the linear elastic range using linear regression. The failure load was estimated preliminary using analytical methods. After reaching about 50 % of the estimated failure load, the aluminium profiles and displacement transducers were removed. The range of linear elastic evaluation was set between $(0.1F_{init}$ and $0.3F_{init})$. The bending stiffness B_x was determined using Equation (7.4). Equation (7.5) follows Equation (C.1) within EN 16351. B_x equals the local bending stiffness. The effective bending stiffness $B_{x,eff}$ is determined by Equation (7.5) (where m_i is the slope of the regression line).

$$(EI)_{CL,local,net} = B_x = \frac{l_2 \cdot l_1}{16} \cdot \frac{F_2 - F_1}{w_2 - w_1} = \frac{l_2 \cdot l_1}{16} \cdot m_{local} \quad (7.4)$$

$$(EI)_{CL,app,net} = B_{x,eff} = \frac{3 \cdot l_2 \cdot l^2 - 4 \cdot l_2^3}{48} \cdot \frac{F_2 - F_1}{w_2 - w_1} = \frac{3 \cdot l_2 \cdot l^2 - 4 \cdot l_2^3}{48} \cdot m_{global} \quad (7.5)$$

7.2.2 Results of the mechanical testing

Figure 7.5 highlights the load-deformation diagrams for the 5-layered uDLT D1 series with an overall thickness of $t = 200$ mm. Since the test specimens are of the same series, the individual specimens are not labeled. Additionally, the force F is given as a function of the deformation of the cylinder ($w_{cylinder}$), showing the loss of force at initial failure, is given in Appendix A5. The failure mechanism has no influence on the stiffness parameters, taken within the linear elastic range of the load-deformation graphs. Furthermore, due to the stacking sequence of the specimens with both diagonal layers arranged under $+45^\circ$, a detailed examination and description of the failure mechanisms is not meaningful regarding failure mechanisms of uDLT $\pm 45^\circ$. Figure 7.6 exemplarily displays the failure mechanisms of one specimen of the DLT $+45^\circ$ D1 series. All of the ten specimens achieved initial failure due to bending.

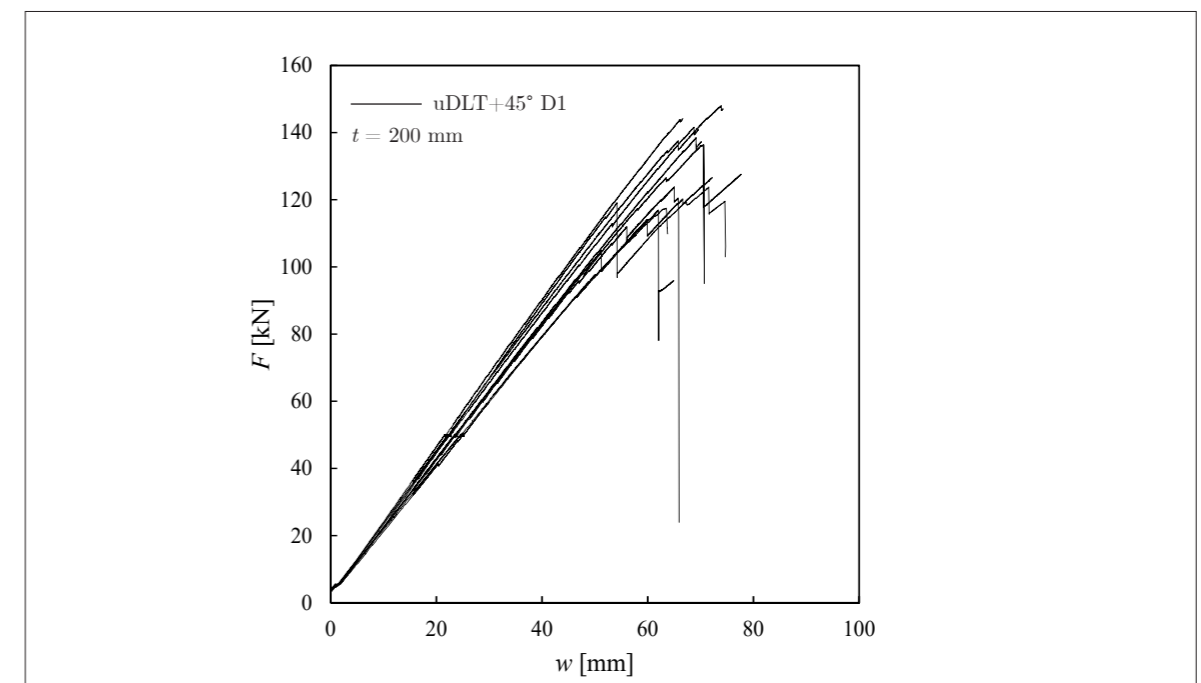


Fig. 7.5: Load-deformation diagrams of the cylinder



Fig. 7.6: Display of an exemplary failure mechanism in bending of D1-4 specimen

Table 7.2 gives the evaluation of the experiments within the linear elastic range. Table 7.3 provides the results of the mechanical testing following Equations (7.4) and (7.5) using the values provided within Table 7.2. In addition, equivalent moduli of elasticity E^* are calculated according to Equations (1) and (2) within EN 408 and given within Appendix A5.

Following the analytical approach, the local bending stiffness of the uDLT D1 series is $B_x = 6.35 \text{ MNm}^2/\text{m}$. This value appears to be higher by $0.70 \text{ MNm}^2/\text{m}$ than the mean value $B_{x,\text{exp}} = 5.65 \text{ MNm}^2/\text{m}$ achieved by the mechanical testing.

The effective bending stiffness of D1 series following an analytical approach appears to be $B_{x,\text{eff}} = 5.95 \text{ MNm}^2/\text{m}$ considering the span of $l = 4.6 \text{ m}$ and $a = 1.5 \text{ m}$ (see Appendix A5 for the analytical derivation of $B_{x,\text{eff}}$ for the four-point bending test). This value differs by $0.61 \text{ MNm}^2/\text{m}$ to the experimental determined effective (global) bending stiffness $B_{x,\text{eff,exp}} = 5.34 \text{ MNm}^2/\text{m}$.

Compared to reference CLT series O5 ($B_{x,\text{eff}} = 4.37 \text{ MNm}^2/\text{m}$ considering the span of $l = 4.6 \text{ m}$ and $a = 1.5 \text{ m}$) the effective bending stiffness of the DLT D1 series is by 22.7 % higher. This result is in a comparable range to the experimental findings on the uniaxial bending stiffness in global x direction of $\text{DLT}\pm 45^\circ$ of (BUCK ET AL. 2016). Here, the four-point bending tests, which were carried out on ten CLT and $\text{DLT}\pm 45^\circ$ test specimens each ($w/l/t = 1200/4136/95 \text{ mm}$; 19-19-19-19-19; $[0^\circ, 45^\circ; 0^\circ; -45^\circ, 0^\circ]_S$; non-edge-glued) according to EN 408, demonstrated an increase in bending stiffness $B_{x,\text{eff,exp}}$ of 15.5 % (BUCK ET AL. 2016).

The experimentally determined shear stiffness values (light gray within Tab 7.4) are only of limited significance due to the high COV (31.6 %). For D1-1, and D1-5 to D1-7 no shear modulus could be determined due to a probable error during the testing (statistical outliers). Even without these values, the mean value of the experimental investigation ($S_{xz,\text{exp}} = 38.75 \text{ MN/m}$) is not in comparable range to the analytical value ($S_{xz} = 28.08 \text{ MN/m}$).

In summary, the four-point bending tests according to EN 16351 seems to be well suited to determine the bending stiffness (local) and the effective bending stiffness (global) of DLT. In contrast to what was hoped for in Chapter 6.2, sufficient out-of-plane shear stiffness values could not be determined by the four-point-bending test. This is astonishing, also in view of the close correlation of the determined bending stiffness values to the analytical solution. Whether this was due to measurement errors or other reasons needs further investigation.

The investigations on the bending stiffness of DLT are followed by the investigations on the torsional stiffness properties.

Tab. 7.2: Evaluation of the four-point bending tests on the uDLT series D1

	F_{max} [kN]	$0.3F_{\text{max}}$ [kN]	$0.1F_{\text{max}}$ [kN]	$w_{0.3F_{\text{max}}}$ [mm]		$w_{0.1F_{\text{max}}}$ [mm]		slope m [1]		R^2 [1]
				global	local	global	local	global	local	
D1-1	98.00 ¹	29.40	9.80	13.86	0.74	3.25	0.17	1847.52	34696.09	1.00
D1-2	144.25	43.28	14.43	19.31	1.00	5.18	0.27	2031.11	39045.22	1.00
D1-3	141.73	42.52	14.17	19.74	1.01	5.05	0.26	1871.52	36424.43	1.00
D1-4	138.54	41.56	13.85	19.61	0.94	5.03	0.24	1907.71	39533.63	1.00
D1-5	137.68 ¹	41.30	13.77	18.95	1.01	4.93	0.26	1987.71	36931.13	1.00
D1-6	104.73 ¹	31.42	10.47	14.89	0.81	3.57	0.19	1824.02	33635.95	1.00
D1-7	125.00 ¹	37.50	12.50	18.13	0.98	4.67	0.25	1851.81	34052.12	1.00
D1-8	117.71	35.31	11.77	17.48	0.90	4.45	0.22	1782.09	34336.11	1.00
D1-9	116.98	35.09	11.70	17.66	0.93	4.17	0.22	1767.58	33412.82	1.00
D1-10	119.15 ¹	35.75	11.92	15.88	0.82	4.31	0.21	2020.56	39349.33	1.00

¹load at initial failure

Tab. 7.3: MOE, bending stiffnesses $B_{x,\text{exp}}$ and $B_{x,\text{eff,exp}}$ and $S_{xz,\text{exp}}$ following the four-point bending tests (EN 16351)

	$B_{x,\text{exp}}$ [MNm ² /m]	$B_{x,\text{eff,exp}}$ [MNm ² /m]	$S_{xz,\text{exp}}$ [MN/m]
D1-1	5.42	5.24	/
D1-2	6.10	5.76	45.89
D1-3	5.69	5.31	34.96
D1-4	6.18	5.41	19.28
D1-5	5.77	5.62	/
D1-6	5.26	5.18	/
D1-7	5.32	5.25	/
D1-8	5.37	5.06	38.76
D1-9	5.22	5.02	56.20
D1-10	6.15	5.73	37.42
mean	5.65	5.36	38.75
COV	6.8 %	5.0 %	31.6 %

8 Investigations on the torsional stiffness

8.1 Theoretical approach and analytical solution

8.1.1 Theoretical approach

Torsion appears to be a combination of different deformations, the latter include uniaxial bending caused by normal stresses in x and y direction, as well as shear deformations in x and y directions. Both have been previously investigated and, together with the findings on laminates, provide the theoretical background to this Chapter. Parts of the investigations of Chapter 8 were previously published within (ARNOLD ET AL. 2022a).

Following the law of elasticity, the torsional stiffness of an isotropic plate element is given by Equation (8.1):

$$G_{xy}I_T = \frac{E}{2(1-\nu)} \frac{t^3}{3} = K_{xy}(1-\nu) = B_{xy} \quad (8.1)$$

Thus, the moment-twist-relation is described by Equation (8.2):

$$m_{xy} = K \frac{1-\nu}{2} \left(\frac{\partial \varphi_x}{\partial y} + \frac{\partial \varphi_y}{\partial x} \right) = K(1-\nu)\kappa_{xy} \quad (8.2)$$

For the assumption of the *Kirchhoff-Love* plate theory, the curvature κ_{xy} can also be derived from the bending surface (Equation (8.3)) (POPOV 1970).

$$\kappa_{xy} = -w'' = -\frac{\partial^2 w}{\partial x \partial y} = -\frac{m_{xy}}{(1-\nu)K} dx dy \frac{1}{\partial x \partial y} = \frac{m_{xy}}{(1-\nu)K} \quad (8.3)$$

By transferring the plate stiffness to a fictitious girder grid model, the relationship between torsional stiffness, torsional moment, and the bending surface may be clarified (Figure 8.1) (POPOV 1970). In the following, the term “torsional stiffness” (torsion only) is defined by the deformation w , achieved without taking into account deformations other than those caused by the resistance of the torsional stiffness B_{xy} to the loading R (Figure 8.1). The torsional stiffness B_{xy} can be taken from the matrix notation (D_{66}) of the *ABD-E* stiffness matrix of the CLT or DLT element, multiplied by a factor 2 (SCHÜRMAN 2007) (Equation (8.4)).

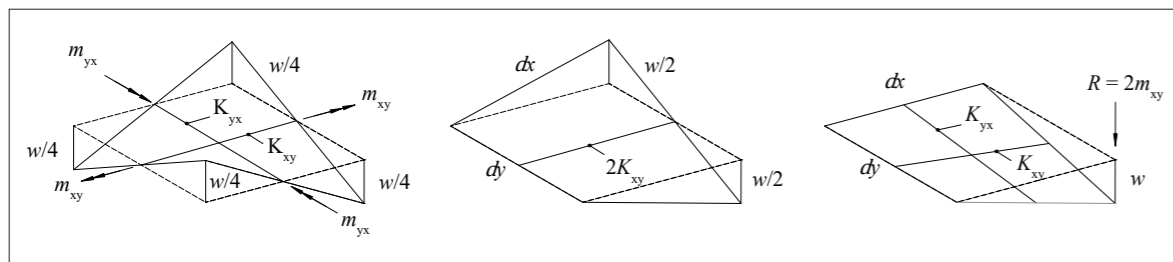


Fig. 8.1: Girder grid model of an infinitesimal plate element under biaxial bending, according to (POPOV 1970)

$$B_{xy} = (K_{xy} + K_{yx}) = 2K_{xy} = 2D_{66} \quad (8.4)$$

The torsional stiffness that includes bending and shear stiffness components is called “effective torsional stiffness” $B_{xy,eff}$. In order to be able to extrapolate the effective torsional stiffness, deformation components from bending and out-of-plane shear must be taken into account by using the method of consistent deformations (force method). Following the energy theorem, this superposition is expressed in Equation (8.5):

$$\delta_{ij} = \sum \frac{1}{K} \int_0^1 (\delta M_i \cdot M_i) de + \sum \frac{1}{S} \int_0^1 (\delta V_i \cdot V_i) de \quad (8.5)$$

Figure 8.2 shows an extended girder grid model. Here, in addition to torsional stiffness, shear and bending stiffnesses are assigned to the girders with the width dx/dy . Following the girder grid model in Figure 8.2, the following energy theorem results in (Equation 8.6):

$$w\delta_{ij} = \int_0^1 \frac{\delta m_{xy} \cdot m_{xy}}{2K_{xy}} dx + \int_0^1 \frac{\delta m_x \cdot m_x}{B_x} dx + \int_0^1 \frac{\delta m_y \cdot m_y}{B_y} dy + \int_0^1 \frac{\delta V_x \cdot V_x}{S_{xz}} dx + \int_0^1 \frac{\delta V_y \cdot V_y}{S_{yz}} dy \quad (8.6)$$

The shear stiffnesses S_{xz} and S_{yz} follow the analytical approaches described in Chapter 6. The bending stiffnesses B_x and B_y follow the respective entries of the *ADE-E* matrix (D_{11} and D_{22}). As previously discussed and shown in Equation (8.4), entry D_{66} in the stiffness matrix of the laminate represents half of the torsional stiffness B_{xy} of the plate elements.

Following the force method and considering the superposition of the distribution of internal forces gained by the virtual and actual stress resultants δm_i and m_i the factors $1/3$ result within Equation (8.7). The virtual displacement $w\delta_{ij}$ is replaced by the relationship between the torsional stiffness and the loading according to Figure 8.1. Therefore, the equilibrium in Equation (8.7) applies to the total deformation w of the element, taking into account the out-of-plane shear deformations and deformations caused by uniaxial and biaxial bending, resulting in the effective torsional stiffness $B_{xy,eff}$.

$$\frac{F \cdot dx \cdot dy}{B_{xy,eff}} = \frac{F \cdot dx \cdot \bar{1} \cdot dy}{2D_{66}} + \frac{1 \cdot F/2 \cdot dx \cdot \bar{1} \cdot dx}{3 D_{22}} + \frac{1 \cdot F/2 \cdot dy \cdot \bar{1} \cdot dy}{3 D_{11}} + \frac{F/2 \cdot \bar{1}}{E_{55}} + \frac{F/2 \cdot \bar{1}}{E_{44}} \quad (8.7)$$

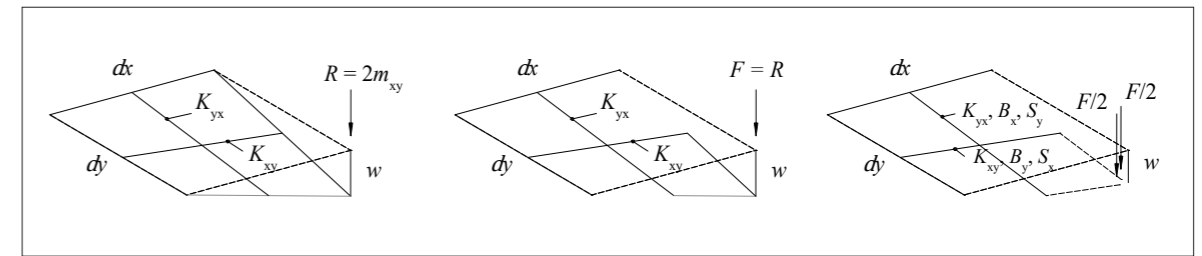


Fig. 8.2: Extended girder grid model of an infinitesimal plate element taking into account bending and shear deformations (Arnold et al. 2022a)

Consequently, the effective torsional stiffness is calculated in accordance to Equation (8.8).

$$\frac{1}{|B_{xy,eff}|} = \frac{1}{|B_{xy}|} + \frac{1}{6|B_x|} + \frac{1}{6|B_y|} + \frac{1}{2|S_{xz}| \cdot dx} + \frac{1}{2|S_{yz}| \cdot dx} \quad (8.8)$$

For the deformations of the CLT and DLT elements under a single point-load F on one corner (torsion), the following approaches apply to the theories according to *Kirchhoff-Love* (Equation (8.9)) and *Reissner-Mindlin* (Equation (8.10)).

$$w_{K-L} = \frac{F \cdot dx dy}{2|D_{66}|} \quad (8.9)$$

$$w_{R-M} = \frac{F \cdot dx dy}{2|D_{66}|} + \frac{F \cdot dx^2}{6|D_{22}|} + \frac{F \cdot dy^2}{6|D_{11}|} + \frac{F}{2|E_{55}|} + \frac{F}{2|E_{44}|} \quad (8.10)$$

8.1.2 Analytical solution

Table 8.1 compares the percentage increases in torsional stiffness of the series with a diagonal layer arrangement, to the series of the same thickness with an orthogonal arrangement of the layers following Equation (8.4).

In addition, Figure 8.3 compares the torsional stiffness values B_{xy} (Equation (8.4)) and the effective torsional stiffness values $B_{xy,eff}$ (Equation (8.8)) for the CLT and DLT series with layer thicknesses $t_1 = 20$ mm and $t_1 = 40$ mm. Within $B_{xy,eff}$ the shear stiffness is implemented according to the laminate theory using shear correction coefficients (dark grey) (see Chapters 5 and 6). As it is for effective bending stiffness values, effective torsional stiffness values according to Equation (8.8) are always dependent on the dimensions of the selected equivalent static system (plate element dx/dy). Following the comparison within Figure 8.3, the dimension of the equivalent plate are chosen to $dx = dy = 1.0$ m. These dimensions are in reference to the later experimental and numerical investigations (Chapters 8.2 and 8.3).

Compared to the 5-layered CLT series O1 with an overall thickness of $t = 100$ mm, the torsional stiffness B_{xy} of DLT±45° series D3 can be increased by 63.5 %, for the DLT±30° series D4 by 47.8 %. The approximate same ratio of increase in stiffness can be determined by comparing the CLT and DLT series with a layer thickness of 40 mm and an overall thickness of $t = 200$ mm. Compared to the CLT series O5, the torsional stiffness of DLT±45° series D5 can be increased by 57.8 %, for DLT±30° series D6 by 43.5 %.

Following the plate theory according to *Reissner-Mindlin*, ($dx = dy = 1.0$ m) and taking into account the bending stiffness values and the out-of-plane shear stiffness values, the effective torsional stiffness $B_{xy,eff}$ of DLT±45° series D3 is increased by 31.4 % compared to the 5-layered CLT series O1 with an overall thickness of $t = 100$ mm. The effective torsional

stiffness $B_{xy,eff}$ of DLT±30° series D4 is increased by 6.9 % compared to CLT series O1. The increase in effective torsional stiffness by rotation of the respective layers is significantly lower than the increase in pure torsional stiffness. This trend appears to be quite similar for the comparison of the effective torsional stiffness of the O5 series with the D5 (+30.1 %) and D6 (+6.5 %) series.

Tab. 8.1: Percentage increase of the torsional stiffness due to diagonal layer arrangements

thickness	$t = 100$ mm			$t = 200$ mm		
series type	O1 CLT	D3 DLT±45	D4 DLT±30°	O5 CLT	D5 DLT±45	D6 DLT±30°
B_{xy} [MNm ² /m]	0.12	0.19	0.17	0.920	1.50	1.36
rate [%]	(=100 %)	+63.5	+47.8	(=100 %)	+57.8	+43.5

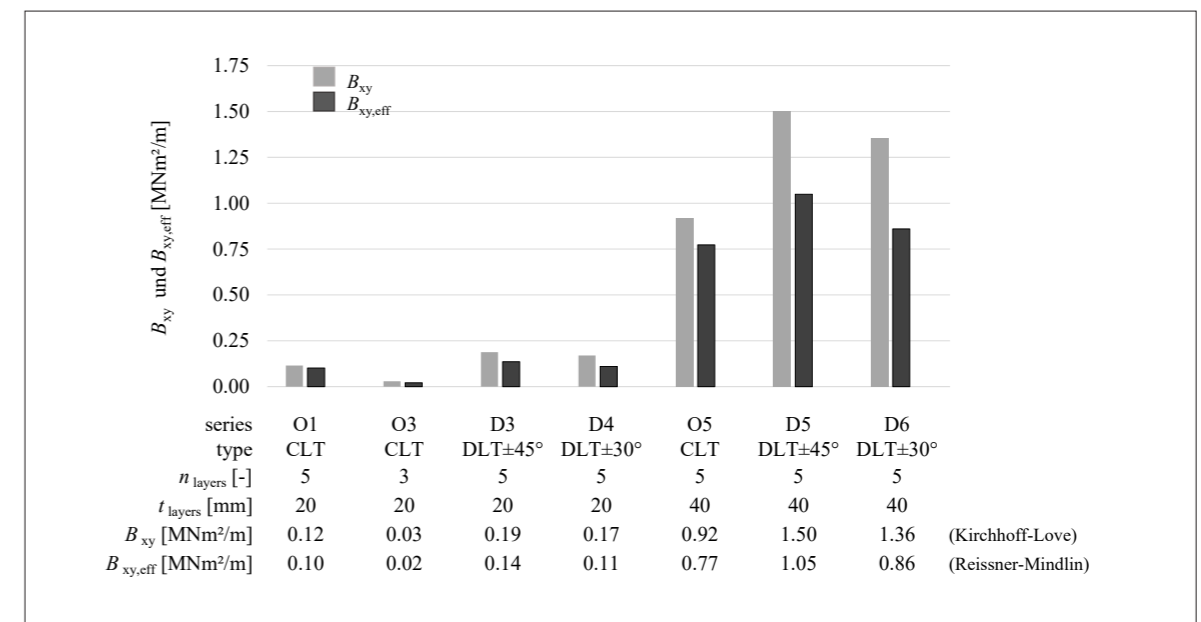


Fig. 8.3: Torsional stiffness of the CLT and DLT elements following the analytical solution ($dx = dy = 1.0$ m)

In addition to the bar charts presented in Figure 8.3, a parameter study using analytical methods is carried out by varying the orientation (arrangement) of the second and fourth layer, so as to determine the torsional stiffness values (Equation (8.4)) and the effective torsional stiffness values (Equation (8.8)) in global x and y direction for $dx = dy = 1.0$ m. The layer thickness is chosen as a constant at $t_i = 40$ mm. The layers are again rotated in opposite directions in steps of 15° , up to the limits of 0° and 90° (see also Figure 6.4).

Figure 8.4 shows the torsional stiffness and effective torsional stiffness in global x and y direction in steps of 15° . The graphical representation highlights the change of the stiffness values against the respective boundary values. The layups of the boundary values $[0^\circ, 0^\circ, 90^\circ, 0^\circ, 0^\circ]_s$ and $[0^\circ, 90^\circ, 90^\circ, 90^\circ, 0^\circ]_s$ provide the same torsional stiffness values B_{xy} , as the reference value of CLT $[0^\circ, 90^\circ, 0^\circ, 90^\circ, 0^\circ]_s$. This follows the laminate theory. On the other hand, the effective bending stiffness values of the extremes ($[0^\circ, 0^\circ, 90^\circ, 0^\circ, 0^\circ]_s$ and $[0^\circ, 90^\circ, 90^\circ, 90^\circ, 0^\circ]_s$) differ, hence the bending and shear stiffness values differ. Same holds true for layer orientations under 30° and 60° — B_{xy} is the same, but the bending and shear stiffness values differ and so do the effective bending stiffness values.

According to Figure 8.4 the maximum torsional stiffness is achieved for the DLT $\pm 45^\circ$ element. The distribution of the torsional stiffness as a function of the layer arrangement appears to be symmetrical. The effective torsional stiffness turns into extreme values for DLT $\pm 60^\circ$ and DLT $\pm 15^\circ$. Additional parameter studies on the torsional stiffness values as a function of the layer thickness can be found at (ARNOLD ET AL. 2022a).

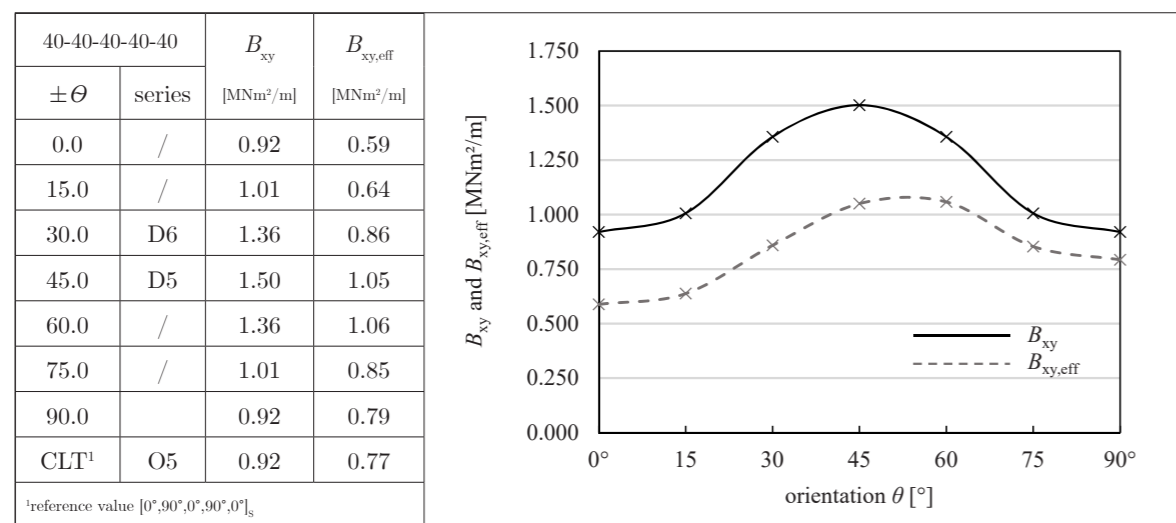


Fig. 8.4: Torsional stiffness and effective torsional stiffness of 5-layered CLT and DLT elements as a function of the layer arrangement θ ($dx = dy = 1.0$ m)

8.2 Experimental determination of the torsional stiffness

8.2.1 Test setup

After the analytical studies on the torsional stiffness properties of CLT and DLT, specimens with a side length $l = 1200$ mm are twisted during biaxial bending tests. Here, the aim is to determine the effective torsional stiffness $B_{xy,eff}$ of the various specimens from the deformation of the elements under an external point-load (Figure 8.5). The chosen test setup mirrors the girder grid model within Figure 8.1 and was proposed in a similar form before by (MESTEK 2011) and (LOEBUS AND WINTER 2017). The mechanical testing is important to confirm the theoretical investigations and to observe the failure mechanisms.

The point-load, directed vertically downward, was applied to the free corner of the specimens by a hydraulic cylinder. The load application point as well as the supports were realized by steel plates (120/120/12 mm). Each of them articulated and offset inwards by 100 mm from the free edges of the specimens. No reinforcement for compression stresses perpendicular to grain in form of self-tapping screws was applied.

The applied loading “force_1” (point-load F) as well as the reaction force on the opposite support “force_2” were measured by force transducers. Deflection “def_1” (deformation w in z direction) is measured using a rope extensometer, which was attached at the opposite side of the load introduction point at the bottom of the test specimens. In addition, the change in

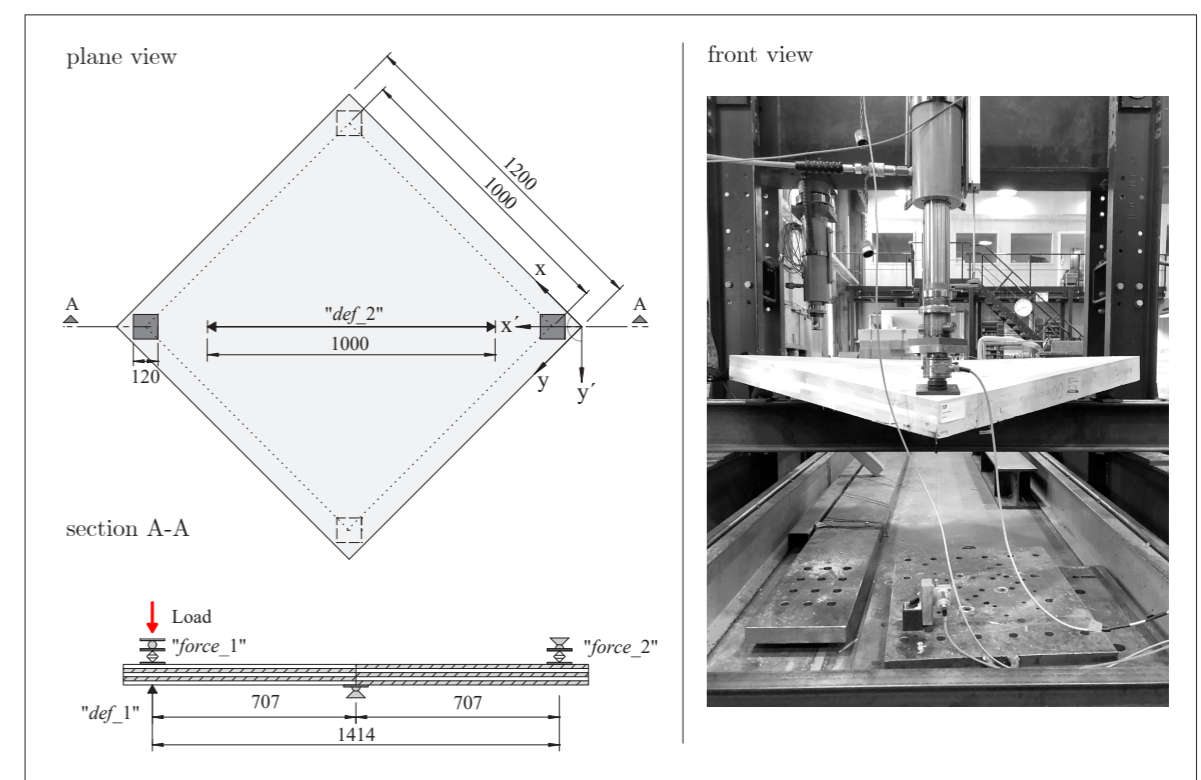


Fig. 8.5: Test setup of the biaxial bending tests

the curvature κ_{xy} was measured determining the arc length “def_2” over 1000 mm by means of a second rope extensometer on the upper side of the specimens. The mechanical testing was carried out in a deformation-controlled manner. In other words, each test specimen was loaded until a unit-deformation w (def_1) of 100 mm (geometrical limit due to load introduction) was reached. All specimens were loaded with a constant feed rate of about 0.30 mm/s. The corresponding forces F (“force_1”=“force_2”) were measured as a function of the time.

Prior to the start of the tests, the moisture content of each specimen was determined by an electrical resistance moisture meter at a depth of approximately 15 mm. Five measurements were taken on each specimen. The mean value u_{mean} of the initial moisture content was 11.2 % (COV 7.6). The effective torsional stiffness for each specimen is calculated according to EN 408 [15] within the linear elastic range $0.1F_{\text{max}}$ ($0.1F_{w100}$) and $0.4F_{\text{max}}$ ($0.4F_{w100}$) using linear regression. Therefore, Equation (8.9) is converted to B_{xy} (Equation (8.11)). As mentioned before, the torsional stiffnesses determined experimentally are effective torsional stiffnesses $B_{xy,\text{eff,exp}}$ since the transversal shear deformations are included in the total deformation w [mm] measured by the rope extensometer. For all specimens that do not reach a failure load (O1, D3, and D4 series), the corresponding load F_{w100} to reach a deformation of 100 mm is used instead of F_{max} to determine the effective torsional stiffness (Equation (8.11)).

$$B_{xy,\text{eff,exp}} = \frac{F \cdot dx \cdot dy}{2w} = \frac{(0.4F_{\text{max}} - 0.1F_{\text{max}}) \cdot l^2}{2(w_{0.4F_{\text{max}}} - w_{0.1F_{\text{max}}})} = \frac{1}{2} \cdot m \cdot l^2 \quad (8.11)$$

8.2.2 Results of the mechanical testing

Figure 8.6 displays the load-deformation diagrams for the 5-layered CLT and DLT series with an overall thickness of $t=100$ mm (upper chart) and $t=200$ mm (lower chart). For the CLT elements of thickness $t=100$ mm (O1 series), no failure mechanism could be identified, as the failure mechanism (large plastic deformation fraction) couldn't be observed when the unit-deformation of $w=100$ mm was reached. The load-deformation curves confirm this observation (Figure 8.6). The flattening of the curves can be explained by the occurrence of single cracks in the cross-layers (rolling shear failure). A cracking noise (tearing of individual wood fibers) was audible from a deformation $w=40$ mm onward. After the test, the specimens of series O1 did not fully return to their original position ($w_{\text{unloaded}} \approx 2.3$ mm). The 3-layered series O3 ($t=60$ mm) did not show any cracks and completely returned to its original condition after unloading (Table 8.2).

The CLT elements with a thickness of $t=200$ mm (O5 series) show clear rolling shear failure in the cross-layers when a deformation w of approx. 60 mm was reached. However, neither brittle failure nor sudden loss of force occurred (Figure 8.6, Table 8.2). After the test, the specimens of O5 series similarly did not fully return to their original position ($w_{\text{unloaded}} \approx 2.4$ mm) (Table 8.2).

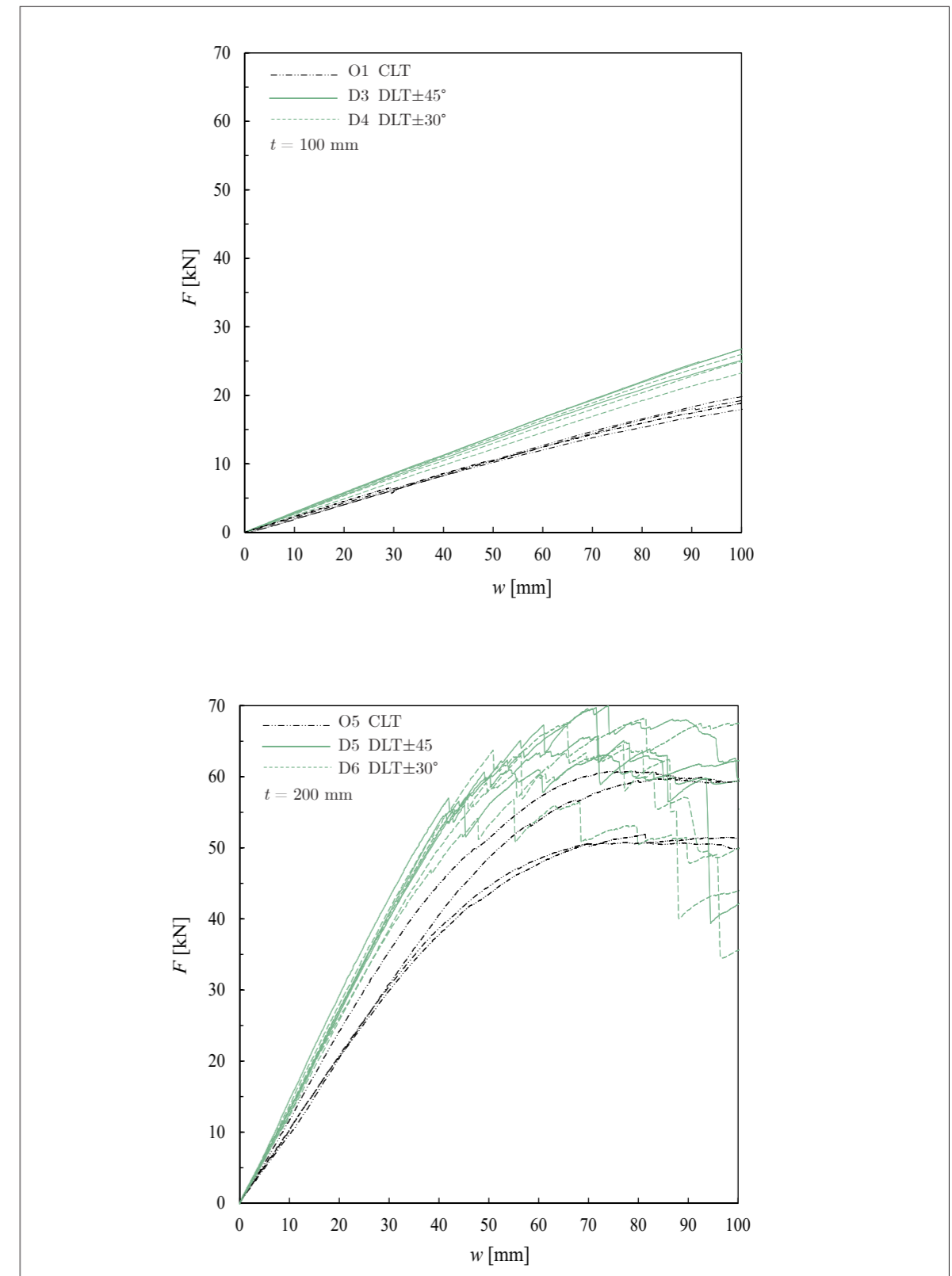
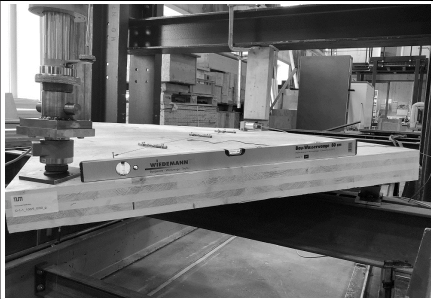
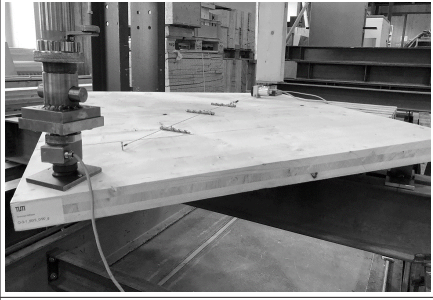
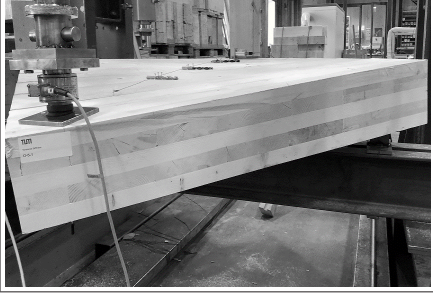


Fig. 8.6: Load-deformation diagrams of the CLT and DLT specimens under biaxial bending


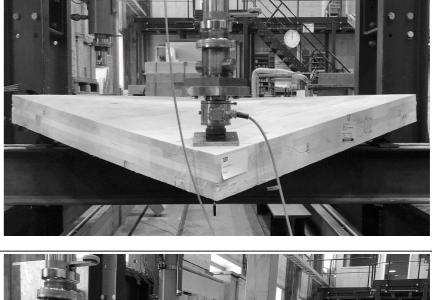

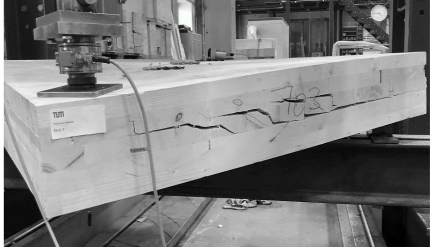
Tab. 8.2: Failure mechanisms of the CLT series

series	layup [mm] / [n°]	deformation figure and crack pattern at $w = 100$ mm	
		observations	side view
O1	CLT (20-20-20-20-20) [0;90;0;90;90] _s	<ul style="list-style-type: none"> » plastic deformations hardly detectable » isolated rolling shear failures in the cross-layers » noticeable cracking noise from a deformation $w = 40$ mm onwards 	
O3	CLT (20-20-20) [0;90;0] _s	<ul style="list-style-type: none"> » no plastic deformations detected » no rolling shear failures detected » no noticeable cracking noise 	
O5	CLT (40-40-40-40-40) [0;90;0;90;90] _s	<ul style="list-style-type: none"> » plastic deformations hardly detectable » rolling shear failures in the cross-layers from a deformation $w = 60$ mm on » noticeable cracking noise from a deformation of $w = 40$ mm onwards 	

The DLT elements with a thickness of $t = 100$ mm (D3 and D4 series) show a very similar deformation behavior as the CLT elements of the same thickness. Until the maximum deformation of $w = 100$ mm was reached, only isolated fine cracks were visible, which indicated the onset of rolling shear failures in the cross-layers. However, a sudden and extensive loss of load carrying capacity did not occur (shear failure of complete layer).

Complicated failure mechanisms occur when reaching the ULS of DLT elements with a thickness of $t = 200$ mm (D5 and D6 series). An extensive loss of the load carrying capacity occurred in all DLT elements ($t = 200$ mm) prior to reaching a deformation of $w = 40$ mm, due to multiple failure mechanisms of rolling shear in combination with tension perpendicular to grain (Figure 8.6, Table 8.3).

Tab. 8.3: Failure mechanisms of the DLT series

series	layup [mm] / [n°]	deformation figure and crack pattern at $w = 100$ mm	
		observations	front view / side view
D3	DLT±45° (20-20-20-20-20) [0;45;90;-45;0] _s	<ul style="list-style-type: none"> » plastic deformations hardly detectable » isolated rolling shear failures in the cross-layers » isolated combined rolling shear and longitudinal shear failures » audible and visible cracking from a deformation of $w = 40$ mm onwards 	
D4	DLT±30° (40-40-40-40-40) [0;30;90;-30;0] _s	<ul style="list-style-type: none"> » plastic deformations hardly detectable » isolated rolling shear failures in the cross-layers » noticeable cracking noise from a deformation of $w = 40$ mm onwards 	
D5	DLT±45° (40-40-40-40-40) [0;45;90;-45;0] _s	<ul style="list-style-type: none"> » rolling shear failures with tension perpendicular to grain » clearly audible cracking from a deformation of $w = 35$ mm onwards » extensive load drop (complete failure) before reaching the unit-deformation » exceeding the permissible compression stress perpendicular to grain at the load introduction plate 	
D6	DLT±30° (40-40-40-40-40) [0;30;90;-30;0] _s	<ul style="list-style-type: none"> » rolling shear failures with tension perpendicular to grain » clearly audible cracking from a deformation of $w = 35$ mm onwards » extensive load drop (complete failure) before reaching the unit-deformation 	

Complementary to Figure 8.6, the respective loads (F_{\max}), the respective deformations, and a evaluation within the linear elastic range of series with $t = 100$ mm are provided in Table 8.4. Table 8.5 lists the loads (maximum loads and loads at initial failure), the respective deformations as well as a evaluation within the linear elastic range of series with $t = 200$ mm.

Tab. 8.4: Evaluation of the biaxial bending tests of the CLT and DLT specimens with $t = 100$ mm

	$^1F_{\max}$ [kN]	$0.4F_{\max}$ [kN]	$0.1F_{\max}$ [kN]	$w_{0.4F_{\max}}$ [mm]	$w_{0.1F_{\max}}$ [mm]	slope m [$^{\circ}$]	R^2 [$^{\circ}$]	$B_{xy,eff,exp}$ [MN/m 2]
O1-1	18.87	² 7.56	1.87	² 27.92	8.18	0.22	1.00	0.16
O1-2	17.96	7.18	1.80	34.67	9.67	0.22	1.00	0.15
O1-3	19.80	7.92	1.98	38.29	10.27	0.21	1.00	0.15
O1-4	19.27	7.71	1.93	36.38	9.12	0.21	1.00	0.15
D3-1	26.78	11.61	2.68	41.35	9.34	0.28	1.00	0.20
D3-2	25.11	10.04	2.52	36.90	9.21	0.27	1.00	0.20
D3-3	26.75	10.07	2.68	35.30	8.93	0.28	1.00	0.20
D4-1	25.99	10.40	2.60	37.49	9.21	0.28	1.00	0.20
D4-2	23.25	9.32	2.33	37.92	9.57	0.25	1.00	0.18
D4-3	24.99	9.99	2.50	38.11	9.35	0.26	1.00	0.19

¹Load for achieving the unit-deformation in z direction " $def_{-1} = w = 100$ mm
²Values for $0.3 F_{w100}$ due to a initial loss in force at O1-1 specimen at $w = 30$ mm (see Figure 8.6)

Tab. 8.5: Evaluation of the biaxial bending tests of the CLT and DLT specimens with $t = 200$ mm

	$^2F_{\max}$ [kN]	$0.4F_{\max}$ [kN]	$0.1F_{\max}$ [kN]	$w_{0.4F_{\max}}$ [mm]	$w_{0.1F_{\max}}$ [mm]	slope m [$^{\circ}$]	R^2 [$^{\circ}$]	$B_{xy,eff,exp}$ [MN/m 2]
O5-1	¹ 60.72	24.29	6.07	20.13	5.35	1.247	1.00	0.90
O5-2	¹ 50.63	20.25	5.06	19.48	4.84	1.051	1.00	0.76
O5-3	¹ 51.77	20.72	5.13	20.18	4.84	1.034	1.00	0.75
O5-4	¹ 59.86	23.94	6.00	23.24	6.14	1.061	1.00	0.76
D5-1	² 60.67	24.23	6.12	18.07	4.64	1.351	1.00	0.97
D5-2	² 54.80	21.95	5.49	16.34	4.29	1.364	1.00	0.98
D5-3	² 55.16	22.11	5.52	16.60	4.48	1.361	1.00	0.98
D5-4	² 57.00	22.82	5.71	15.58	4.27	1.512	1.00	1.09
D6-1	² 55.43	22.17	5.56	16.25	4.17	1.371	1.00	0.99
D6-2	² 60.40	24.17	6.03	18.82	4.91	1.309	1.00	0.94
D6-3	² 63.75	25.50	6.38	18.16	4.65	1.430	1.00	1.02
D6-4	² 54.17	21.68	5.41	16.59	4.20	1.321	1.00	0.95

¹Maximum value
²Load at initial failure

The torsional stiffness for each series calculated by Equation (8.11) is highlighted in the following box-plot diagram (Figure 8.7).

Compared to the 5-layered CLT series O1 with an overall thickness of $t = 100$ mm, the effective torsional stiffness $B_{xy,eff,exp}$ of the DLT $\pm 45^\circ$ series D3 can be increased by 28.4 %, for the DLT $\pm 30^\circ$ series D4 by 21.9 % (mean values). Following the results of the mechanical testing, nearly the same ratio of stiffness increase can be determined by comparing the CLT and DLT series with a layer thickness of 40 mm and an overall thickness of $t = 200$ mm. Compared to the CLT series O5, the effective torsional stiffness of the DLT $\pm 45^\circ$ series D5 can be increased by 27.1 %, for the DLT $\pm 30^\circ$ series D6 by 23.0 % (mean values).

The comparison of the experimentally determined effective torsional stiffnesses $B_{xy,eff,exp}$ and the torsional stiffnesses previously derived analytically—according to the plate theories of *Kirchhoff-Love* (B_{xy}) and *Reissner-Mindlin* ($B_{xy,eff}$)—provide good correlation (see Figure 8.3 and 8.10).

After introducing additional reference values using numerical models, Table 8.6 and Figure 8.10 in the following Chapter 8.3 will summarize and compare the results of the investigations on the torsional stiffness following the analytical, experimental, and numerical approaches by means of bar charts in order to provide better comparability of the results.

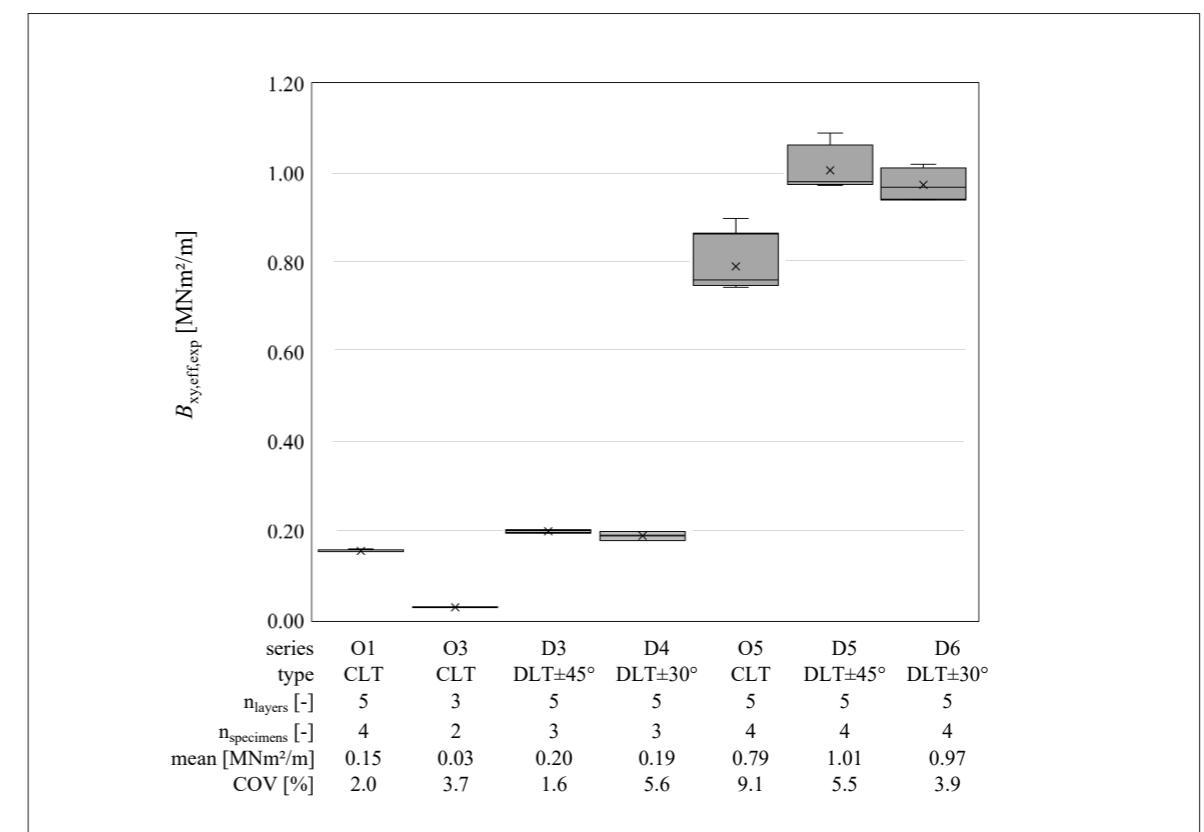


Fig. 8.7: Torsional Stiffness of the orthogonal and diagonal laminated series (CLT and DLT) given from the mechanical testing

8.3 Investigations on the effective torsional stiffness using numerical models

8.3.1 General information and modelling approach

The mechanical testing was accompanied by numerical modeling, using parametric 3D FE volume models (Ansys, Version 2021.R1). The modelling of the CLT and DLT specimens was once again carried out with Solid186 elements with 20 nodes each. The contact between the layers was considered to be rigid and thus was defined as type “composite”. No contact was defined between the narrow sides of the single boards. The mesh was generated automatically. The size of the mesh was set to 10 mm. Further parameters for the numerical models are summarized in tabular manner in Appendix A4.

The bearing as well as the application of the displacement was carried out using "external displacements", related to the surface of the cylindrical elevation of the load plate. In order to model a support free of constraint, one fixed support was defined. The opposite bearing point was fixed in the global z direction only and was free in the global x and y direction. The material parameters according to Table 4.9 (T14; ETA20/0023) and the *Poisson's* ratios according to (HALÁSZ AND SCHEER 1996) were applied. The material parameters for structural steel were used ($E = 200.000$ MPa, $G = 76.923$ MPa, $\nu = 0.3$).

8.3.2 Determination of the torsional stiffness and comparison of the results

The determination of the effective torsional stiffness from the numerical FE model ($B_{xy,eff,num}$) was deformation-controlled. To display the deformations, so-called deformation paths were defined in the model. By applying a deformation "def_1" to the models, the corresponding force coordinate in the z direction was obtained (Figure 8.8). The effective torsional stiffness was determined using Equation (8.1), inserting the corresponding force given from the numerical model.

In addition, the mesh fineness (element size) was alternated from 20 mm to 5 mm for exemplary series of each thickness. No remarkable influence of the mesh fineness on the

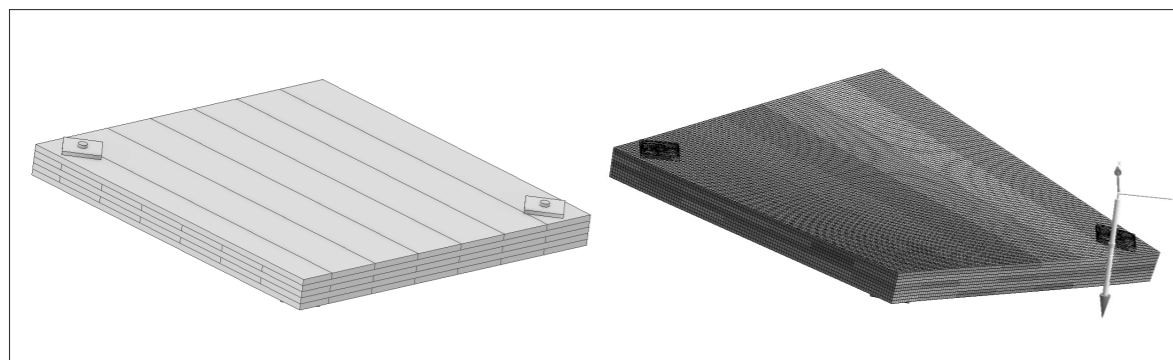


Fig. 8.8: Exemplary 3D model of O1 series (Inventor) and FE volume model of O1 series under biaxial bending (Ansys)

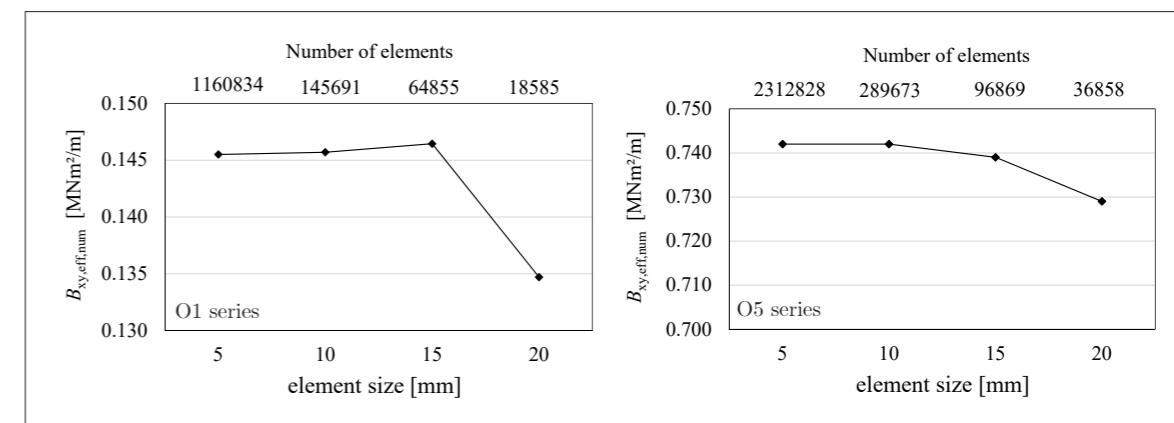


Fig. 8.9: Exemplary mesh-convergence-diagrams of O1 series (left) and O5 series (right)

results given within the examined parameters was observed. Figure 8.9 exemplifies two mesh-convergence-diagrams, one for the O1 series ($t = 100$ mm) and one for the O5 series ($t = 200$ mm).

Table 8.6 gives the results of the numerical studies and compares the results of the investigations on the torsional stiffness following the different approaches. The effective torsional stiffness values that were determined from the numerical models ($B_{xy,eff,num}$) are almost the same as the values gained in the experiments. Thus, the model can be assumed to be validated and used for further parameter studies. The adjustment of a load path of the arc length "def_2" serves as an additional validation of the numerical models in comparison with the results of the mechanical testing (Table 8.6). The numerical models were loaded in analogy to the mechanical testing within the linear elastic range until the corresponding deformations "def_1" were reached (see Table 8.4 and Table 8.5).

Tab. 8.6: Evaluation of the mechanical testing of the CLT and DLT specimens with $t = 200$ mm

layup		analytical approach		mechanical testing ¹			numerical model		
series	t [mm]	B_{xy} [MN/m ²]	$B_{xy,eff}$ [MN/m ²]	def_1 ² [mm]	def_2 [mm]	$B_{xy,eff,exp}$ [MN/m ²]	def_1 [mm]	def_2 [mm]	$B_{xy,eff,num}$ [MN/m ²]
O1	100	0.12	0.10	36.45	1.94	0.16	36.45	2.02	0.15
O3	60	0.03	0.03	39.05	1.45	0.03	39.05	1.31	0.03
O5	200	0.92	0.77	20.76	1.83	0.79	20.76	2.08	0.74
D3	100	0.19	0.13	37.85	2.06	0.20	37.85	1.84	0.20
D4	100	0.17	0.11	37.84	1.86	0.19	37.84	2.19	0.19
D5	200	1.50	1.01	16.65	1.32	1.01	16.65	1.69	1.00
D6	200	1.36	0.82	17.45	1.23	0.97	17.45	1.76	0.94

¹mean values from the experimental investigations
²values "def_1" = $w_{0.4 F_{max}}$ (see Table 8.4 and Table 8.5)

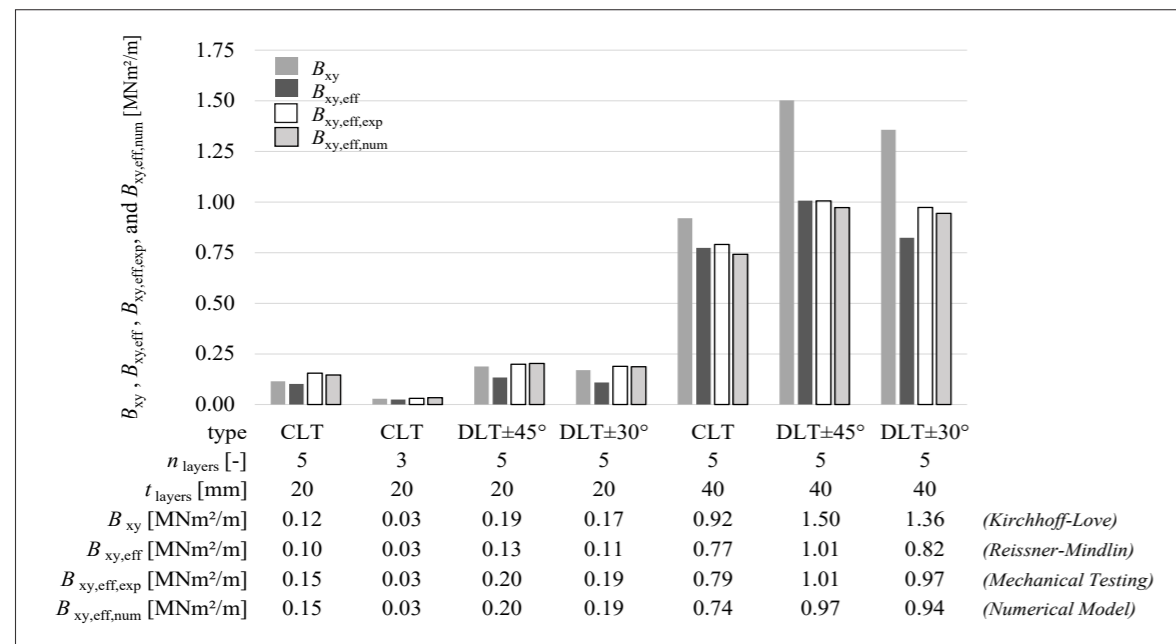


Fig. 8.10: Torsional stiffness of the CLT and DLT elements following the analytical, experimental, and numerical investigations

Table 8.6 and Figure 8.10 summarize all torsional stiffnesses determined for the series investigated. It becomes clear that, for thin plates ($1/10 > t/dx > 1/50$) the torsional stiffness according to *Kirchhoff-Love* makes for a good correlation to the experimentally determined effective torsional stiffness. For thick plates ($1/5 > t/dx > 1/10$), the calculated torsional shear stiffness taking into account transversal shear deformations, provides good correlations (*Reissner-Mindlin*). When calculating effective torsional stiffness values with the help of girder grid models, the shear stiffness values should be taken into account according to the laminate theory using transformed engineering constants.

In addition, the influence of the board width and edge-gluing on the effective torsional stiffness is determined with the help of numerical models. Again, 5-layered DLT elements with a layer thickness of 20 mm were considered. For a DLT±30° and a DLT±45° of the same dimension, the widths of the lamellas (board widths) were varied from $w = 80$ mm to $w = 240$ mm, at intervals of $\Delta w = 40$ mm.

Figure 8.11, left, presents the respective values of the effective torsional stiffness. On the right-hand side, a graphical representation of the change in the effective torsional stiffness as a function of the board width is given. Differing from the results by (SILLY 2010), this parameter study shows that the board width has a noticeable influence on the effective torsional stiffness only at widths of less than $w = 160$ mm. While the factor of $B_{xy,eff,num}$ increases between board widths of $w = 80$ mm and $w = 160$ mm is still 13.7 %, it is only 3.0 % between board widths of $w = 160$ mm and $w = 240$ mm. For board widths greater than $w = 180$ mm, edge-gluing can be assumed. According to the evaluation, this has no further positive effect on the effective torsional stiffness.

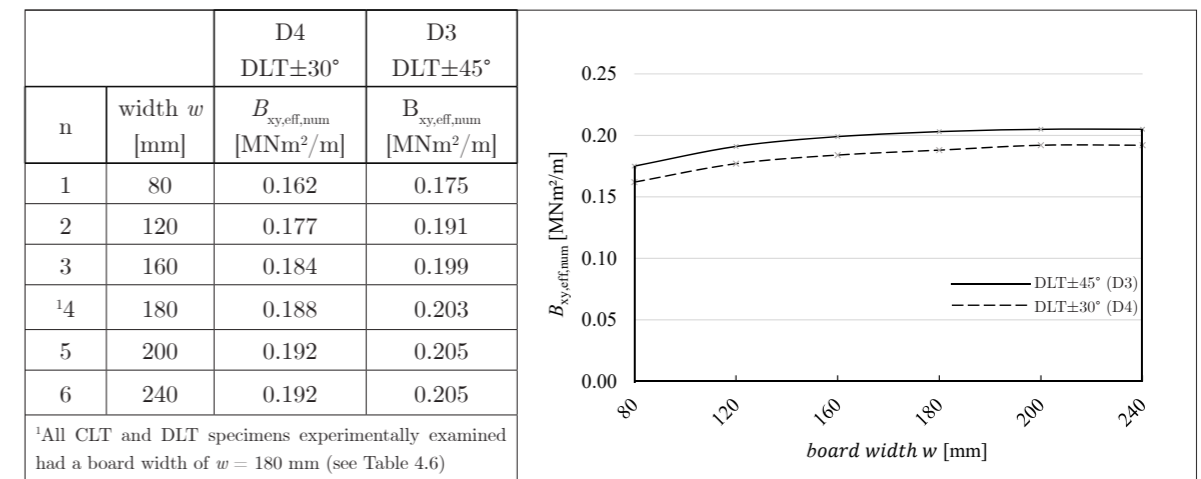


Fig. 8.11: Parameter set for the different board widths w of a 5-layered CLT and DLT ($t=100$ mm) ($dx=dy=1.0$ m)

All in all, the investigations on the torsional stiffness values, comparing the analytical results with experimental and numerical approaches, seem to provide sufficient results.

Before investigations on the in-plane shear stiffness properties of DLT are carried out (Chapter 9), Chapter 8.4 aims to give a statement on the long-term deformation behavior of DLT plate elements undergoing biaxial bending.

8.4 Long-term deformation under biaxial bending

8.4.1 General information

This Chapter gives an outlook on the predicted long-term deformation behavior of DLT plate elements undergoing biaxial bending, in comparison to CLT plate elements.

For this purpose, long-term deformation values are calculated for the CLT and DLT series, which were previously as part of the experimental investigations (O1, D3, and D4 as well as O5, D5, and D6, and D1). The deformations are calculated for a plate under biaxial bending using the static system according to the experimental investigations on the torsional stiffness within Chapter 8.3 (Figure 8.5). Instead of linear elastic material parameters, viscoelastic material parameters are used for the analytical solution—previously introduced in Chapter 4.2.3. It is therefore useful to briefly return to Chapter 4.2.3 (Viscoelastic material properties of timber):

Table 4.5 summarizes deformation coefficient taking into account the different time phases of the long-term deformation behavior of timber ($t_0 = 1$ min delay after loading, $t_{\text{fin}} = 11$ a = end of primary phase (end of creep deformations), $t_{\infty} > 50$ a = infinite time state (nearly all stresses redistributed into longitudinal layers))—please see Chapter 4.2.3. The deformation coefficients following Table 4.5 influence the moduli of elasticity and shear moduli of the respective UD layers (see Equations (4.16) and (4.17)). In order to derive long-term stiffness properties, the principal engineering constants and the deformation coefficients are inserted into the stiffness matrix of the UD layer (Equation (5.10))—for detailed explanations see Chapter 5.2.2 (Implementation of long-term deformation coefficients).

Table 8.8 summarizes the long-term stiffness properties of the series previously investigated experimentally. The stiffness values at t_0 , the stiffness values after the creep phase (t_{fin}), and in the infinite time state (t_{∞}) are provided. The deformation-coefficients are chosen according to Table 8.7, which is an extract from Table 4.5.

Table 8.8 shows, that after the creep phase (t_{fin}), for CLT elements of $t = 100$ mm, the loss in bending stiffness is low compared to the initial stiffness properties (B_x : -17.0 %; B_y : -20.8 %). In contrast, the decrease in torsional stiffness and shear stiffness after the creep phase is eminent (B_{xy} : -78.7 %; S_{xz} : -71.4 %; S_{yz} : -71.4 %). On the other hand, the decrease in the stiffness values of DLT±45° after the creep phase is much lower for B_{xy} , compared to initial values, while the loss in bending stiffness and shear stiffness stays at a comparable

Tab. 8.7: Deformation coefficients chosen for the exemplary long-term deformation analytical analysis

long-term deformation coefficient/ time-phase	k_L	k_T	k_{shear}
t_0	0	0	0
t_{fin}	0.2	1.2	2.5
t_{∞}	0.2	19.0	19.0

Tab. 8.8: Time-dependent stiffness values of the series investigated

	series type		O1 CLT	D3 DLT±45°	D4 DLT±30°	O5 CLT	D5 DLT±45°	D6 DLT±30°	D1 DLT+45°
t_0	B_x [MNm ² /m]	A_{11}	0.74	0.79	0.84	5.90	6.29	6.74	6.35
	B_y [MNm ² /m]	A_{22}	0.22	0.09	0.06	1.73	0.76	0.46	0.70
	B_{xy} [MN/m]	D_{66}	0.12	0.19	0.17	0.92	1.50	1.36	1.50
	S_{xz} [MN/m]	E_{44}	7.96	7.68	9.52	15.92	15.36	19.03	28.08
	S_{yz} [MN/m]	E_{55}	4.89	12.86	10.33	9.78	25.72	20.66	9.94
t_{fin}	B_x [MNm ² /m]	A_{11}	0.61	0.65	0.70	4.90	5.18	5.57	5.23
	B_y [MNm ² /m]	A_{22}	0.17	0.06	0.03	1.37	0.50	0.26	0.45
	B_{xy} [MN/m]	D_{66}	0.03	0.11	0.09	0.26	0.85	0.70	0.85
	S_{xz} [MN/m]	E_{44}	2.32	2.26	2.86	4.64	4.52	5.73	8.31
	S_{yz} [MN/m]	E_{55}	1.34	4.19	3.49	2.68	8.38	6.97	2.91
t_{∞}	B_x [MNm ² /m]	A_{11}	0.61	0.64	0.69	4.87	5.15	5.55	5.21
	B_y [MNm ² /m]	A_{22}	0.16	0.05	0.02	1.29	0.39	0.14	0.42
	B_{xy} [MN/m]	D_{66}	0.01	0.09	0.07	0.05	0.68	0.52	0.68
	S_{xz} [MN/m]	E_{44}	0.41	0.40	0.52	0.82	0.80	1.03	1.47
	S_{yz} [MN/m]	E_{55}	0.22	0.78	0.75	0.45	1.56	1.49	0.50

level to the loss of stiffness of the CLT element (B_x : -18.1 %; B_y : -34.0 %; B_{xy} : -43.6 %, S_{xz} : -71.4; S_{yz} : -71.4 %). This is due to the higher deformation coefficients perpendicular to grain (k_T and k_{shear}), compared to k_L (longitudinal). Approximately the same relationship is valid for CLT and DLT elements of the thickness $t = 200$ mm. Due to the stress redistribution processes from cross to longitudinal layers—see Chapter 4.2.3—the difference in the loss of torsional stiffness between CLT and DLT further increases within the time range towards the infinite state. In case of biaxial bending the diagonal layers of DLT in x' and y' direction, take much more stresses, than layers oriented in x and y direction. Since the inconsistency in the deformation coefficients at t_{fin} , Table 8.9 additionally gives the maximum stiffness values at t_{fin} using $k_L = 0.1$, $k_T = 0.8$, and $k_{\text{shear}} = 2.3$, instead of $k_L = 0.2$, $k_T = 1.2$, and $k_{\text{shear}} = 2.5$.

Tab. 8.9: Maximum stiffness values at t_{fin} of the series investigated, using minimum values k_i

	series type		O1 CLT	D3 DLT±45°	D4 DLT±30°	O5 CLT	D5 DLT±45°	D6 DLT±30°	D1 DLT+45°
t_{fin}	B_x [MNm ² /m]	A_{11}	0.74	0.79	0.84	5.90	6.29	6.74	6.35
	B_y [MNm ² /m]	A_{22}	0.22	0.09	0.06	1.73	0.76	0.46	0.70
	B_{xy} [MN/m]	D_{66}	0.12	0.19	0.17	0.92	1.50	1.36	1.50
	S_{xz} [MN/m]	E_{44}	2.46	2.39	3.03	4.92	4.79	6.07	8.08
	S_{yz} [MN/m]	E_{55}	1.43	4.35	3.59	2.86	8.71	7.17	3.11

8.4.2 Proposal for a test setup

In view of possible experimental investigation on the effects of long-term deformations, a possible test facility is proposed in Figure 8.12. The cuboid test frame ($w/l/h = 1.4/1.4/1.0$ m) could be assembled from a number of individual steel profiles. To make the transport and assembly of the test frame as simple as possible, bolted connections at the nodes provide detachable connections (Figure 8.12 (1)). The test frame should be installed

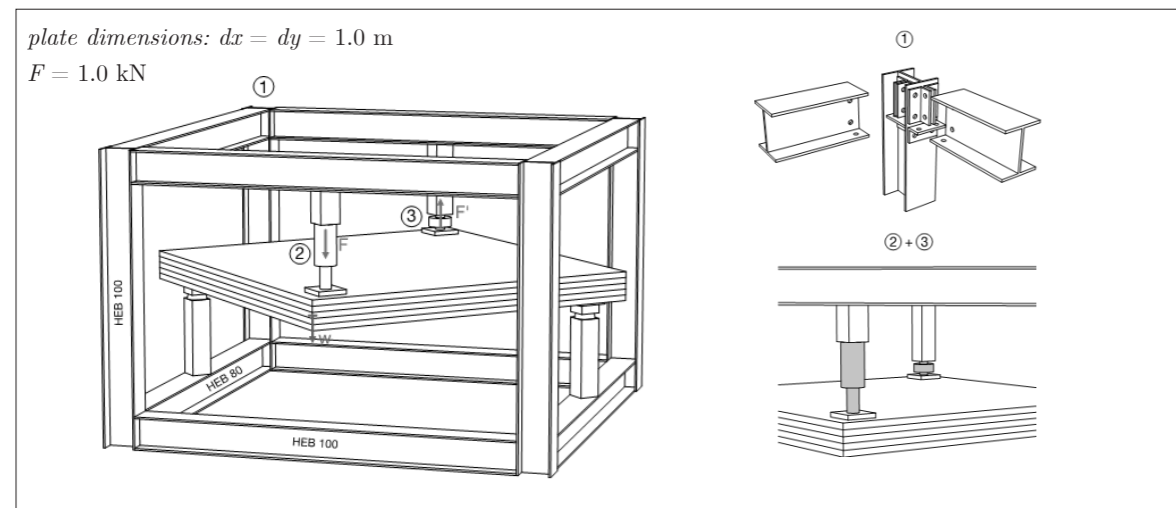


Fig. 8.12: Exemplary test facility for the determination of long-term deformation behavior of CLT and DLT under biaxial bending (VOGEL 2021)

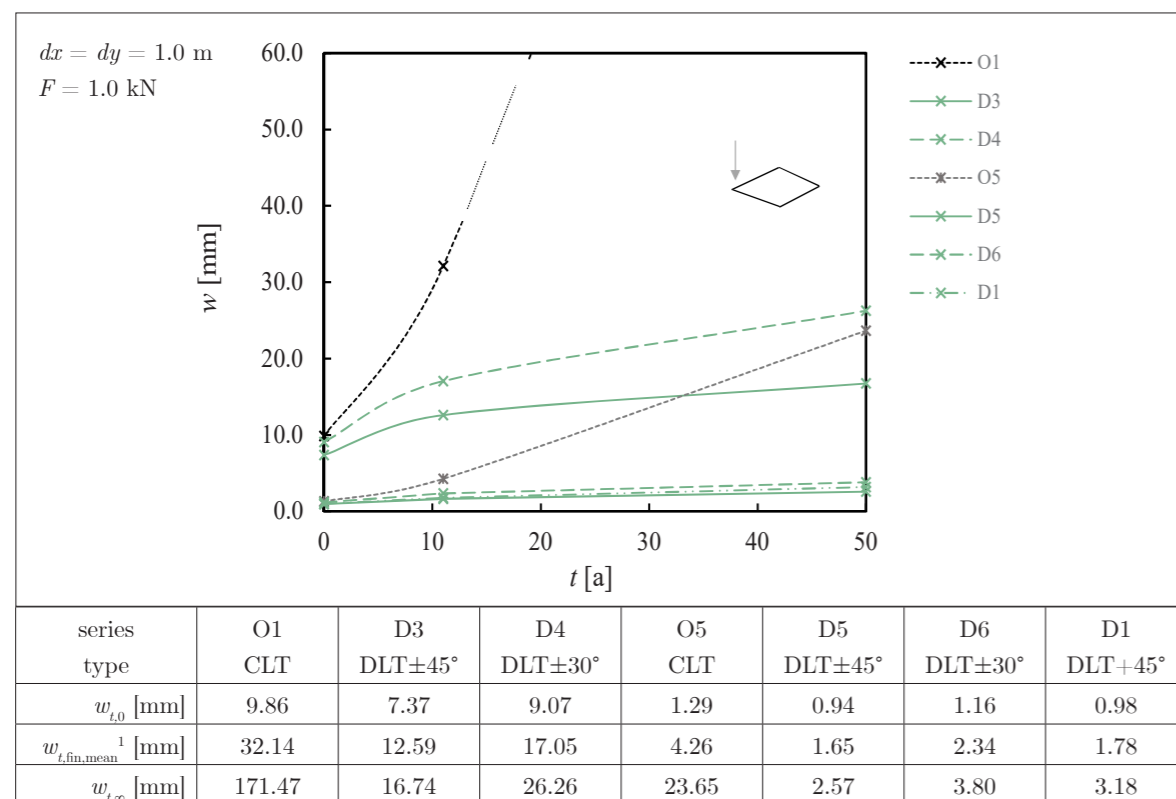


Fig. 8.13: Long-term deformation of all series as a function of the time ($F = 1.0$ kN; $dx = dy = 1.0$ m)

in a climatic chamber providing climatic conditions in accordance to service class 1 (20°C , 65% RH). With the exception of the hydraulic cylinder, the experimental setup within the steel frame corresponds to the one used in the biaxial bending tests (Chapter 8.2). The plate dimensions are chosen to $dx = dy = 1.0$ m and the loading is chosen as constant to 40 % of 2.5 kN/m² ($F = 0.4 \cdot 2.5$ kN/m² · 1.0 m² = 1.0 kN). Since the test may have a test duration of $t > 11$ a, instead of the hydraulic cylinder, a permanent load should be applied by means of a pendent weights ($m = 98,1$ kg) (2). This guarantees a simple and robust test setup. The deformation is measured on the opposing site of the load introduction by means of a laser or a rope extensometer (distance between steel frame and bottom of the test specimen) within the measurement intervals (for example $\Delta t = 2$ weeks). This excludes the risk of measuring long-term deformations of the steel frame or of the timber around the load-application area (perpendicular to grain). The load-level can be cross-checked by the load-cell on the opposing plate corner (3).

Based on the stiffness values according to Table 8.8, Figure 8.13 gives the expected deformations of each series for the proposed long-term test as a function of the time (following the analytical approach within Equation (8.10)). The graphical representation in Figure 8.13 underlines the potential of DLT for plates under biaxial bending regarding long-term deformations. At t_{fin} , the long-term deformation of CLT is on average 59.7 % larger than for DLT $\pm 45^{\circ}$, and 45.7 % larger than for DLT $\pm 30^{\circ}$. Considering load redistribution, at the infinitesimal time phase (> 50 a), the long-term deformation of CLT is on average 84.8 % higher than for DLT $\pm 45^{\circ}$ and by 79.2 % higher than for DLT $\pm 30^{\circ}$. For uniaxial bending, on the other hand, hardly any difference between DLT and CLT is expected following the stiffness values in Table 8.8.

Figure 8.14 additionally compares the expected deformations $w_{fin,min}$ of each series—using the minimum shear deformation coefficients at t_{fin} (Table 8.9)—to the expected deformations using the deformation coefficient at t_{fin} recommended by previous investigations (Table 8.8) (see references at Table 4.5, Chapter 4.2.3).

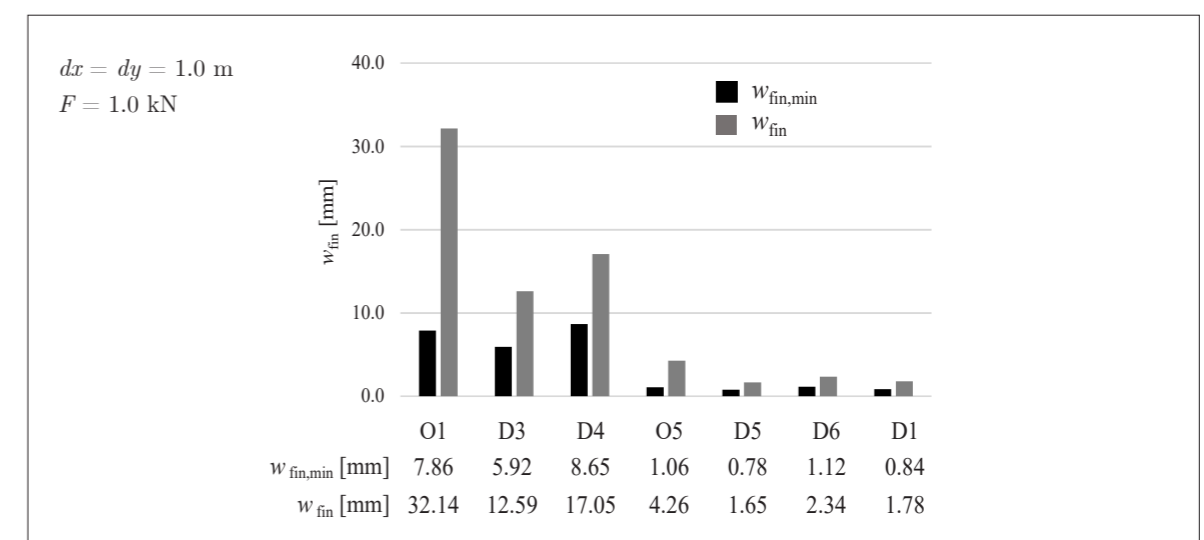


Fig. 8.14: Comparison on the deformation at t_{fin} using the minimum and recommended deformation coefficients

9 Investigations on the in-plane shear stiffness

9.1 General information and analytical solution

Even though this thesis prioritizes on CLT and DLT loaded out of the plane, and especially the biaxial load transfer, tactile in-plane shear tests are carried out in order to give a statement on the in-plane shear capacity of DLT, compared to CLT. Within DLT, the diagonal arrangement of single layers promises an increase in in-plane shear stiffness properties due to the higher in-plane shear properties of the UD layer under orientations deviating from 0° and 90°.

The in-plane shear stiffness refers to the entry A_{66} of the global stiffness matrix following the laminate theory (Equation (9.1) (Appendix **A2**)).

$$A_{ij} = \int_{-t/2}^{t/2} \bar{Q}_{ij} dz = \sum_{k=1}^n [\bar{Q}_{ij}]_k \cdot (z_k - z_{k-1}) \quad (9.1)$$

Therefore, the in-plane stiffness values of CLT and DLT are calculated according to the sum of the reduced and transformed stiffness terms of the UD layer, multiplied by the respective layer thicknesses ($\Sigma \bar{Q}_{ij} t_i$). It is important to keep in mind, that within the laminate theory the assumptions of the UD layer with ideally straight and continuous fibres stay valid. Gaps or stress-reliefs between the boards can not be considered within the laminate theory. Inversely, this means that within the analytical solution, the percentage increase in stiffness can be quantified, but not the actual in-plane shear stiffness value of the DLT series without edge-gluing.

Introducing an analytical solution following EC 5, the in-plane shear stiffness of non-edge-glued CLT is calculated according to Equation (9.2) (DIN EN 1995-1-1/NA) using an approximate reduction factor of 1/4, with respect to failure mechanism of "torsion" only (failure in the adhesive joint of the single laminations) (see Chapter 1.4.1). However, experimental investigations by *Brandner* and *Dietsch* (BRANDNER ET AL. 2017) showed, that the factor of 1/2 seems to provide sufficient in-plane stiffness values for CLT. Their statement on the reduction factor is based on experimental findings on CLT. The analytical approach for the evaluation of the shear compression test, on the other hand, is also based on the transformation relations of the UD layer (see Equation (9.9) within Chapter 9.2.4)

$$D_{xy} = \frac{1}{4} \cdot \sum (G_{xy,i} \cdot d_i) = 1/4 \cdot A_{66} \quad (9.2)$$

Note, that Equation (9.2) initially refers to the engineering constant of the in-plane shear modulus G_{xy} of the single laminations ($G_{xy} = 690$ MPa for spruce, T14).

Table 9.1 gives exemplary the in-plane shear stiffness values of O1, D3, and D4 series following the laminate theory ($\Sigma \bar{Q}_{ij} t_i$), using an approximate reduction factor of 1/4. The

stiffness values should be treated with caution, especially when compared to the tactile values of the experiments. The analytical values in Table 9.1 only serve as a qualitative benchmark regarding the effects of diagonal layer arrangements on the in-plane shear stiffness, but not as quantitative analytical values.

Tab. 9.1: In-plane shear stiffness values according to the laminate theory, using a reduction factor of 0.25

	$A_{66} = \Sigma \bar{Q}_{xy,i} t_i$ [MPa]	$D_{xy} = 1/4 \cdot A_{66}$ [MN/m]	percentage increase / decrease
O1	69.00	17.25	(= 100 %)
D3	153.01	38.25	+ 122 %
D4	132.00	33.00	+ 91 %

9.2 Preliminary experimental investigations

9.2.1 Test setup and analytical approach—shear frame test

For the experimental investigations on the in-plane shear stiffness, two different test methods are applied: Compression tests in accordance with the method proposed by *Kreuzinger* and *Sieder*, mostly applicable for CLT elements (KREUZINGER AND SIEDER 2013) and a newly proposed test setup in accordance with the picture frame test by *Andreolli* and *Turesson*, applicable for DLT (ANDREOLLI ET AL. 2014, TURESSON ET AL. 2019). The shear frame test used for the preliminary determination of the in-plane shear stiffness of CLT and DLT is a combination of both, a picture frame test and a diagonal compression test (Figure 9.1).

The picture frame test uses a steel frame, which is connected to the edges of a square mass timber specimen using dowel-type fasteners or bonding. Mostly, the load is brought into the specimen over the shear connection at the edges of the specimen. In case of bolted connections, the shear connection of the specimen to the frame is a weak point that may hardly achieve a force-fit due to its semi-rigid behavior (e.g. due to rope-effects). The diagonal compression test, on the other hand, is carried out without a shear frame. The compression force is brought into the specimen over two opposing corners of the specimen. In the picture frame test, panels are equally stretched along one of the diagonals as they are compressed along the other diagonal. This is not the case for panels in the diagonal compression test. In the latter case, the shear modulus was determined to substantially higher values than for the picture frame test (TURESSON ET AL. 2019).

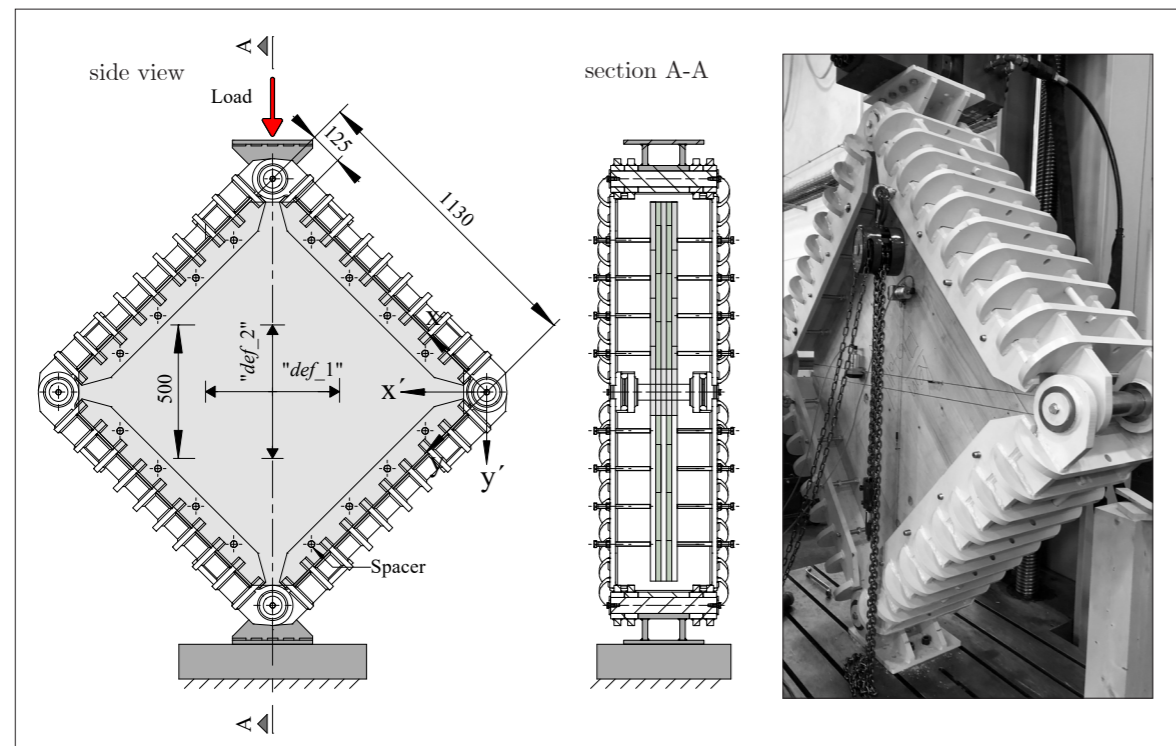


Fig. 9.1: Test setup of the shear frame test based on construction sketches by (MASSIV-HOLZ-MAUER GMBH 2021) and (HOLZINGER 2021)

The shear frame test developed for the investigations on DLT uses a shear frame, which is not rigidly or semi-rigidly connected to the edges of the square specimens. The force is brought into the specimen in compression only over edges of the specimen (see Figure 9.1 and Figure 9.3). The bolts within the shear frame are used as spacers for the placing of specimens with differing overall thickness and not for the purpose of load introduction (Figure 9.1). The specimens have the dimensions of $w/l = 1130/1130$ mm.

The outer corners of the elements are cut away in order to guarantee load introduction over the edges of the specimens and not via compression on the corner. Here, the specimens act only in in-plane shear. Possible errors by the load introduction due to semi-rigid mechanical connections or a concentrated compression forces are reduced. Furthermore, the method enables to carry out a large number of tests within a short amount of time, because the specimens are put in and out of the steel frame without gluing or attachment of mechanical fasteners.

The steel frame used for the experiments was developed in the frame-work of a master's thesis (HOLZINGER 2021) and was produced in cooperation with the company MASSIV-HOLZ-MAUER GMBH (MASSIV-HOLZ-MAUER GMBH 2021).

The applied load F is limited by the load capacity and deformations of the steel frame. For a loading of less than 0.5 MN, the minor deformations of the steel structure and bolts at the corners may be neglected. The introduction of the load into the specimen is described by triangular fictive compression loads with the resulting component of $F/\sqrt{2}$ within the third-point (Figure 9.2). Rope-displacement transducers are used to measure displacements over a length of $d = 500$ mm at the core of the CLT and DLT elements. The transducers are applied along the two diagonal directions and cover the central region. The latter represents one third of the panel and follows the fictive force components $F/\sqrt{2}$ (see Figure 9.2). For the central region (core), it is assumed that effects of the boundary conditions can be neglected (ANDREOLLI ET AL 2014, based on FROCHT 1931).

$$\gamma = \frac{\sqrt{2} \cdot \Delta w}{l/3} \quad (9.3)$$

The shear stress acting within the core can be calculated by Equation (9.4):

$$\tau = C_i \cdot \frac{F}{\sqrt{2} \cdot l \cdot t} \quad (9.4)$$

The coefficient C_i describes the ratio of the estimated shear stresses τ amassed in the core of the specimens and therefore within the chosen measuring range. Following the thesis by Frocht from 1931, the compression and tensile stresses of a compressed square element are given as a function of its diagonals and describe a non-linear distribution (TURESSON ET AL. 2019, FROCHT 1931). Using Mohr's circle a mean value of the ratio $C_i = \tau/\tau_{pu}$ is calculated for points on the diagonals (length d). Therefore, C_i depends on the ratio a/l (TURESSON ET AL. 2019, ANDREOLLI ET AL. 2014). For the given test setup ($d = 500$ mm, $a = l/3 = 1130/3$ mm), the coefficient C_i is 1.377 (see Appendix A6). The effective in-plane shear moduli of the specimens are calculated using the well-know mechanical relation between shear stresses and strains (Equation (9.5)).

$$G_{xy,eff} = \frac{\tau}{\gamma} = \frac{F}{\Delta w} \cdot \frac{C_i}{6t} = m \cdot \frac{C_i}{6t} \quad (9.5)$$

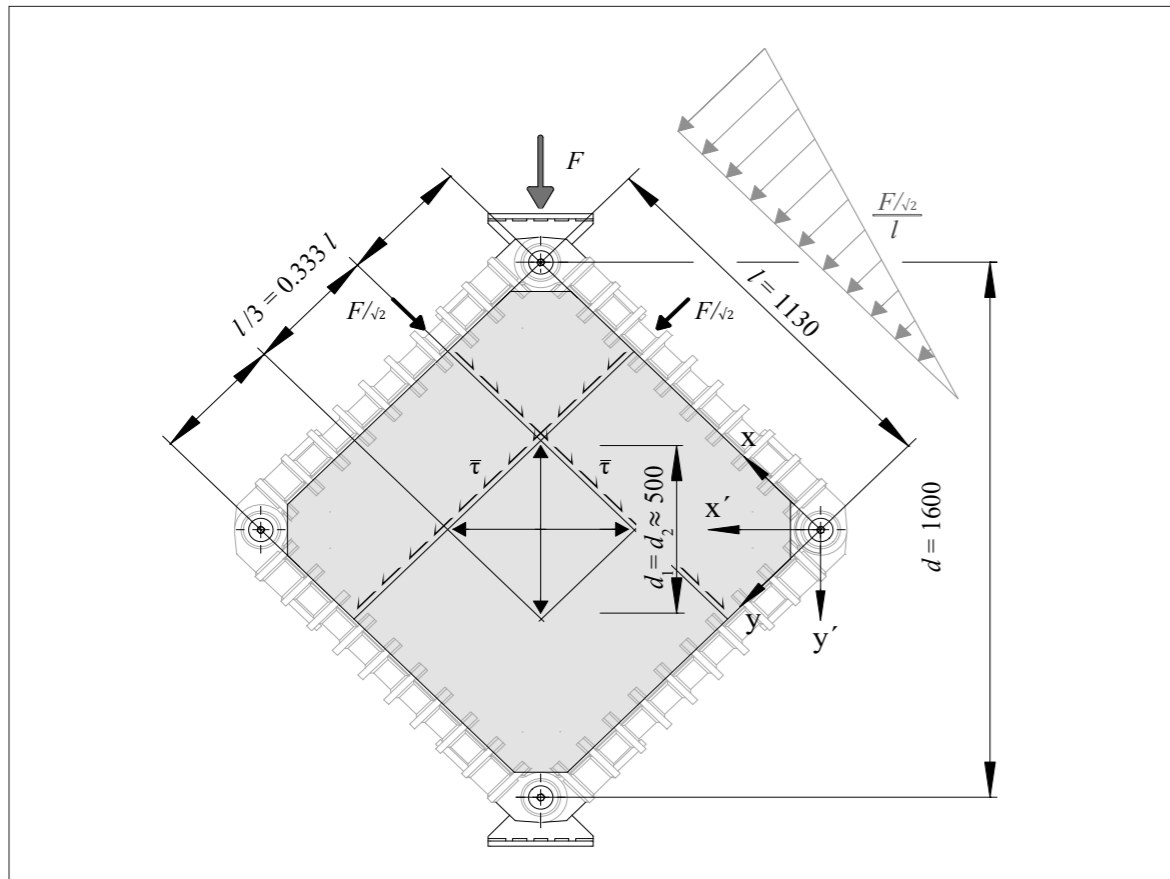


Fig. 9.2: Geometrical parameters and static system for the experimental investigations

9.2.2 Results of the experimental investigations—shear frame test

The tactile tests were carried out for one specimen of each series with $t = 100$ mm (O1, D3, D4 series). The chosen test setup is not suitable for series with $t > 100$ mm due to the limitation of the load-bearing capacity of the steel frame. Figure 9.3 gives the load-deformation diagrams of each series within the linear elastic range. The displacement Δw is the absolute value of the relative deformations in global x and y direction, measured over the distances d_1 and d_2 ($\Delta w = |\Delta d_1| + |\Delta d_2|$). The shear strain within the core ($a = l/3$) is calculated using Equation (9.3). The testing was carried out deformation controlled with a constant feed rate of 3 mm/min. A analysis of the failure mechanisms or crack patterns is not possible, hence a failure load was not reached for any of the specimens.

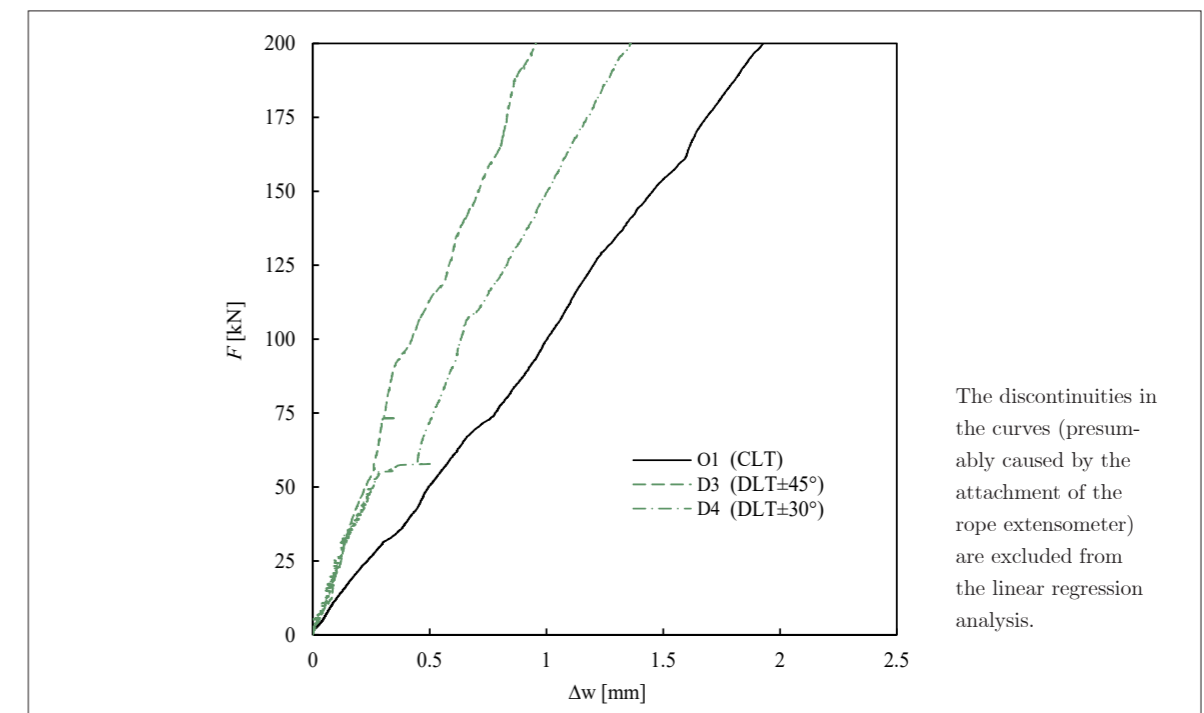


Fig. 9.3: Load-deformation diagrams of the shear-frame test

Table 9.2 provides evaluation of the shear frame tests. Compared to the orthogonal O1 series, the in-plane shear stiffness of DLT±45° D3 series is 184 % higher, for DLT±30° D4 series 132 %.

Tab. 9.2: Evaluation of the shear frame tests

	1F_1 [kN]	${}^1w_{F1}$ [mm]	${}^10.5F_1$ [kN]	${}^1w_{0.5F1}$ [mm]	slope m [/]	R^2 [/]	C_i [/]	$G_{xy,eff}$ [MPa]	D_{xy} [MN/m]
O1	199.99	1.928	100.06	1.003	105.89	1.00	1.377	243.02	24.30
D3	199.89	0.954	100.12	0.424	194.44	1.00	1.377	446.24	44.62
D4	199.89	1.360	100.02	0.632	139.72	1.00	1.377	320.65	32.07

¹Chosen values for the evaluation within a linear elastic relationship (see coefficient of determination R^2)

9.2.3 Test setup and analytical approach—shear compression test

In addition to the shear frame tests, shear compression tests were carried out according to the method proposed by *Kreuzinger and Sieder* (KREUZINGER AND SIEDER 2013) within the framework of the research project InnoCrossLam. The method proposed by *Kreuzinger and Sieder* is applicable for CLT specimens only due to the loading of the specimens under a force-to-grain angle of 45° (Figure 9.4). Introducing specimens made from $DLT\pm 45^\circ$ into the shear compression tests could lead to single laminations acting in compression only. Using shear compression tests, *Brandner and Dietsch* conducted extensive series of mechanical investigations on CLT elements (BRANDNER ET AL. 2017). The shear compression test could also be applicable to $DLT\pm 30^\circ$ since in this case, no lamination would be loaded only in compression. However, this assumption needs to be further investigated. The experiments presented within this section refer to investigations on CLT and multifunctional CLT elements and were therefore not carried out using $DLT\pm 30^\circ$ series (see ARNOLD ET AL. 2021).

The shear compression tests are carried out on three CLT specimens ($w/l = 500/1250$ mm) of O1 series. The supports are made from teflon, so as to minimize friction in x direction. The vertical (global y) and horizontal (global x) deformations are measured on both sides of the specimen over a length of 300 mm by means of rope displacement transducers (Figure 9.3). The testing was carried out deformation controlled with a feed rate of 2 mm/min. Unlike the shear frame tests, the shear compression tests can be conducted until failure of the specimens occurs (net-shear failure, gross-shear failure, torsion). This is explained by the lack of limitation by deformations in the test setup (steel frame). Hence, the shear compression tests expand and validate the results of the tactile shear frame tests for CLT.

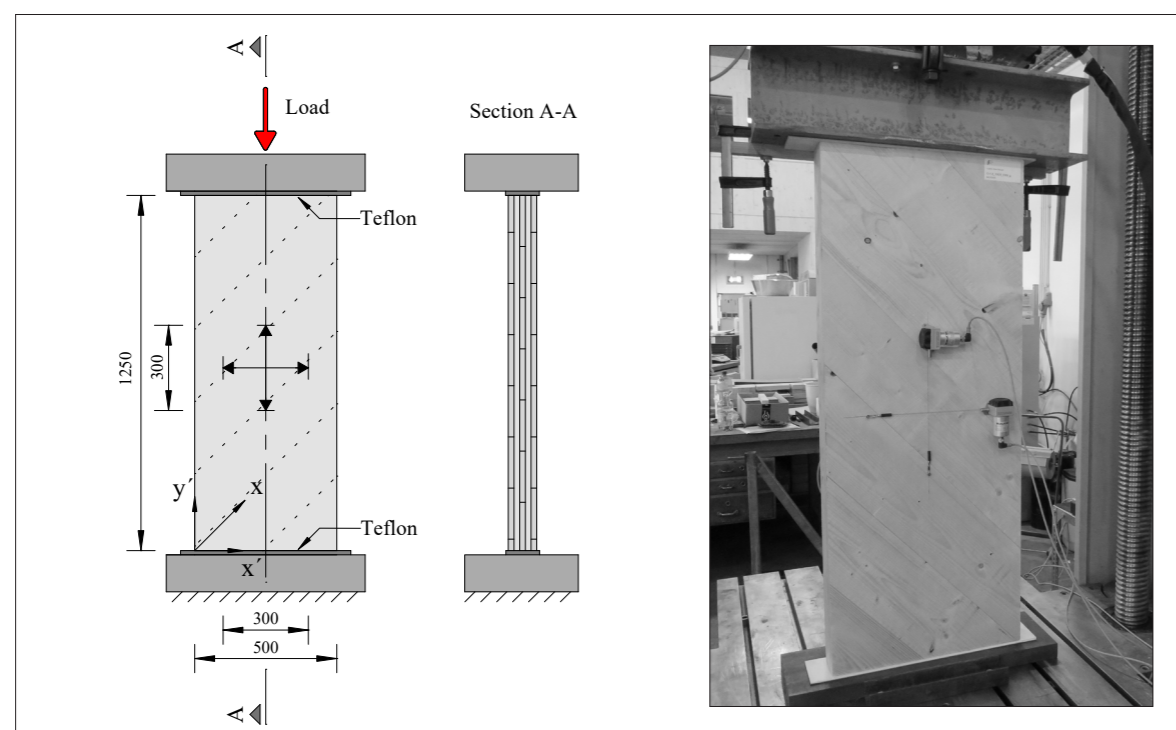


Fig. 9.4: Test setup of the in-plane shear compression tests, based on (BRANDNER ET AL. 2017)

In a first step the overall (effective) moduli of elasticity in the x and y direction of the CLT specimens are calculated similar to the analytical investigations. Therefore, the modulus of elasticity of each 0° and 90° layer is multiplied by the respective layer thickness t_i . In the end, the sum is divided by the overall thickness t of the CLT element (Equations (9.6) and (9.7)).

$$E_{x,eff} = \frac{\sum t_{i,x}E_0 + \sum t_{i,y}E_{90}}{t} \quad (9.6)$$

$$E_{y,eff} = \frac{\sum t_{i,y}E_0 + \sum t_{i,x}E_{90}}{t} \quad (9.7)$$

The effective modulus of elasticity in y' direction is calculated according to Equation (9.8). Due to the orientation of front and back layers under 45° , this modulus of elasticity is derived using the deformation in vertical direction and horizontal direction measured by the rope displacement transducers within the linear elastic range of $0.4F_{max}$ and $0.1F_{max}$. Thus, the strains $\Delta\varepsilon$ are absolute values that take into account the relative deformations in global x and y direction, measured in horizontal and vertical direction ($\Delta\varepsilon_i = \Delta\varepsilon_{i,vert} + \Delta\varepsilon_{i,horiz}$).

$$E_{y',eff} = \frac{\sigma}{\varepsilon} = \frac{F}{\varepsilon \cdot A} = \frac{(0.4F_{max} - 0.1F_{max})}{(\Delta\varepsilon_{0,4F} - \Delta\varepsilon_{0,1F}) \cdot t \cdot w} \quad (9.8)$$

Using the moduli of elasticity calculated previously, the effective shear moduli $G_{xy,eff}$ are calculated according to Equation (9.9) which is based on the transformed and reduced stiffness matrix of the UD layer, at an angle of 45° .

$$G_{xy,eff} = \frac{1}{\left(\frac{4}{E_{y'}} - \frac{1}{E_x} - \frac{1}{E_y}\right)} \quad (9.9)$$

9.2.4 Results of the experimental investigations—shear compression test

Table 9.3 lists the evaluation of the shear compression tests. For all specimens, a net shear failure in the second and fourth layer of the CLT was observed. The in-plane shear stiffnesses of the three specimens are all within the same range. The mean value of the shear modulus of O1 series following the shear compression tests appears to be $G_{xy,mean} = 320.42$ MN/m² (COV 7.6).

Tab. 9.3: Evaluation of the shear compression tests

	F_{max} [kN]	$F_{0.4}$ [kN]	$F_{0.1}$ [kN]	$\varepsilon_{0.4}$ [1]	$\varepsilon_{0.1}$ [1]	$E_{y'}$ [MN/m ²]	E_x [MN/m ²]	E_y [MN/m ²]	$G_{xy,eff}$ [MN/m ²]	D_{xy} [MN/m]
O1-1	378.93	151.57	37.89	0.0037737	0.0007658	1261.8	6748.0	4400.0	315.5	31.55
O1-2	348.72	139.49	34.87	0.0035940	0.0007434	1190.2	6748.0	4400.0	297.5	29.75
O1-3	337.38	134.95	33.74	0.0036699	0.0008137	1085.5	6748.0	4400.0	271.4	27.14
(COV 7.6), mean									320.42	32.04

9.3 Comparison of the experimental and analytical results

The analytical values among themselves, reflect well the relation in the stiffness change as a result of the rotation of individual layers—regardless of which reduction coefficient is implemented. However, the comparison of the experimental results and the analytical values should be viewed with caution, which is also reflected by the large number of different test methods. It is important to point out again the limited significance and evidence of the values determined experimentally by means of the shear frame test, due to the small number of test specimens. Further experiments must be carried out to confirm the experimental setup and results.

Furthermore, the question of determining shear strength values arises with regard to future research. These cannot be determined due to the limited load capacity of the shear frame. Here, the shear compression test offers a promising alternative - at least for determining the in-plane shear strengths of CLT.

Comparing the results of the shear frame testing to the results of the shear compression testing reveals a discrepancy in the in-plane shear stiffness for the orthogonal O1 series of $\Delta D_{xy} = 7.74$ MN/m (Table 9.4). The value of the shear frame test ($D_{xy,O1} = 24.30$ MN/m) is therefore by 31.9 % smaller compared to the in-plane shear stiffness determined using the shear compression test ($D_{xy} = 32.04$ MN/m).

The shear stiffness of O1 series according to the analytical solution appears to be very low. The stiffness values of 17.25 MN/m is 40.9 % lower than the value determined in the shear frame test and 85.7 % lower than the value determined by the shear compression test. Thus, the analytical approach according to DIN EN 1995-1-1/NA may appear to be conservative and approximate for non-edge-glued CLT and DLT, also reflecting the findings of *Danielsson* and *Jeleč* (DANIELSSON AND JELEČ 2022) and *Brandner* and *Dietsch* (BRANDNER ET AL. 2017).

For the DLT, on the other hand, the values of the analytical approach correlate well to the results of the shear frame test. The analytical in-plane shear stiffness of D3 series is 16.7 % lower compared to the experimentally determined value. The analytical in-plan shear stiffness of D4 series nearly equals the in-plane shear stiffness determined experimentally.

Tab. 9.4: Comparison of the in-plane shear stiffnesses and shear moduli following the analytical approach and mechanical testing

series	analytical solution ¹		shear frame test		shear compression test	
	G_{xy} [MN/m ²]	D_{xy} [MN/m]	$G_{xy,exp}$ [MN/m ²]	$D_{xy,exp}$ [MN/m]	$G_{xy,exp}$ [MN/m ²]	$D_{xy,exp}$ [MN/m]
O1	172.50	17.25	243.02	24.30	320.42	32.04
D3	382.53	38.25	446.24	44.62	/	/
D4	330.03	33.00	320.65	32.07	/	/

¹simplified approach using a reduction factor of 0.25 according to EC 5

By the results on the in-plane shear stiffness, the investigations on the stiffness properties of CLT and DLT are concluded within this thesis. Theoretical, analytical and numerical approaches for the characterization of DLT were derived and applied. Despite all positive findings, however, it was also noted that some test setups—e.g. the experiments for determining the out-of-plane shear stiffness in the y direction—need to be further optimized in order to demonstrate the increase or optimization in the stiffness properties of DLT that is undoubtedly present according to the analytical approach.

Within the following Chapter, by means of possible application scenarios, it will be shown in which design situations diagonal layer arrangements are reasonable and provide benefits regarding deformations and stress distributions around point-supports. The following investigations are carried out using 2D and 3D numerical models of linear and point-supported mass timber slabs, which are close to real-scale structures in terms of their represented dimension ($w/l = 3.0/3.0$ m). The models aim to provide information regarding deformations in the SLS and stress distributions in the ULS.

10 Evaluation and quantification using real-scale numerical models

10.1 Deformation analysis using 2D FE models (SLS)

10.1.1 General information and modelling approach

The limiting factors for the design of mass timber slabs are deformations in the SLS and concentrated stresses in the ULS. By using DLT instead of CLT, lower total deformation may be expected, especially under biaxial bending. This is, among others, due to the higher torsional stiffness, which was proven by the analytical and experimental investigations in the previous chapters.

The overall deformation behavior of CLT and DLT within static systems commonly used for mass timber floors is analyzed as a function of the number of layers and their respective orientation. The static systems investigated feature dimensions of $w/l = 3.0/3.0$ m and represent possible application scenarios in real-scale structures. The chosen systems further feature different support conditions (point-support and linear supports) to analyze different cases of predominant internal forces. The systems are loaded with a constant surface load of $p = 5.0$ kN/m² or a point-load of $P = 5.0$ kN. The chosen layups equal the series presented in Table 4.8.

Systematically, the overall deformations and maximum deformations of the slabs are analyzed and compared to each other. Linear-elastic 2D FE models were used for the modeling of the plate elements. The models were created by means of the FEM software Dlubal RFEM (version 5.24). The plates were defined as orthotropic plate elements. Therefore, the stiffness matrices were calculated manually using the laminate theory. Herby, the material parameters according to Table 4.9 (T14; ETA20/0023) and the *Poisson's* ratios according to (HALÁSZ AND SCHEER 1996) were applied. Each stiffness matrix of the investigated series is provided in Appendix A7.

Within the 2D models, no individual solids were modelled. Contacts between layers were considered rigid. In using 2D models, furthermore no board width was taken into account. This is consistent with the assumption of UD layers. However, for the deformation behavior under uniaxial bending, the edge-gluing is not relevant in any case. Under biaxial bending, the influence of edge-gluing seems negligible for board width of $w \geq 180$ mm (see Figure 8.11). The mesh size was chosen to be 50 mm and generated automatically. The solver follows an iterative approach. The modelling of the CLT and DLT specimens was carried out with Serendipity elements with 8 nodes each. The most important parameters of the 2D FE models are summarized in Appendix A4. The boundary conditions and support conditions were chosen according to the respective static system. For centric point-supported plates, the respective column was fixed in all directions ($x = y = z = 0$) and defined as torsionally rigid ($\varphi_x = \varphi_y = \varphi_z = 0$). For plates, point-supported at several corners, only one corner was fixed horizontally, so as to refrain from violating the static system's degrees of freedom and induce constraint stresses. Rotational restrained plate edges were defined by line bearings with the respective attributes ($\varphi_x = 0$ or $\varphi_y = 0$).

10.1.2 Deformation analysis of 5-layered CLT and DLT elements

In a first step, the deformations of 5-layered CLT and DLT series are analyzed. Table 10.1 gives six exemplary static systems of point-supported mass timber slabs (row 2). The static systems are numbered from (1) to (6). The dimensions of all plates are $w/l = 3.0/3.0$ m (4.5 m in case of an additional cantilever). The dimensions of the columns are $w/l = 0.2/0.2$ m. The loading of the respective system is given within row 1. The uniformly distributed surface load $p = 5.0$ kN/m² represents a value which may be expected in residential buildings by the service load (payload) and self-weight of the timber slab.

Regarding the number and orientation of the layers, the 5-layered CLT O7 series and DLT±45° D7 series correspond to the O5 and D5 series, that were used within the previous experimental investigations. However, the layer thickness is now specified as $t_l = 30$ mm instead of $t_l = 40$ mm. The total plate thickness is thus $t = 150$ mm. This may correspond to a common thicknesses for mass timber slabs within the selected construction grid.

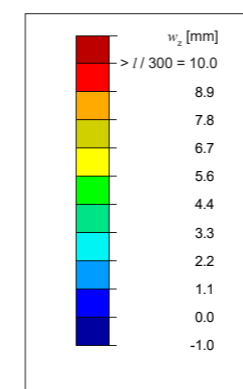
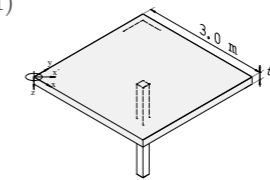
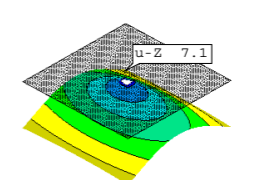
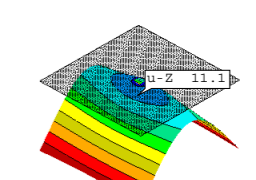
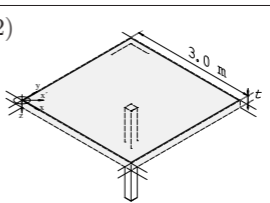
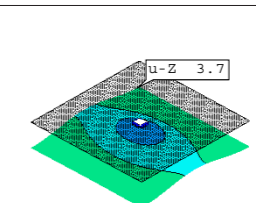
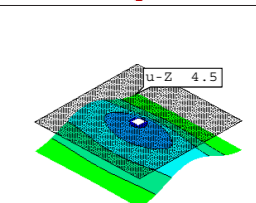
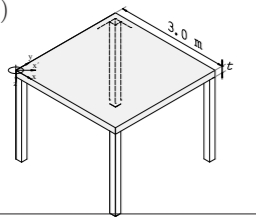
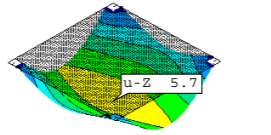
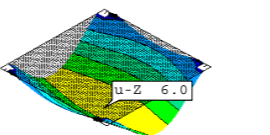
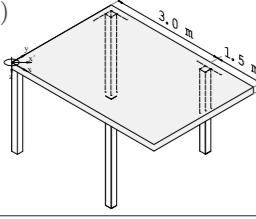
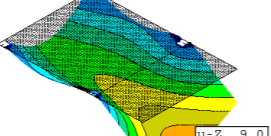
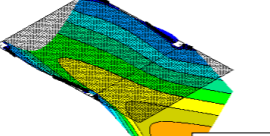
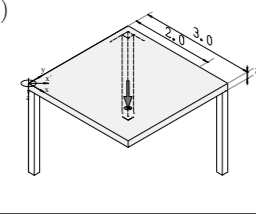
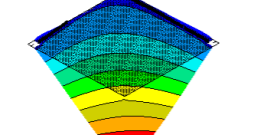
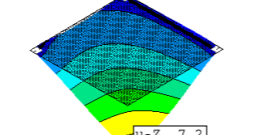
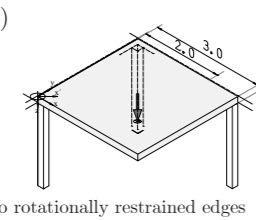
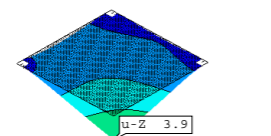
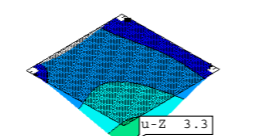


Fig. 10.1: Scale for the deformation analysis

The overall deformations of the CLT and DLT series are shown within rows 3 and 4. For a better readability, the supports and loads are hidden within the graphical representation. The colored gradation makes possible the analysis of the amplitudes and distribution of the deformations. The corresponding scale is shown in Figure 10.1. The maximum value (dark red) is reached for deformation values $w \geq l/300$. In addition, the respective maximum deformation $w_{z,max}$ (u-z) is given within the graphical representation of each system. Row 5 gives the percentage change (increase or decrease) of the maximum deformation values of the DLT element compared to those of the CLT element.

Tab. 10.1: 5-layered CLT O7 and DLT±45° D7 series under uniaxial and biaxial bending due to point-supports

loading	system	deformations w_z		$w_{z,max}$
		CLT (O7 series)	DLT±45° (D7 series)	
	w / l			
p / P	3.0 m / 3.0 m	30-30-30-30-30 [0°,90°,0°,90°,0°]	30-30-30-30-30 [0°,45°,90°,-45°,0°]	DLT/ CLT
5.0 kN/m ²	(1) 			+ 56.3 %
5.0 kN/m ²	(2)  four rotationally restrained edges			+ 21.6 %

loading	system	deformations w_z		$w_{z,max}$
		CLT (O7 series)	DLT $\pm 45^\circ$ (D7 series)	
p / P	w / l 3.0 m / 3.0 m	CLT (O7 series) 30-30-30-30-30 [0°,90°,0°,90°,0°]	DLT $\pm 45^\circ$ (D7 series) 30-30-30-30-30 [0°,45°,90°,-45°,0°]	DLT/ CLT
5.0 kN/m ²	(3) 			+ 5.3 %
5.0 kN/m ²	(4) 			+ 11.1 %
5.0 kN	(5) 			- 41.0 %
5.0 kN	(6)  two rotationally restrained edges			- 15.4 %

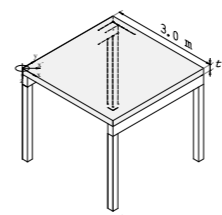
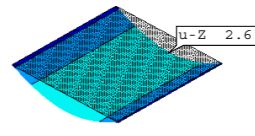
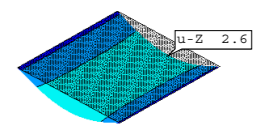
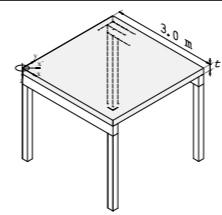
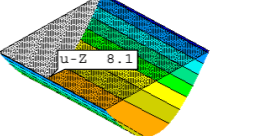
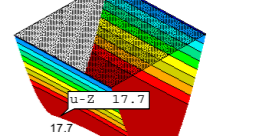
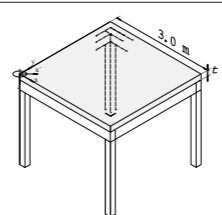
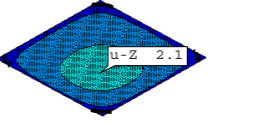
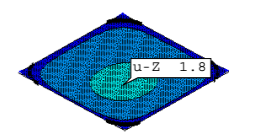
The maximum deformation of a centric point-supported slab (system (1)) is significantly higher for the 5-layered DLT series, than for CLT (+56.3 %). This is mainly due to the lower bending stiffness in y direction of the DLT $\pm 45^\circ$ series ($B_{y,D7} = 0.32$ MNm²/m; $S_{yz,D7} = 19.29$ MN/m), compared to the CLT O7 series ($B_{y,O7} = 0.73$ MNm²/m; $S_{yz,O7} = 7.33$ MN/m). The relative high shear stiffness value in y direction of the DLT element loses importance within the total deformation according to *Reissner-Mindlin* (see Chapters 7 and 8). The DLT element deforms primarily uniaxial around the x axis. Additional bending around the y axis is locked by the uniaxial curvature. This locking effect is also observed for the CLT element, but in the latter case is much less pronounced. For the centric point-supported slab with rotationally restrained plate edges (system (2)) the locking effect is less pronounced.

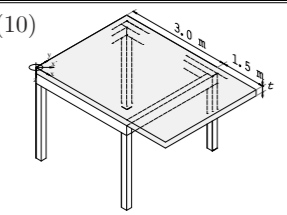
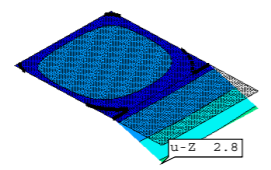
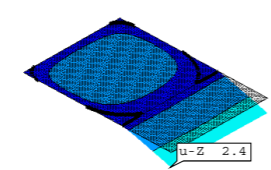
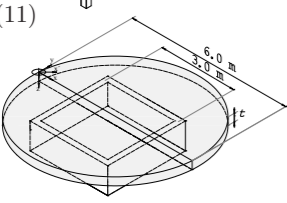
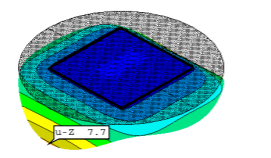
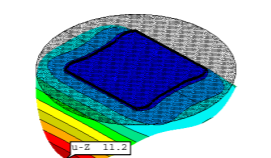
The low bending stiffness of the 5-layered DLT $\pm 45^\circ$ governs the deformation behavior also for point-supports at all corners of the plate, with and without a cantilever (systems (3) and (4)). For system (3), the maximum deformation of the DLT slab is 5.3 % higher than the one of the CLT slab. For system (4), with an additional 1.5 m long cantilever, the deflection of the DLT element is higher by 11.1 %. The overall deformations of the DLT elements following static systems (3) is close to the exemplary limiting value of $l/300 = 10$ mm.

In summary, the uniaxial deformations are much more pronounced for the DLT D7 series than for the CLT O7 series. Within systems (1) to (4) predominantly uniaxial bending around the x axis occurs. For a load-cases of pure torsion, this effect is reversed (see system (5)). For the given point-load ($P = 5.0$ kN) on the cantilevered corner of the slab, the corner of the CLT element lowers by 12.2 mm and the corner of the DLT $\pm 45^\circ$ by 7.2 mm. This reflects the significantly higher torsional stiffness of the DLT $\pm 45^\circ$ element ($B_{xy,D7} = 3.16$ MNm²/m) compared to the CLT element ($B_{xy,O7} = 1.94$ MNm²/m). For system (6) cantilevered corner with additional rotational constrained plate edges, the uniaxial bending stiffnesses are activated in addition to the torsional stiffness. This equalizes the deformations of the CLT and DLT element. In summary, the chosen DLT layup of the D7 series may only be more efficient than CLT series for point-supported slabs, if the resulting load case results in torsion. This does not mean that DLT elements are generally less suitable for point-supported slabs.

Within further investigations, the deformation behavior of the 5-layered CLT O7 and DLT D7 series due to linear support is examined (Table 10.2). The exemplary construction grid and the dimensions of the plates remain constant at $w/l = 3.0/3.0$ m. The cantilevered corner of systems (5) and (6) are replaced by a linearly supported circular slab with a radius of $r = 3.0$ m (system (11)). The surface load remains at $p = 5.0$ kN/m². The colored scale for the deformation analysis according to Figure 10.1 is left unchanged.

Tab. 10.2: 5-layered CLT O7 and DLT $\pm 45^\circ$ D7 series under uniaxial and biaxial bending due to linear supports

loading	system	deformations w_z		$w_{z,max}$
		CLT (O7 series)	DLT $\pm 45^\circ$ (D7 series)	
p / P	w / l 3.0 m / 3.0 m ($r = 3.0$ m)	CLT (O7 series) 30-30-30-30-30 [0°,90°,0°,90°,0°]	DLT $\pm 45^\circ$ (D7 series) 30-30-30-30-30 [0°,45°,90°,-45°,0°]	DLT/ CLT
5.0 kN/m ²	(7) 			\pm 0 %
5.0 kN/m ²	(8) 			+ 118.5 %
5.0 kN/m ²	(9) 			- 14.3 %

loading	system	deformations w_z		$w_{z,max}$
		CLT (O7 series)	DLT $\pm 45^\circ$ (D7 series)	
	w / l	CLT (O7 series)	DLT $\pm 45^\circ$ (D7 series)	DLT/ CLT
p / P	3.0 m / 3.0 m ($r = 3.0$ m)	30-30-30-30-30 [0°,90°,0°,90°,0°]	30-30-30-30-30 [0°,45°,90°,-45°,0°]	
5.0 kN/m ²	(10) 			- 14.3 %
5.0 kN/m ²	(11) 			+ 45.5 %

Slabs modelled by the 5-layered CLT and DLT series behave almost identical for uniaxial bending in the main load-bearing direction (system (7)). Due to the slightly higher bending and shear stiffnesses in the x direction of the DLT D7 series, the deformations at the free corners of the slabs are lower by 1.0 %, compared to the CLT series ($B_{x,O7} = 2.48$ MNm²/m; $B_{x,D7} = 2.65$ MNm²/m; $S_{xz,O7} = 11.94$ MN/m; $S_{xz,D7} = 11.52$ MN/m). For uniaxial bending in y direction (system (8)), the findings of Table 10.1 are further confirmed. The maximum deformation for the DLT D5 series is higher by 118.5 % than the one for CLT O5 series. This is due to the significant smaller bending stiffness in y direction of the DLT series ($B_{y,O7} = 0.73$ MNm²/m; $B_{y,D7} = 0.32$ MNm²/m; $S_{yz,O7} = 7.33$ MN/m; $S_{yz,D7} = 19.29$ MN/m).

The opposite is observed for systems that provide linear support of all plate edges, which prevents uniaxial curvatures (see systems (9) and (10)). For the slab with linear support on all edges, the maximum deformations of the DLT $\pm 45^\circ$ D5 series are by 14.3 % lower, compared to those of the CLT O5 series. This follows a logical order, since uniaxial bending is less pronounced and biaxial bending becomes more dominant. For the circular slab over linear supports (system (11)), a single curvature occurs due to bending around the x-axis. This observation is consistent to the deformation behavior within static systems (8). The maximum deformation of the DLT D7 series is by 45.5 % higher, compared to the CLT O7 series.

Within the following Chapter, the deformation analysis is carried out on 7-layered CLT and DLT series of comparable overall thickness t . Different deformation behaviors are expected for the 7-layered series. This may be due to the higher number of layers and thus the higher ratio of homogenization of the stiffness parameters in x and y directions.

10.1.3 Deformation analysis of 7-layered CLT and DLT elements

The previous investigations based on the 2D FE models of 5-layered mass timber elements demonstrated that DLT can hardly benefit from its advantages—regarding for example the high torsional stiffness—if the structure acts predominately in uniaxial bending as a result of the chosen static system and loading.

In the following, CLT and DLT $\pm 45^\circ$ series of comparable overall thickness but with a higher number of layers, are chosen for further investigations. The number of layers is increased from $n = 5$ to $n = 7$, while the thickness of the individual layers is reduced from $t_1 = 30$ mm to $t_1 = 20$ mm. The resulting layups provide a thickness of $t = 140$ mm and correspond to O8 and D8 series (see Table 4.8). The bending stiffnesses in x and y direction of DLT D8 series are $B_{x,D8} = 1.70$ MNm²/m and $B_{y,D8} = 0.84$ MNm²/m, the torsional stiffness is $B_{xy,D8} = 1.94$ MNm²/m. The bending stiffnesses of the CLT O8 series are $B_{x,O8} =$

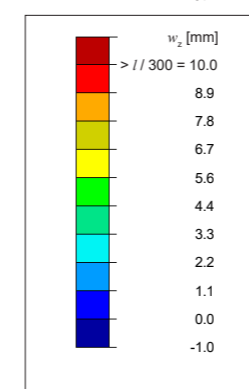
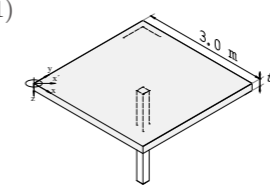
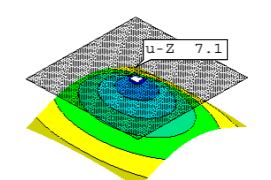
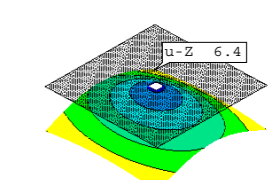
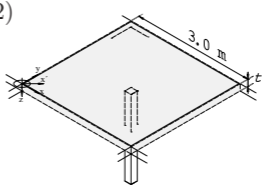
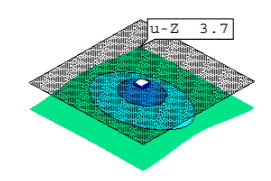
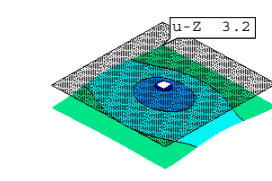
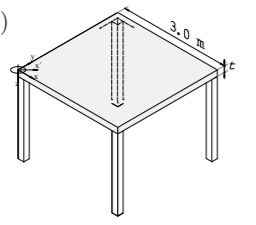
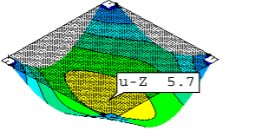
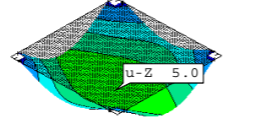
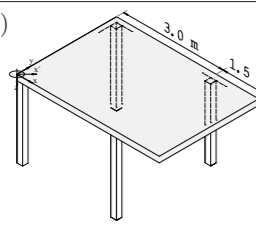
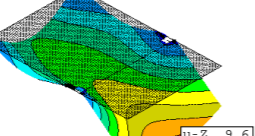
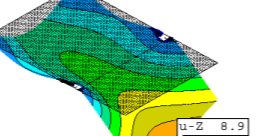
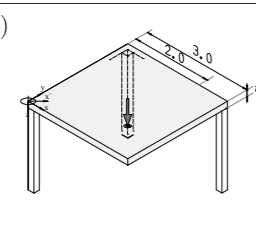
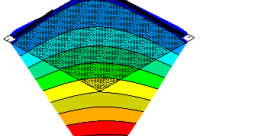
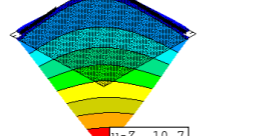
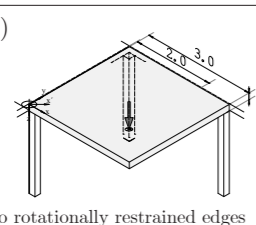
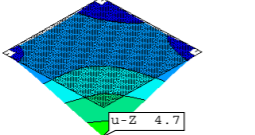
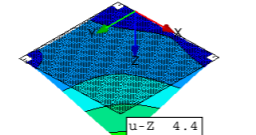


Fig. 10.2: Scale for the deformation analysis

$= 1.82$ MNm²/m and $B_{y,O8} = 0.79$ MNm²/m, the torsional stiffness is $B_{xy,O8} = 1.03$ MNm²/m. The bending stiffnesses in y direction of these CLT O8 and DLT D8 series are almost identical. The corresponding stiffness matrices of the 7-layered series are also presented in Appendix A7. In analogy to Table 10.1, Table 10.3 shows the deformation behavior of the mass timber slabs due to point-supports, modelled by 7-layered CLT and DLT series. The static systems (1) to (6) equal those of Table 10.1. The loading remains unchanged. This guarantees comparability to the deformation analysis on the 5-layered CLT and DLT elements. The colored scale of the deformations remains unchanged and is given once more in Figure 10.2.

Tab. 10.3: 7-layered CLT O8 and DLT $\pm 45^\circ$ D8 series under uniaxial and biaxial bending due to point-supports

loading	system	deformations w_z		$w_{z,max}$
		CLT (O8 series)	DLT (D8 series)	
	w / l	CLT (O8 series)	DLT (D8 series)	DLT/ CLT
p / P	3.0 m / 3.0 m	20-20-20-20-20-20-20 [0°,90°,0°,90°,0°,90°,0°]	20-20-20-20-20-20-20 [0°,90°,45°,90°,-45°,90°,0°]	
5.0 kN/m ²	(1) 			- 9.9 %
5.0 kN/m ²	(2)  four rotationally restrained edges			- 13.5 %

loading	system	deformations w_z		$w_{z,max}$
		CLT (O8 series)	DLT (D8 series)	
p / P	w / l	CLT (O8 series)	DLT (D8 series)	DLT/ CLT
p / P	3.0 m / 3.0 m	20-20-20-20-20-20-20 [0°,90°,0°,90°,0°,90°,0°]	20-20-20-20-20-20-20 [0°,90°,45°,90°,-45°,90°,0°]	
5.0 kN/m ²	(3) 			- 12.3 %
5.0 kN/m ²	(4) 			- 7.3 %
5.0 kN	(5) 			- 21.3 %
5.0 kN	(6) 			- 6.4 %

The maximum deformations for the 7-layered CLT O8 series within systems (1) to (4) are in the same range as the deformations of the 5-layered CLT O7 series (see Table 10.1). On the other hand, the 7-layered DLT D8 series experiences smaller deformations than its 5-layered counterpart D7 series within the static systems (1) to (4).

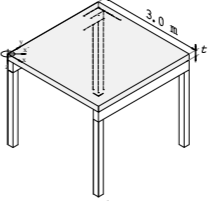
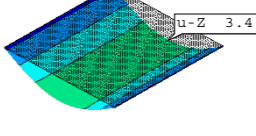
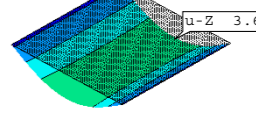
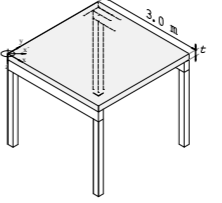
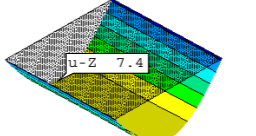
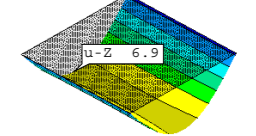
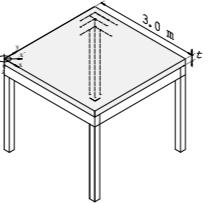
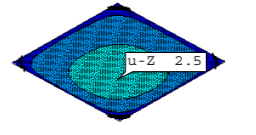
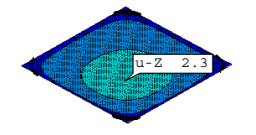
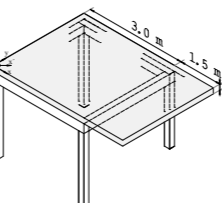
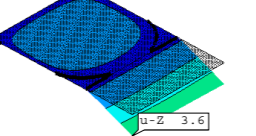
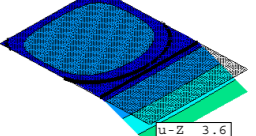
When comparing maximum deformations due to centric point-supports of the 7-layered CLT O8 series to the 7-layered DLT D8 series, the observations from Table 10.1 are reversed (system (1)). Now, the 7-layered DLT±45° element experiences lower deformations than the 7-layered CLT element (-9.9%). The previously uniaxial curvature and the locking effect for bending around the y axis disappear. For the centric point-supported slab with rotationally restrained edges, the deformations of DLT D7 series are smaller by 13.5%, than those of CLT O7 series (system (2)). For point-supports at all corners of the slab, the maximum deformation for the DLT is by 14.5% lower than for the CLT element (system (3)). For the same support conditions, yet with an additional cantilever of $l = 1.5$ m, the deformations of the DLT slab compared to the CLT plate are reduced within a comparable range (-7.3%; system (4)). This is remarkable, since for the 5-layered DLT D5 element the

deformations were higher by 5.3% in situation (3) and by 11.1% than those of the 5-layered CLT O5 series (Table 10.1).

For the plate acting in pure torsion (system (5)), the 7-layered DLT series experiences significantly lower deformation values (-21.3%), compared to the 7-layered CLT element; even though, within the comparison of the 5-layered DLT element to the 5-layered CLT series this increase was much more pronounced (-41.0%) (Table 10.1). The results according to Table 10.3 show, that a higher number of orthogonal layers in the cross-section decrease the impact and differences within the torsional stiffness of DLT compared to CLT. At the same time, the bending stiffnesses are harmonized, which leads to moderate deformations—even and especially under uniaxial bending. Table 10.3 validates, that the use of 7-layered DLT elements featuring the chosen layup of D8 series is in general more appropriate within point-supported systems governed by both, uniaxial and biaxial bending.

Table 10.4 summarizes the deformation behavior of the 7-layered CLT and DLT series due to linear supports, analogous to Table 10.2.

Tab. 10.4: 7-layered CLT O8 and DLT±45 D8 series under uniaxial and biaxial bending due to linear supports

loading	system	deformation w_z		$w_{z,max}$
		CLT (O8 series)	DLT (D8 series)	
p / P	w / l	CLT (O8 series)	DLT (D8 series)	DLT/ CLT
p / P	3.0 m / 3.0 m ($r = 3.0$ m)	20-20-20-20-20-20-20 [0°,90°,0°,90°,0°,90°,0°]	20-20-20-20-20-20-20 [0°,90°,45°,90°,-45°,90°,0°]	
5.0 kN/m ²	(7) 			+ 5.9 %
5.0 kN/m ²	(8) 			- 7.2 %
5.0 kN/m ²	(9) 			- 8.0 %
5.0 kN/m ²	(10) 			± 0 %

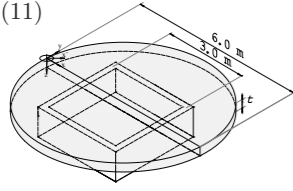
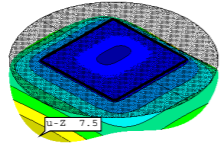
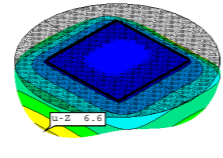
loading	system	deformation w_z		$w_{z,max}$
		CLT (O8 series)	DLT (D8 series)	
	w / l			
p / P	3.0 m / 3.0 m ($r = 3.0$ m)	20-20-20-20-20-20 [0°,90°,0°,90°,0°,90°,0°]	20-20-20-20-20-20 [0°,90°,45°,90°,-45°,90°,0°]	DLT/ CLT
5.0 kN/m ²	(11) 			- 12.0 %

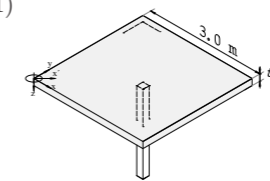
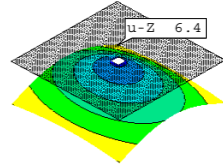
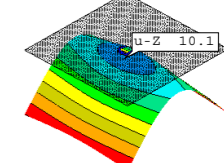
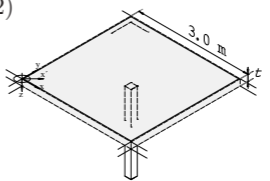
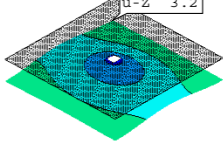
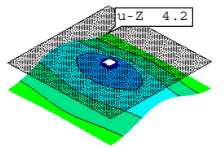
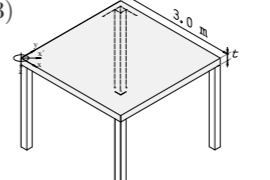
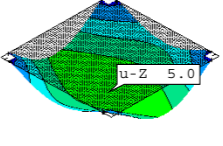
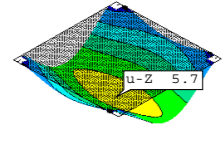
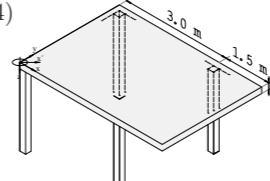
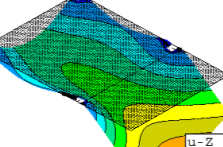
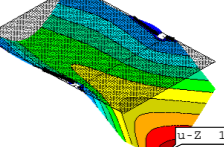
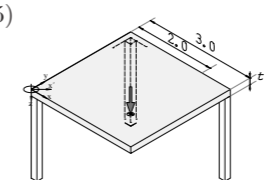
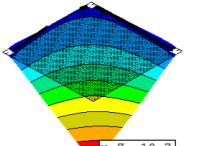
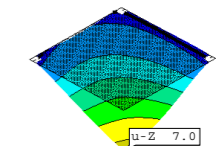
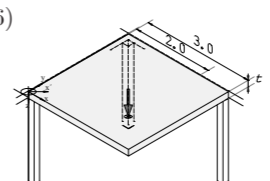
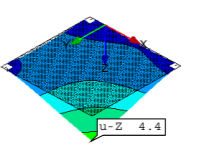
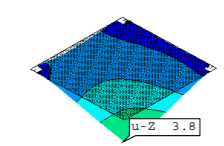
Table 10.4 shows, that the 7-layered DLT±45° D8 series is in general more efficient for uniaxial and biaxial load transfer of linearly supported mass timber slabs, than its 7-layered CLT counterpart. Only for uniaxial bending around the y axis (system (7)), the maximum deformation of the DLT D8 series is higher by 5.9 %, than the deformation of the CLT O8 series. When considering the layup as well as the stiffness matrices, this is not surprising. The bending stiffness in x direction (B_x) of O8 series is slightly higher than the one of D8 series, while the out-of-plane shear stiffness values (S_{xz}) of both series are in the same range (Appendix A7).

Instead of an increase of +118.5 %—as achieved for the 5-layered DLT in comparison to the 5-layered CLT (Table 10.2, system (8))—, the 7-layered DLT D8 series provides a decrease of the maximum deformation by 6.8 % for uniaxial bending around the x axis (Table 10.4, system (8)). For slabs linearly supported on all edges, similar to the 5-layered DLT, the 7-layered DLT experiences 8.8 % less deformations than it does for the CLT. If a cantilever is added, the maximum deformations of the 7-layered DLT and 7-layered CLT series resemble (system (10)). For the special construction of circular mass timber slab over linear support (circular platform), the 7-layered DLT element achieves 12.0 % less deformations than its CLT counterpart (system (11)).

In the context of application-optimized mass timber elements, the layouts can and should be adjusted depending on the prevailing static systems and load cases. Therefore, an additional deformation analysis is carried out for a 7-layered DLT±45° series with a higher number of diagonally arranged layers. The 7-layered DLT D9 series features four layers oriented at +45° and -45° (see Table 4.8).

Table 10.5 compares the deformations of DLT D9 series to DLT D8 series for slabs with point-supports. The hypothesis is, that the deformation behavior of D9 series under biaxial bending is much better, than for D8 series. This may be due to the higher torsional stiffness of D9 series ($B_{xy,D9} = 3.31$ MNm²/m), compared to D8 series ($B_{xy,D8} = 1.94$ MNm²/m). The static systems (1) to (6) equal those of Tables 10.1 and 10.3. The loading remains unchanged.

Tab. 10.5: 7-layered DLT±45° D8 and D9 series under uniaxial and biaxial bending due to point-supports

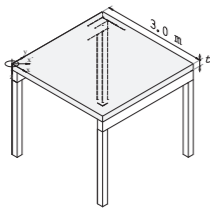
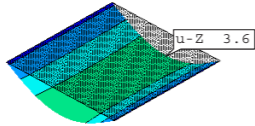
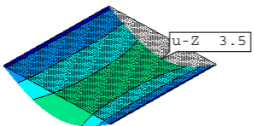
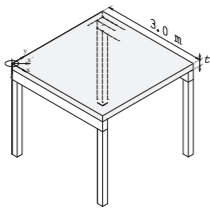
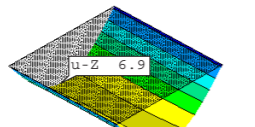
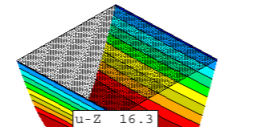
loading	system	deformation w_z		$w_{z,max}$
		DLT (D8 series)	DLT (D9 series)	
	w / l			
p / P	3.0 m / 3.0 m	20-20-20-20-20-20 [0°, 90°,45°,90°,-45°,90°,0°]	20-20-20-20-20-20 [0°,45°,-45°,90°,45°,-45°,0°]	D9/ D8
5.0 kN/m ²	(1) 			+ 57.8 %
5.0 kN/m ²	(2)  four rotationally restrained edges			- 34.4 %
5.0 kN/m ²	(3) 			+ 14.0 %
5.0 kN/m ²	(4) 			+ 20.2 %
5.0 kN	(5) 			- 34.6 %
5.0 kN	(6)  two rotationally restrained edges			- 13.7 %

On the one hand, the absence of the additional cross-layers in the layout of the DLT D9 series leads to significantly higher bending deformations around the x axis than for the DLT D8 series (+ 47.8 %, situation (1)). On the other hand, if the four plate edges are rotationally

restrained and the locking effect due to a single curvature is prevented, the centrally point-supported DLT D9 series provides by 34.4 % smaller deformations than the DLT D8 element (see system (2)). Within system (5) (plate under pure torsion), the maximum deformation of D9 series is lower by 34.6 %, than the deformation of D8 series and therefore lower by 48.6 % compared to the CLT O8 series providing same layer thicknesses.

For completeness, Table 10.6 compares the uniaxial deformations of the DLT $\pm 45^\circ$ D9 series with D8 series due to linear support. The static systems and the loading are identical to those in Tables 10.2 and 10.6, however, only the two governing systems (7) and (8) are presented.

Tab. 10.6: 7-layered DLT $\pm 45^\circ$ D8 and D9 series under uniaxial and biaxial bending due to linear supports

loading	system	deformation w_z		$w_{z,max}$	
		w/l	DLT (D8 series)		DLT (D9 series)
p/P	$3.0\text{ m} / 3.0\text{ m} (r = 3.0\text{ m})$		20-20-20-20-20-20-20 [0°, 90°, 45°, 90°, -45°, 90°, 0°]	20-20-20-20-20-20-20 [0°, 45°, -45°, 90°, 45°, -45°, 0°]	D9/ D8
5.0 kN/m ²	(7) 			- 2.8 %	
5.0 kN/m ²	(8) 			+ 136.2 %	

In the following, 3D FE models are created of centric point-supported slabs with rotationally restrained edges (in reference to system (2)) and slabs, point-supported at three corners (in reference to system (5) and (6)). The volume models are generated representing both, mass timber slabs made from CLT and DLT. The models are used to analyze the distribution of normal stresses and shear stresses over the cross-sections. The construction grid and the static systems of the 3D FE models follow the static system of the respective 2D FE models. Therefore it is possible, to cross-check and validate the 3D FE models by comparing the deformations of the 3D FE models to those of the 2D FE models.

10.2 Stress distribution analysis using 3D FE models (ULS)

10.2.1 General information and modelling approach

For the calculation of the stress values and the analysis of their distribution over the cross-section, volume models can be a useful tool. Therefore, the software Ansys (version 2022.R1) is used. The models and results obtained should be relevant for practical implementation of DLT and the strength verification in the ULS.

In a first step models of centric point-supported slabs are chosen for the detailed stress analyses (see Figure 10.3). The rotationally restrained plate edges represent continuous flat slabs. The static systems are equivalent to system (2) of the investigations using the 2D FE models featuring the dimension $w/l = 3.0/3.0\text{ m}$ (see Tables 10.1, 10.3 and 10.5). The models are again loaded with a constant surface load of $p = 5.0\text{ kN/m}^2$.

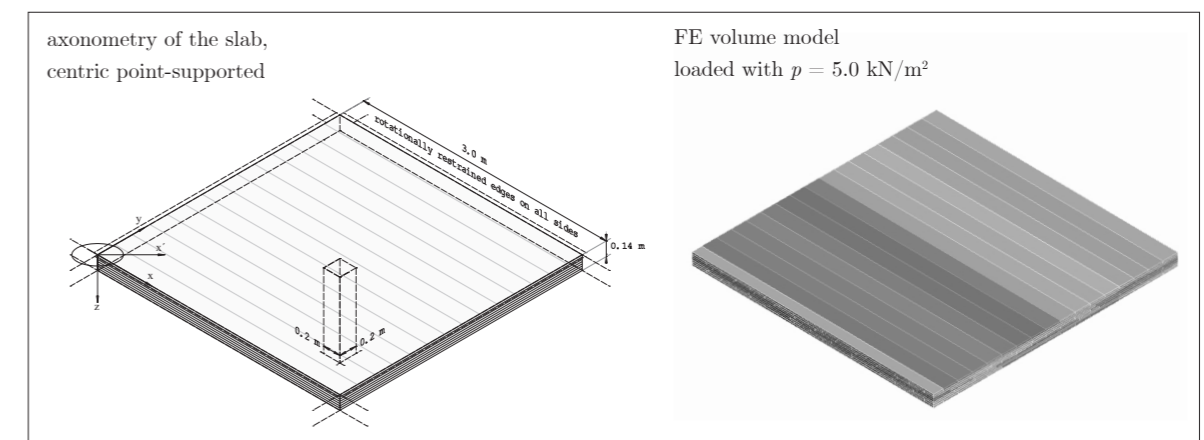


Fig. 10.3: Axonometry of the centric point-supported slab (left) and an exemplary 3D FE model (Ansys)

In addition, models of flat slabs with point-supports at three corners are created ($w/l = 3.0/3.0\text{ m}$). The models are loaded with a point-load $P = 45\text{ kN}$, equivalent to the vertical reaction force of the centric point-supported slab. Two edges of the plate are rotationally restrained, the opposing edges are free (see Figure 10.4). Afterwards, the rotational constraint at the edges is removed.

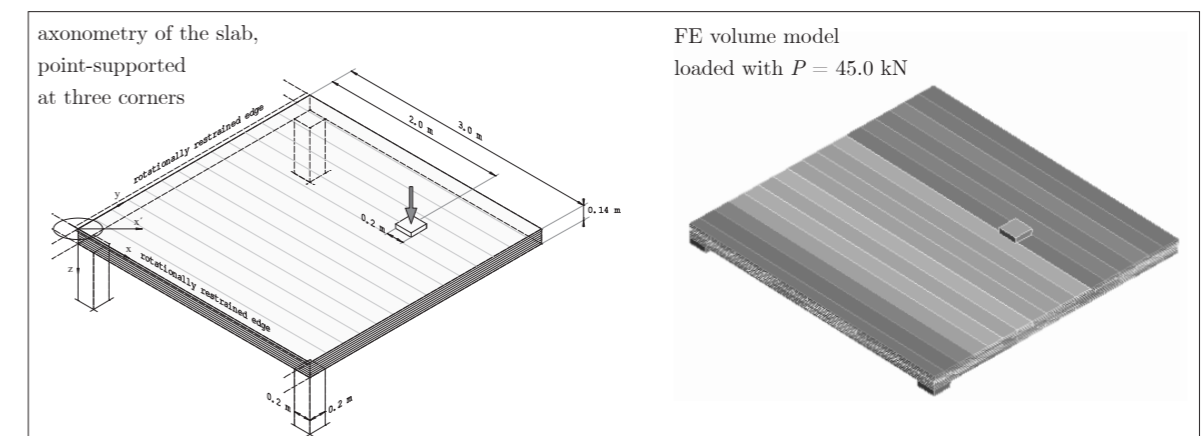


Fig. 10.4: Axonometry of the slab, point-supported at three corners (left) and an exemplary 3D FE model (Ansys)

The investigations are carried out on 7-layered CLT O8 series, and the 7-layered DLT $\pm 45^\circ$ D8 series. These series provide appropriate deformation values in their respective main application area in the SLS, and may therefore be well suited for direct comparison in the ULS. For CLT O8, the advantages in the SLS became clear for uniaxial load transfer, and for DLT D8, the advantage became clear for uniaxial and biaxial load transfer (see Chapter 10.1).

Within the 3D models each lamination was modeled separately and the contacts were defined afterwards (the board width was 180 mm without edge-gluing). The size of the mesh was set to 10 mm (layer thickness $t_i/2$). Additionally, the essential parameters for the numerical models are summarized in tabular manner in Appendix A4.

The bearing as well as the application of the surface loads were realized by "external displacements" and "forces", related to the respective surfaces. Following the procedure of the 2D FEM models, the column of the centric point-supported slab is fixed in all directions ($x = y = z = 0$) and defined as rotationally rigid ($\varphi_x = \varphi_y = \varphi_z = 0$). For plates that are point-supported at three corners, only one horizontal fixed support is defined. The opposite bearing points were fixed in the global z direction only and are free in the global x and y direction. Rotational constrained plate edges were defined by adding external displacements with the attributes ($\varphi_x = 0$ or $\varphi_y = 0$) to the respective surfaces. The material parameters according to Table 4.9 (T14; ETA20/0023) and the *Poisson's* ratios according to (HALÁSZ AND SCHEER 1996) were applied.

In order to validate the volume models, Figure 10.5 exemplifies and compares the deformations of DLT D8 series of the 3D FE model with the deformation of the 2D models previously investigated. The static system equals the centric point-supported plate with rotationally restrained edges. The deformations are given within sections A-A (diagonal over the mid-plane). Both models are loaded with a constant surface load of $p = 5.0 \text{ kN/m}^2$. Even if the functions of the deformations differ slightly, the maximum values are almost identical ($w_{z,\max,3D} = 3.27 \text{ mm}$; $w_{z,\max,2D} = 3.19 \text{ mm}$).

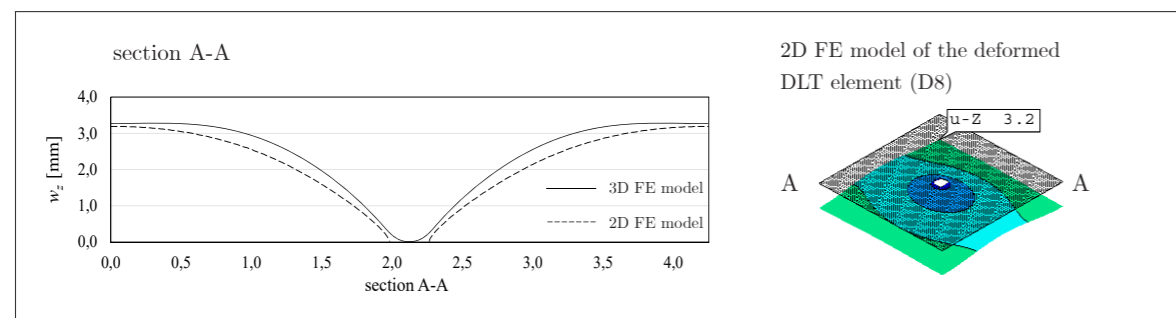


Fig. 10.5: Comparison of the deformations of centric point-supported mass timber slab using 3D and 2D FE models

10.2.2 Stress distribution analysis of a centric point-supported plate

For the analysis and display of the stress distributions, longitudinal sections in x and y direction are defined over a length of 1.0 m. In addition, sections in x' and y' directions are defined within the plate element. The sections are arranged in a star shape around the load introduction point (center of the column). The edges of the longitudinal sections describe a circular section with a radius of 1.0 m (see Figure 10.6).

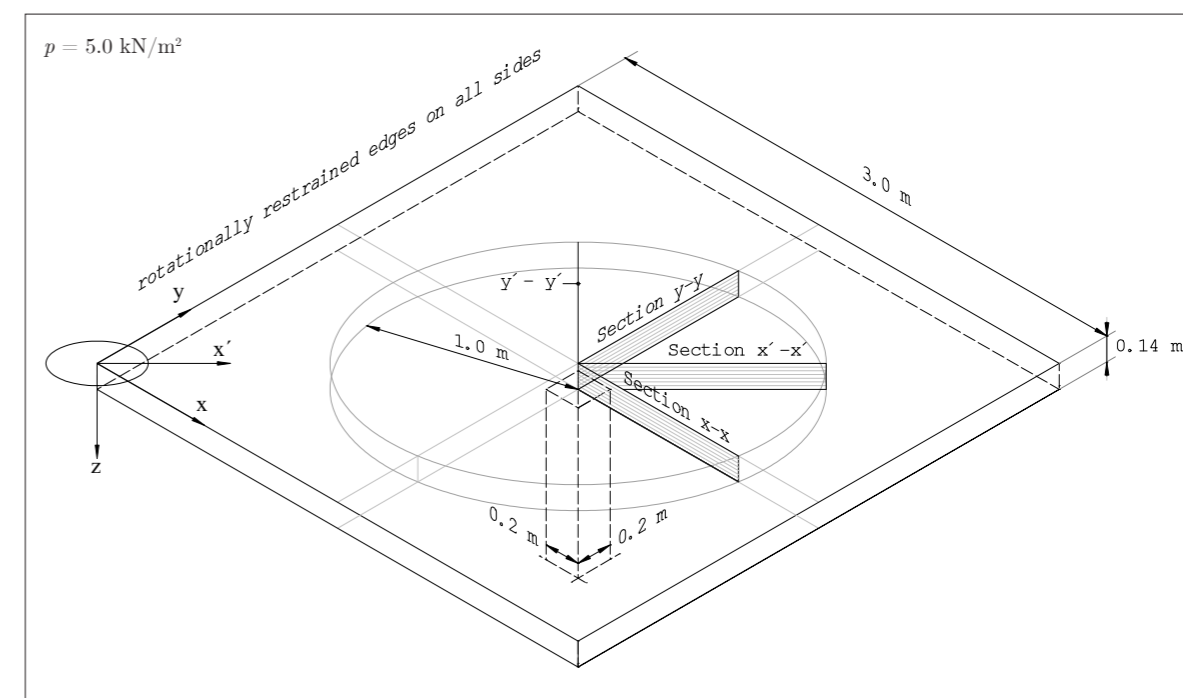


Fig. 10.6: Circular and longitudinal design sections within the centric point-supported mass timber slab

Within the longitudinal sections, normal stresses due to bending and the out-of-plane shear stresses are given for design-relevant punching shear perimeters. These perimeters are considered as the critical sections, in which shear failures could occur (perimeters for stress verification). The perimeters are dependent on the thickness of the plate and the dimensions of the column (d). For the plates with the thickness of $t = 140 \text{ mm}$, the first perimeter is defined by the distance $d/4 = 0.05 \text{ m}$ (see Figure 10.7). This value appears to be in accordance with the suggestions of Working Draft SC5.T1, following a load-distribution angle of $\alpha = 35^\circ$. The second perimeter is specified as $2d = 0.4 \text{ m}$ in accordance with EC 2 (DIN EN 1992-1-1). The third perimeter equals the radius $r = 1.0 \text{ m}$ of the circular section.

In the following, the stress distributions occurring within the 3D CLT and 3D DLT $\pm 45^\circ$ models are compared to each other (Figures 10.7 to 10.9). The aim of this stress analysis is a statement regarding the load-bearing capacity in the ULS. On the left side of these figures, the graphical display of the stresses within the CLT elements are given. On the right side, the stresses within the DLT element are given.

Each layer is assigned a color according to its orientation to the considered section. Layers oriented longitudinally to the considered section are displayed in white, layers oriented

crosswise to the considered section are displayed in gray. Diagonally oriented layers are displayed in green (in this case $+45^\circ$ or -45° to the considered section). In addition, the respective layer orientation and designation of the sections (x - x ; x' - x' ; y - y ; y' - y') is indicated on the left hand side of each section.

- Normal stresses due to bending (centric point-support)

Figure 10.7 shows the normal stresses due to bending (bending stresses) for each layer in the critical sections $d/4$ and $2d$ as well as in the circular section r . The sections are scaled 1:20. A stress amplitude of 10 mm equals 2.0 MN/m². Tensile stresses are signified in red, compression stresses are given in blue. The extreme values of each stress amplitude are given beneath or above the respective section.

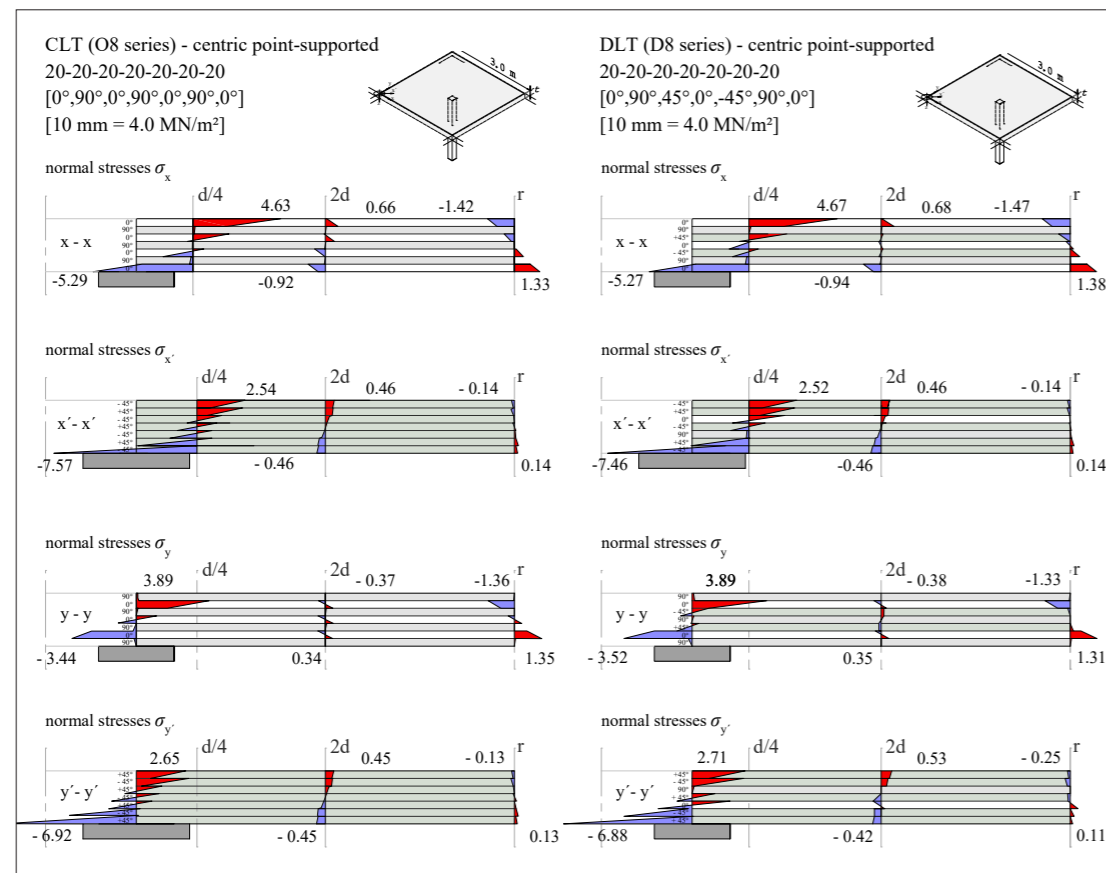


Fig. 10.7: Normal stresses due to bending acting along the critical sections (centric point-support)

The bending moment is always the same for the CLT and DLT at the considered perimeters, since the former depends on the static system and the load. The moment results from the integration of the bending stresses over the cross-section. Thus, the value of the integral is always constant, but the respective distribution of the stresses are not. The extreme values of the normal stresses due to bending are in a comparable range for the CLT and DLT elements. Within section x - x , the maximum bending stress value appears to be slightly higher for the CLT ($\sigma_{x,CLT} = -5.29$ MN/m²), compared to

the DLT element ($\sigma_{x,DLT} = -5.27$ MN/m²) (see $d/4$ perimeter). The slightly different maximum values observed for the DLT result from the different stress distribution over the cross-section compared to the CLT. This can be seen, for example, in the longitudinal y' - y' section (upper edge of $d/4$ perimeter). The diagonal $+45^\circ$ layer of the DLT element is oriented at 90° with respect to the y' - y' section. Due to the low modulus of elasticity in transversal direction, almost no normal stresses act in the respective layer. These are transferred to the layers above and below. In this case, slightly higher stress peaks in the outer layers (upper edge) of the DLT element occur, compared to the CLT element. However, these minor differences will hardly influence the load-bearing capacity.

- Compression stresses perpendicular to grain (centric point-support)

Figure 10.8 highlights the compression stresses perpendicular to grain acting along the longitudinal sections. The values are given in the midplane of the plate and in a distance of 30 mm to the load-introduction point. The aim is to analyze the compression stresses in the areas relevant for the verification of the out-of-plane shear capacity (due to the interaction compression perpendicular to grain and shear). The sections are again scaled 1:20. A stress amplitude of 10 mm equals 1.0 MN/m².

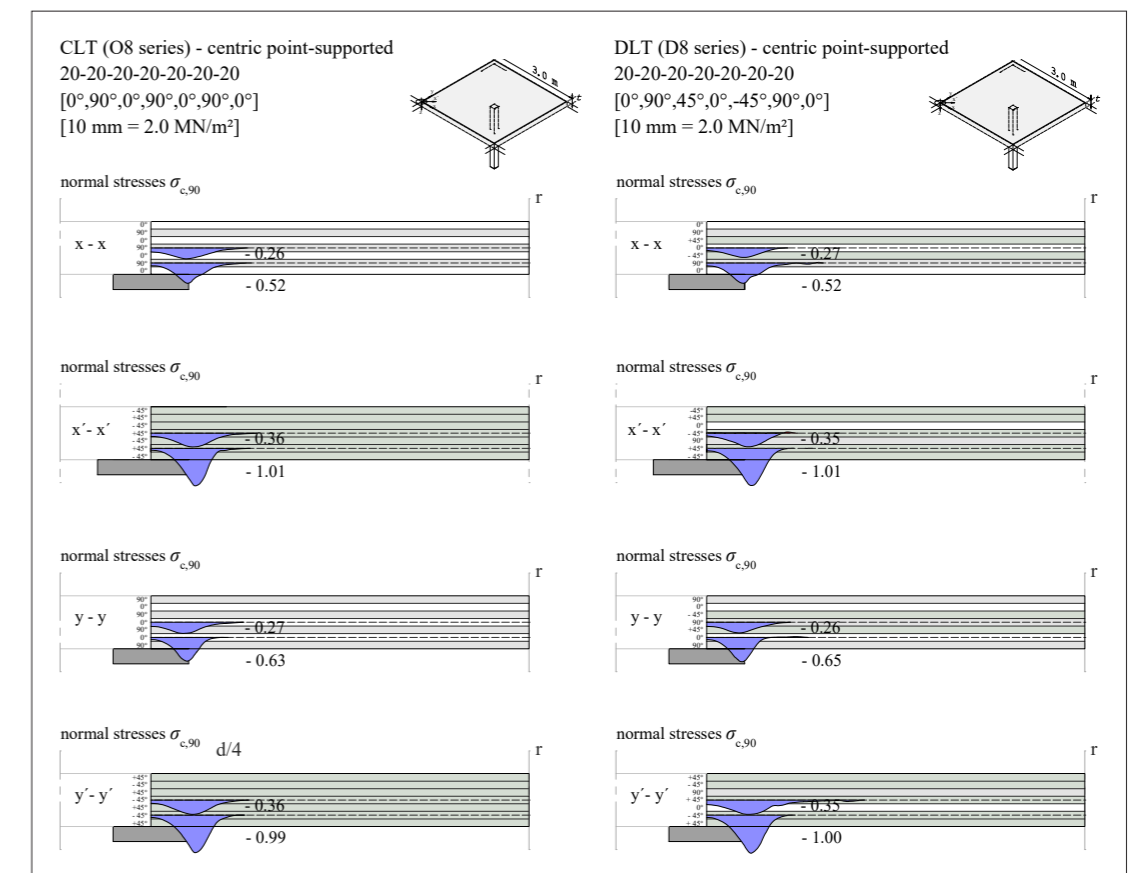


Fig. 10.8: Compression stresses acting along the longitudinal sections (centric point-support)

A concentration of compressive stresses perpendicular to grain occurs in the sections near the supports. These stress concentrations are clearly higher in the diagonal sections $x'-x'$ and $y'-y'$ than in the $x-x$ and $y-y$ sections. This can be explained by the rectangular shape of the supports, whose corners lead to stress concentrations. Local constrictions in the support area at the corners of the column cannot be prevented under biaxial bending. In general, the compression stresses perpendicular to grain in the design-relevant and critical sections vary between 0.3 MN/m^2 and 1.0 MN/m^2 . During the experimental investigations, a value of 0.5 MN/m^2 was chosen (see Chapter 6.2).

- Out-of-plane (punching) shear stresses (centric point-support)

Figure 10.9 displays the out-of-plane shear stresses in the critical sections $d/4$, $2d$, and r . The sections are in a scale of 1:20 and a stress amplitude of 10 mm equals 1.0 MN/m^2 . The maximum punching shear stress values of each stress amplitude are given below the respective perimeter.

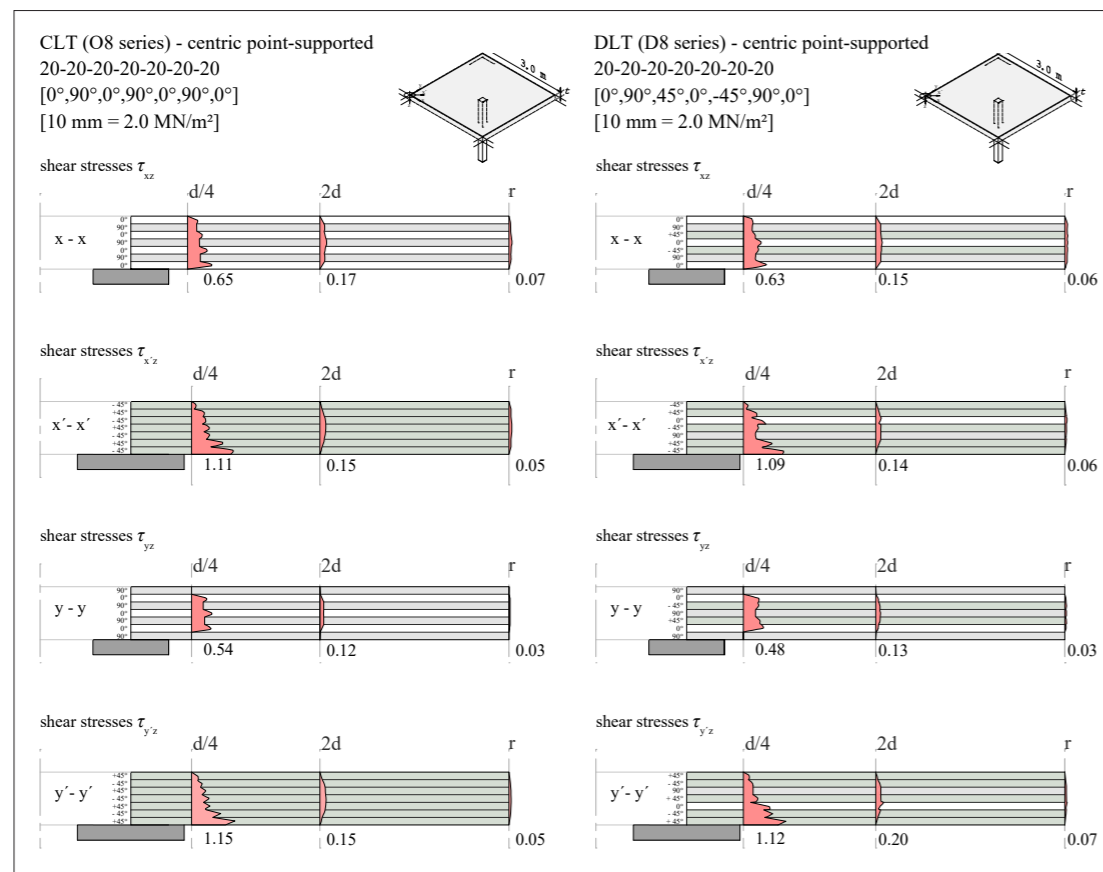


Fig. 10.9: Punching shear stresses acting along the critical sections (centric point-support)

For CLT and DLT, the maximum values of shear stresses are observed in x' and y' direction. The largest shear stresses occur close to the point-support ($d/4$ perimeter). This is consistent with the design specifications of Working Draft SC5.T1.

As is the case for the bending stresses and the moment m , the integration of the shear stresses over the cross-section results in the same value of the shear force q_{iz} (V_i) for CLT and DLT at the respective perimeters. On the other hand, the distribution of the shear stresses over the cross-section depends on the stiffness parameters of the single layers and their orientation. The advantage regarding the distribution of shear stresses in DLT compared to CLT becomes obvious. Similar to the distribution of bending stresses, the stiffer layers oriented at 0° , with respect to the $x'-x'$ and $y'-y'$ sections, accumulate shear stresses and thus reduce the governing design values.

Considering only the global x and y directions, it is also becomes clear that the shear stresses within DLT are more uniformly distributed over the cross-section as they are within CLT. In x and y direction, a homogenization effect is achieved for DLT with respect to the shear stresses. This is particularly evident in the y direction.

In the following, the static system is modified. Instead of centric point-supported plates, the stress analysis is carried out on plates with point-support at three corners.

10.2.3 Stress distribution analysis of a plate, point-supported at three corners

In order to analyze stress distributions within CLT and DLT elements within load cases governed by biaxial bending, the stress analysis is carried out for a slab with point-supports at three corners. The dimensions of the slab remain the same compared to the previous static system ($w/l = 3.0/3.0$ m). Each column has the dimensions of $w/l = 0.20/0.20$ m. In a first step, two edges of the plates are modelled with rotational restraint, so as to simulate a continuous flat slab with a cantilevered corner (see Figure 10.10). These 3D FE models are consistent to system (6) of the 2D FE models (see Chapter 10.1, Tables 10.1, 10.3, and 10.5). In a second step, the plate elements, point supported at three corners, are modelled with four free edges (see Figure 10.14, consistent to system (5)).

Once more, stress analysis are carried out in longitudinal sections, forming a circular section with radius $r = 1.0$ m. The center of this circular section is located beneath the load application point (see Figure 10.10). The longitudinal sections are again arranged in a star shape around this point. However, the model is now loaded with a point load of $P = 45$ kN, equivalent to the vertical reaction force of the centric point-supported slab. This guarantees comparability.

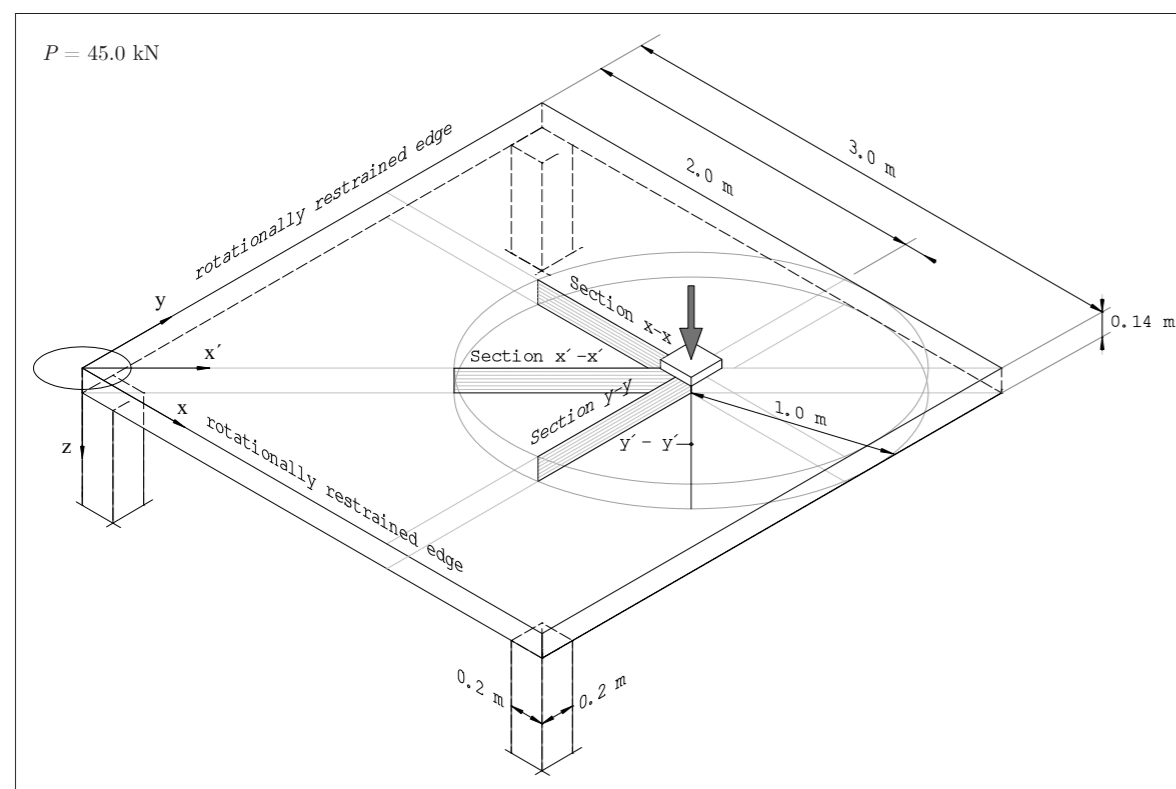


Fig. 10.10: Circular and longitudinal design sections within the mass timber slab, point-supported at three corners, with rotational restraint at two edges

- Normal stresses due to bending (point-supported at three corners)

Figure 10.11 gives the normal stresses due to bending for each layer in the critical sections $d/4$ and $2d$ as well as in the circular section r . The sections are scaled 1:20 and a stress amplitude of 10 mm equals 2.0 MN/m².

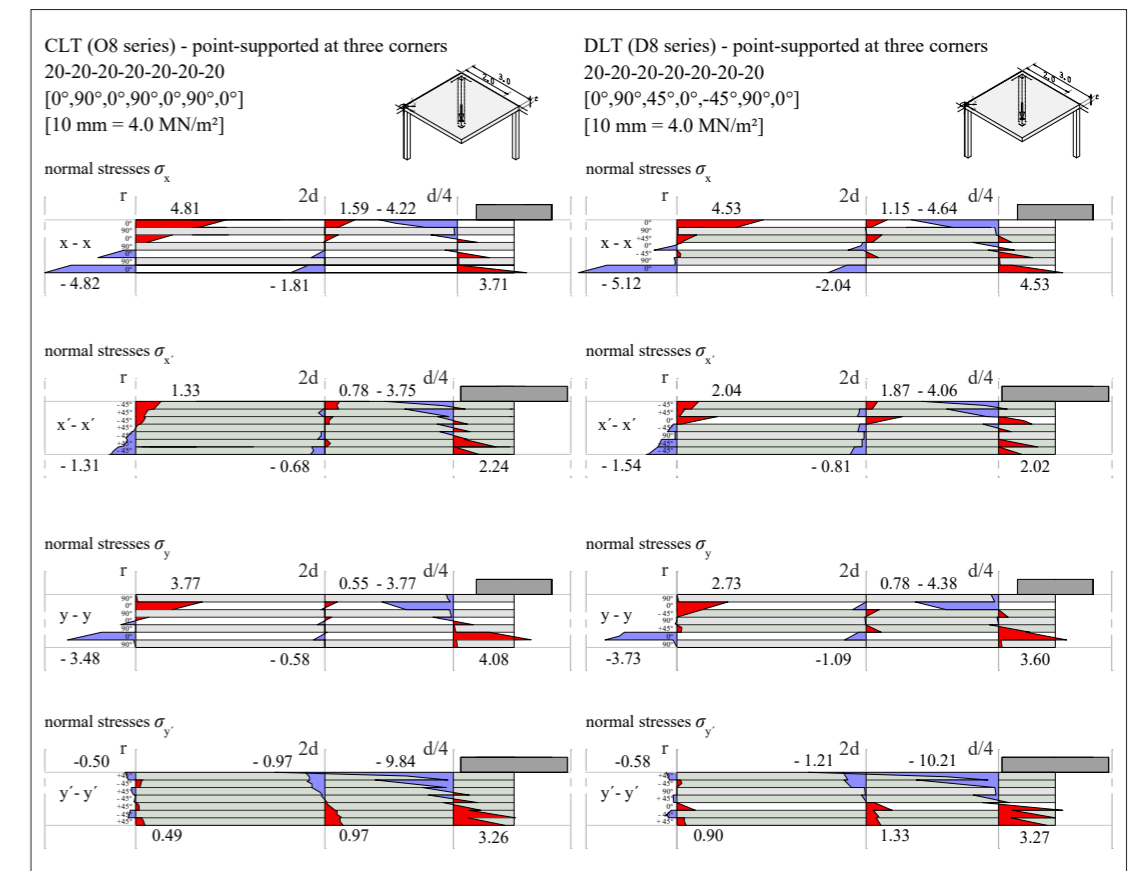


Fig. 10.11: Normal stresses due to bending acting along the critical sections (point-supported at three corners)

The maximum normal stresses in the $d/4$ perimeter are higher for the DLT element in the x' and y' directions than for the CLT element. The zero point of stresses (change from compression to tension) of the normal stresses in the DLT element is shifted by the $+45^\circ$ respective -45° layers towards the compression zone. This is due to the fact that the layer, which is now oriented at 0° to the longitudinal $x'-x'$ and $y'-y'$ section takes higher normal forces. Looking at the stresses in the rotational section r , this effect becomes even more evident. In the main load-bearing directions x and y , the maximum bending tensile stresses in the DLT are lower than those in the CLT. Vice versa, the bending compression stresses are higher, due to the displacement of the zero point of stresses. In the y direction, for example, the maximum bending tensile stress in the critical radius is 2.73 MN/m² distributed over the layers oriented at 0° and -45° , whereas in the CLT element 3.77 MN/m² occur at the same location, distributed over the 0° layer.

- **Compression stresses perpendicular to grain (point-supported at three corners)**

Figure 10.12 gives the compression stresses perpendicular to grain within the longitudinal sections. The scale of the sections stays at 1:20. An amplitude of 10 mm represents 1.0 MN/m².

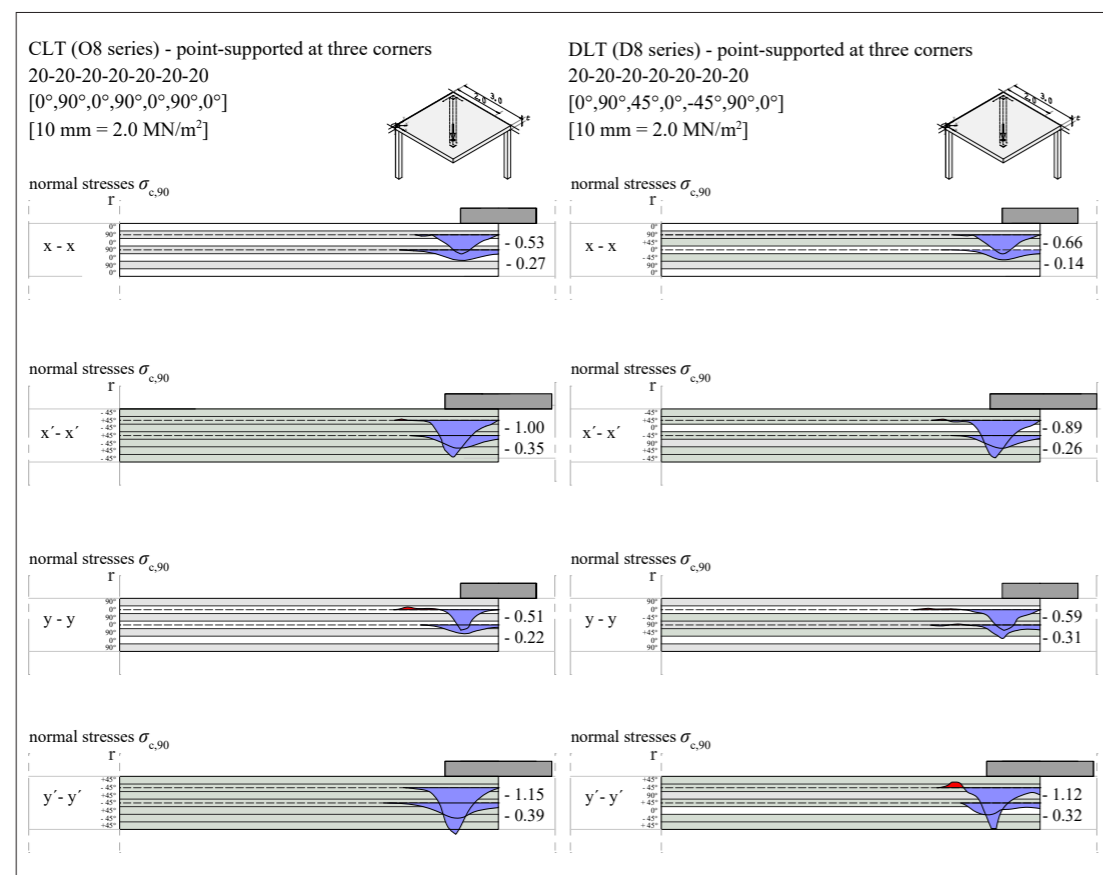


Fig. 10.12: Compression stresses acting along the longitudinal sections (point-supported at three corners)

The distribution of the compression stresses should be almost identical for the CLT and DLT elements in the respective sections. The plots confirm this assumption. Compared to the compression stresses perpendicular to grain for the centric point-supported slab (Figure 10.8), whose reaction force corresponds to the point-load within this system, the stresses perpendicular to grain are increased in the y and y' directions. This can be explained by the asymmetric loading of the slab with point-supports at three corners and rotationally restrained edges.

The increased compression stresses beneath the load application area lead to slight tensile stresses perpendicular to grain next to the load application (see Figure 10.12). These reduce the shear strength, leading to rolling shear failures in combination with tension perpendicular to grain. Such combined failure mechanism were also observed in the biaxial bending test (see Tables 8.2 and 8.3).

- **Out-of-plane (punching) shear stresses (point-supported at three corners)**

Figure 10.13 demonstrates the out-of-plane shear stresses in the critical sections $d/4$ and $2d$ as well as in the circular section r . The sections are again displayed in a scale of 1:20. A stress amplitude of 10 mm equals 1.0 MN/m². Similar to Figure 10.9, the maximum punching shear stress values of each stress amplitude are given below the respective perimeter.

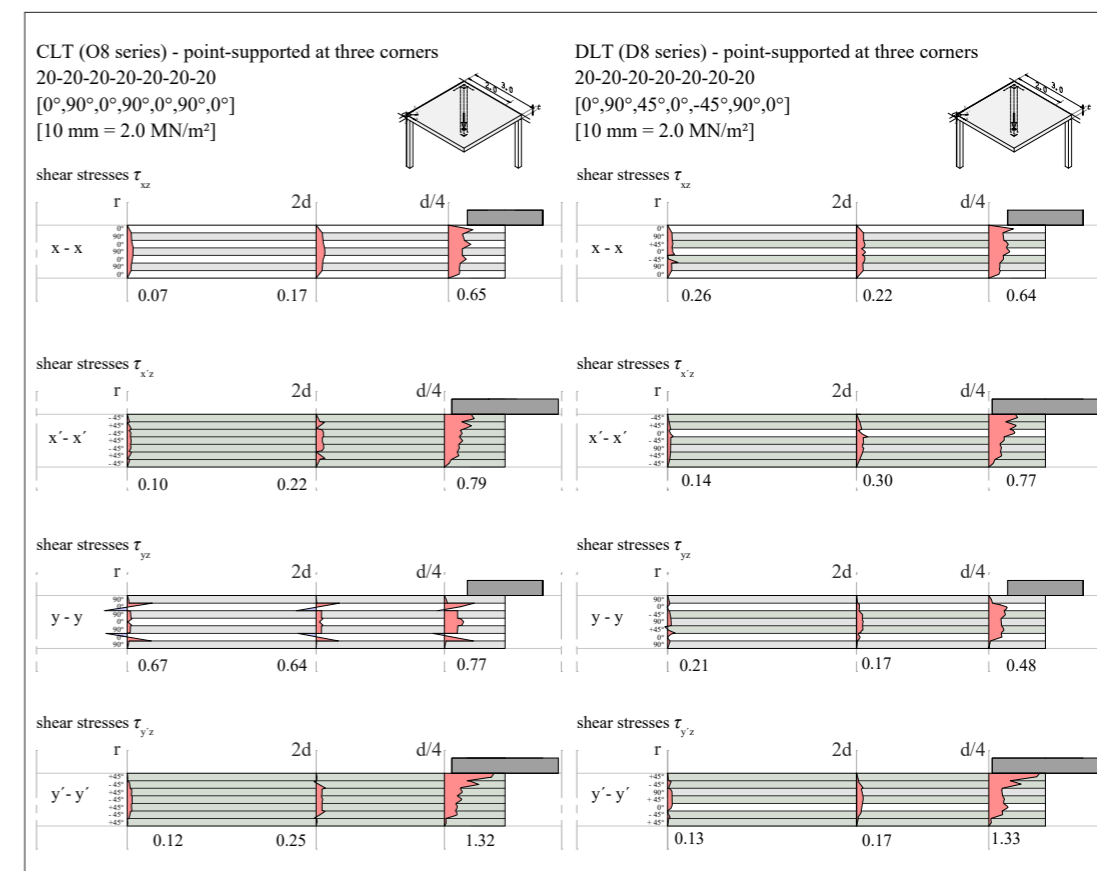


Fig. 10.13: Punching shear stresses acting along the critical sections (point-supported at three corners)

For CLT and DLT, the maximum values of the shear stresses in the slab are again obtained in the x' and y' directions. The maximum stresses are reached in the area of load application ($d/4$ perimeter). Within the longitudinal x-x and x'-x' sections as well as in the y'-y' section, no significant differences between CLT and DLT can be observed for the distribution and the maximum values of the shear stresses.

On the other hand, the distribution of the out-of-plane shear stresses of the CLT and DLT elements in y-y section is striking. The homogenization effects of the shear stresses, which were already observed in Figure 10.13, are now more pronounced for DLT. In the CLT element, clear stress peaks occur within the distribution of shear stresses in the longitudinal 0° layers of section y-y. These shear stress profiles are typical for a cross-section under torsional stresses. The out-of-plane shear stresses in y-y direction are therefore referred to torsional shear stresses mainly. The linear stress

distribution is caused by the torsional moments, acting longitudinally to the 0° layers. Within the chosen CLT element, the shear flow can hardly be transferred from the stiff 0° layers to the soft 90° layers. For DLT on the other hand, the distribution of shear stresses over the cross-section is homogenized by the comparatively high moduli of elasticity and shear moduli of the $+45^\circ$ and -45° layers within the inner layers. Moreover, for both, CLT and DLT, the outer layers in the y-y section are nearly taking zero shear stresses, due to the missing edge-gluing (also see Chapter 6.1). Therefore the shear stresses are concentrated within the inner five layers. For the stress verification in the ULS, shear verification for both, longitudinal and transversal oriented layers to the respective longitudinal sections have to be considered.

In the following the rotational restraint is removed (see Figure 10.14). The dimensions of the slab remain at $w/l = 3.0 \text{ m} / 3.0 \text{ m}$. Also the point-load stays constant at $P = 45 \text{ kN}$. The plate acts in pure torsion. The static system of the presented 3D FE models is consistent to system (5) of the 2D FE models (see Chapter 10.1).

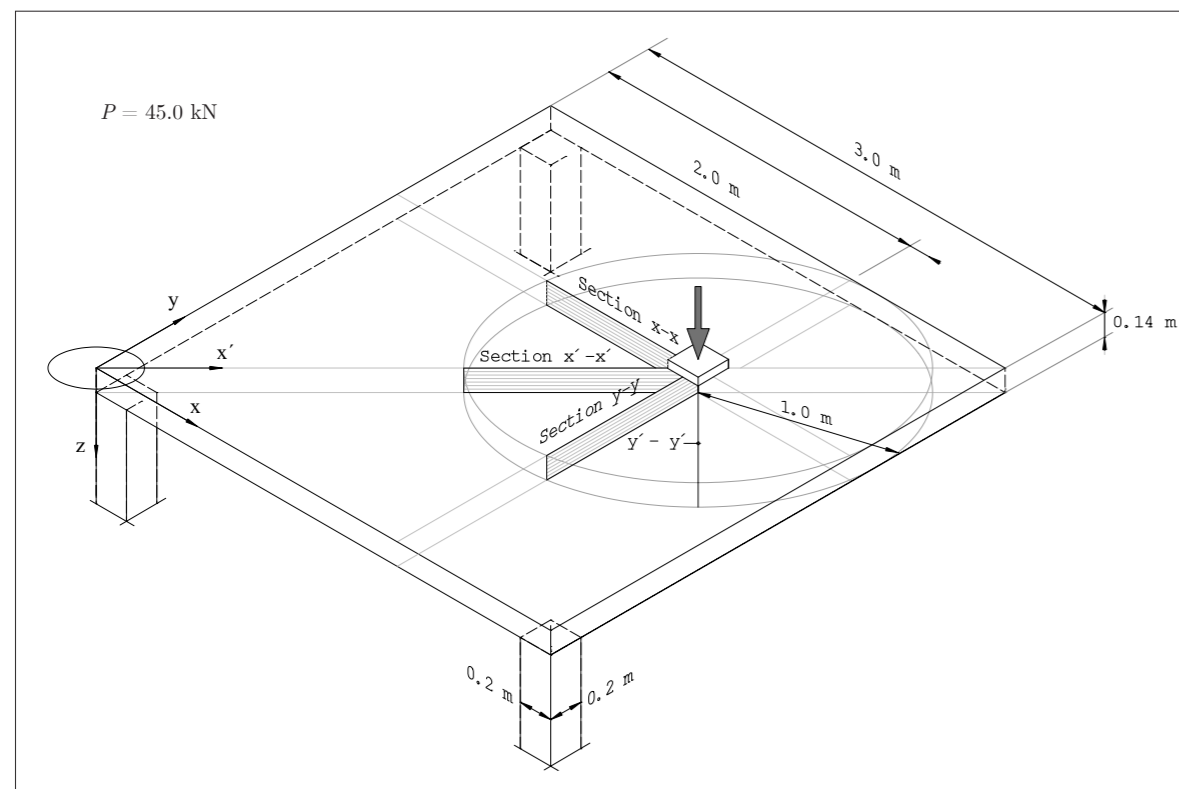


Fig. 10.14: Circular and longitudinal design sections within the mass timber slab, point-supported at three corners without rotationally restrained edges.

- Normal stresses due to bending (point-support at three corners, without rotationally restrained edges)

Figure 10.15 gives the normal stresses due to biaxial bending in the critical sections $d/4$ and $2d$ as well as in the circular section r . The sections are scaled 1:20 and a stress amplitude of 10 mm equals 2.0 MN/m².

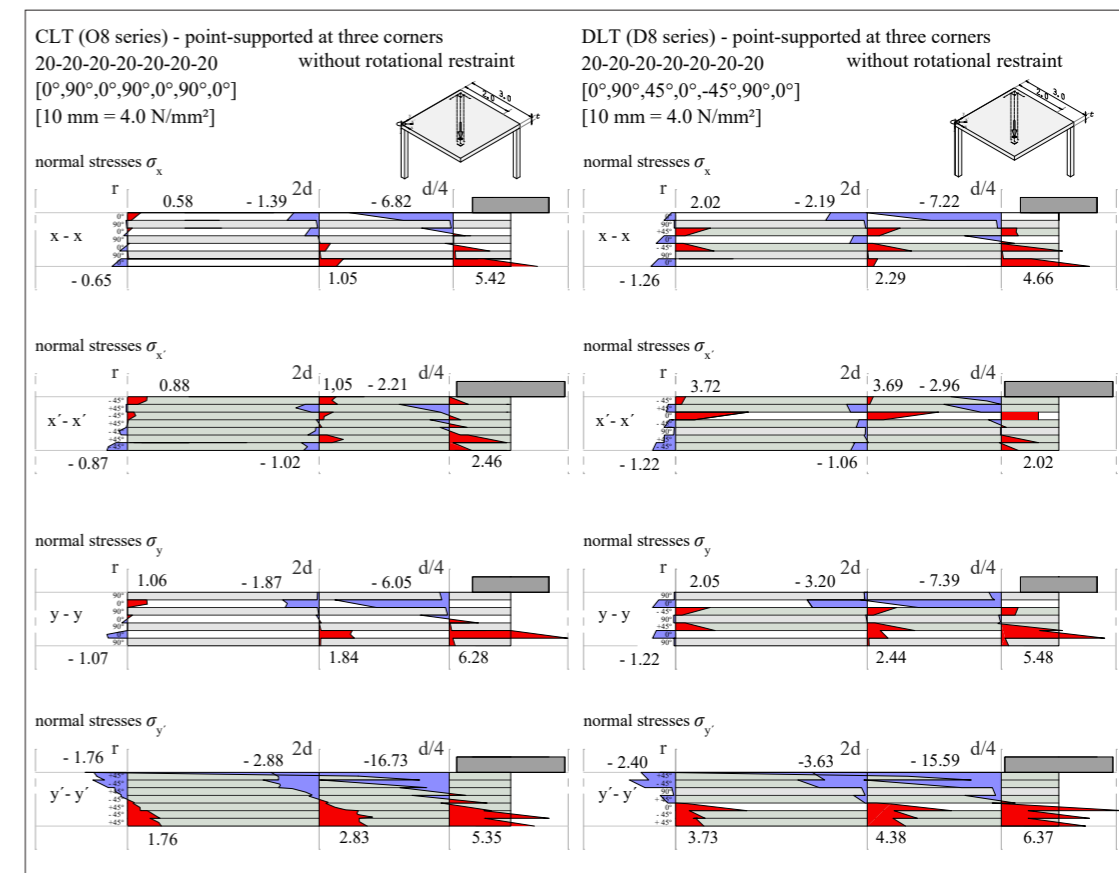


Fig. 10.15: Normal stresses due to bending acting along the critical sections (point-supported at three corners without rotationally restrained edges)

The maximum normal stresses in y'-y' direction at $d/4$ perimeter are highly increased for the CLT and DLT specimens, due to the missing boundary condition of the rotationally restrained edges. Even though the deformation of the CLT O8 element under pure torsion is smaller by 21.3 % than the maximum deformation of D8 series, the maximum normal stress value (bending compression stress) in y' direction of O8 series is higher by -1.14 MN/m^2 , than for D8 series (see $d/4$ perimeter, y'-y' section).

The y'-y' section acts as a single axis beam under bending. In x'-x' direction, the section can be regarded as a single axis beam, which bends over the y'-y' section (with opposite curvature and thus opposite orientation of the compression and tension zones in the cross-section). The global $+45^\circ$ layer of the DLT (oriented at 0° in x' and y' section) accommodates the higher bending tensile stresses ($\sigma_{x',\max} = 3.72 \text{ MN/m}^2$ and $\sigma_{y',\max} = 6.37 \text{ MN/m}^2$). It is thus provoked that, unlike in the CLT, the layer oriented at 0° to the considered section absorbs the maximum normal stresses. This follows the theoretical approach of fictive tension and compression parabolas (also see ARNOLD ET AL. 2023a).

- **Out-of-plane shear stresses (point-support at three corners, without rotationally restrained edges)**

Figure 10.16 highlights the distribution of the out-of-plane shear stresses due to biaxial bending in the critical sections $d/4$ and $2d$ as well as in the circular section r . The sections are set to a scale of 1:10. A stress amplitude of 10 mm equals 1.0 MN/m².

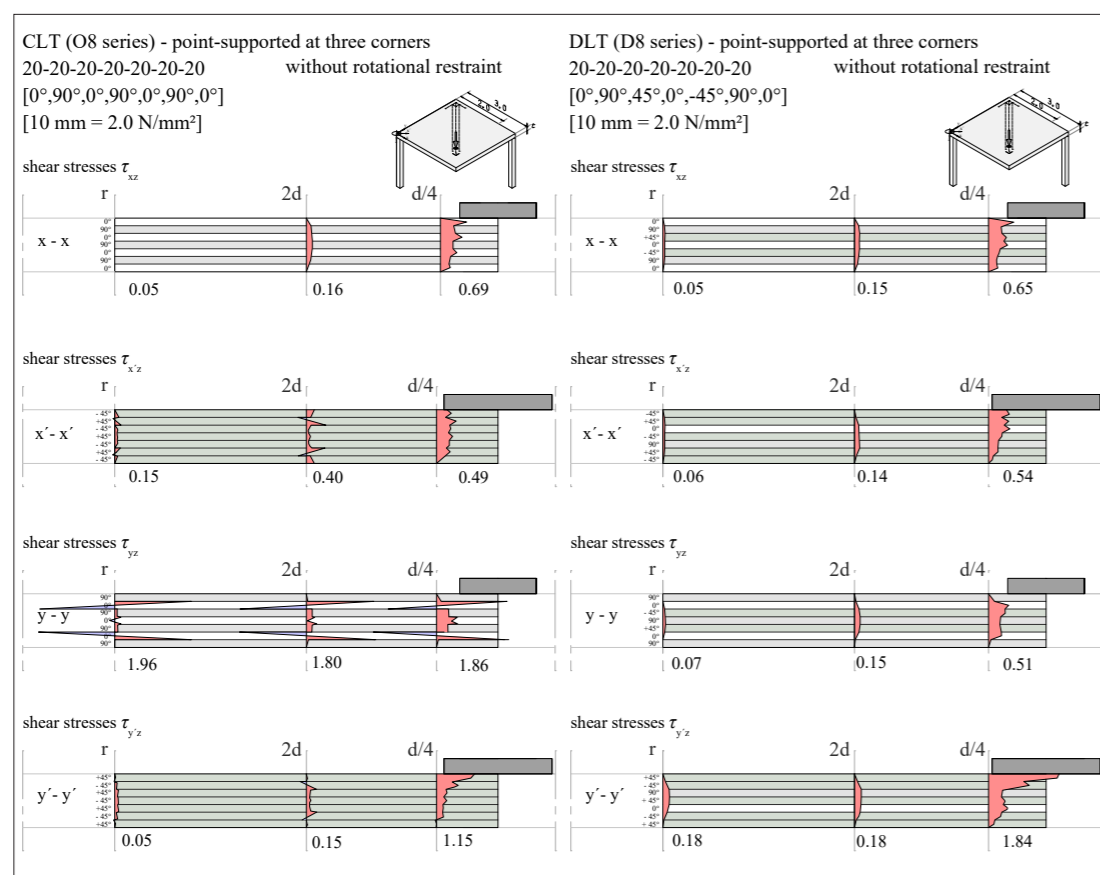


Fig. 10.16: Punching shear stresses acting along the critical sections (point-supported at three corners without rotationally restrained edges)

The maximum values of the shear stresses under mainly torsion are in a comparable range for CLT and DLT in x-x section. In sections x'-x' and y'-y', the large torsional shear stresses in the CLT now also affect the overall shear stress distributions within the 2nd layers (see $d/2$ perimeter, x'-x' and y'-y' perimeter). For the DLT, on the other hand, the distribution of shear stresses remains rather homogeneous in the x' and y' directions. The previously explained homogenization effect of shear stresses within DLT is even more pronounced. In y direction, the maximum shear stress values of the CLT and DLT appear in the layers oriented at 0° to the y-y section. This value is significantly higher at the $d/4$ perimeter for CLT, than it is for DLT. As previously described, this highly linear and unsteady shear stress distribution within the CLT results from the high torsional moments. However, regarding rolling shear verifications in the ULS, the shear stresses in the cross-layers are nearly on the same level for DLT and CLT in y direction (see cross-layers within the y-y sections).

10.3 Discussion based on the results derived from 2D and 3D FE models

The deformation analyses on various static systems (application scenarios) showed, that a general statement regarding the advantages of DLT in terms of deformations is difficult. The deformations result from the stiffness parameters of the chosen material and layup, undergoing the stress resultants. The stress resultants in turn depend on the static system, the loading, and the chosen layup of the plate element.

To clarify this, Table 10.7 exemplary gives the respective stress resultants (for DLT D7 series) under a constant surface load of 5.0 kN/m² for the static systems (1) and (2) used in Chapter 10.1.

While the torsional moments are the same for both systems with centric point-support, the bending moments m_x and m_y vary considerably. Without the boundary condition of rotationally restrained edges (system (1)), the maximum values m_x and m_y are almost twice as large as those in system (2). This leads to the conclusion, that within system (1) the chosen layup should provide a bending stiffness in y direction being in comparable range to its bending stiffness in x direction. Otherwise, highly uniaxial deformations are to be expected.

This, in turn, is consistent with the findings on the 5-layered elements of the DLT D7 series and the CLT O7 series (see Table 10.1). The maximum deformation in system (1) was significantly higher for the 5-layered DLT series, than for the CLT series (+56.3%), since the spread in bending stiffness in y direction ($B_{y,D7} = 0.32$ MNm²/m; $B_{y,O7} = 0.73$ MNm²/m). If a layup is chosen that provides a more homogeneous distribution of the bending stiffness values in the x and y directions (as it is for DLT D8 series—see Table 10.3), the higher torsional stiffness of DLT becomes apparent and the total deformations are lower than those for CLT.

Tab. 10.7: Comparison of stress resultants within two different static systems for DLT D7 series

system	internal forces (stress resultants)		
$w/l = 3.0 \text{ m} / 3.0 \text{ m}$ $p = 5.0 \text{ kN/m}^2$	m_{xy} [kNm/m]	m_x [kNm/m]	m_y [kNm/m]
(1) 			
(2) 			

By deformation analysis on the chosen 5-layered and 7-layered CLT and DLT elements by means of 2D FE models, it can be stated that for the most application scenarios deformations within the SLS of CLT were higher, than those of DLT. This is based on the respective higher stiffness values of DLT (Appendix A8)—especially regarding the torsional stiffness. Mass timber elements with a strongly asymmetric spread of the bending and shear stiffness values in x and y direction are an exception. This is the case, e.g., for the 5-layered DLT D5 and D6 series, and for the 7-layered DLT D9 series, investigated in this thesis. These series feature only one layer oriented in global y direction. Therefore, their comparable low bending stiffness in y direction, leads to an uniaxial deformation behavior within static systems governed by bending moment m_x and m_y . Nevertheless, these 5-layered elements are still and above all suitable for biaxial load transfer and point-supported slabs governed by torsional moments. This is due to their comparably high torsional stiffness, in contrast to the low bending stiffness in y direction.

- In conclusion, the deformations of the chosen 5-layered DLT $\pm 45^\circ$ series D7 ($t = 150$ mm) were much higher for point-supported slabs (systems (1) to (4): up to +56.3 %) and systems mainly undergoing uniaxial bending in y direction (systems (8) and (11): up to +118.5 %), than of the 5-layered CLT O7 series. As previously described, this is due to the comparable low bending stiffness of the D7 series in y direction ($B_{y,D7} = 0.32$ MNm²/m vs. $B_{y,O7} = 0.73$ MNm²/m) (see Table 10.8).
- For static systems mainly undergoing uniaxial bending in x direction (system (7)), the deformations were in a comparable range, mirroring the similar bending stiffness in x direction of the chosen laminates ($B_{x,D7} = 2.65$ MNm²/m vs. $B_{x,O7} = 2.48$ MNm²/m).
- For static systems governed by torsional moments (systems (5), (6), (9), and (10)), the comparable high torsional stiffness of the DLT D7 series led to smaller deformations compared to the 5-layered CLT O7 series (up to -41.0 %) ($B_{xy,D7} = 3.16$ MNm²/m vs. $B_{xy,O7} = 1.94$ MNm²/m).
- Adding two additional cross-layers achieving 7-layered series D8 and O8 ($t = 140$ mm), results in smaller deformations for the DLT series compared to the CLT series for point-supported slabs (systems (1) to (4): up to -13.5 %) and for systems mainly undergoing uniaxial bending in y direction (systems (8) and (11): up to -12.0 %). This is due to the comparable low spread of the bending and shear stiffness values between the D8 and O8 series ($B_{y,D8} = 0.84$ MNm²/m, $S_{yz,D8} = 8.05$ MN/m vs. $B_{y,O8} = 0.79$ MNm²/m, $S_{yz,O8} = 8.31$ MN/m).
- The same holds true for systems undergoing uniaxial bending in x direction, resulting in nearly similar deformations (system (7): +5.9%).
- For static systems governed by torsional moments (systems (5), (6), (9), and (10)), the impact of the torsional stiffness values of DLT compared to CLT is decreased by the additional cross-layers leading up to -21.3 % smaller deformations of the 7-layered DLT compared to CLT ($B_{xy,D8} = 1.94$ MNm²/m vs. $B_{xy,O8} = 1.03$ MNm²/m).

The deformation analysis of the different DLT and CLT layouts have shown that in the majority of the static systems, the influence of the bending and shear stiffness values become dominant for the resulting total deformation. The torsional stiffness in the form of diagonally arranged layers should be added as an additional benefit so that the distribution of the bending deformation in x and y remains as homogeneous as possible.

Due to this, the terminology "ratio of homogenization" with respect to the number of layers oriented diagonally or crosswise in relation to the overall number of layers, is introduced. Hereby, the layer arrangements θ_i are taken into account by the square of the sinus function ($\sin^2\theta_i$) (Equation 10.1). An isotropic plate element could be stated as an extreme value, providing the range $t_{di}/t_i = 1$. In conclusion, the ratio ξ may serve as an indicator due to the applicability of the chosen layout, regarding structures undergoing uniaxial in addition to biaxial bending in the SLS. However, the ratio introduced should not lead to omitting the advantages of DLT in deformation behavior due to higher torsional stiffness.

$$\xi = \frac{\sum(t_i \cdot \sin^2\theta_i)}{t} \quad (10.1)$$

Tab. 10.8: Exemplary examined static systems featuring point-supports ((1) - (6)) and linear supports ((7) - (11))

point-supports (plate dimension $w/l = 3.0/3.0$ m)					
system (1)	system (2)	system (3)	system (4)	system (5)	system (6)
linear supports (plate dimension $w/l = 3.0/3.0$ m)					
system (7)	system (8)	system (9)	system (10)	system (11)	
DLT $\pm 45^\circ$ D7	CLT O7	DLT $\pm 45^\circ$ D8	DLT $\pm 45^\circ$ D9	CLT O8	
					see Appendix A8

Regarding the stress distribution analysis: The 3D FE models indicated homogenization effects for the stress distributions within DLT elements—especially regarding out-of-plane shear stresses around concentrated load-application. This is remarkable, given that the DLT elements of D8 series experienced smaller deformations than the CLT elements of O8 series, while featuring almost the same extreme values of normal stresses due to bending. For the plates governed by torsion (point-supported plate at three corners under a single load P , without rotationally restrained edges), the stresses were slightly smaller for the DLT element—especially with respect to the out-of-plane shear stresses.

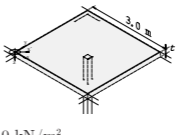
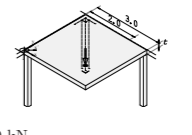
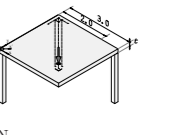
As it is for the stress resultants, the stress values depend on the static system and the loading only. The deformations and the stress distribution over the cross-section, on the other hand, are caused by the stresses in relation to the corresponding layup and stiffness values of the laminate. For example, the interaction of shear modulus and shear stress distributions defines the out-of-plane shear stiffness and vice versa. The same applies to the distribution of normal stresses due to bending over the cross-section and the related moduli of elasticity.

Table 10.9 summarizes the maximum stress values of the previous investigations using the 3D FE models. These stress values are relevant for the strength verifications (stress verifications) within the ULS. The location of the design-relevant stress value (critical section) is given below each value. In addition, the respective deformations in the SLS and the ratio of homogenization are provided. Table 10.9 shows that in nearly all design-relevant perimeters, higher stresses are achieved for the CLT element than for the DLT element at the same load level. This occurs despite the fact that the deformations for the investigated DLT D8 series remain lower than for the CLT O8 series (the D8 and O8 series were chosen for the 3D FE models). The stress distribution analysis does not replace a strength verifications in the ULS and the deformation analysis does not replace a verification of serviceability in the SLS.

The linear elastic models do not include fracture mechanics. Consequently, the determined stresses and deformations have to be transferred to common design rules for mass timber slabs.

The following Chapter aims to provide guidance for planners regarding the design processes when adapting and producing DLT elements.

Tab. 10.9: Comparison of exemplary design-relevant stress values for strength verifications in the ULS, given by the 3D FEM models

system	centric point-support		point-support at three corners		point-support at three corners	
						
series	CLT O8	DLT±45° D8	CLT O8	DLT±45° D8	CLT O8	DLT±45° D8
ξ [/]	0.571	0.571	0.571	0.571	0.571	0.571
max. deformations [mm]	3.7 ¹	3.2 ¹	4.7 ¹	4.4 ¹	13.6 ¹	10.7 ¹
max. shear stresses (longitudinal) [N/mm ²]	0.65	0.63	0.77	0.64	1.96	0.65
location ²	x-x section, 1 st layer, d/4	x-x section, 1 st layer, d/4	y-y section, 2 nd layer, d/4	x-x section, 7 th layer, d/4	y-y section, 6 th layer, r	x-x section, 7 th layer, d/4
max. bending ³ tensile stresses [N/mm ²]	4.63	4.67	4.81	4.53	6.28	6.37
location ²	x-x section, 1 st layer, d/4	x-x section, 1 st layer, d/4	x-x section, 7 th layer, r	x-x section, 7 th layer, r	y-y section, 2 nd layer, d/4	y'-y' section, 3 rd layer, d/4
max. bending ³ compression stresses [N/mm ²]	- 5.29	- 5.27	- 4.22	- 4.64	- 6.82	- 7.39
² location	x-x section, 7 th layer, d/4	x-x section, 7 th layer, d/4	x-x section, 7 th layer, d/4	x-x section, 7 th layer, d/4	x-x section, 7 th layer, d/4	y-y section, 6 th layer, d/4

¹deformations close to the SLS ($P = 5.0$ kN), Tab. 10.3
²the layers are numbered from the lower to the upper edge of the specimens (see Figure 3.1)
³normal stresses due to bending

11 Outlook on design processes and production stages of DLT

10.4 Design processes of point-supported DLT slabs

Regarding the design process of point-supported mass timber slabs made of DLT, the thesis aims to provide guidance regarding layer orientations and additional strength verifications. After the construction grid and static system are developed and set, the planners decide whether to use CLT or DLT elements for the slab. As previously examined, the application of DLT does not generally provide the respective characteristics needed to achieve a high material efficiency.

If the decision on DLT is made, the next step is to define the layout and the layer orientations. With regard to the former, the ratio of homogenization ζ can be addressed. The latter refers to the given geometry of the construction grid. When using DLT, the diagonal layers can be arranged regarding the corresponding diagonals between the single columns of a point-supported slab (also see Figure 1.5, Chapter 1). However, if the orientation of these diagonals is not obvious due to, for example, varying construction grids, a mathematical approach can be used to determine the optimized orientation of the layers:

For a point-supported slab under a constant distributed surface load, there is a particular angle φ where the bending moments acting in the direction of the respective diagonals become extreme values, called m_1 and m_2 (see also Figure 10.5). With the help of the *Mohr's circle* the angle φ for an optimized arrangement of the layers can be found with Equation (11.1). Figure 11.1 demonstrates the relationship between bending and torsional moments and the angle φ according to Equation (11.1). In this context, DLT could be utilized as application-optimized mass timber elements.

$$\tan\varphi = -\frac{m_x - m_y}{2 \cdot m_{xy}} \pm \frac{1}{m_{xy}} \sqrt{\frac{m_x - m_y}{2} - m_{xy}^2} \quad (11.1)$$

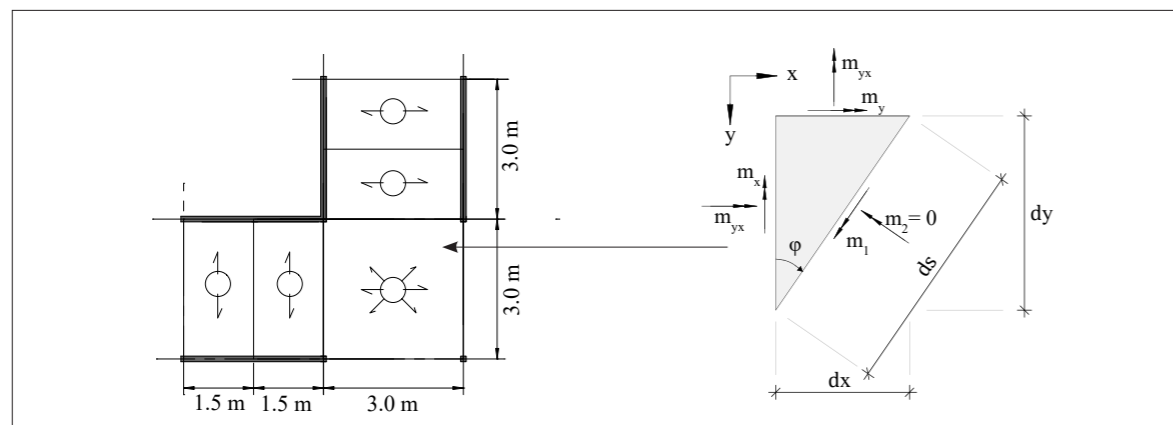


Fig. 11.1: Relationship between bending and torsional moments and the angle φ

In general, most of the methods of strength verification of DLT slabs should be carried out in a similar way as is the case for CLT slabs. The dimensioning of CLT slabs is carried out according to EC 5. The determination of stresses follows analytical methods or can be taken from FE models (see Chapter 10.3, Table 10.9). In any case, stresses and stress resultants derived from FE models should be critically reviewed and additionally verified by manual calculation. For DLT, the stresses in x' and y' direction, following the respective diagonal layers, also have to be considered for strength verifications (marked green), since the stresses in these directions may be dominant. The following strength verifications within the design process of mass timber slabs are mandatory:

- Bending verification due to normal stresses (tension);

$$\frac{\sigma_{x/y,d}}{f_{m,d}} \leq 1.0 \quad \frac{\sigma_{x'/y',d}}{f_{m,d}} \leq 1.0 \quad (11.2)$$

- Shear verification due to out-of-plane shear stresses in the longitudinal layers;

$$\frac{\tau_{l,xz/yz,d}}{f_{v,d}} \leq 1.0 \quad \frac{\tau_{l,x'z'/y'z',d}}{f_{v,d}} \leq 1.0 \quad (11.3)$$

- Rolling shear verification due to out-of-plane shear stresses in the cross-layers;

$$\frac{\tau_{r,xz/yz,d}}{f_{r,d}} \leq 1.0 \quad \frac{\tau_{r,x'z'/y'z',d}}{f_{r,d}} \leq 1.0 \quad (11.4)$$

- and compression verification due to compression perpendicular to plane,

$$\frac{\sigma_{c,90,d}}{k_p \cdot k_{c,90} \cdot f_{c,90,d}} \leq 1.0 \quad (11.5)$$

wherein k_p and $k_{c,90}$ are the factors to take into account material behavior and degree of compressive deformation perpendicular to grain (see Table 8.1 and Figure 8.6; prEN 1995-1-1:2023 (E)). Within future research, the transferability of these factors from CLT to DLT should be examined (see Chapter 11.3).

Furthermore, within the second generation of EC 5 (prEN 1995-1-1:2023), additional content is added with narrow and specific scope to CLT and its design rules. Regarding out-of-plane loading, Annex G ("Annex G (normative) special design provisions for cross laminated timber (CLT)") provides additional design rules for among others:

- Concentrated loads perpendicular to plane without reinforcement.
- Concentrated loads perpendicular to plane with reinforcement.

Since reinforcement at the load-introduction points was not investigated within this thesis, this topic should also be addressed within future investigations. The question of whether, and to what extent, the observed stress homogenizations and redistributions due to diagonal layer arrangements reduce the need for additional reinforcement in the form of fully thread screws, for example, cannot be answered from the investigations to date.

The same holds true for the strength verifications on DLT connection techniques. Regarding connection techniques, some of the common connections for CLT plate elements may be applied analogous on DLT elements. However, before any reliable statements can be made on connection techniques, further specific research and experimental results are required—this applies in particular for rigid connections, considering the diagonally arranged layers.

Regarding deformations and the serviceability limit states (SLS) of DLT floors under uniaxial and biaxial bending, the well-known deformation criteria following EC 5 and DIN EN 1995-1-1/NA, Table NA.13, should be applied. Regarding vibrations of DLT floors under uniaxial load transfer, the design rules following prEN 1995-1-1:2023 - Chapter 9.3, may be used. The following rules are valid for human induced vibrations of timber floors in the categories of use A, B, C1, C3 and D as defined in EN 1991-1-1:2002 - Table 6.1.

11.1 Considerations on the production stages of DLT

The aim is to investigate the possibility to add specially arranged laminates into the production lines of conventional CLT without excessive effort and additional costs. An economical manufacturing process is crucial for a successful market launch of DLT. Together with our partner and producer of the DLT test specimens, Holzbau Unterrainer GmbH, it was discussed in the production halls in East Tyrol how the production process can be further optimized.

Optimized production processes in terms of layer arrangement and speed of manufacturing require close cooperation and a flexible, project dependent adaptation of the production parameters. Hence, close cooperation between planners, customers, and production industries should be prioritized, in order to implement and automate the optimization of mass timber panels, as early as the planning phase. Therefore, within the previous Chapter, the design process and selection of layups and layer arrangements was described.

Figure 11.2 reveals the basic production stages of mass timber elements, specified for DLT. Furthermore, the interaction of forestry and production industries on the one hand and the researcher, planner, and client on the other is shown. Figure 11.2 shows that most of the well-known CLT production stages can in principle be converted to DLT without great effort. Even though, the production of the DLT test specimens according to Tables 4.6 and 4.7 was characterized by labor-intensive processes, Holzbau Unterrainer GmbH managed to introduce diagonal layer arrangements into their production lines.

As it is for CLT, the single boards are finger-joint to endless lamellas. The next step—cutting the endless lamellas according to the joinery plan—requires the input of the planners and researchers (marked with (1) within Figure 11.2). The planners forward the project-specific layer dimensions and arrangements to the producer (see Chapter 11.1).

Afterwards, the cutting of the lamellas is carried out (see (2) in Figures 11.2 and 11.3). For the production of the test specimens, the lamellas were numbered according to manually created CAD models and were individually mitred. In a standard saw (2), however, this process can be carried out automatically (Holzbau Unterrainer GmbH). In this case, every second board cut from the endless lamella serves as a board in the oppositely oriented layer of the antisymmetric laminates, in order to minimize cutoffs. At best, the dimensions and layer arrangements of the individual plate element are stored in a 3D model and provided by the planners.

After the cutting, the assembly of the specific layup is initiated by placing the individual boards side by side on the alignment table (3) forming solid wood layers. Until now, this process is carried out manually, even though an automation would be possible. The lifter with the vacuum suction heads picks up the boards of a whole layer and places them on the adjacent production line of the press (4). Every layer of the later CLT or DLT element is sprayed with an adhesive and afterward pressed together with a hydraulic or vacuum press. Then, the panels are cut to size, milled, and finished as required (4).

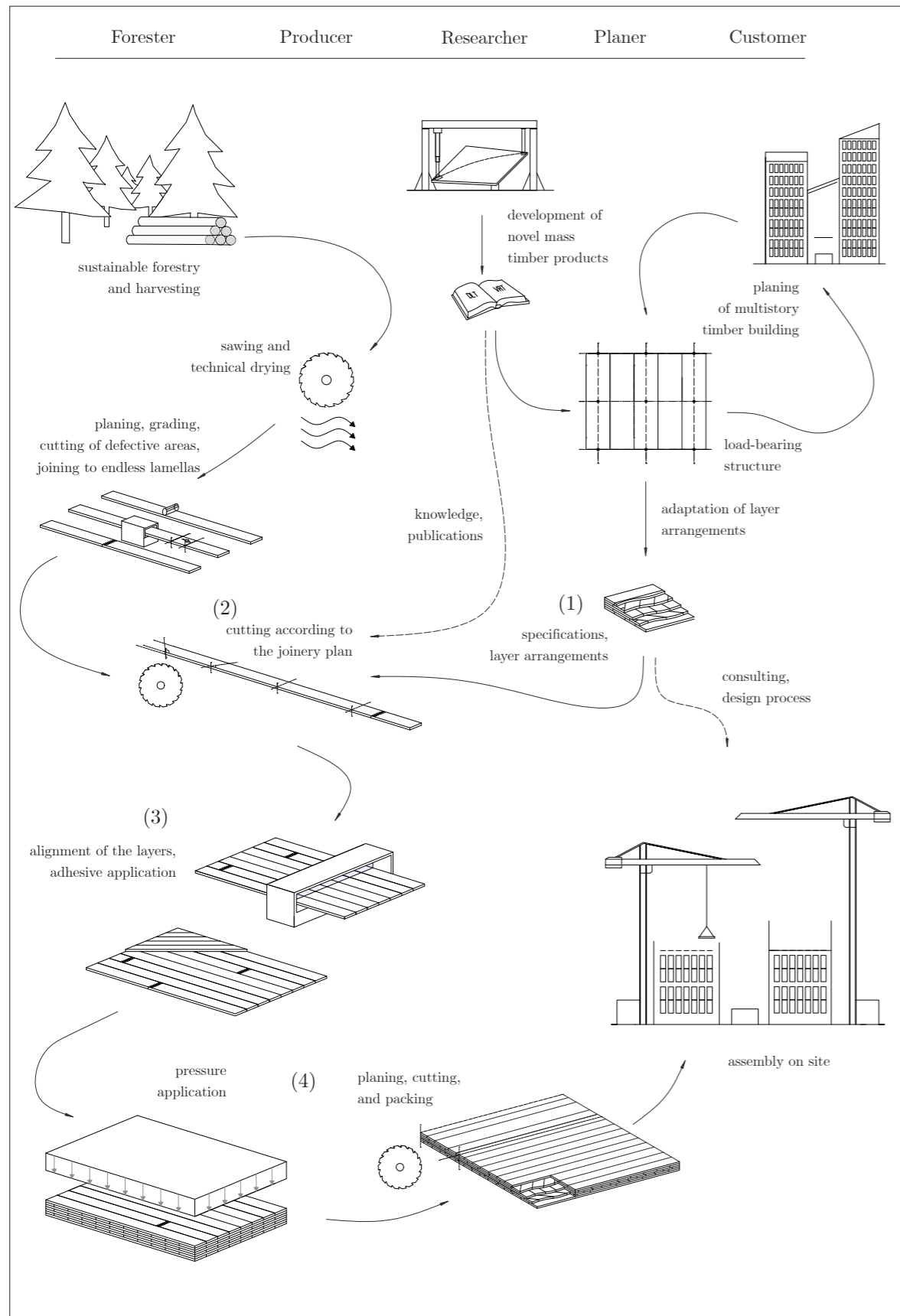


Fig. 11.2: Production processes of CLT and DLT and their interaction to the input by researchers and planers

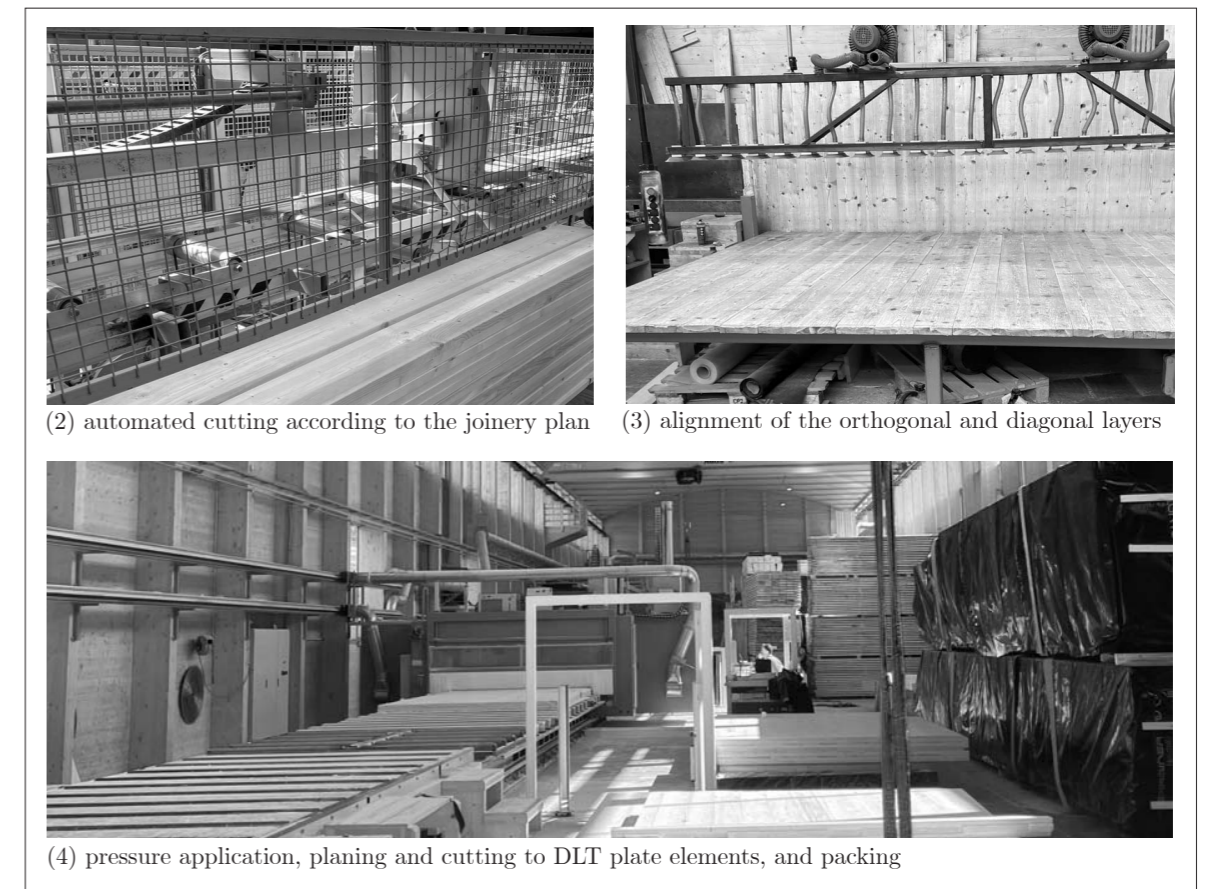


Fig. 11.3: Stages within the CLT and DLT production of Holzbau Unterrainer GmbH

11.2 Further research tasks regarding the practical implementation of DLT

The overall aim of this thesis was the study and further development of the building product DLT and to make a contribution to towards its maturity for application. Before a detailed summary of the results achieved so far is given (Chapter 12), future research needs are to be addressed. Needs for further research became already apparent and were partly addressed within the previous Chapters.

At the regulatory level, the main objectives for new building and construction products are to achieve the technical and regulatory requirements according to the Construction Product Regulation (CPR). On an organizational level, the development of a construction product and its successful implementation on the market can be summarized in four stages (Figure 11.4). These form a coherent cycle, which strives for constant optimization and interaction. The aim is to show which steps towards market maturity have already been taken with this thesis and which still need to be taken.

Conceptualization:

This stage includes the development of innovative concepts and new configurations. Regarding Figure 11.2, this stage is related to researchers and planners, based on the needs of the production industries and clients. In terms of DLT, this stage is related to layups and material properties.

With this thesis, the product DLT was defined and the expected benefits were addressed. Different configurations regarding layups and layer arrangements were presented. Future research may address additional configurations using hardwood lamellas for diagonal or crosswise arranged layers. Regarding environmental relevance and sustainability, the usage of biodegradable adhesives may be considered for the production of DLT. Currently, DLT is not covered by EAD 130005-00-0304, due to the orientation of individual layers deviating from 0 and 90° to each other. A future goal should be a new EAD document or the extension of EAD 130005-00-0304 towards laminated mass timber elements featuring diagonal layer arrangements.

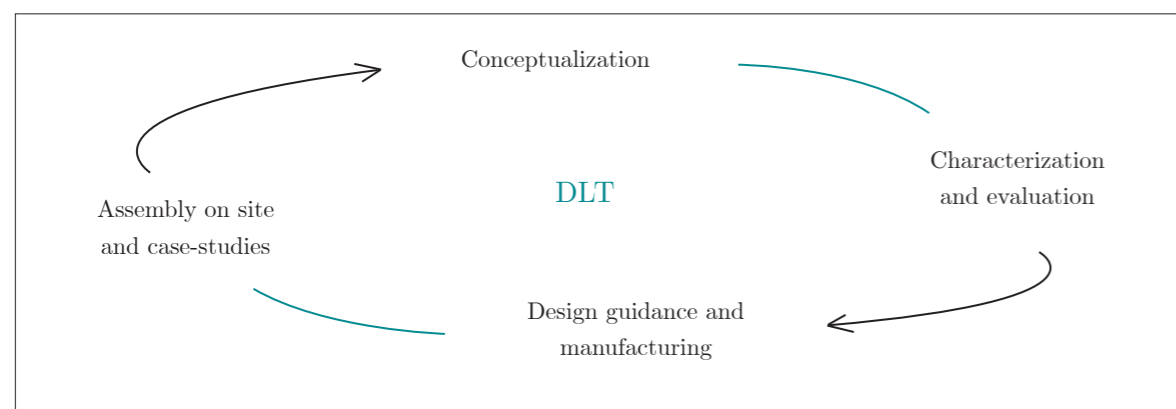


Fig. 11.4: Stages of product development and the implementation on markets

Characterisation and evaluation:

This stage includes the characterisation and evaluation of the product performance at the component level. This stage is applicable to researchers and planners as well as to the producers. The main task is the characterisation and evaluation in terms of data acquisition from experimental and numerical investigations. In general, this stage is concerned with how well DLT fulfills the seven essential requirements for construction products according to the CPR. By now, DLT was characterized regarding its stiffness properties and the related deformation behavior. Additional numerical investigations served as indicator on stress distribution undergoing concentrated loading due to point-supports. Additional experimental investigations should cover:

- Punching shear test on 5-layered and 7-layered DLT and CLT series, with and without reinforcement. This could help to quantify the failure mechanisms regarding punching shear and the positive effects of the diagonal layer arrangements on the stress distributions in case of concentrated load application. Anyway, reinforcement measures might be required for the construction of point-supported slabs with larger spans or point-supported slabs under higher loads, than the ones investigated.
- Additional in-plane and out-of-plane shear tests on a larger number of specimens should be carried out to determine shear strength properties.
- The analytical studies on the long-term deformation behavior are promising. However, long-term experiments are necessary to prove these indications. The proposed experimental long-term test setup (Chapter 8.4.2) should be considered within these investigations.
- Investigations on the fire resistance and dimensional stability under different climatic conditions should be carried out.
- Further experiments should also investigate vibrations of CLT and DLT slabs under biaxial bending. These results may also lead to findings regarding the sound-insulation criteria.

In addition to the centric and multiple point-supported slab, the results of the analytical, mechanical, and numerical investigations promise further advanced application areas for DLT, which should be characterized and quantified.

The additional layers arranged under for example $\pm 45^\circ$ may further provide improved load-bearing capacity towards rigid plate joints. As previously mentioned, the segmentation of DLT slabs and the load-bearing capacity of resulting joints need to be investigated analytically and experimentally (STIEB ET AL 2023).

Regarding openings and notches in deep beam elements or beam elements acting in the in-plane stress state, the in-plane shear stiffness of DLT promises improved load-bearing capacity (Figure 11.5, left). By arranging layers at 45° or 60° , for example, the diagonal layers act as trusses between which openings can be integrated into the plane element (also see BEJTKA 2011). In the case of openings and notches in slabs, the diagonal layers may act as reinforcement analogous to reinforced concrete structures (Figure 11.5, middle).

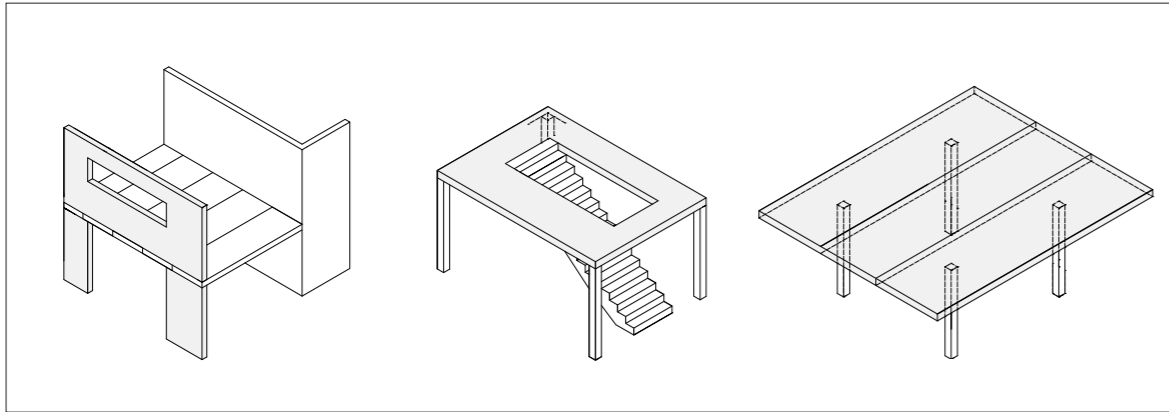


Fig. 11.5: Deep-beam with openings (left), plate elements with opening and notches (middle), and segmentation and joints of DLT slabs (right)

Design guidance manufacturing:

The production of the DLT test specimens within the standard CLT production has already demonstrated that production of DLT elements can be integrated into existing production lines without additional machinery due to the resemblance of the manufacturing processes. The future goal is the production of a large number of DLT specimens on industrial scale in order to achieve economic efficiency. The objective must be that additional costs due to planning and production efforts for DLT are compensated and exceeded by material savings compared to CLT cross-sections. Furthermore, strength verification methods given in current codes and standards need to be transferred to DLT, in particular regarding the specific reduction factors.

Assembly on site and case-studies:

The construction steps on site using DLT do not differ from those for CLT. The construction of a reference building using DLT elements in addition to CLT elements should therefore be the goal. Further studies and measurements could then be carried out on the reference object (for example with regard to vibrations and deformations). The outcomes and experiences of stage 4 provide the basis of future research and thus create the newly input to stage 1 (Figure 11.4). This input can include proposals for novel products or suggestions for improvement of the existing ones (see also research project INNOTLT 2023-2026).

12 Summary

The overall aim of this thesis was to extend the development of a new timber laminate, optimized for plates under biaxial bending and concentrated loading, as required for point-supports. The presented work aims to provide a proof of concept and detailed results for the realization of the idea of future mass timber elements made from softwood featuring improved stiffness properties by optimized layer arrangements. In particular, DLT was characterized with respect to its mechanical properties as a laminate. Different layups of conventional CLT were compared to their DLT counterparts regarding the effects of diagonal layer arrangements on the stiffness properties by means of theoretical, analytical and numerical investigations. Therefore, analytical and experimental approaches already available for CLT were expanded and transferred to DLT.

The mechanics of composite materials featuring moderately thick and orthotropic layers were derived. The derived stiffness matrices formed the basis of the analytical studies. The stiffness properties of different series of CLT and DLT elements were derived by a number of different experimental investigations. For the mechanical experiments, test specimens for various series, featuring different layups were developed and produced.

The out-of-plane shear properties of CLT and DLT were determined by means of small-scale shear tests. The investigated stiffness values were compared to the different analytical solutions and numerical models. In order to derive statements regarding the suitability of DLT for uniaxial load transfer, the bending stiffness of DLT was determined by four-point-bending tests and compared to analytical solutions, taking into account shear deformations. The torsional stiffness of CLT and DLT was studied by means of extensive analytical, experimental, and numerical investigations. Parameter studies on the layer arrangements were carried out. Subsequently, statements on the long-term deformation behavior under biaxial bending were derived. Chapter 9 contains preliminary considerations and different tactile experiments for the determination of the in-plane shear stiffness properties of DLT. Although the focus of this thesis prioritized the out-of-plane stiffness properties of mass timber elements, the in-plane shear stiffness parameters were determined by means of diagonal shear compression tests.

By the comparison of CLT to DLT using numerical 2D and 3D models on different real-scale static systems of point-supported slabs the benefits of DLT were quantified regarding deformations and homogenization effects around concentrated load-application. Within the previous Chapter, future research needs, in order to achieve maturity for application for DLT, were addressed.

The main outcomes of the analytical, experimental and numerical investigations achieved are given in the following:

Out-of-plane shear stiffness

Based on investigations in this thesis on the out-of-plane shear properties, for laminates with 3 to 7 layers of the same thickness each, the introduction of shear correction coefficients is mandatory. When determining the out-of-plane shear stiffness of DLT in the course of the experimental, analytical, and numerical investigations one finding was that shear correction coefficients $k_{i,z}$ based on transformed engineering constants provide realistic values within the analytical solutions following the laminate theory. It was found, that within previous version of common 2D FE tools, e.g. RF Laminate, an possible overestimation of the out-of-plane shear stiffness values of DLT occurred, since transformed and reduced stiffness terms were used within the calculation of shear correction coefficients, and not the transformed engineering constants (also see flowchart in Appendix A2). This needs to be further investigated.

- The out-of-plane shear stiffness values refer to the entries E_{55} , E_{45} , and E_{44} of the ABD-E stiffness matrix. According to the laminate theory, the out-of plane shear stiffness of the DLT $\pm 45^\circ$ D3 series ($t = 100$ mm) in y direction is much higher than of the CLT O1 series ($t = 100$ mm), while the values in x direction remain in a comparable range ($S_{xz,D3} = 7.68$ MN/m to $S_{xz,O1} = 7.96$ MN/m; and $S_{yz,D3} = 12.86$ MN/m to $S_{yz,O1} = 4.89$ MN/m).
- The out-of-plane shear stiffness values of DLT can also be determined analytically in x direction by the *Shear Analogy Method*. Therefore, the respective values of the shear moduli are applied as a function of the fibre orientation to the global x axis (for example $G_{45^\circ} = 94$ MPa for spruce T14). These shear stiffness values of DLT in x direction provide good correlation to the values according to the laminate theory using shear correction coefficients. This is not fulfilled for the out-of-plane shear stiffness in y direction, due to assumptions of linearly distributed shear stresses over the cross-section. The *Shear Analogy Method* therefore underestimates the shear stiffness values of DLT in y direction.
- The experimental results on the 5-layered DLT series, gained by shear test on three inner layers, provided good correlation in x direction to both analytical approaches. The out-of-plane shear stiffness of the 5-layered CLT O1 series on the other hand were much higher, than the analytical approaches. The very high experimental results of the O1 series in x direction could indicate a measurement error. Also, the O1 series in x direction is the only series featuring two layers oriented under 90° within the three inner layers (shear area), which is contrary to an actual homogeneous distribution of the shear stress over the inner layers. This needs to be further investigated.

In y direction, the experimental values are quite inconsistent and differ from the analytical and numerical solutions for both, the CLT and DLT series. The experiments therefore failed to point-out the increase in shear stiffness in y direction due to diagonal layer arrangements. The experiments showed deformations at the load-

introduction areas of the specimens. It is therefore questionable, whether the chosen experimental test setup is suitable for the determination of the actual out-of-plane shear stiffness of DLT in y direction.

- Alternatively, experimental results could be gained by shear-bending tests according to EN 16351 or according to EN 408, using steel lamellas for load-introduction.

Bending stiffness

The unidirectional bending properties of DLT depend on the chosen layup. Which means, that the arrangement of DLT can be adopted in order to provide maximum bending stiffness values in x direction (see uDLT specimens), or in order to achieve a high ratio of homogenization (see Chapter 10.3).

- The bending stiffness of the elements is determined by the laminate theory and can therefore be taken from the entries D_{11} and D_{22} . The bending stiffnesses in x direction B_x of the DLT±45° D3 series is increased by 6.6 % compared to CLT O1 series and by 14.2 % for DLT±30° D4 series. On the other hand, the bending stiffnesses in the y direction B_y are decreased by 56.4 % for D3 series and by even 73.6 % for D4 series in comparison to the CLT O1 series.
- Comparing the uDLT±45° D1 series also used for the experimental investigations ($t = 200$ mm) to the CLT O5 series ($t = 200$ mm), the bending stiffness is increased by 7.6 % in x direction and decreased by 39.9 % in y direction.
- Taking into account the shear deformations and the static system regarding the ratio l/d , effective bending stiffness values $B_{x,\text{eff}}$ and $B_{y,\text{eff}}$ can be calculated using the method of consistent deformations. These values are, among others, needed, for the comparison to global stiffness values following experimental investigations and comparable thick cross-sections undergoing high shear deformations.
- The experimental investigations on the bending stiffness follows four-point-bending tests according to EN 16351, seems to be well suited for investigations on DLT. Following the analytical approach, the local bending stiffness B_x of D1 series is 6.35 MNm²/m. This value appears to be higher by 0.70 MNm²/m than the mean value $B_{x,\text{exp.}} = 5.65$ MNm²/m achieved in mechanical testing.
- The effective bending stiffness $B_{x,\text{eff}}$ of D1 series, following the analytical approach, appears to be 5.95 MNm²/m (considering the span of $l = 4.6$ m and $a = 1.5$ m of the four-point bending tests). This value differs by 0.61 MNm²/m to the experimental determined effective (global) bending stiffness $B_{x,\text{eff,exp}}$ (5.34 MNm²/m).

Torsional stiffness and effective torsional stiffness

Based on investigations in this thesis the increase in torsional stiffness due to diagonal layer arrangements is significant and therefore one of the main benefits of DLT.

- The torsional stiffness values B_{xy} are obtained from the ABD stiffness matrix (entry D_{66}). B_{xy} of the 5-layered DLT±45° D3 series ($t = 100$ mm) is increased by 60 % on average compared to the conventional CLT O1 series and by 45 % on average for the DLT±30° D4 series. Comparing the 7-layered DLT±45° D9 series ($t = 140$ mm), featuring four diagonally oriented layers, to CLT O8 series ($t = 140$ mm) the torsional stiffness B_{xy} is increased by 70.6 %.
- Considering deformations from uniaxial bending and out-of-plane shear, as well as the static system regarding the plate dimensions $dx/dy/t$, effective torsional stiffness values $B_{xy,\text{eff}}$ are achieved. The values are needed to determine deformations under a combination of both, bending and shear in two directions.
- Based on investigations in this thesis, the analytical determined torsional stiffness values and effective torsional stiffness values are consistent with the experimental determined values according to the proposed biaxial bending test for the 5-layered CLT and DLT specimens with $t = 100$ mm and $t = 200$ mm.
- Regarding the experimental investigations within the plate dimension $dx = dy = 1.0$ m, increase in the effective torsional stiffness within of DLT elements compared to the CLT elements is undeniable. Compared to the 5-layered CLT series O1 and O5 with an thickness of 100 mm and 200 mm, the effective torsional stiffness $B_{xy,\text{eff}}$ of DLT±45° elements is increased 32 % on average. For DLT±30° the increase is 25 % on average.
- A parameter study shows that the board width has a noticeable influence on the effective torsional stiffness for board widths $w \leq 160$ mm. For board widths $w \geq 180$ mm, the torsional stiffness of CLT and DLT with edge-gluing is the same as for CLT and DLT without edge-gluing.

In-plane shear stiffness

The advantages of DLT over CLT in terms of in-plane shear stiffness appear to be another benefit of diagonal layer arrangements.

- The in-plane stiffness refers to the entry A_{66} of the ABD matrix and therefore refers directly to the laminate theory. It is important to keep in mind, that within the laminate the assumption of the UD layer with ideally straight fibres are valid. Gaps or stress-reliefs between the boards can not be considered within the laminate theory. The in-plane stiffness values therefore refer to the sum of the transformed stiffness terms $\sum Q_{ij}$ of the UD layer, multiplied by the respective thickness.
- Following the laminate theory, the in-plane shear stiffness D_{xy} of DLT±45° D3 series is

- increased by 123.8 % compared to CLT O1 series and by 91.3 % for DLT±30° for D4 series. These ratios are based on the assumption of the continuous and ideally straight UD layer.
- The analytical values reflect the relation in the stiffness change as a result of the rotation of individual layers. However, the comparison of the experimental results and the analytical values should be viewed with caution, which is also reflected by the large number of different available test methods and approaches.
 - Comparing the results of the shear frame testing to the results of the shear compression testing reveals a discrepancy in the in-plane shear stiffness for the orthogonal CLT O1 series of $\Delta D_{xy} = 7.74$ MN/m. The value of the shear frame test ($D_{xy,O1} = 24.30$ MN/m) is therefore by 31.9 % smaller compared to the in-plane shear stiffness determined using the shear compression test ($D_{xy} = 32.04$ MN/m).
 - The analytical stiffness value of the CLT O1 series of 17.25 MN/m is 40.9 % lower than the value determined in the shear frame test and 85.7 % lower than the value determined by the shear compression test. Thus, the analytical approach according to DIN EN 1995-1-1/NA appears to be somewhat conservative and approximate for non-edge-glued CLT and DLT, also reflecting the findings of (BRANDNER ET AL. 2017).
 - The experimental investigations resulted in an increase of 83.6 % for the DLT D3 series compared to the experimental in-plane shear stiffness value of the CLT O1 series. For the DLT D4 series the increase of the experimentally determined in-plane shear stiffness is 32.0 % compared to the CLT O1 series. Comparing the experimental values of DLT D3 and D4 series to the analytical in-plane shear stiffness value of CLT O1 series results in an increase of 159.7 % (D3) and 85.9 % (D4).
 - Due to the small number of tactile tests carried out, the results of the experimental investigation are only of limited validity. Further investigations need to be carried out.

Deformation behavior and stress distribution

The deformation analysis of the different DLT and CLT layups have shown that in the majority of the static systems, the influence of the bending and shear stiffness values becomes dominant for the resulting total deformation. The torsional stiffness in the form of diagonally arranged layers should be added as an additional benefit so that the distribution of the bending deformation in x and y remains as homogeneous as possible. Due to this, the terminology "ratio of homogenization" with respect to the number of layers oriented diagonally or crosswise in relation to the overall number of layers, was introduced. In addition, and by adapting the orientation of single layers regarding the respective static system and loading, the term "application-optimized" laminated timber element was introduced.

- In conclusion, the deformations of the chosen 5-layered DLT±45° series D7 ($t = 150$ mm) are much higher for point-supported slabs (up to +56.3 %) and systems mainly undergoing uniaxial bending in y direction (up to +118.5 %), than of the 5-layered CLT O7 series. This is due to the comparable low bending stiffness of the D7 series in y direction ($B_{y,D7} = 0.32$ MNm²/m vs. $B_{y,O7} = 0.73$ MNm²/m).
- For static systems mainly undergoing uniaxial bending in x direction the deformations are in a comparable range, mirroring the similar bending stiffness in x direction of the chosen DLT and CLT series ($B_{x,D7} = 2.65$ MNm²/m vs. $B_{x,O7} = 2.48$ MNm²/m).
- For static systems governed by torsional moments, the comparable high torsional stiffness of the DLT D7 series leads to smaller deformations compared to the 5-layered CLT O7 series (up to -41.0 %) ($B_{xy,D7} = 3.16$ MNm²/m vs. $B_{xy,O7} = 1.94$ MNm²/m).
- Adding two additional cross-layers achieving 7-layered series D8 and O8 ($t = 140$ mm), results in smaller deformations for the DLT series compared to the CLT series for point-supported slabs (up to -13.5 %) and for systems mainly undergoing uniaxial bending in y direction (up to -12.0 %). This is due to the comparable low spread of the bending and shear stiffness values between the D8 and O8 series ($B_{y,D8} = 0.84$ MNm²/m, $S_{yz,D8} = 8.05$ MN/m vs. $B_{y,O8} = 0.79$ MNm²/m, $S_{yz,O8} = 8.31$ MN/m).

The 3D FE models indicated homogenization effects for the stress distributions within DLT elements—especially regarding out-of-plane shear stresses around concentrated load-application. This is remarkable, given that the DLT±45° D8 series also experienced smaller deformations than the CLT O8 series for point-supported slabs. The results therefore indicate a slightly higher load-bearing capacity of point-supported DLT slabs compared to CLT slabs and offers interesting prospects for future research.

However, the stress distribution in combination with low deformations due to uniaxial and biaxial bending, may lead to brittle and sudden failure mechanisms of the DLT when reaching the ULS. The question of whether, and to what extent, the observed stress homogenizations due to diagonal layer arrangements reduce the need for additional reinforcement around point-supports cannot be answered from the investigations to date. Future experimental investigations such as punching shear test on 5-layered and 7-layered DLT and CLT series could help to quantify the failure mechanisms and the positive effects of the diagonal layer arrangements on the stress distributions in case of concentrated load application.

Based on these investigations and findings, the potential of DLT becomes more obvious. DLT promises potential to increasing the efficiency of laminated mass timber elements—efficient regarding optimized mechanical properties, regarding the use of the valuable resource timber, and regarding the realization of demanding constructions, such as point-supported slabs.

Bibliography

References	176
Standards	185
European Technical Assessments	187
Legal Texts and International Agreements	187
Others	188

References

- ALTENBACH ET AL. (2016)
Altenbach, H. ; Altenbach, J. ; Naumenko, K.: Ebene Flächentragwerke : Grundlagen der Modellierung und Berechnung von Scheiben und Platten. 2nd ed., Springer, Berlin Heidelberg, 2016.
- ANDREOLLI ET AL. (2014)
Andreolli, M. ; Rigamonti, M. ; Tomasi, R.: Diagonal compression test on cross laminated timber panels. Conference thesis, World Conference on Timber Engineering WCTE 2014, Quebec, Canada, 2014.
- AONDIO (2014)
Aondio, P.: Berechnung von Zylinderschalen aus Holz und Holzwerkstoffen unter Berücksichtigung der Spannungsrelaxation. Dissertation, Chair of Timber Structures and Building Construction, Technical University of Munich, 2014.
- ARMSTRONG ET AL. (1984)
Armstrong, J. P. ; Skaar, C. ; Zeeuw, d. C.: The effect of specific gravity on several mechanical properties of some world woods', Wood Science and Technology, 18, 137-146, 1984.
- ARNOLD ET AL. (2021)
Arnold, M. ; Dietsch, P. ; Winter, S.: Mechanical properties of innovative multifunctional cross laminated timber. World Conference on Timber Engineering WCTE 2020/21. Santiago, Chile, 2021.
- ARNOLD ET AL. (2022a)
Arnold, M. ; Dietsch, P. ; Maderebner, R. ; Winter, S.: Diagonal laminated timber—Experimental, analytical, and numerical studies on the torsional stiffness. Construction and Building Materials 322, p. 126455, 2022.
- ARNOLD ET AL. (2022b)
Arnold, M. ; Schenk, M. ; Kainz, N. ; Dietsch, P. ; Cabrero, J. M. ; Maderebner R. ; Winter, S.: Schlussbericht zum Europäischen Forschungsvorhaben InnoCrossLam – Innovative Solutions for Cross Laminated Timber Structures; Arbeitspakete 5 und 6 (Deutschland). Bundesministerium für Landwirtschaft und Ernährung; Fachagentur Nachwachsende Rohstoffe; Gülzow-Prüzen, 2022.
- ARNOLD ET AL. (2023a)
Arnold, M. ; Dietsch, P. ; Winter, S.: Hyperbolic paraboloid shells made of diagonal laminated timber elements. World Conference on Timber Engineering WCTE 2023, Oslo, Norway, 2023.
- ARNOLD ET AL. (2023b)
Arnold, M. ; Maderebner, R. ; Dietsch, P. ; Winter, S.: Diagonallagenholz (DLH) – Ressourceneffizienz durch diagonale Orientierung einzelner Lagen: Bestimmung der Steifigkeitsparameter und Verformungsanalysen. Bautechnik, Nr. 100, Heft 8, 2023.
- BAHMANZAD ET AL. (2020)
BAhmanzad, A. ; Clouston, P. ; Schreyer, A. C.: Shear Properties of Eastern Hemlock with Respect to Fiber Orientation for Use in Cross Laminated Timber. Journal of Materials in Civil Engineering 32(7), 2020.
- BEJTKA (2011)
Bejtka, I.: Cross (CLT) and diagonal (DLT) laminated timber as innovative material for beam elements. Karlsruher Berichte zum Ingenieurholzbau, Band 17, KIT Scientific Publishing, Karlsruhe, 2011.

- Bittner (1951)
Bittner, J.: Furniere - Sperrholz Schichtholz. Erster Teil: Technologische Eigenschaften; Prüf- und Abnahmevorschriften; Mess-, Prüf- und Hilfsgeräte. 2. verbesserte Auflage, Springer, Berlin, Göttingen, Heidelberg, 1951.
- BLASS AND GÖRLACHER (2002)
Blass, H. J. ; Görlacher, R.: Zum Trag- und Verformungsverhalten von Brettsperrholz-Elementen bei Beanspruchung in Plattenebene. *Bauen mit Holz*, 12:30-34, 2002.
- BOGENSPERGER AND SILLY (2014)
Bogensperger, T. ; Silly, G.: Zweiachsige Lastabtragung von Brettsperrholzplatten. *Bautechnik* 91, No. 10, 742-752, 2014.
- BOSL (2002)
Bosl, R.: Zum Nachweis des Trag- und Verformungsverhaltens von Wandscheiben aus Brettlagenholz. Dissertation, Universität der Bundeswehr, München, 2002.
- BRANDNER ET AL. (2013)
Brandner, R. ; Bogensperger, T. ; Schickhofer, G.: In plane Shear Strength of Cross Laminated Timber (CLT): Test Configuration, Quantification and influencing Parameters. CIB-W18/46-12-2, Vancouver, 2013.
- BRANDNER ET AL. (2017)
Brandner, R. ; Dietsch, P. ; Dröscher, J. ; Schulte-Wrede, M. ; Kreuzinger, H. ; Sieder M.: Cross laminated timber (CLT) diaphragms under shear: Test configuration, properties and design. *Construction and Building Materials*, 147:312-327, 2017.
- BRANDNER ET AL. (2023)
Brandner, R. ; Ringhofer, A. ; Sieder, R.: Bending Properties out-of-Plane of Cross Laminated Timber (CLT): Test Experience, Model Refinement and Validation. Proceedings 10th INTER 2023, International Network on Timber Engineering Research, Biel, 2023.
- BUCK ET AL. (2016)
Buck, D. ; Wang, X. A. ; Hagman, O. ; Gustaffson, A.: Bending Properties of Cross Laminated Timber (CLT) with a 45° Alternating Layer Configuration. In: *BioResources*, 11(2), p. 4633-4644, 2016.
- CLAUSS ET AL. 2014
Clauss, S. ; Pescatore, C. ; Niemz, P.: Anisotropic elastic properties of common ash (*Fraxinus excelsior* L.). *Holzforschung* ; 68(8): 941-949, 2014.
- CSOKAS (2021)
Csokas, W.: Determination of the Torsional Stiffness Properties of Diagonal Laminated Timber (DLT). Master's thesis, Chair of Timber Structures and Building Construction, Technical University of Munich, 2021.
- DANIEL AND ISHAI (2006)
Daniel, I. M. ; Ishai, O.: *Engineering mechanics of composite materials*. 2. ed., Oxford Univ. Press, New York, 2006.
- DANIELSSON AND JELEČ (2021)
Danielsson, H. ; Jeleč, M.: A unified design proposal for shear stress prediction in crossing areas for cross laminated timber at in-plane shear and beam loading conditions. *Construction and Building Materials*, 355 , p. 129167, 2022.

- DIETSCH (2022)
Dietsch, P.: Kennt der Holzbau Grenzen des Wachstums? *Bautechnik*, Nr. 99, Sonderheft *Holzbau*, S2, 2022.
- DONHAUSER (2022)
Donhauser, T.: Analytical and experimental determination of the out-of-plane shear capacity of diagonal lamianted timber. Master's thesis, Chair of Timber Structures and Building Construction, Technical University of Munich, 2022.
- EBNER (2022)
Ebner, G.: BSH-Bedarf 2021. Deutschland klare Nummer 1. *Holzkurier* 09/2022, Österreichischer Agrarverlag, Wien, 2022.
- EPP (2018)
Epp, L.: *Dowel Laminated Timber, A new mass timber product in North America*. Wood, Design & Building, The official publication of the Canadian Wood Council, Ottawa, 2018.
- ERHARDT ET AL. (2015)
Ehrhart, T. ; Brandner, R. ; Schickhofer, G. ; Frangi, A.: Rolling Shear Properties of some European Timber Species with Focus on Cross Laminated Timber (CLT): Test Configuration and Parameter Study. International Network on Timber Engineering Research (INTER 2015), Proceedings, pp. 61-76, Croatia, 2015.
- FARSHAD (1992)
Farshad, M.: *Design and analysis of shell structures*. Springer, Luxemburg, 1992.
- FEICHTER (2013)
Feichter, I.: Spannungs- und Traglastberechnungen an ausgewählten Problemen der Holz-Massivbauweise in Brettsperrholz. Master's thesis, Institut für Holzbau und Holztechnologie, Technische Universität Graz, 2013.
- FELLMOSER AND BLAß (2004)
Blass, H.J. ; Fellmoser, P.: Influence of rolling shear modulus on strength and stiffness of structural bonded timber elements. International council for research and innovation in building and construction, Working Comission W18 - Timber Structure (CIB-W18/37-6-5). Meeting 37, UK, Edinburgh, 2004.
- FROCHT (1931)
Frocht, M. M.: Recent advances in photoelasticity and an investigation of the stress distribution in square blocks subjected to diagonal compression. *Transactions, ASME*, Vol. 55, pp. 135-153, 1931.
- FUCHS (2020)
Fuchs, M.: Hyperboloidal Roof Structures made of Timber. Master's thesis, Chair of Timber Structures and Building Construction, Technical University of Munich, 2020.
- GEBHARDT (2018)
Gebhardt, C.: *Praxisbuch FE mit Ansys Workbench : Einführung in die lineare und nichtlineare Mechanik*. 3., aktualisierte Auflage, Hanser, München, 2018.
- Gindl et al (2001)
Gindl, W. ; Teischinger, A. ; Schwanninger, M. ; Hinterstoisser, B.: The relationship between near infrared spectra of radial wood surfaces and wood mechanical properties. *J. Near Infrared Spectrosc.* 9, 255-261, 2001.

- GRÄFE ET AL. (2018)
Gräfe, M. ; Dietsch, P. ; Hipper, A. ; Wilde, M.: Vorspannung von Brettspertholzkonstruktionen. Schlussbericht zum Forschungsvorhaben. Technical University of Munich, 2018.
- GOODMAN AND BODIG (1970)
Godman, J.; Bodig, J.: Orthotropic Elastic Properties of Wood. Materials Science, Engineering Journal of the Structural Division, : 2301–2319, 1970.
- GRESSEL (1971)
Gressel, P. :Untersuchungen über das Zeitstandbiegeverhalten von Holzwerkstoffen in Abhängigkeit von Klima und Belastung. Dissertation, Universität Hamburg, 1971.
- GRESSEL (1984)
Gressel, P. (1984). Kriechzahlen von Holz und Holzwerkstoffen. Bauen mit Holz, Jg. 86, Nr. 4, 1984.
- HALÁSZ AND SHEER (1996)
Halász R. von ; Scheer, C.: Grundlagen, Entwurf, Bemessung und Konstruktionen. Holzbau-Taschenbuch, 9. Aufl., ErnstSohn, Berlin, 1996.
- HOLZINGER (2021)
Holzinger, D. P.: Konzeption eines Scheibenschubversuches für diagonal vernageltes Brettspertholz. Master's thesis, Chair of Timber Structures and Building Construction, Technical University of Munich, 2021.
- Hankinson (1921)
Hankinson, R. L.: Investigation of crushing strength of spruce at varying angles of grain, Air Force Information Circular No. 259, U. S. Air Service, 1921.
- Jauk (2020)
Jauk, G.: BSP-Kapazität wird sich bis 2022 verdoppeln. Holzkurier, 11/2020. Österreichischer Agrarverlag, Wien, 2020.
- Jauk (2023)
Jauk, G.: Weiterer Wachstumsschub für BSP - Rückblick 2022 / Ausblick 2023. Holzkurier, 01/2023. Österreichischer Agrarverlag, Wien, 2023.
- JONES (2014)
Jones, R. M.: Mechanics of Composite Materials. 2nd ed., Chapman and Hall/CRC, Boca Raton, 2014.
- JÖBSTL AND SCHICKHOFER (2007)
Jöbstl, R. ; Schickhofer, G.: Comparative examination of creep of GLT and CLT slabs in bending. Working Commission W18 - Timber Structures, Bled, Slovenia, 2007.
- JONG AND CLANCY (2004)
Jong, F. ; Clancy, P.: Compression properties of wood as functions of moisture, stress and temperature. Fire and Materials 28, Nr. 24, p. 209–225, 2004.
- KATZ ET AL. (2008)
Katz, L.J. ; Spencer, P. ; Wang, Y. ; Misra, A. ; Marangos, O. ; Friis, L.: On the elastic properties of woods. Journal of Materials Science, 43:139-145, 2008.
- KEYLWERTH (1951)
Keylwerth, R.: The anisotropic elasticity of wood and plywood. In: VDI-Forschungsheft, Nr. 430, 1951.

- KLARMANN AND SCHWEIZERHOF (1993)
Klarmann, R. ; Schweizerhof, K.: A Priori Verbesserung von Schubkorrekturfaktoren zur Berechnung von geschichteten anisotropen Schalentragerwerken. Archive of Applied Mechanics 63, 73-85, 1993.
- KLEINHENZ ET AL. (2016)
Kleinhenz, M. ; Winter, S. ; Dietsch, P.: Eurocode 5 - a halftime summary of the revision process. World Conference on Timber Engineering WCTE 2016, Vienna, Austria, 2016.
- Krauss (1969)
Krauss, F.: Hyperbolisch paraboloiden Schalen aus Holz. Karl Krämer Verlag, Stuttgart, 1969.
- KREUZINGER AND SCHOLZ (1999)
Kreuzinger, H ; Scholz A.: Wirtschaftliche Ausführungs- und Bemessungsmethode von ebenen Holzelementen (Brücken, Decken, Wände). Schlußbericht. Technische Universität München, Institut für Tragwerksbau, München, 1999.
- KREUZINGER AND SCHOLZ (2001)
Kreuzinger, H ; Scholz A.: Schubtragverhalten von Brettspertholz. Abschlussbericht. Technische Universität München, Institut für Baustoffe und Konstruktion, München, 2001.
- KREUZINGER AND SIEDER (2013)
Kreuzinger, H. ; Sieder, M.: Einfaches Prüfverfahren zur Bewertung der Schubfestigkeit von Kreuzlagenholz/Brettspertholz. Bautechnik, 90(5): 314-316, Berlin, 2013.
- LECHNER (2021)
Lechner, M.: Holzbewehrtes Holz. Entwicklung eines furnierverstärkten stabförmigen Holzprodukts für tragende Zwecke. English title: Veneer-reinforced Timber. Dissertation, Technical University of Munich, Chair of Timber Structures and Building Construction, 2021.
- LECHNER ET AL. (2021)
Lechner, M. ; Dietsch, P. ; Winter, S.: Veneer-reinforced timber–Numerical and experimental studies on a novel hybrid timber product. Construction and Building Materials, 298, p. 123880, 2021.
- LOEBUS AND WINTER (2017)
Löbus, S. ; Winter, S.: Zweiachsige Tragwirkung bei Holz Beton-Verbundkonstruktionen – Entwicklung von Bemessungsverfahren und Konstruktionsdetails für zweiachsige Lastabtragung bei der Holz-Beton-Verbundbauweise. Schlussbericht zum Forschungsvorhaben. Bundesamt für Bauwesen und Raumordnung. Forschungsinitiative Zukunft Bau. 2017.
- MADEREBNER (2021)
Maderebner, R.: European Manufacturing: What's next. International Mass Timber Conference, Online Conference, 2021.
- MADEREBNER AND MAURER (2021)
Maderebner, R. ; Maurer, B.: Cross Laminated Timber under concentrated Compression Loads - Methods of Reinforcements. Engineering Structures 245, p. 112534, 2021.

- MAURER (2020)
Maurer, B.: Lösungsansätze für punktgestützte Flachdecken aus Brettsperrholz. English title: Solution approaches for point-supported flat slabs made of cross-laminated timber. Dissertation, University of Innsbruck, 2020.
- MESTEK (2011)
Mestek, P.: Punktgestützte Flächentragwerke aus Brettsperrholz (BSP) – Schubmessung unter Berücksichtigung von Schubverstärkungen. Dissertation, Technical University of Munich, 2011.
- MESTEK AND WINTER (2011)
Mestek, P. ; Winter, S.: Point-supports of Cross Laminated Timber (CLT) Structures - Shear Design including Reinforcement. Bauingenieur, Nr. 86, p. 529–540, 2011.
- MUSTER (2020)
Muster, M.: Column-Slab Connection in Timber Flat Slabs. Dissertation, Eidgenössische Technische Hochschule Zürich, Zurich, 2020.
- NAVI AND STANZL-TSCHEGG (2009)
Navi, P. ; Stanzl-Tschegg, S.: Micromechanics of creep and relaxation of wood. A review : COST Action E35 2004-2008: Wood machining - micromechanics and fracture. Holzforschung 63, Nr. 2, 2009.
- NAVI AND GILANI (2004)
Parviz Navi, Marjan Sedighi Gilani: Modelling the influences of microfibril angles and natural defects on the forceextension behavior of single wood fibers. COST Action E20 Wood Fiber Cell Wall Structure, 2004.
- NETTLES (1994)
Nettles, A. T.: Basic Mechanics of Laminated Composite Plates. NASA Reference Publication 1351, National Aeronautics and Process Laboratory, Science and Engineering Direction, Washington, DC, 1994.
- NEUHAUS (1981)
Neuhaus, H.: Elastizitätszahlen von Fichtenholz in Abhängigkeit von der Holzfeuchtigkeit. Dissertation, Ruhr-Universität Bochum, 1981.
- NIEMZ AND SONDEREGGER (2017)
Niemz, P. ; Sonderegger, W.: Elastomechanische und inelastische Eigenschaften von Holz und Holzwerkstoffen. In: Holzphysik. Carl Hanser Verlag GmbH and Co. KG., p. 266–335, München, 2017.
- O’CEALLAIGH ET AL. (2018)
O’Ceallaigh, C ; Sikora, K. ; Harte, A.M.: The Influence of Panel Lay-Up on the Characteristic Bending and Rolling Shear Strength of CLT. Buildings, 8, 114, 2018.
- OZYHAR ET AL (2013)
Ozyhar, T. ; Hering, S. ; Niemz, P.: Viscoelastic characterization of wood: Time dependence of the orthotropic compliance in tension and compression. Journal of Rheology 57, Nr. 2, p. 699–717, 2013.
- PRAVIZ AND GILANI (2004)
Praviz, N. ; Gilani, M. S.: Modelling the influences of microfibril angles and natural defects on the forceextension behavior of single wood fibers. COST Action E20 Wood Fiber Cell Wall Structure, 2014.

- POPOV (1970)
Popov, E. P.: Kelvin’s Solution of Torsion Problem. In: Journal of the Engineering Mechanics Division 1970, Vol. 96, S. 1005–1012, 1970.
- RADCLIFFE (1965)
Radcliffe B. M.: A theoretical evaluation of Hankinson's formula for modulus of elasticity of wood at an angle to the grain. Quart. Bull. Mich. Agric. Exp. Sta 48(2): 286-95, 1965.
- RAVENSHORST (2015)
Ravenshorst, G.: Species independent strength grading of structural timber. Dissertation, Delft University of Technology, Delft, 2015.
- REDDY (2004)
Reddy, J. N.: Mechanics of laminated composite plates and shells: Theory and analysis. 2. ed. Boca Raton, CRC Press, 2004.
- REUTERS (1971)
Reuters R. C.: Concise Property Transformation Relations for an Anisotropic Lamina. Journal of Composite Materials, Vol 5, Issue 2, 1971.
- ROYLANCE (2000)
Roylance, D.: Laminated composite plates. Department of Materials Science and Engineering. Massachusetts Institute of Technology. Cambridge, 2000.
- SILLY (2010)
Silly G.: Numerische Studien zur Drill- und Schubsteifigkeit von Brettsperrholz (BSP). Diplomarbeit, Institut für Holzbau und Holztechnologie, Technische Universität Graz, 2010.
- SCHÄNZLIN (2010)
Schänzlin, J.: Modeling the long-term behavior of structural timber for typical service-class-II-conditions in South-West Germany. Dissertation, Universität Stuttgart, 2010.
- SCHENK AND WINTER 2021
Schenk M. ; Winter S.: Second generation of Eurocode 5—Publication schedule and interface between design and product standards. World Conference on Timber Engineering WCTE 2020/21, Santiago, Chile, 2021.
- SCHENK ET AL. 2022
Schenk M. ; Hübner C. ; Cabrero J.M.: Cross-Laminated Timber: A Survey on Design Methods and Concepts in Practise. CivilEng 2022, 1, 1-19.
- SCHICKHOFER (1994)
Schickhofer, G.: Starrer und nachgiebiger Verbund bei geschichteten, flächenhaften Holzstrukturen. Dissertation, Technischen Universität Graz, 1994.
- SCHICKHOFER ET AL. (2010)
Schickhofer, G. ; Bogensberger, T. ; Moosbrugger, T.: BSPhandbuch, Holz Massivbauweise in Brettsperrholz: Nachweise auf Basis des neuen europäischen Normenkonzepts. Technischen Universität Graz, Graz, 2010.
- SCHNEIDER ET AL. (2018)
Schneider J. ; Tannert T. ; Tesfamariam S.; Stierner S.F.: Experimental assessment of a novel steel tube connector in cross-laminated timber. Engineering Structures 177:283-290, 2018.

- SCHÜRMAN (2007)
Schürmann, H.: Konstruieren mit Faser-Kunststoff-Verbunden. 2., bearbeitete und erweiterte Auflage, VDI Buch, Springer Verlag, Berlin, Heidelberg, 2007.
- STIEB ET AL. (2023)
Stieb, T. ; Maurer, B. ; Bestler, M. ; Dietsch, P. ; Maderebner, R.: Solutions for edge connections to build two-way spanning cross laminated timber slabs. World Conference on Timber Engineering WCTE 2023, Oslo, Norway, 2023.
- TAPIA ET AL. (2021)
Tapia, C. ; Stimpfle, L. ; Aicher, S.: A new column-to-slab connection for multi-storey timber buildings. World Conference on Timber Engineering WCTE 2020/21, Santiago, Chile, 2021.
- TAVOUSSI ET AL. (2010)
Tavoussi, K. ; Winter, W. ; Pixner, T.: Das erdbebensichere Holzhaus. Bauingenieur Nr. 85, S. 129–135, 2010.
- TESSLER (2015)
Tessler, C.: Refined zigzag theory for homogeneous, laminated composite, and sandwich beams derived from Reissner's mixed variational principle. *Meccanica* 50:2621–2648, 2015.
- TIMOSHENKO (1921)
Timoshenko, S. P.: On the correction for shear of the differential equation for transverse vibrations of prismatic bars. *The London, Edinburgh and Dublin Philosophical Magazine and Journal of Science*, 41:245, 744–746, 1921.
- TURESSON ET AL. (2019)
Turesson, J. ; Björnrot, A. ; Berg, S. ; Ekevad, M. ; Tomasi, R.: Picture frame and diagonal compression testing of cross-laminated timber. *Materials and Structures*, 52:60, 2019.
- TURESSON ET AL. (2020)
Turesson, J. ; Björnrot, A. ; Berg, S. ; Ekevad, M.: Shear modulus analysis of cross-laminated timber using picture frame tests and finite element simulations. *Materials and Structures*, 53:112, 2020.
- TONG ET AL. (2020)
Tong, D. ; Brown, S. A. ; Corr, D. ; Custais, G.: Wood creep data collection and unbiased parameter identification of compliance functions. *Holzforschung* 74, Nr. 11, p. 1011–1020, 2020.
- VOORMANN AND PFEIFER (2007)
Voormann, F. ; Pfeifer, M.: Die Kämpf-Stegträger der Eissporthalle Bad Reichenhall. Eine typische Holzkonstruktion der 1950er und 1960er Jahre? *Bautechnik*, Nr. 84, Heft 1, 2007.
- VOGEL (2021)
Vogel, F.: Investigations on the Long-term Deformation Behavior of CLT and DLT. Master's thesis, Chair of Timber Structures and Building Construction, Technical University of Munich, 2021.
- WALLNER-NOVAK ET AL. (2013)
Wallner-Novak, M. ; Koppelhuber, J. ; Pock, K.: Brettsperrholz Bemessung : Grundlagen für Statik und Konstruktion nach Eurocode. *ProHolz Austria*, Wien, 2013.
- WINTER (1955)
Winter, H.: Unterlagen und Richtlinien für den Holzflugzeugbau B III b. Sperrhölzer. Braunschweig, 1955.

- WINTER ET AL. (2018)
Winter, S. ; Lechner, M. ; Köhler, C.: Industrialization of Building Processes - a chance for timber to take the lead. World Conference on Timber Engineering WCTE 2018, Seoul, Korea, 2018.
- WINTER (2021)
Winter, K.: A new Approach to Determine and Evaluate the Poisson's Ratio of Spruce Wood. Master's thesis, University of Innsbruck, 2021.
- ZOELLING ET AL. (2019)
Zoellig, S. ; Muster, M. ; Themessl, A.: Butt-joint bonding of timber as a key technology for point-supported, biaxial load-bearing flat slabs made of cross-laminated timber. *Earth and Environmental Science*, 323, 012144, 2019.

Standards

- DIN EN 408
EN 408:2010+A1:2012, Timber structures - Structural timber and glued laminated timber - Determination of some physical and mechanical properties. Deutsches Institut für Normung, Berlin, 2010.
- DIN 1052-10
DIN 1052-10:2012-05: Herstellung und Ausführung von Holzbauwerken - Teil 10: Ergänzende Bestimmungen. English title: Design of timber structures - Part 10: Additional provisions. Deutsches Institut für Normung Berlin, 2012.
- DIN 13343
DIN 13343:1994-04, Linear-viskoelastische Stoffe - Begriffe, Stoffgesetze, Grundfunktionen. Deutsches Institut für Normung Berlin, 1994.
- DIN EN 1995-1-1/NA
DIN EN 1995-1-1/NA:2013-08, Eurocode 5: Nationaler Anhang - National festgelegte Parameter - Eurocode 5: Bemessung und Konstruktion von Holzbauten - Teil 1-1: Allgemeines - Allgemeine Regeln und Regeln für den Hochbau. Deutsches Institut für Normung (DIN), Berlin, 2013.
- DIN 68364
DIN 68364:2003-05, Kennwerte von Holzarten - Rohdichte, Elastizitätsmodul und Festigkeiten. Deutsches Institut für Normung Berlin, 2003.
- EN 338
EN 338:2016, Structural timber - Strength classes. CEN - Comité Européen de Normalisation, Brussels, 2016.
- EN 384
EN 384:2016, Structural timber - Determination of characteristic values of mechanical properties and density. CEN - Comité Européen de Normalisation, Brussels, 2016.
- EN 789
Timber structures - Test methods - Determination of mechanical properties of wood based panels. CEN - Comité Européen de Normalisation, Brussels, 2005.
- EN 10080
EN 10080:2005, Steel for the reinforcement of concrete - Weldable reinforcing steel - General. CEN - Comité Européen de Normalisation, Brussels, 2005.
- EN 13183
EN 13183-1:2002, Moisture content of a piece of sawn timber - Part 1: Determination by oven dry method. CEN - Comité Européen de Normalisation, Brussels, 2002
- EN 13183-2
EN 13183-2:2002 Moisture content of a piece of sawn timber - Part 2: Estimation by electrical resistance method. CEN - Comité Européen de Normalisation, Brussels, 2002.
- EN 1990-1-1
EN 1991-1-1:2010-1: Eurocode 1: Actions on structures - Part 1-1: General actions - Densities, self-weight, imposed loads for buildings. CEN - Comité Européen de Normalisation, Brussels, 2010.
- EN 1902-1-1
EN 1992-1-1:2004/A1:2014: Eurocode 2: Design of concrete structures - Part 1-1: General rules and rules for buildings - Part 1-1 General. CEN - Comité Européen de Normalisation, Brussels, 2014.

- EN 1995-1-1
EN 1995-1-1:2010-12, Eurocode 5: Design of timber structures - Common rules and rules for buildings - Part 1-1: General. CEN - Comité Européen de Normalisation, Brussels, 2010.
- EN 14081-2
EN 14081-2:2018, Timber structures - Strength graded structural timber with rectangular cross-section - Part 2: Machine grading; additional requirements for type testing. CEN - Comité Européen de Normalisation, Brussels, 2018.
- EN 16351
EN 16351:2021, Timber structures - Cross laminated timber - Requirements. CEN - Comité Européen de Normalisation, Brussels, 2021.
- EN 16485
EN 16485:2014, Round and sawn timber - Environmental Product Declarations - Product category rules for wood and wood-based products for use in construction. CEN - Comité Européen de Normalisation, Brussels, 2021.
- ÖNORM B 1995-1-1
ÖNORM B 1995-1-1:2015, Eurocode 5: Bemessung und Konstruktion von Holzbauten - Teil 1-1: Allgemeines - Allgemeine Regeln und Regeln für den Hochbau - Nationale Festlegungen zur Umsetzung der ÖNORM EN 1995-1-1, nationale Erläuterungen und nationale Ergänzungen. Österreichische Normungsinstitut für Normung e.V. (ON), Wien, 2015.
- prEN 1995-1-1
prEN 1995-1-1:2023-10, Working Document, Eurocode 5: Design of timber structures - Common rules and rules for buildings - Part 1-1: General, CEN-CENELEC/TC 250 - Comité Européen de Normalisation, Brussels, 20xx, Stated as of 2023-08-25.
- JCSS (2006)
Joint Committee on Structural Safety: JCSS Probabilistic Model Code, Part 3: Resistance Models – 3.5 Properties of Timber. Probabilistic Model Code
- WORKING DRAFT SC5.T1 (2018)
Workind Draft SC5.T1 (2018), Working draft of design of cross laminated timber in a revised Eurocode 5-1-1, Version 2018-04-13.

European Technical Assessments and European Assessment Documents

- EAD 13005-00-0304
EAD 13005-00-0304, Solid wood slab element to be used as a structural element in buildings. European Assessment Document, Official Journal of the European Union (OJEU) 2015/C 226/05, Brussels, 2015.
- ETA-20/0023
ETA-20/0023, Pfeifer CLT Brettsperrholz. European Technical Assessment. Austrian Institute of Construction Engineering, Vienna, 2020.
- ETA-16/0055
ETA-16/0055, Radiusholz. European Technical Assessment. Austrian Institute of Construction Engineering, Vienna, 2020.

Legal Texts and International Agreements

- EUROPEAN COMMISSION (2011)
Construction Products Regulation (CPR), Regulation (EU) No 305/2011 of the European Parliament and of the Council, harmonised conditions for the marketing of construction products and repealing Council Directive 89/106/EEC, European Commission, Brussels, 2011.
- EUROPEAN COMMISSION (2012)
European Commission, Mandate M/515 - Mandate for amending existing Eurocodes and extending the scope of structural Eurocodes'. Enterprise and Industry Directorate-General, Brussels, 2012.

Others

- DLUBAL SOFTWARE GMBH (2016)
Add-on Module RF-LAMINATE, Design of Laminate Surfaces, Program Description. Dlubal Software GmbH 2016, Am Zellweg 2, D-93464 Tiefenbach, Germany.
- EOTA (2023)
The European Organisation for Technical Assessment (EOTA): ETA database, URL: <https://www.eota.eu/etassessments> — Stated as of 2023-08-25.
- HOLZBAU UNTERRAINER GMBH (2021a)
Layouts and plans for the production of CLT and DLT test specimens, 2021.
- HOLZBAU UNTERRAINER GMBH (2021b)
Component report delamination of CLT and DLT test specimens. Report on the moisture content, density and material parameters. Components 9017 to 9037, 2021-03-11.
- IGE (1946)
Eidgenössisches Institut für Geistiges Eigentum (IGE): Schweizerisches Patent Nr. 254319: Verfahren zur Verleimung aus einzelnen Teilen zusammengesetzter Holzträger. Eingereicht am 7. September 1946, Bern.
- INNOCROSSLAM (2019-2022)
European Union's Horizon 2020 research and innovation programme under grant agreement N° 773324: Research Project InnoCrossLam (Innovative Solutions for Cross Laminated Timber Structures). URL: <https://forestvalue.org/project/innocrosslam/> — Stated as of 2023-09-15.
- InnoTLT (2023-2026)
Swedish Government Agency for Innovation Systems (Vinnova): Research Project InnoTLT (Innovative Timber Construction with Tailored Laminated Timber). URL: <https://portal.research.lu.se/en/projects/innotlt-innovative-timber-construction-with-tailored-laminated-ti> — Stated as of 2023-09-15.
- MASSIV-HOLZ-MAUER ENTWICKLUNGS GMBH (2021)
Massiv-Holz-Mauer Entwicklungs GmbH: Produkte. Massiv-Holz-Mauer. URL: <https://https://www.massivholzmauer.de/de/produkte/massiv-holz-mauerr-clt-/nlt> — Stated as of 2023-09-15.

Index of figures and tables

Figures	190
Tables	196

Figures

Fig. 1.1:	Exemplary layups of CLT elements compared to DLT elements	3
Fig. 1.2:	Fictive circular and longitudinal design sections within the centric point-supported mass timber slab.....	4
Fig. 1.3:	Uniaxial load transfer of conventional CLT elements with linear support.....	5
Fig. 1.4:	Biaxial load transfer of DLT elements with point-supports.....	5
Fig. 1.6:	Uniaxial load transfer of conventional CLT elements with linear support.....	6
Fig. 1.5:	Exemplary construction grid of point-supported slabs with the recommended arrangement of diagonal layers (dashed lines).....	6
Fig. 1.7:	Layup (left) and test setup (right) for investigations on the in-plane load-bearing capacity of mass timber elements with orthogonal and diagonal layer arrangement (BOSL 2002).....	7
Fig. 1.9:	Laminated mass timber elements prepared for the diagonal compression test (left) and picture frame test (right) (TURESSON ET AL. 2019).....	10
Fig. 1.8:	Diagonal compression test on 3-layered CLT and DLT elements (TURESSON ET AL. 2020).....	10
Fig. 1.10:	DLT panel with alternating layer configuration in four-point-bending tests (BUCK ET AL 2016).....	10
Fig. 1.11:	Punching test on CLT element using system connectors (MAURER AND MADEREBNER 2021).....	12
Fig. 1.12:	Section through locally reinforced column-slab connections (MUSTER 2021).....	12
Fig. 1.13:	Column-to-slab connection realized by pyramid-shaped LVL inserts (TAPIA ET AL. 2021).....	12
Fig. 2.1:	Small-scale shear testing on CLT and DLT specimens, without (left) and with (right) compression perpendicular to grain.....	17
Fig. 2.2:	Four-point bending tests on DLT elements at University of Innsbruck.....	17
Fig. 2.3:	Biaxial bending tests on CLT and DLT elements.....	17
Fig. 2.4:	Determination of the in-plane shear stiffness using shear frame tests.....	18
Fig. 3.1:	Notation of laminates on a CLT element (left) and DLT element (right).....	19
Fig. 3.2:	CEN/TC 250 and CEN/TC 250/SC 5 work structure (SCHENK AND WINTER 2021).....	22
Fig. 4.1:	Stresses and Strains acting on the 3D continuum, according to (NIEMZ AND SONDEREGGER 2017).....	25

Fig. 4.2:	Principal material directions of unprocessed wood.....	26
Fig. 4.3:	Boltzmann's superposition principle (VOGEL 2021) based on (SCHÜRMANN 2007).....	30
Fig. 4.4:	Presentation of the rheological models according to DIN 13343.....	31
Fig. 4.5:	Phases of the long-term deformation behavior of timber, according to (GRESSEL 1971).....	34
Fig. 4.6:	Load redistribution principle within laminates like CLT (Vogel 2021) based on (SCHÜRMANN 2007).....	34
Fig. 5.1:	Load case of pure torsion acting on a plate element.....	41
Fig. 5.2:	Linear and non-linear approach for considering the out-of-plane shear strain of a formerly plane section, formerly normal to the midplane (SCHICKHOFER 1994).....	43
Fig. 5.3:	Stress components in unidirectional lamina referred to loading and material axes (DANIEL AND ISHAI 2006).....	45
Fig. 5.4:	Modulus of elasticity (a) and shear modulus (b) of spruce as a function of the fibre orientation.....	48
Fig. 5.5:	Modulus of elasticity of ash (a) and shear modulus of eastern hemlock (b) as a function of the fibre orientation (experimental values based on (CLAUSS ET AL. 2014 and BAHMANZAD 2020).....	50
Fig. 5.6:	Flowcharts for determination of transformed elastic constants (left) and laminate stiffness matrices (right) based on DANIEL AND ISHAI (2006), extended by own approaches (dashed lines).....	52
Fig. 5.7:	Designation of the parameters and indices of z_i	54
Fig. 5.8:	Quantitative shear stresses and shear deformations of an exemplary 5-layered DLT element.....	56
Fig. 6.1:	Shear stresses and shear deformations in global x and y direction of an exemplary 5-layered CLT element (upper sketch) and an exemplary 5-layered DLT element (lower sketch).....	60
Fig. 6.2:	Analytical out-of-plane shear stiffness values of selected 5-layered CLT and DLT series in x direction.....	64
Fig. 6.3:	Analytical out-of-plane shear stiffness values of selected 5-layered CLT and DLT series in y direction.....	64
Fig. 6.4:	Parameter set for the arrangement of the second and fourth layer of 5-layered DLT elements.....	66
Fig. 6.5:	Out-of-plane shear stiffness (Shear Analogy Method) as a function of the layer arrangement.....	66

Fig. 6.6:	Out-of-plane shear stiffness (laminare theory) as a function of the layer arrangement.....	66
Fig. 6.7:	Different tests setups for the determination of out-of-plane shear properties.....	67
Fig. 6.8:	Test setup of the shear testing—with and without compression perpendicular to grain.....	68
Fig. 6.9:	Expected shear stresses, shear deformations, and shear strains in x (left) and y (right) direction of DLT following the Shear Analogy Method (upper sketch) and the test setup (lower sketch).....	70
Fig. 6.10:	Exemplary FE volume model of D3 series and static systems of the numerical test setup.....	71
Fig. 6.11:	Load-deformation diagrams (def_1) for the specimens oriented in x (left) and y (right) direction, without external compression.....	75
Fig. 6.12:	Load-deformation diagrams (hydraulic cylinder) for the specimens oriented x (left) and y (right) direction, without external compression.....	75
Fig. 6.13:	Out-of-plane shear stiffnesses of the CLT and DLT series ($t = 100$ mm) following the experimental investigations and analytical solutions, without compression perpendicular to grain.....	79
Fig. 6.14:	Pre-tests on the test setup to determine the friction (left) and resistance to shearing (right).....	80
Fig. 6.15:	Load-deformation diagrams and evaluation of the pre-tests on the test setup.....	80
Fig. 6.16:	Load-deformation diagrams (def_1) in x (left) and y (right) direction, with external compression perpendicular to grain ($\sigma_c = 0.5$ MN/m ²).....	82
Fig. 6.17:	Load-deformation diagrams (hydraulic cylinder) in x (left) and y (right) direction, with external compression perpendicular to grain ($\sigma_c = 0.5$ MN/m ²).....	82
Fig. 6.18:	Out-of-plane shear stiffnesses of the CLT and DLT series ($t = 100$ mm) following the experimental investigations and analytical solutions, with and without external compression ($\sigma_c = 0.50$ MN/m ²).....	86
Fig. 6.19:	Out-of-plane shear stiffnesses of the CLT and DLT series ($t = 100$ mm) following the experimental investigations and analytical solutions with and without external compression ($\sigma_c = 0.50$ MN/m ²).....	89
Fig. 7.1:	Bending stiffness of 5-layered CLT and DLT elements as a function of the layer arrangement θ	92
Fig. 7.2:	Bending stiffness B_x of 5-layered CLT and DLT elements as a function of the layer thickness t_i	93
Fig. 7.3:	Bending stiffness B_y of 5-layered CLT and DLT elements as a function of the layer thickness t_i	93

Fig. 7.4:	Test setup of the four-point bending tests.....	94
Fig. 7.5:	Load-deformation diagrams of the cylinder.....	96
Fig. 7.6:	Display of an exemplary failure mechanism in bending of D1-4 specimen.....	96
Fig. 8.1:	Girder grid model of an infinitesimal plate element under biaxial bending, according to (POPOV 1970).....	99
Fig. 8.2:	Extended girder grid model of an infinitesimal plate element taking into account bending and shear deformations (Arnold et al. 2022a).....	100
Fig. 8.3:	Torsional stiffness of the CLT and DLT elements following the analytical solution ($dx = dy = 1.0$ m).....	102
Fig. 8.4:	Torsional stiffness and effective torsional stiffness of 5-layered CLT and DLT elements as a function of the layer arrangement Θ ($dx = dy = 1.0$ m).....	103
Fig. 8.5:	Test setup of the biaxial bending tests.....	104
Fig. 8.6:	Load-deformation diagrams of the CLT and DLT specimens under biaxial bending.....	106
Fig. 8.7:	Torsional Stiffness of the orthogonal and diagonal laminated series (CLT and DLT) given from the mechanical testing.....	110
Fig. 8.8:	Exemplary 3D model of O1 series (Inventor) and FE volume model of O1 series under biaxial bending (Ansys).....	111
Fig. 8.9:	Exemplary mesh-convergence-diagrams of O1 series (left) and O5 series (right).....	112
Fig. 8.10:	Torsional stiffness of the CLT and DLT elements following the analytical, experimental, and numerical investigations.....	113
Fig. 8.11:	Parameter set for the different board widths w of a 5-layered CLT and DLT ($t=100$ mm) ($dx=dy=1.0$ m).....	114
Fig. 8.12:	Exemplary test facility for the determination of long-term deformation behavior of CLT and DLT undergoing biaxial bending (VOGEL 2021).....	117
Fig. 8.13:	Long-term deformation of all series as a function of the time ($F = 1.0$ kN; $dx = dy = 1.0$ m).....	117
Fig. 8.14:	Comparison on the deformation at t_{in} using the minimum and recommended deformation coefficients.....	118
Fig. 9.1:	Test setup of the shear frame test based on construction sketches by (MASSIV-HOLZ-MAUER GMBH 2021) and (HOLZINGER 2021).....	121
Fig. 9.2:	Geometrical parameters and static system for the experimental investigations.....	123
Fig. 9.3:	Load-deformation diagrams of the shear-frame test.....	124

Fig. 9.4:	Test setup of the in-plane shear compression tests, based on (BRANDNER ET AL. 2017).....	125
Fig. 10.1:	Scale for the deformation analysis.....	130
Fig. 10.2:	Scale for the deformation analysis.....	134
Fig. 10.3:	Axonometry of the centric point-supported slab (left) and an exemplary 3D FE model (Ansys).....	140
Fig. 10.4:	Axonometry of the slab, point-supported at three corners (left) and an exemplary 3D FE model (Ansys).....	140
Fig. 10.5:	Comparison of the deformations of centric point-supported mass timber slab using 3D and 2D FE models.....	141
Fig. 10.6:	Circular and longitudinal design sections within the centric point-supported mass timber slab.....	142
Fig. 10.7:	Normal stresses due to bending acting along the critical sections (centric point-support).....	143
Fig. 10.8:	Compression stresses acting along the longitudinal sections (centric point-support).....	144
Fig. 10.9:	Punching shear stresses acting along the critical sections (centric point-support).....	145
Fig. 10.10:	Circular and longitudinal design sections within the mass timber slab, point-supported at three corners, with rotational restraint at two edges.....	147
Fig. 10.11:	Normal stresses due to bending acting along the critical sections (point-supported at three corners).....	148
Fig. 10.12:	Compression stresses acting along the longitudinal sections (point-supported at three corners).....	149
Fig. 10.13:	Punching shear stresses acting along the critical sections (point-supported at three corners).....	150
Fig. 10.14:	Circular and longitudinal design sections within the mass timber slab, point-supported at three corners without rotationally restrained edges.....	151
Fig. 10.15:	Normal stresses due to bending acting along the critical sections (point-supported at three corners without rotationally restrained edges).....	152
Fig. 10.16:	Punching shear stresses acting along the critical sections (point-supported at three corners without rotationally restrained edges).....	153
Fig. 11.1:	Relationship between bending and torsional moments and the angle φ	159
Fig. 11.2:	Production processes of CLT and DLT and their interaction to the input by researchers and planers.....	163

Fig. 11.3:	Stages within the CLT and DLT production of Holzbau Unterrainer GmbH.....	164
Fig. 11.4:	Stages of product development and the implementation on markets.....	165
Fig. 11.5:	Deep-beam with openings (left), plate elements with opening and notches (middle), and segmentation and joints of DLT slabs (right).....	167

Tables

Tab. 2.1:	Investigations carried out within this thesis.....	18
Tab. 3.1:	Abbreviations used for mass timber products.....	21
Tab. 4.1:	Exemplary orthotropic material properties of different wood species (mean values) (GOODMAN AND BODIG 1970), (SCHICKHOFER 1994), (KATZ ET AL 2007), (NIEMZ AND SONDEREGGER 2017), (DIN 68364).....	27
Tab. 4.2:	Elastic material properties of different strength classes according to EN 338 (mean values).....	28
Tab. 4.3:	Strength parameters and density values for spruce or equivalent softwood (strength class C24 / T14) according to EN 338 (characteristic values).....	28
Tab. 4.4:	Poisson's ratios for spruce or equivalent softwood (strength class C24 / T14) according to selected authors.....	28
Tab. 4.5:	Deformation coefficients for different phases of the long-term deformation.....	34
Tab. 4.6:	Chosen series for the analytical, experimental and, numerical investigations—mainly on the out-of-plane shear stiffness, the torsional stiffness, and the in-plane shear stiffness.....	35
Tab. 4.7:	Chosen series for the analytical, experimental, and numerical investigations on the bending stiffness.....	36
Tab. 4.8:	Chosen virtual series for the additional numerical investigations using real-scale 2D and 3D FE models.....	37
Tab. 4.9:	Moduli of elasticity and shear moduli of single laminations used for the production of the specimens according to two different ETAs.....	38
Tab. 5.1:	Moduli of elasticity and shear moduli of spruce of single laminations as a function of the layer arrangements, following different analytical approaches.....	48
Tab. 5.2:	Moduli of elasticity of ash and shear moduli of eastern hemlock of single laminations following different experimental and analytical investigations.....	49
Tab. 6.1:	Comparison of the out-of-plane shear stiffnesses of CLT compared to DLT following different approaches.....	62
Tab. 6.2:	Shear stresses in global x and y direction, with and without external compression ($\sigma_{c,90} = 0.50 \text{ MN/m}^2$), following the 3D-FE models for $F = 60 \text{ kN}$ following "path_1" (graphics by DONHAUSER 2022).....	72
Tab. 6.3:	Stresses perpendicular to grain for $F = 60 \text{ kN}$, without and with external compression perpendicular to grain ($\sigma_{c,90} = 0.50 \text{ MN/m}^2$) following "path_2", (graphics by DONHAUSER 2022).....	74
Tab. 6.4:	Failure mechanisms of the CLT and DLT series oriented in x direction, without external compression.....	76

Tab. 6.5:	Failure mechanisms of the CLT and DLT series in y direction, without external compression.....	77
Tab. 6.6:	Evaluation of the mechanical testing on the out-of-plane shear properties in global x and y direction of the CLT and DLT series (t = 100 mm), without compression perpendicular to grain.....	78
Tab. 6.7:	Failure mechanisms of the CLT and DLT series in x direction, with ext. compression ($\sigma_{c,90} = 0.50 \text{ MN/m}^2$).....	83
Tab. 6.8:	Failure mechanisms of the CLT and DLT series in y direction, with ext. compression ($\sigma_{c,90} = 0.50 \text{ MN/m}^2$).....	84
Tab. 6.9:	Evaluation of the mechanical testing on the out-of-plane shear properties in global x and y direction of the CLT and DLT specimens (t = 100 mm) with compression perpendicular to grain ($\sigma_{c,90} = 0.50 \text{ MN/m}^2$).....	85
Tab. 6.10:	Percentage increase of the shear strength f_v due to external compression.....	87
Tab. 6.11:	Out-of-plane shear stiffness values of the O1, D3, and D4 series following the numerical investigations, the mechanical testing, and the analytical approach	88
Tab. 7.1:	Percentage increase and decrease of the bending stiffness due to diagonal layer arrangements	92
Tab. 7.2:	Evaluation of the four-point bending tests on the uDLT series D1.....	98
Tab. 7.3:	MOE, bending stiffnesses $B_{x,exp}$ and $B_{x,eff,exp'}$ and $S_{xz,exp}$ following the four-point bending tests (EN 16351).....	98
Tab. 8.1:	Percentage increase of the torsional stiffness due to diagonal layer arrangements	102
Tab. 8.2:	Failure mechanisms of the CLT series.....	107
Tab. 8.3:	Failure mechanisms of the DLT series.....	108
Tab. 8.4:	Evaluation of the biaxial bending tests of the CLT and DLT specimens with t = 100 mm.....	109
Tab. 8.5:	Evaluation of the biaxial bending tests of the CLT and DLT specimens with t = 200 mm.....	109
Tab. 8.6:	Evaluation of the mechanical testing of the CLT and DLT specimens with t = 200 mm.....	112
Tab. 8.7:	Deformation coefficients chosen for the exemplary long-term deformation analytical analysis.....	115
Tab. 8.8:	Time-dependent stiffness values of the series investigated.....	116

Tab. 8.9:	Maximum stiffness values at t_{fin} of the series investigated, using minimum values k_i	116
Tab. 9.1:	In-plane shear stiffness values according to the laminate theory, using a reduction factor of 0.25.....	120
Tab. 9.2:	Evaluation of the shear frame tests.....	124
Tab. 9.3:	Evaluation of the shear compression tests.....	126
Tab. 9.4:	Comparison of the in-plane shear stiffnesses and shear moduli following the analytical approach and mechanical testing.....	127
Tab. 10.1:	5-layerd CLT O7 and DLT $\pm 45^\circ$ D7 series under uniaxial and biaxial bending due to point-supports.....	130
Tab. 10.2:	5-layered CLT O7 and DLT $\pm 45^\circ$ D7 series under uniaxial and biaxial bending due to linear supports.....	132
Tab. 10.3:	7-layered CLT O8 and DLT $\pm 45^\circ$ D8 series under uniaxial and biaxial bending due to point-supports.....	134
Tab. 10.4:	7-layered CLT O8 and DLT $\pm 45^\circ$ D8 series under uniaxial and biaxial bending due to linear supports.....	136
Tab. 10.5:	7-layered DLT $\pm 45^\circ$ D8 and D9 series under uniaxial and biaxial bending due to point-supports.....	138
Tab. 10.6:	7-layered DLT $\pm 45^\circ$ D8 and D9 series under uniaxial and biaxial bending due to linear supports.....	139
Tab. 10.7:	Comparison of stress resultants within two different static systems	154
Tab. 10.8:	Exemplary examined static systems featuring point-supports ((1) - (6)) and linear supports ((7) - (11)).....	156
Tab. 10.9:	Comparison of exemplary design-relevant stress values for strength verifications in the ULS, given by the 3D FEM models.....	158

Appendix

A1: Derivation of the transformed stiffness terms and engineering constants in non-principal directions	200
A2: Derivation of the ABD-E matrix	201
A3: Tabular calculation of shear correction coefficients	202
A4: Input parameters for the FE models	203
A5: Additional results of the four-point bending tests	204
A6: Computations of compression and tension forces within a square element	205
A7: Stiffness matrix of the chosen CLT and DLT elements for the deformation analysis and stress distribution analysis	207
A8: Layups of the series investigated and radar charts on the distribution of out-of-plane stiffness properties	209

A1: DERIVATION OF THE TRANSFORMED STIFFNESS TERMS AND ENGINEERING CONSTANTS IN NON-PRINCIPAL DIRECTIONS

The derivation of the transformed stiffness terms can be taken exemplarily from (SCHICKHOFER 1994) or (JONES 2014) (Equations (A1) to (A9)).

$$\bar{Q}_{11} = Q_{11} \cos^4 \theta + 2(Q_{12} + 2Q_{66}) \sin^2 \theta \cos^2 \theta + Q_{22} \sin^4 \theta \quad (\text{A1})$$

$$\bar{Q}_{12} = (Q_{11} + Q_{22} - 4Q_{66}) \sin^2 \theta \cos^2 \theta + Q_{12}(\sin^4 \theta + \cos^4 \theta) \quad (\text{A2})$$

$$\bar{Q}_{22} = Q_{11} \sin^4 \theta + 2(Q_{12} + 2Q_{66}) \sin^2 \theta \cos^2 \theta + Q_{22} \cos^4 \theta \quad (\text{A3})$$

$$\bar{Q}_{16} = (Q_{11} - Q_{12} - 2Q_{66}) \sin \theta \cos^3 \theta + (Q_{12} - Q_{22} + 2Q_{66}) \sin^3 \theta \cos \theta \quad (\text{A4})$$

$$\bar{Q}_{26} = (Q_{11} - Q_{12} - 2Q_{66}) \sin^3 \theta \cos \theta + (Q_{12} - Q_{22} + 2Q_{66}) \sin \theta \cos^3 \theta \quad (\text{A5})$$

$$\bar{Q}_{66} = (Q_{11} + Q_{22} - 2Q_{12} - 2Q_{66}) \sin^2 \theta \cos^2 \theta + Q_{66}(\sin^4 \theta + \cos^4 \theta) \quad (\text{A6})$$

$$\bar{Q}_{55} = Q_{55} \cos^2 \theta + Q_{44} \sin^2 \theta + 2Q_{45} \cos \theta \sin \theta \quad (\text{A7})$$

$$\bar{Q}_{45} = Q_{45}(\cos^2 \theta - \sin^2 \theta) + (Q_{44} - Q_{55}) \cos \theta \sin \theta \quad (\text{A8})$$

$$\bar{Q}_{44} = Q_{44} \cos^2 \theta + Q_{55} \sin^2 \theta - 2Q_{56} \cos \theta \sin \theta \quad (\text{A9})$$

Equations (A10) to (A14) give the engineering constants in non-principal directions.

$$E_x(\theta) = \left[\frac{1}{E_x} \cos^4 \theta + \left(\frac{1}{G_{xy}} - \frac{2\nu_{xy}}{E_x} \right) \sin^2 \theta \cos^2 \theta + \frac{1}{E_y} \sin^4 \theta \right]^{-1} \quad (\text{A10})$$

$$E_y(\theta) = \left[\frac{1}{E_x} \sin^4 \theta + \left(\frac{1}{G_{xy}} - \frac{2\nu_{xy}}{E_x} \right) \sin^2 \theta \cos^2 \theta + \frac{1}{E_y} \cos^4 \theta \right]^{-1} \quad (\text{A11})$$

$$G_{xy}(\theta) = \left[2 \left(\frac{2}{E_x} + \frac{2}{E_y} + \frac{4\nu_{xy}}{E_x} - \frac{1}{G_{xy}} \right) \cos^2 \theta \sin^2 \theta + \frac{1}{G_{xy}} (\cos^4 \theta \sin^4 \theta) \right]^{-1} \quad (\text{A12})$$

$$G_{yz}(\theta) = \left[\frac{1}{G_{yz}} \left(\cos^2 \theta + \sin^2 \theta \cdot \frac{G_{yz}}{G_{xz}} \right) \right]^{-1} \quad (\text{A13})$$

$$G_{xz}(\theta) = \left[\frac{1}{G_{xz}} \left(\cos^2 \theta + \sin^2 \theta \cdot \frac{G_{xz}}{G_{yz}} \right) \right]^{-1} \quad (\text{A14})$$

A2: DERIVATION OF THE OF THE ABD-E MATRIX

Equation (A15) gives the extensional stiffness terms, Equation (A16) gives the bending-extension coupling stiffness terms, Equation (A17) gives the bending stiffness terms, and Equation (A18) gives the shear stress-strain coupling stiffness terms.

In addition, Figure A1 gives the flowcharts for the determination of transformed elastic coefficients and laminate stiffness matrices.

$$A_{ij} = \int_{-t/2}^{t/2} \bar{Q}_{ij} dz = \sum_{k=1}^n [\bar{Q}_{ij}]_k \cdot (z_k - z_{k-1}) \quad (\text{A15})$$

$$B_{ij} = \int_{-t/2}^{t/2} \bar{Q}_{ij} z dz = \frac{1}{2} \sum_{k=1}^n [\bar{Q}_{ij}]_k \cdot (z_k^2 - z_{k-1}^2) \quad (\text{A16})$$

$$D_{ij} = \int_{-t/2}^{t/2} \bar{Q}_{ij} z^2 dz = \frac{1}{3} \sum_{k=1}^n [\bar{Q}_{ij}]_k \cdot (z_k^3 - z_{k-1}^3) \quad (\text{A17})$$

$$E_{ij} = k_{i,z} \cdot \int_{-t/2}^{t/2} \bar{Q}_{ij} dz = k_i^S \cdot \sum_{k=1}^n [\bar{Q}_{ij}]_k \cdot (z_k - z_{k-1}) \quad (\text{A18})$$

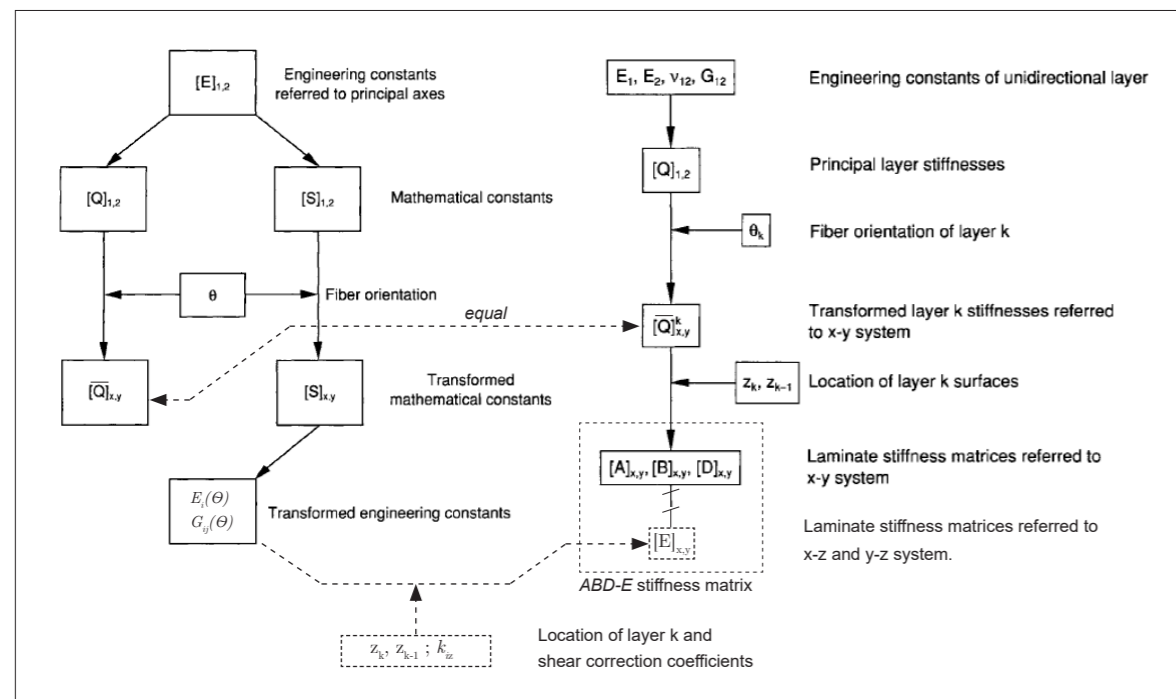


Fig. A1: Flowcharts for the determination of transformed elastic constants (left) and laminate stiffness matrices (right) based on DANIEL AND ISHAI (2006), extended by own findings (dashed lines)

A3: TABULAR CALCULATION OF SHEAR CORRECTION COEFFICIENTS

Table A1 provides the calculation of the shear correction coefficients and out-of-plane shear stiffness values according for O1 series in tabular manner ($t = 100$ mm; 20-20-20-20-20; $[0^\circ, 90^\circ, 0^\circ, 90^\circ, 0^\circ]_S$; spruce T14, EN 338).

Tab. A1: Shear correction coefficients for O1 series:

	t_i	$[n^\circ]$	E_i		z_i	$[ES]_{z_{k,max}^{z_{k,min}}}$		$\sum_{k=1}^{i-1} [ES]_{z_{k,max}^{z_{k,min}}}$		$\int_{z_{Lo}}^{z_{Li}} [ES]_{z_{k,max}^{z_{k,min}}}$		$\frac{\int_{z_{Lo}}^{z_{Li}} ([ES]_{z_{k,max}^{z_{k,min}}})^2}{G_i}$	
			x	y		x	y	x	y	x	y		
1	20	0	11071.9	372.4	-50	-8.8576E+09	-2.9794E+08	-8.8576E+09	-2.9794E+08	5.9169E+20	6.6944E+17	8.5752E+14	1.3389E+13
2	20	90	370.0	11000.0	-30	-1.4800E+08	-4.4000E+09	-9.0056E+09	-4.6979E+09	1.5999E+21	1.9692E+20	3.1998E+16	2.8539E+14
3	20	0	11071.9	372.4	0	-5.5360E+08	-1.8621E+07	-9.5592E+09	-4.7166E+09	8.7911E+20	2.2187E+20	1.2741E+15	4.4374E+15
3	20	90	370.0	11000.0	10	-5.5360E+08	1.8621E+07	-9.5592E+09	-4.6793E+09	sym.		sym.	
4	20	90	370.0	11000.0	30	-1.4800E+08	-4.4000E+09	-9.0056E+09	-4.6979E+09				
5	20	0	11071.9	372.4	50	-8.8576E+09	-2.9794E+08	-8.8576E+09	-2.9794E+08				
											Σ	6.8259E+16	9.4725E+15
											$1/k_z$	5.4516	6.2563
											k_z	0.183	0.160
											$S_{i,z}$ [MN/m]	7.961	4.891

Table A2 gives the calculation of the shear correction coefficients and out-of-plane shear stiffness values for D3 series in tabular manner ($t = 100$ mm; 20-20-20-20-20; $[0^\circ, 45^\circ, 90^\circ, -45^\circ, 0^\circ]_S$; spruce T14, EN 338).

Tab. A2: Shear correction coefficients for D3 series:

	t_i	$[n^\circ]$	E_i		z_i	$[ES]_{z_{k,max}^{z_{k,min}}}$		$\sum_{k=1}^{i-1} [ES]_{z_{k,max}^{z_{k,min}}}$		$\int_{z_{Lo}}^{z_{Li}} [ES]_{z_{k,max}^{z_{k,min}}}$		$\frac{\int_{z_{Lo}}^{z_{Li}} ([ES]_{z_{k,max}^{z_{k,min}}})^2}{G_i}$	
			x	y		x	y	x	y	x	y		
1	20	0	11071.9	372.4	-50	-8.8576E+09	-2.9794E+08	-8.8576E+09	-2.9794E+08	5.9169E+20	6.6944E+17	8.5752E+14	1.3389E+13
2	20	45	958.4	958.4	-30	-3.8334E+08	-3.8334E+08	-9.2409E+09	-6.8128E+08	1.6496E+21	5.6894E+18	1.7691E+16	6.1016E+13
3	20	90	372.4	11071.9	0	-1.8621E+07	-5.5360E+08	-9.2595E+09	-1.2349E+09	8.5624E+20	1.1305E+19	1.7125E+16	1.6383E+13
3	20	45	958.4	958.4	10	-1.8621E+07	5.5360E+08	-9.2595E+09	-1.2768E+08	sym.		sym.	
4	20	-45	958.4	958.4	30	-3.8334E+08	-3.8334E+08	-9.2409E+09	-6.8128E+08				
5	20	0	11071.9	372.4	50	-8.8576E+09	-2.9794E+08	-8.8576E+09	-2.9794E+08				
											Σ	7.1347E+16	1.8158E+14
											$1/k_z$	4.2097	1.5185
											k_z	0.238	0.659
											$S_{i,z}$ [MN/m]	7.680	12.861

A4: INPUT PARAMETERS FOR THE FE MODELS

Table A3 summarizes the most important input parameters for the FE models in tabular manner. The order of the models are given in the row 1 and follows the order of the numerical investigations in in this thesis. The boundary conditions of the static systems are described within the respective chapters.

Tab. A3: Input parameters for the FE models

model and Chapter	software version	element type	mesh size	mesh generation	mesh refinements	solver	² bond between the layers
out-of-plane shear tests, Ch. 6.2.2	Ansys, 2022 R1	Solid 186, 20 nodes	$t_i/3$ (6.67 mm)	automatic, quadratic functions	load-introduction points and screws	iterative	type composite
biaxial bending tests, Ch. 7.3.2	Ansys, 2021 R1	Solid 186, 20 nodes	¹ min $t_i/2$ 10 mm	automatic, quadratic functions	load-introduction points	direct	type composite
uniaxial 3-point bending tests, Ch. 8.3.1	Ansys, 2021 R2	Solid 186, 20 nodes	min $t_i/2$ 10 mm	automatic, quadratic functions	no	iterative	type composite
real-scale 2D models for deformation analysis Ch. 10.1	Dlubal, RFEM 5.24	Serendipity elements 8 nodes	50 mm	automatic	yes, adaptive (automatic)	iterative	rigid
real-scale 3D models for stress distribution analysis Ch. 10.2	Ansys, 2022 R1	Solid 186, 20 nodes	min $t_i/2$ 10 mm	automatic, quadratic functions	load-introduction points	iterative	type composite

¹Additional mesh-convergence studies were carried out for mesh sizes between 5 to 20 mm
²No contact was defined between the narrow sides of the single boards

A5: ADDITIONAL RESULTS OF THE FOUR-POINT BENDING TESTS

Table A4 gives the local and global moduli of elasticity E^* according to Equations (1) and (2) within EN 408, as an additional result to the four-point bending test (EN 16351). The given moduli of elasticity refer to the cross-section of D1 series only. The global modulus of elasticity is calculated with the equivalent shear modulus, considering the shear stiffness S_{xz} according to the analytical solution ($G = S_{xz}/A = 28.08 \text{ MN} / 0.12 \text{ m}^2 = 234 \text{ MPa}$).

In addition the load-deformation curves measured by the displacement transducers (w_{local} and w_{global}).

Tab. A4: Local and global MOE following the four-point bending tests on D1 series (left) and load-deformation diagram of the local and global displacements.

EN 408	
E^*_{local} [MN/m ²]	E^*_{global} ¹ [MN/m ²]
8358.48	8131.90
9246.89	9151.22
8473.94	8536.98
8648.51	9265.69
8992.17	8655.73
8245.54	7883.43
8379.07	7980.97
8044.51	8047.53
7975.09	7831.13
9195.50	9222.50

¹with equivalent shear modulus $G = 234 \text{ MN/m}^2$

Determination of effective bending stiffness values following four-point bending tests:

$$B_x = \frac{3al^2 - 4a^3}{12 \cdot \left(2 \cdot \frac{w_{EI+GA}}{F} - \frac{6a}{5S_{xz}} \right)} \quad w_{EI+GA} = \frac{3al^3 \cdot F}{24B_x} + \frac{6a \cdot F}{5S_{xz}} - \frac{Fa^3}{6B_x} \quad (\text{A19})$$

$$EI \cdot w = \frac{F \cdot l^3 \cdot \left(3 \left(\frac{a}{l} \right) - 4 \left(\frac{a}{l} \right)^3 \right)}{24} \quad w = \frac{F \cdot l^3 \cdot \left(3 \left(\frac{a}{l} \right) - 4 \left(\frac{a}{l} \right)^3 \right)}{24B_{x,eff}} \quad (\text{A20})$$

$$w_{EI+GA} = w$$

$$\frac{3al^3 \cdot F}{24B_x} + \frac{6a \cdot F}{5S_{xz}} - \frac{Fa^3}{6B_x} = \frac{F \cdot l^3 \cdot \alpha}{24B_{x,eff}} \quad \text{with } \alpha = \left(3 \left(\frac{a}{l} \right) - 4 \left(\frac{a}{l} \right)^3 \right) \quad (\text{A21})$$

$$\frac{1}{B_{x,eff}} = \frac{3a}{B_x \cdot l \cdot \alpha} + \frac{144a}{5S_{xz} \cdot l^3 \cdot \alpha} - \frac{a^3}{4B_x \cdot l^3 \cdot \alpha}$$

A6: COMPUTATIONS OF COMPRESSION AND TENSION FORCES WITHIN A SQUARE ELEMENT UNDER DIAGONAL COMPRESSION

Figure A2 reveals the stress trajectories and isoclinics of a square element under diagonal compression following (FROCHT 1931).

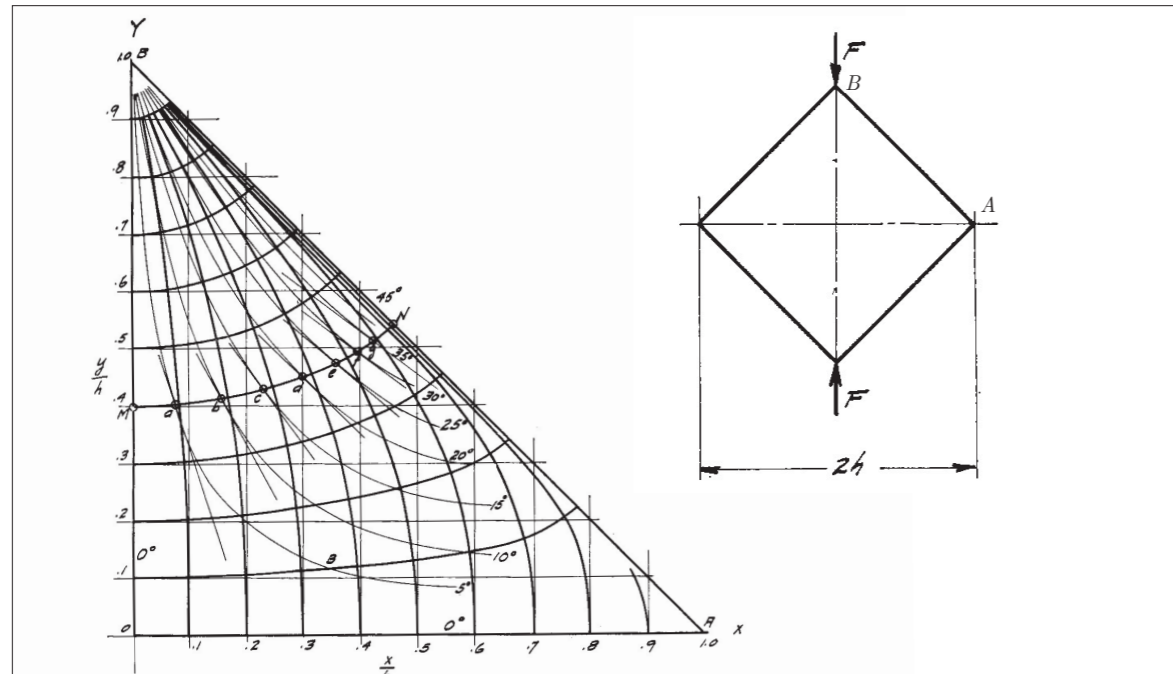


Fig. A2: Stress trajectories (heavy lines) and isoclinics (light lines), FROCHT 1931

Table A4 gives the values of the tension and compression forces for the axes of symmetry in reference to (FROCHT 1931).

Tab. A5: Tension and compression forces for the axes of symmetry within a square element

r	C_{ix}		C_{iy}	
	tension P F/h	compression Q F/h	tension P F/h	compression Q F/h
0.0	0.3668	-1.1900	0.3668	-1.1900
0.1	0.3520	-1.1300	0.3593	-1.2040
0.2	0.3100	-0.9850	0.3379	-1.2530
0.3	0.2510	-0.8000	0.3025	-1.3420
0.4	0.1860	-0.6130	0.2573	-1.4800
0.5	0.1250	-0.4730	0.2048	-1.7000
0.6	0.0741	-0.2600	0.1492	-2.0540
0.7	0.0380	-0.1270	0.0950	-2.6700
0.8	0.0151	-0.0498	0.0476	-3.9360
0.9	0.0045	-0.0170	0.0134	-7.7900
1.0	0.0010	0.0116	0.0000	∞

example: $2h = 1.6$ m; $d_1/2 = r = 0.25$ m; $C_{comp,y} = -1.337$

A7: STIFFNESS MATRICES OF THE CHOSEN CLT AND DLT ELEMENTS FOR THE DEFORMATION ANALYSIS AND STRESS DISTRIBUTION ANALYSIS

In the following, the stiffness matrices used within the real-scale FE models are given (Equations (A15) to (A19)) (for spruce T14, EN 338).

CLT O7 series, $t = 150$ mm; 30-30-30-30-30; $[0^\circ, 90^\circ, 0^\circ, 90^\circ, 0^\circ]_S$:

$$[\bar{Q}] = \begin{bmatrix} 1017.00 & 21.19 & 0 & 0 & 0 & 0 & 0 & 0 \\ 21.19 & 696.68 & 0 & 0 & 0 & 0 & 0 & 0 \\ 0 & 0 & 103.50 & 0 & 0 & 0 & 0 & 0 \\ 0 & 0 & 0 & -2.484 & -0.040 & 0 & 0 & 0 \\ 0 & 0 & 0 & -0.040 & -0.730 & 0 & 0 & 0 \\ 0 & 0 & 0 & 0 & 0 & -0.194 & 0 & 0 \\ 0 & 0 & 0 & 0 & 0 & 0 & 7.33 & 0 \\ 0 & 0 & 0 & 0 & 0 & 0 & 0 & 11.94 \end{bmatrix} \quad (\text{A22})$$

CLT O8 series, $t = 140$ mm; 20-20-20-20-20-20-20; $[0^\circ, 90^\circ, 0^\circ, 90^\circ, 0^\circ, 90^\circ, 0^\circ]_S$:

$$[Q] = \begin{bmatrix} 906.60 & 19.78 & 0 & 0 & 0 & 0 & 0 & 0 \\ 19.78 & 693.00 & 0 & 0 & 0 & 0 & 0 & 0 \\ 0 & 0 & 96.60 & 0 & 0 & 0 & 0 & 0 \\ 0 & 0 & 0 & -1.822 & -0.032 & 0 & 0 & 0 \\ 0 & 0 & 0 & -0.032 & -0.790 & 0 & 0 & 0 \\ 0 & 0 & 0 & 0 & 0 & -0.102557 & 0 & 0 \\ 0 & 0 & 0 & 0 & 0 & 0 & 11.35 & 0 \\ 0 & 0 & 0 & 0 & 0 & 0 & 0 & 8.31 \end{bmatrix} \quad (\text{A23})$$

DLT D7, $t = 150$ mm; 30-30-30-30-30; $[0^\circ, 45^\circ, 90^\circ, -45^\circ, 0^\circ]_S$:

$$[Q] = \begin{bmatrix} 891.40 & 146.90 & 0 & 0 & 0 & -4.806 & 0 & 0 \\ 146.90 & 570.90 & 0 & 0 & 0 & -4.806 & 0 & 0 \\ 0 & 0 & 229.24 & -4.806 & -4.806 & 0 & 0 & 0 \\ 0 & 0 & -4.806 & -2.650 & -0.162 & 0 & 0 & 0 \\ 0 & 0 & -4.806 & -0.162 & -0.318 & 0 & 0 & 0 \\ -4.806 & -4.806 & 0 & 0 & 0 & -0.316 & 0 & 0 \\ 0 & 0 & 0 & 0 & 0 & 0 & 11.52 & 0 \\ 0 & 0 & 0 & 0 & 0 & 0 & 0 & 19.29 \end{bmatrix} \quad (\text{A24})$$

DLT D8, $t = 140$ mm; 20-20-20-20-20-20-20; $[0^\circ, 90^\circ, 45^\circ, 0^\circ, -45^\circ, 90^\circ, 0^\circ]_S$:

$$[Q] = \begin{bmatrix} 823.78 & 103.61 & 0 & 0 & 0 & -2.136 & 0 & 0 \\ 103.61 & 609.14 & 0 & 0 & 0 & -2.136 & 0 & 0 \\ 0 & 0 & 180.43 & -2.136 & -2.136 & 0 & 0 & 0 \\ 0 & 0 & -2.136 & -1.701 & -0.069 & 0 & 0 & 0 \\ 0 & 0 & -2.136 & -0.069 & -0.839 & 0 & 0 & 0 \\ -2.136 & -2.136 & 0 & 0 & 0 & -0.194 & 0 & 0 \\ 0 & 0 & 0 & 0 & 0 & 0 & 11.65 & 0 \\ 0 & 0 & 0 & 0 & 0 & 0 & 0 & 8.05 \end{bmatrix} \quad (\text{A25})$$

DLT D9, $t = 140$ mm; 20-20-20-20-20-20-20; $[0^\circ, 45^\circ, -45^\circ, 90^\circ, 45^\circ, -45^\circ, 0^\circ]_S$:

$$[Q] = \begin{bmatrix} 738.90 & 187.40 & 0 & 0 & 0 & -2.136 & 0 & 0 \\ 187.40 & 525.30 & 0 & 0 & 0 & -2.136 & 0 & 0 \\ 0 & 0 & 264.26 & -2.136 & -2.136 & 0 & 0 & 0 \\ 0 & 0 & -2.136 & -1.906 & -0.206 & 0 & 0 & 0 \\ 0 & 0 & -2.136 & -0.206 & -0.360 & 0 & 0 & 0 \\ -2.136 & -2.136 & 0 & 0 & 0 & -0.331 & 0 & 0 \\ 0 & 0 & 0 & 0 & 0 & 0 & 11.23 & 0 \\ 0 & 0 & 0 & 0 & 0 & 0 & 0 & 14.22 \end{bmatrix} \quad (\text{A26})$$

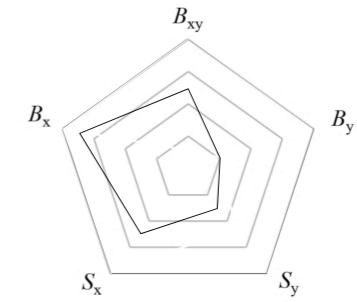
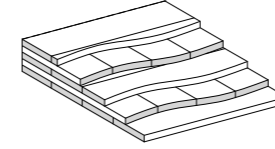
Appendix A8 summarizes the layups of the series investigated (analytical, experimental, and numerical) within this thesis and gives radar charts on their stiffness values (for spruce T14, EN 338). The radar charts provide a qualitative comparison of the bending, shear, and torsional stiffness values of each series. The maximum values of the respective stiffness parameters define the reference values within the charts for each series of the same thickness.

In addition, Tab. A6 summarizes the stiffness parameters of each series.

Tab. A6: Stiffness properties of O1, D3, D4, O5, D5, and D6 series (spruce T14)

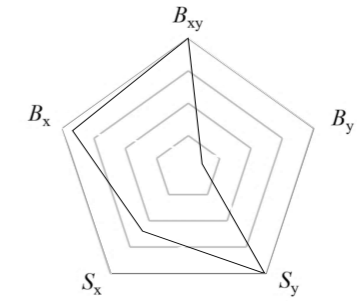
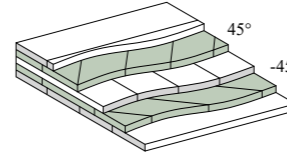
series	t [mm]	B_x [MNm ² /m]	B_y [MNm ² /m]	B_{xy} [MNm ² /m]	S_{xz} [MN/m]	S_{yz} [MN/m]
O7 CLT	100	0.74	0.22	0.12	7.96	4.89
D3 DLT±45°	100	0.79	0.09	0.19	7.68	12.86
D4 DLT±30°	100	0.84	0.06	0.17	9.52	10.33
O5 CLT	200	5.90	1.73	0.92	15.92	9.78
D5 DLT±45°	200	6.29	0.76	1.50	15.36	25.72
D6 DLT±30°	200	6.73	0.46	1.36	19.03	20.66

t_i 20-20-20-20-20
 Θ_i 0°, 90°, 0°, 90°, 0°



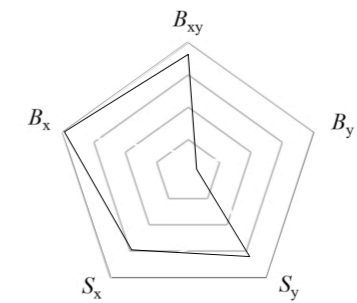
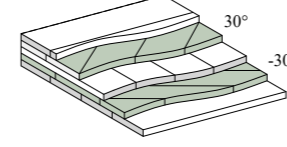
CLT O1
 $t = 100$ mm
 $B_{xy} = 0.12$
 $B_x = 0.74$
 $B_y = 0.22$
 $S_x = 7.96$
 $S_y = 4.89$

t_i 20-20-20-20-20
 Θ_i 0°, 45°, 90°, -45°, 0°



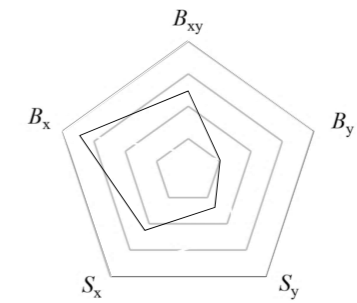
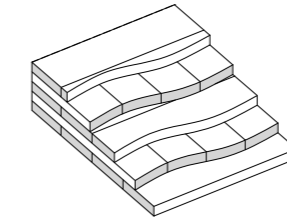
DLT D3
 $t = 100$ mm
 $B_{xy} = 0.19$
 $B_x = 0.79$
 $B_y = 0.09$
 $S_x = 7.68$
 $S_y = 12.86$

t_i 20-20-20-20-20
 Θ_i 0°, 30°, 90°, -30°, 0°



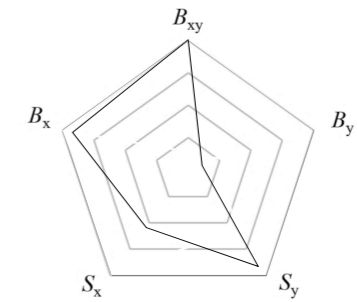
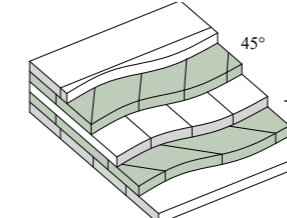
DLT D4
 $t = 100$ mm
 $B_{xy} = 0.17$
 $B_x = 0.84$
 $B_y = 0.06$
 $S_x = 9.52$
 $S_y = 10.33$

t_i 40-40-40-40-40
 Θ_i 0°, 90°, 0°, 90°, 0°



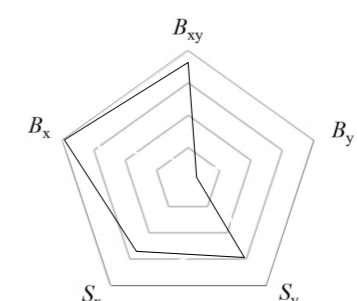
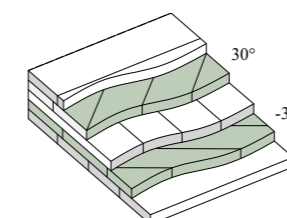
CLT O5
 $t = 200$ mm
 $B_{xy} = 0.92$
 $B_x = 5.90$
 $B_y = 1.73$
 $S_x = 15.92$
 $S_y = 9.78$

t_i 40-40-40-40-40
 Θ_i 0°, 45°, 90°, -45°, 0°



DLT D5
 $t = 200$ mm
 $B_{xy} = 1.50$
 $B_x = 6.29$
 $B_y = 0.76$
 $S_x = 15.36$
 $S_y = 25.72$

t_i 40-40-40-40-40
 Θ_i 0°, 30°, 90°, -30°, 0°



DLT D6
 $t = 200$ mm
 $B_{xy} = 1.36$
 $B_x = 6.73$
 $B_y = 0.46$
 $S_x = 19.03$
 $S_y = 20.66$

A8: LAYUPS OF THE SERIES INVESTIGATED AND RADAR CHARTS OF THE OUT-OF-PLANE STIFFNESS DISTRIBUTION

series:

O1, D3, D4,
O5, D5, D6

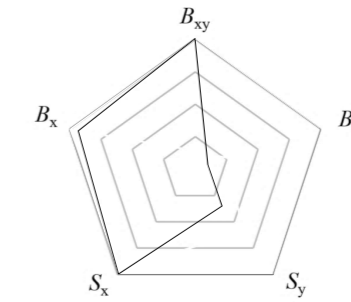
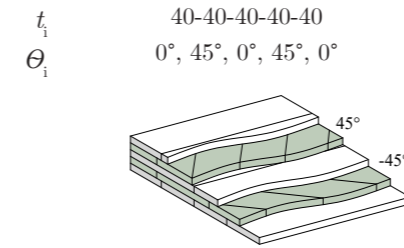
unfold →

Appendix A8 summarizes the layups of the series investigated (analytical, experimental, and numerical) within this thesis and gives radar charts on their stiffness values (for spruce T14, EN 338). The radar charts provide a qualitative comparison of the bending, shear, and torsional stiffness values of each series. The maximum values of the respective stiffness parameters define the reference values within the charts for each series of the same thickness.

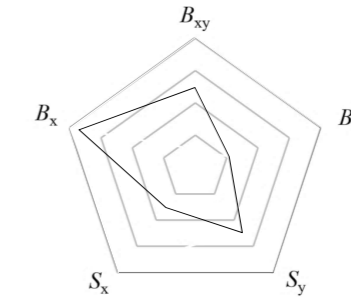
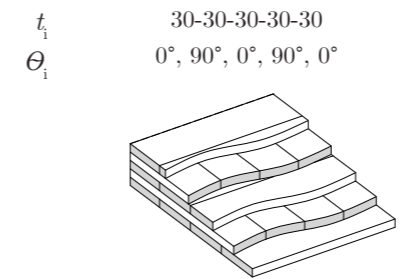
In addition, Tab. A7 summarizes the stiffness parameters of each series.

Tab. A7: Stiffness properties of D1, O7, D7, O8, D8, and D9 series (spruce T14)

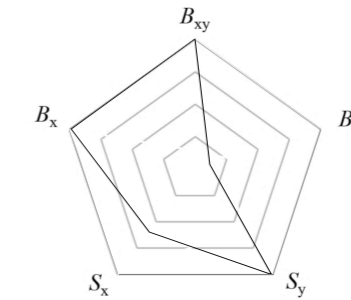
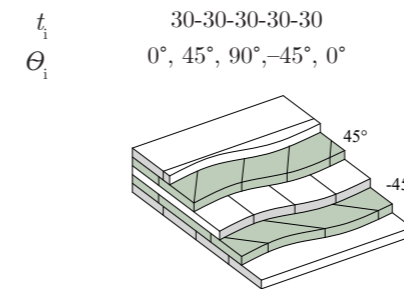
series	t [mm]	B_x [MNm ² /m]	B_y [MNm ² /m]	B_{xy} [MNm ² /m]	S_{xz} [MN/m]	S_{yz} [MN/m]
D1 uDLT+45°	200	6.35	0.70	1.50	28.08	9.94
O7 CLT	150	2.48	0.73	1.94	7.33	11.94
D7 DLT±45°	150	2.65	0.32	3.16	11.52	19.29
O8 CLT	140	1.82	0.79	1.03	11.35	8.31
D8 DLT±45°	140	1.70	0.84	1.94	11.65	8.05
D9 DLT±45°	140	1.91	0.36	3.31	11.23	14.22



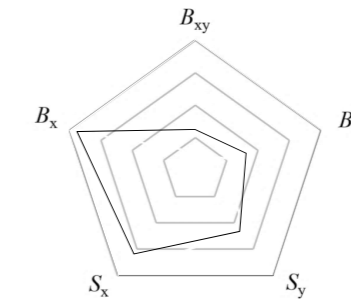
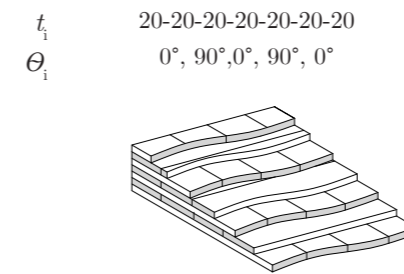
DLT D1
 $t = 200$ mm
 $B_{xy} = 1.50$
 $B_x = 6.35$
 $B_y = 0.70$
 $S_x = 28.08$
 $S_y = 9.94$



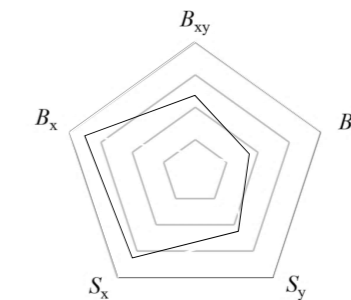
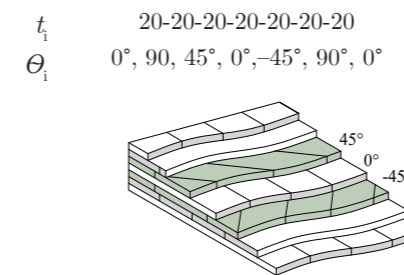
CLT O7
 $t = 150$ mm
 $B_{xy} = 1.94$
 $B_x = 2.48$
 $B_y = 0.73$
 $S_x = 7.33$
 $S_y = 11.94$



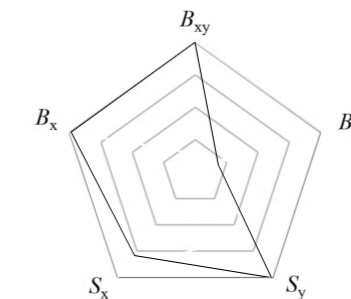
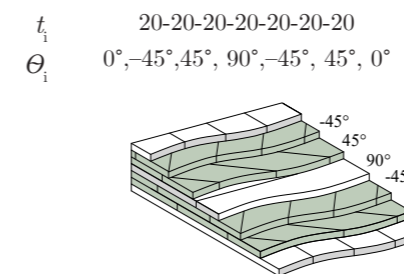
DLT D7
 $t = 150$ mm
 $B_{xy} = 3.16$
 $B_x = 2.65$
 $B_y = 0.32$
 $S_x = 11.52$
 $S_y = 19.29$



CLT O8
 $t = 140$ mm
 $B_{xy} = 1.03$
 $B_x = 1.82$
 $B_y = 0.79$
 $S_x = 11.35$
 $S_y = 8.31$



DLT D8
 $t = 140$ mm
 $B_{xy} = 1.94$
 $B_x = 1.70$
 $B_y = 0.84$
 $S_x = 11.65$
 $S_y = 8.05$



DLT D9
 $t = 140$ mm
 $B_{xy} = 3.31$
 $B_x = 1.91$
 $B_y = 0.36$
 $S_x = 11.23$
 $S_y = 14.22$

A8: LAYUPS OF THE SERIES INVESTIGATED AND RADAR CHARTS OF THE OUT-OF-PLANE STIFFNESS DISTRIBUTION

series:

D1

O7, D7

O8, D8, D9

please unfold →

*"Die Zweifel gehören zum Prozess,
aber nicht zum Resultat."*

- Peter Zumthor -